Functionalization of Oxidic Semiconductor Surfaces by Covalently Bound Molecular Thin Films

Philipps Universität Marburg

Dissertation

zur
Erlangung des Doktorgrades
der Naturwissenschaften
(Dr. rer. nat.)

dem

Fachbereich Physik
der Philipps-Universität Marburg

vorgelegt von

Alexandra Ostapenko

aus

Tscheboksary, Russland

Marburg/Lahn, 2016

Contents

Abstract

The study was intended to achieve covalent fixation of self-assembled monolayers (SAMs) on metal oxide surfaces, in particular rutile titanium dioxide (TiO_2) and zinc oxide (ZnO), and to distinguish the microscopic character of their linkage. Unlike in widely studied systems of thiol-based organic layers on noble metal surfaces like gold, molecules with carboxylic acid (CA) and phosphonic acid (PA) anchoring units are used to functionalize metal oxide surfaces. For this purpose CA SAMs exhibit good electron coupling with oxidic surfaces, though PA-based modifiers show longer stability. SAMs are powerful tools in tuning the interfacial electronic properties of a wide range of surfaces. In addition, they allow a selective covalent attachment of molecular dyes to metal oxides in thin film electronic devices such as organic light emitting diodes, photovoltaics, for example in dye-sensitized solar cells, and field effect transistors. For this purpose, the electronic coupling at the organic/inorganic heterojunction is significant since the charge transport across the heterojunction is decisive for charge carrier separation. Though such modifications have already been successfully implemented in device applications, a microscopic understanding of the binding mechanism as well as the thermal and chemical stability of such molecular systems has not yet been achieved. Unlike TiO_2, where only the $TiO_2(1\,1\,0)$ surface is stable, zinc oxide has several stable orientations including the polar terminated $(0\,0\,0\pm1)$ or non-polar $(1\,0\,\bar{1}\,0)$ surfaces, which allows its implementation for many purposes in model studies as well as in device application.

To avoid the typically problematic oxygen reduction at the surface during the preparation of metal oxide samples in ultrahigh vacuum, a specially designed chamber was constructed and successfully turned into service. Small SAMs of CA or PA with phenyl or aliphatic backbone on top of well-defined single crystalline metal oxides have been used as model systems in this work. Monolayer films have been prepared by immersing samples in ethanolic solutions and its structure and thermal stability have been analyzed by combining of atomic force microscopy (AFM), X-ray photoelectron spectroscopy (XPS), near-edge X-ray absorption spectroscopy (NEXAFS) and thermal desorption spectroscopy (TDS) measurements.

It was shown in this work, that molecules with CA anchoring attached to ZnO surfaces do not form stable monolayer films. Those films are rather weakly attached to surface or poorly ordered. In contrast, PA-based SAMs exhibit high thermal stability indicating a strong bonding to the surface. TDS spectra reveal two desorption channels at 690 K and 720 K, which are attributed to bi- and tri-dentate binding modes found in previous studies. By analyzing the molecular dichroisms in NEXAFS measurements, the conclusion has been made, that molecules within the film are upright oriented. The film structure and stability was found to be similar for different surface terminations (oxygen-, zinc- and mixed-terminated) as well as surface roughness. In addition, it was shown that variations in the molecule structure by molecular backbone substitution do not significantly affect the film stability and molecular orientation, though aromatic PA-based SAMs were found to form more ordered, dense films than aliphatic. Besides, an additional parasitic chemical reaction was found during the immersion, which results in the dissolution of surface Zn atoms and the formation of precipitations. From the collaborative work with the group of Prof. Dr. S. Dehnen precipitations have been identified as zinc-phosphonates. The group of Prof. Dr. B. Meyer from Erlangen demonstrated from density functional calculations, that the formation of zinc-phosphonate phase is energetically more favorable than the monolayer formation. In previous studies it was shown, that the ZnO surface can be dissolved in strong acids and its stability depends on the pH value of the solution. However, increased etching efficiency has been found when using aqueous buffer solutions. This is attributed to the presence of water in the reaction. Another important parameter is the presence of surface defects like step edges, which act as nucleation sites for the formation of precipitations. Reduced etching was found for phenylphosphinic acid.

To overcome this complication, another preparation technique has been introduced, namely organic molecular beam deposition. This method allows the *in-situ* preparation of monolayer films by desorbing multilayers from the surface, which are stable only up to 400K. The quality of these films is similar to wet-chemically prepared monolayers. The question about the influence of surface roughness or hydroxylation on the film structure was addressed and experimentally realized by roughening samples with an ion beam or precoating metal oxides with a NaOH layer. Two binding modes have been identified and attributed to the bidentate and tridentate PA attachment. The tridentate binding scenario was found to be more preferable, while the presence of H- or OH- surface groups hampers its formation. Experimental results were supported by density functional theory (DFT) calculations.

The results obtained for the PA-SAMs on rutile $TiO_2(1\,1\,0)$ present similar film stability as for ZnO. Unfortunately, the poor conductivity of TiO_2 makes the XPS and NEXAFS investigations complicated due to the charging effect. This can be solved by doping crystals

with Nb, while Cr doping does not suppress the surface charging. These samples can be prepared by cycles of ion bombardment and annealing in oxygen. Such a preparation results in sharp patterns in low-energy electron diffraction measurements, proving the high quality of the surfaces. Nevertheless, we observe a surface reconstruction of Nb-doped titanium dioxide after a continued annealing process. Based on first measurements, we believe that Nb separation takes place in the bulk and its subsequent segregation at domain boundaries and the surface occurs.

The present work treats and summarizes experimental findings about the SAMs formation on oxidic surfaces. The results obtained confirm the importance of a detailed, comprehensive analysis of such experiments. The main achievement of this work is a very profound investigation of the influence of preparation pathways as well as structure of supporting substrates on the resulting thin film quality and stability. Many essential issues crucial for the attachment of PA-based SAMs on metal oxide surfaces were addressed for the first time in this work. Obtained results reveal possibilities for further investigations of some phenomena.

Zusammenfassung (Abstract in German)

Ziel dieser Arbeit war die Untersuchung der kovalenten Bindung von selbstassemblierten Monolagen (SAMs) auf Metalloxidoberflächen, insbesondere Rutil Titandioxid (TiO_2) und Zinkoxid (ZnO), und die Charakterisierung der mikroskopischen Eigenschaften dieser Bindung. Im Gegensatz zu dem eingehend untersuchten System Thiol-basierter organischer Schichten auf Edelmetallen (z.B. Gold) wurden dazu Carboxyl- (CA) und Phosphorsäure (PA) Ankergruppen eingesetzt um die Metalloxidoberflächen zu funktionalisieren. Während CA SAMs gute Elektronen-Kopplung mit Oxid Oberflächen aufweisen, zeigen PA-basierte Modifikatoren höhere Stabilität. SAMs sind ein vielversprechänder Ansatz um die Grenzflächeneigenschaften einer großen Bandbreite von Oberflächen zu beeinflussen, sowie auch zur selektiven Anbindung molekularer Farbstoffe an Metalloxide. Dies wird beispielsweise in Dünnfilm-basierten elektronischen Geräten, wie organischen lichtemittierenden Dioden, Solarzellen wie der Grätzel-Zelle und Feldeffekttransistoren eingesetzt. Hierfür ist besonders die elektronische Kopplung des organisch/anorganischen Heteroübergangs bedeutsam, da der Ladungstransport über den Heteroübergang entscheidend für die Trennung der Ladungsträger ist. Obwohl solche Modifikationen bereits erfolgreich in elektronischen Anwendungen eingesetzt werden, fehlt bisher ein tiefgreifendes mikroskopisches Verständnis der Bindungsmechanismen und der thermischen und chemischen Stabilität solcher molekularer Systeme. Im Gegensatz zu TiO_2, bei welchem nur $TiO_2(1\,1\,0)$ Oberflächen stabil sind, stehen bei Zinkoxid mehrere mögliche stabile Orientierungen zur Verfügung. Hierzu zählt neben der polaren $(0\,0\,0\pm 1)$ auch die unpolare $(1\,0\,\overline{1}\,0)$ Oberflächenterminierung, wodurch ZnO für Oberflächenexperimente und unterschiedliche Anwendungen vielseitig eingesetzt werden kann.

Um die Sauerstoffverarmung an der Oberfläche während der Präparation der Metalloxidproben in Ultrahochvakuum zu verhindern, wurde eine spezielle Vakuumkammer entworfen und erfolgreich aufgebaut. In dieser Untersuchung wurden kleine SAMs mit CA oder PA, mit einem Rückgrat aus Phenylringen oder aliphatischen Ketten, auf wohldefinierten einkristallinen Metalloxiden als Modellsystem untersucht. Monolagenschichten wurden nasschemisch

via Immersion der Proben in Ethanollösungen synthetisiert und ihre Struktur und thermische Stabilität mittels Rasterkraftmikroskopie (AFM), Röntgenphotoelektronenspektroskopie (XPS), Röntgen-Nahkanten-Absorptionsspektroskopie (NEXAFS) und Thermodesorptionsspektroskopie (TDS) analysiert.

In dieser Arbeit konnte gezeigt werden, dass Moleküle mit CA-Verankerung an ZnO-Oberflächen keine stabilen Monolagen bilden. Die Schichten sind nur schwach gebunden oder schlecht geordnet. Im Gegensatz hierzu weisen PA-basierte SAMs eine hohe thermische Stabilität auf. TDS Spektren zeigen zwei Desorptionskanäle bei 690 K und 720 K, welche in früheren Studien auf bi- und tridentate Bindungen zurückgeführt werden konnten. Durch Analyse des molekularen Dichroismus in NEXAFS-Messungen konnte nachgewiesen werden, dass die Moleküle bevorzugt aufrecht orientiert sind. Die Schichtstruktur und Stabilität war für unterschiedliche Oberflächenterminierungen (Sauerstoff-, Zink- oder gemischt terminiert) sowie Oberflächenrauheit vergleichbar. Darüberhinaus konnte gezeigt werden, dass eine Variation der molekularen Struktur durch Substitution des molekularen Rückgrats die Schichtstabilität und Molekülorientierung nicht signifikant beeinflusst. Allerdings zeigten aromatische PA-basierte SAMs höher geordnete und dichtere Schichten als aliphatische. Während der Immersion konnte jedoch eine störende chemische Reaktion beobachtet werden, welche zur Ablösung von Oberflächenzinkatomen und der Bildung einer Oberflächenpräzipitation führt. Durch Zusammenarbeit mit der Arbeitsgruppe von Prof. Dr. S. Dehnen konnten diese Oberflächenpräzipitationen als Zinkphosphonate identifiziert werden. Die Arbeitsgruppe von Prof. Dr. B. Meyer aus Erlangen konnte mit Hilfe von Dichtefunktionaltheorie (DFT) Rechnungen nachweisen, dass die Bildung der Zinkphosphonatphase energetisch günstiger als die Bildung der Monolage ist. In früheren Untersuchungen konnte gezeigt werden, dass Zinkoxid mit starken Säuren gelöst werden kann und dass seine Stabilität vom pH-Wert der Lösung abhängt. Eine erhöhte Effizienz des Ätzvorgangs konnte durch Verwendung einer wässrigen Pufferlösung erzielt werden. Grund hierfür ist die Anwesenheit von Wasser in der Reaktion. Ein weiterer wichtiger Parameter sind Oberflächenfehlstellen, wie Substratsstufen, welche als Nukleationskeime für die Bildung der Präzipitationen agieren. Eine geringere Oberflächenablösung wurde bei Verwendung von Phenylphosphonsäure festgestellt.

Um die genannten Schwierigkeiten zu vermeiden wurde als alternative Präparationstechnik die organische Molekularstrahldeposition eingeführt. Diese Methode erlaubt die *in-situ* Präparation von Monolagen durch die Desorption von Multilagen von der Oberfläche, welche nur bis zu Temperatur von 400 K stabil sind. Die Qualität der gebildeten Schichten ist vergleichbar mit nasschemisch erzeugten Monolagen. Die Frage des Einflusses der Oberflächenrauigkeit oder Hydroxylierung des Films wurde experimentell durch Aufrauen

der Proben mittels Ionenstrahlung oder Vorbeschichtung mit NaOH untersucht. Zwei weitere Bindungen wurden identifiziert, wobei das tridentate Bindungsverhalten bevozugt ist und H- oder OH-Gruppen an der Oberfläche die tridentate Bindung behindern. DFT Berechnungen in der Gruppe von Prof. Dr. B. Meyer zeigen Monolagen Bildungsschritte, welche die experimentellen Ergebnisse unterstützen.

Die Ergebnisse für PA-SAMs auf Rutil $TiO_2(1\,1\,0)$ zeigen eine vergleichbare Schichtstabilität wie für ZnO. Die geringe Leitfähigkeit von TiO_2 erschwert allerdings Untersuchungen mit XPS oder NEXAFS durch Oberflächenaufladung. Dies kann durch die Dotierung des Kristalls mit Nb gelöst werden, während eine Dotierung mit Cr die Oberflächenaufladung nicht verhindert. Die Proben können durch Schritte von Ionenbeschuss und Ausglühen unter Sauerstoff präpariert werden. Sie zeigen scharfe Reflexe in LEED-Experimenten, was die Qualität der Proben nachweist. Allerdings kann die TiO_2-Oberfläche durch kontinuierliches Ausglühen rekonstruiert werden. Aus ersten Messungen kann auf eine Ablösung von Nb aus dem Festkörper und eine nachfolgende Oberflächensegregation geschlossen werden.

Diese Thesis fasst Erkenntnisse experimenteller Untersuchungen über die Formation von SAMs auf Oxidoberflächen zusammen. Die gesammelten Ergebnisse bestätigen die Wichtigkeit einer detaillierten, umfassenden Analyse der Experimente. Das Hauptziel dieser Arbeit ist eine eingehende Untersuchung sowohl der Einflüsse von Präparierungsmethoden, als auch der Struktur der unterstützenden Substrate auf die Dünnfilmqualität und -stablität. Viele zentrale Faktoren, die für die Anlagerung von PA-basierten SAMs auf Metalloxidoberflächen notwendig sind, werden in dieser Arbeit erstmalig untersucht. Die Ergebnisse eröffnen neue Möglichkeiten um einige Phänomene näher zu untersuchen.

CHAPTER 1

Introduction

1.1 Motivation and Objective

Since the first discovery of photoconductivity in antracene molecules in 1906[1] and first demonstrations of conducting organic materials utilized in classical semiconductor devices in mid 70's [2–7] a major breakthrough in the field of *Organic Electronics* was observed which opened many new and exciting applications. [8–12] Nowadays organic electronics emerges science and engineering and includes a wide variety of scientific disciplines like chemistry, materials science, physics and device engineering. The combination of organic and inorganic materials can be used as an active component in electronic and optical devices especially organic light emitting diodes (OLEDs), organic photovoltaic cells (OPVs), organic thin film transistors (OTFTs). In comparison to traditional, typically silicon-based inorganic semiconductors used in optoelectronic devices, organic semiconductors possess several unique technologically valuable properties such as that they are lightweight, not expensive and can be processed at low-temperatures and from a solution allowing large area coverage and low cost device manufacturing even on flexible substrates. [13–19] Moreover, recent success in material science and chemistry support the adjustment of organic compounds depending on the areas of future application. For example, a technological application of OLEDs has already been introduced in thin high-resolution displays which unlike traditional liquid-crystal displays (LCDs) have faster response time, higher brightness and contrast, wider viewing angles and generate their own light. Thereby they enable a minimization of size and power requirements. In addition, a major work is currently focused on adopting this technology into flexible displays. Regarding organic photovoltaic cells commercial inorganic materials still outperform organic materials. However, a power conversion efficiency (PCE) for organic

solar cells was already obtained above 11.5 %.[20–22] Through continued progresses in both, new material development and device innovation a further increase in the device PCE of up to 15% or even more is predicted.[23–25]

Such organic/inorganic devices also called as hybrid devices have similar "sandwich" structure which includes different functional layers on top of each other: two electrodes of which at least one is transparent in the visible light range and organic/inorganic or organic/organic active layers. The active layer typically incorporates an organic hole transport layer (HTL) and an electron transport layer (ETL). Simplified structures of such hybrid devices are visualized in Figure 1.1. Note, that real devices can have more complex architecture and include additional functional layers. As transmitting electrodes in thin film solar cells or flat panel displays graphene or transparent conductive oxides (TCOs), like indium tin oxide (ITO) or zinc oxide (ZnO) are utilized.[26–34] TCOs are electrical materials showing good conductive properties and a comparably low absorption of light. Their conductivity can be adjusted from conducting via semiconducting to insulating as well as their transparency can be tuned depending on a future application. Among different materials ZnO is a promising wide band gap semiconductor and an electron acceptor due to its high transparency in the visible and near visible spectral region, non-toxicity, low cost and abundance in earth crust.[35–39] Moreover, ZnO allows preparation of highly-doped films with high electron density and low resistivity as well as deposition of TCO layers on large areas by both vacuum-based and wet-chemical methods. The morphology of ZnO varies from single crystals and grown crystalline films to powder or well-ordered ZnO nanostructures, which supports its application in devices with different architecture.[38–41] In addition, single crystalline ZnO is a good choice for model studies of molecular adsorption since it obtains polar and non-polar surfaces. In the photovoltaic and photocatalytic application wide band gap semiconductor titanium dioxide (TiO$_2$) material is mostly utilized.[42–48] In addition to its excellent photocatalytic activity, other key functional features of TiO$_2$ are its chemicall stability, non-toxicity, exceptional biocompatibility, transparency and low cost. Changing a chemical composition of TiO$_2$ allows to tune its electrical conductivity. Organic semiconductor materials traditionally used in active layers are conjugated organic molecules or polymers.[49] Polymers often have a good solubility unlike majority of polycyclic aromatic hydrocarbons (PAHs). However, modifying PAHs by attachment of side-groups changing structure and composition of these molecules enables some semiconducting molecules to be processed from a solution.

Despite the similar device architecture processes which occur in OLEDs and OPVs slightly differ. In such hybrid systems, where the organic semiconducting material is used as an active component, the charge injection from an electrode into the organic material is ruled by energy barriers which can be crucial for the device performance.[50,51] In organic

materials the primary excitation is represented by a system of bound electron and hole pairs called excitons. The boundary between a donor material and an acceptor material influences
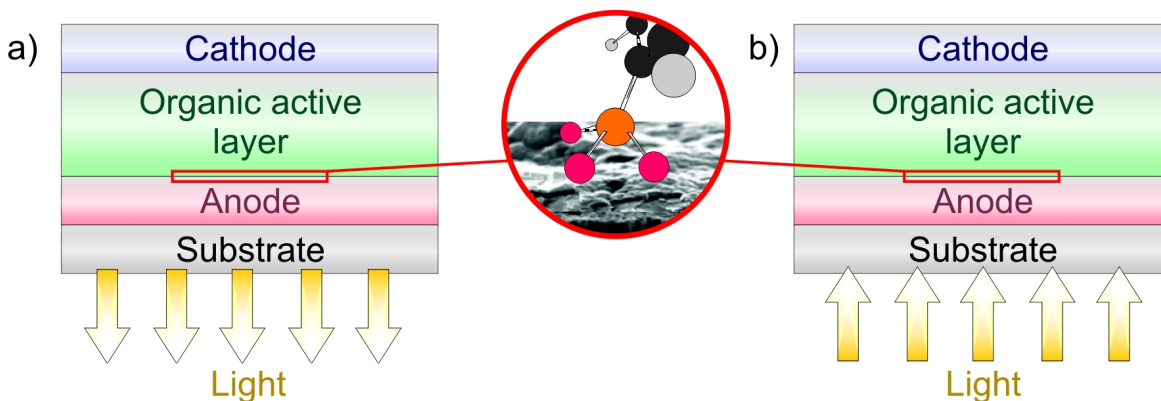
Figure 1.1: Simplified schematic illustration of basic organic electronic devices: (a) OLEDs, (b) OPVs. The interface between an organic material and a transparent anode (ITO or ZnO) is crucial for charge injection and charge recombination processes and can be tuned by means of SAMs.

a charge separation before excitons recombine. Charge injection barriers are defined as the difference between the Fermi level E_F of the anode and the highest unoccupied molecular orbital (HOMO) level of the organic material, namely hole-injection barrier (HIB), and the energy difference between the cathode and the lowest unoccupied molecular orbital (LUMO) of the organic material, namely the electron-injection barrier (EIB).[52] Additional important parameters that directly influence the device operation are the work functions of electrodes (a minimum energy required to extract an electron from the Fermi level above the vacuum level).[52–54] Basic steps of the light absorption and conversion to a current in OPVs or light emission in OLEDs include: photon absorption, exiton formation and diffusion, exciton dissociation and charge separation, charge transport to the electrodes, charge collection at the electrodes or sending voltage between electrodes, the current flows from the cathode to the anode, electrons and holes gain together at the organic heterojunction, recombination of holes and electrons, photon emission. For the effective charge carrier injection the work functions of the anode and the LUMO energy level (typically higher) and the cathode and the HOMO energy level (typically lower) of the organic semiconductor material have to match. Otherwise in order to overcome the HIB and EIB barriers high voltages have to be applied to the heterojunction, which hampers the device performance.

The alignment of energy levels can be achieved by means of a contact primer layer which self-assembles on the electrode surface.[55–61] Such self-assembled monolayers (SAMs) composed of densely packed organic molecules with permanent dipole moments have already been successfully used for tuning the work function of an anode to improve the device

performance. Their low-temperature solution deposition, selective adsorption and ability to form strong chemical attachment toward semiconductor surfaces together with the ability to carry specific functionalities make SAMs a key element in hybrid heterostructures. The pioneer system in this field are organo thiols on gold, while corresponding modification of metal oxide surfaces is generaly obtained by carboxylic acid, phosphonic acid or silanes. Excellent stability of phosphonic acid towards exposure to ambient, illumination or temperature make these groups a promising unit for technological application. Besides, SAMs can be used as coupling units for selective adsorption of large dye molecules in Grätzel solar cells. Such dye-sensitized solar cells (DSSCs) are based on the light absorption by means of an organic dye, mostly phthalocyanines, covalently attached to TiO_2 and placed between two electrodes in an electrolyte solution containing iodine ions, which allows low-cost power generation. PCE in such devices depends not only on the range of the solar energy absorption by a dye but also on the quality of its attachment. Since many essential processes such as charge injection in OLEDs and charge recombination in OSCs occur at the interface between organic/inorganic and in some cases organic/organic layers the quality, structure and stability of such SAMs are critical for the resulting device performance (cf. Fig. 1.1). Moreover, it was shown, that in OFETs ~95 % of the charge transport properties are defined within the first few layers at an interface.[62] Therefore, the understanding of molecular adsorption and how different surface morphology of a substrate material affects SAMs formation and stability is necessary and addressed in this work. The research presented here contributes to the systematic investigation of phosphonic acid based SAMs, their structure and stability on zinc oxide and titanium dioxide regarding different ZnO surface termination and surface pretreatment. In the framework of oxidic substrates stability during the SAM formation different preparation routes are thoughtfully investigated.

1.2 Scope of this Thesis

The interface structure of hybrid devices is crucial for the resulting device performance and can limit some technologically important properties like stability or manufacturing from a solution. The aim of this thesis is to achieve covalent fixation of organic molecules on metal oxide surfaces and to analyze their attachment mechanism, structure and stability. It is also important to determine critical parameters for the resulting film quality in the surface fictionalization by SAMs as well as to establish reliable experimental conditions or alternative preparation methods. In order to grasp the importance of interface physics on the molecular attachment, well defined model systems are required. The essential part of

the current study is focused on the modification of ZnO single crystalline samples owing different surface terminations by means of phosphonic acid based SAMs. In addition, SAMs on single crystalline TiO_2 samples have been studied.

The thesis comprises six parts. Introduction is followed by Chapter 2 which gives an overview of materials and sample preparation techniques. Structure and main properties of metal oxides and organic molecules relevant for the current research are described. In addition, preparation pathways for metal oxide substrates and organic thin films, their advantages and limitations are discussed.

In order to course results section and understand experimental findings basics of used techniques are summarized in Chapter 3. It includes description of techniques employed for morphological and structural analysis, elemental composition analysis and thermal stability.

Experimental findings concerning the reliability and universality of SAMs formation by wet-chemical method are discussed in Chapter 4. Phophonic acid SAM formation on ZnO is limited by a number of process parameters and contend with surface etching. Devoted to the importance of the interface degradation on the resulting device efficiency main reaction parameters which influence ZnO etching are determined. Theoretical support to experimental results is provided.

In Chapter 5 an alternative to immersion preparation accomplished by vacuum deposition is proposed and successfully implemented in the experiment. Stability and film structure of SAMs prepared by two different methods are examined and compared. Besides, important questions allowed by the new *in-situ* preparation concerning the influence of the sample surface structure on the film formation are addressed.

Chapter 6 covers a comprehensive analysis on the influence of SAMs backbone substitution on film structure and stability. The assembly of hardly studied phosphinic acid SAMs on ZnO samples is investigated in the chapter as well. To expand the study molecular attachment by carboxylic acid and thiol has been analysed and was found to be less promising than phosphonic acid based SAMs in terms of thermal stability.

The final section of the thesis (Chapter 7) reports results on the use of TiO_2 crystals for phosphonic acid SAMs attachment and associated to that challenges including surface charging and surface reconstruction of doped TiO_2 crystals. Supplementary information about the Nb incorporation into TiO_2, a brief summary of literature reports about the metastable character of doped TiO_2 and first experimental results on this topic are given in Appendix 1, Appendix 2 and Appendix 3 respectively.

CHAPTER 2

Materials and Sample Preparation Techniques

This chapter summaries the most important properties of materials which have been investigated throughout this thesis. Zinc oxides and titanium dioxides have been chosen as TCO substrates for deposition of organic molecular films with phosphonic acid anchoring groups. Other compounds that have been concerned for the study which are organic molecules with carboxylic acid, thiol and phosphinic acid anchoring units are discussed within the corresponding chapter 6. In additions, information about main preparation techniques for substrates and molecular films is given here as well.

2.1 Metal oxides

2.1.1 Zinc oxide (ZnO)

Zinc oxide represents the group of II-VI binary semiconductor materials with a direct bandgap of 3.3 eV at room temperature and owns an n-type conductivity.[63–65] The ionicity of ZnO lies in between the covalent and ionic semiconductors. Three crystal structures are accessible for the material: wurtzite, zinc blende and rocksalt.[66] However, under ambient conditions stable ZnO phase is found to exist only for wurtzite structure and therefore was chosen for the current study. Wurtzite ZnO has a hexagonal unit cell (space group P6$_3$mc - C$_{6V}^4$), where tetrahedrally coordinated Zn^{2+} and O^2 ions schematically represent a number of alternating planes along the c-axis as one can see in Figure 2.1 (a).[67] The tetrahedral coordination of Zn and O is typical for the sp^3 covalent bonding. The unit cell parameters for an ideal wurtzite structure are related as $c/a = \sqrt{8/3} = 1.633$. Under realistic conditions the ratio is typically smaller.
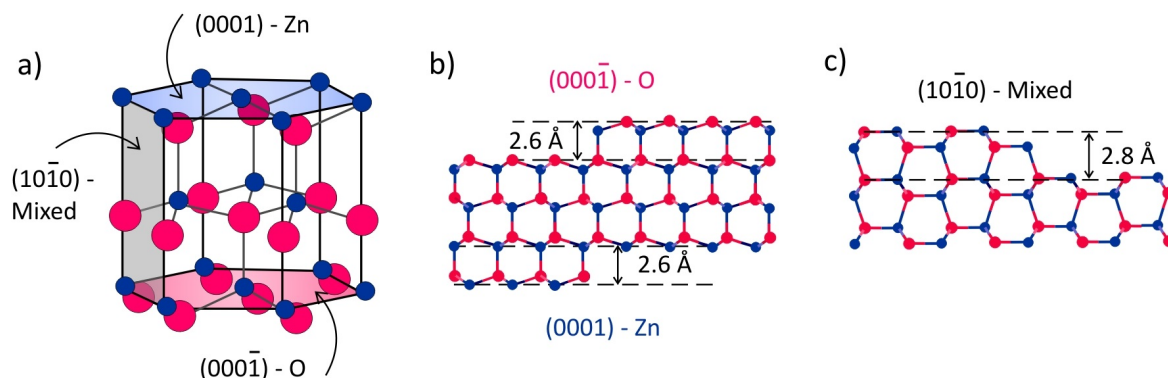
**Figure 2.1:** (a) Schematic representation of ZnO wurtzite crystal structure. (b) Side view of an ideal, unreconstructed ZnO sample with the (0001)-Zn surface termination on the top and the $(000\bar{1})$-O surface termination on the bottom obtained by the cleavage of single crystalline ZnO along the (0001) plane. (c) Side view of the mixed-terminated ZnO$(10\bar{1}0)$ surface. Blue and red spheres denote Zn and O atoms respectively.

On wurtzitic ZnO crystals three types of low-index surfaces can be prepared by cutting: non-polar $(10\bar{1}0)$ surface and two polar surfaces, (0001) and $(000\bar{1})$. Non-polar surfaces contain an equal number of zinc and oxygen atoms, while polar surfaces have either an excess of O or Zn atoms. The crystal cut along the (0001) plane derives crystals with zinc termination on one side and oxygen on the other side (cf. Fig. 2.1 (b)), which exhibit different physical and chemical properties. Polar surfaces are typically characterized by non-zero dipole moments perpendicular to the surface which leads to their instability. However, due to the charge reduction at the topmost surface layer, the non-reconstructed ZnO (0001) and $(000\bar{1})$ surfaces are stable. The microscopic stabilization mechanisms of such polar surfaces is not fully understood yet, although three possible explanations for the charge rearrangement process have been proposed: charge transfer of a negative charge from the O to the Zn face without significant rearrangement of geometric positions[68–73]; removal of surface atoms[74,75]; and positively (negatively) charged impurity atoms on the surface[75–80]. The morphology of Zn-terminated surface is rather different from O-terminated. Several scanning tunneling microscopy (STM) studies on these ZnO surfaces were recently presented in the literature[70,80–84]. Figures 2.2 (a) and (b) represent STM micrographs of Zn-terminated samples obtained in the Diebold group.[81] Samples of the Zn surface termination exhibit triangular shaped large terraces or islands decorated with oxygen step-edge atoms as well as surface pits and holes which are typical for samples prepared under ultrahigh vacuum (UHV) conditions. An oxygen terminated ZnO surface obtains large smooth terraces with hexagonal holes (cf. Fig. 2.2 (c,d)). The ZnO$(10\bar{1}0)$ surface consists of rows of slightly tilted ZnO dimers separated by trenches schematically illustrated on Figure 2.1 (c). STM micrographs

of energetically most favorable mixed-terminated ZnO surface are presented in Figure 2.2 (e) and (f). The surface is morphologically flat and exhibits rectangular terraces with two different step-edge structures. In contrast to both polar surfaces no electrostatic instability was reported for this surface.

Point defects, typical for single crystalline ZnO surfaces, are native defects like oxygen vacancies, interstitial zinc atoms (Schottky and Frenkel defects), Zn-O dimer vacancies (e.g. missing Zn-O units), impurities and defect complexes[64,86–93]. Surface defects strongly influence many electrical and optical properties in semiconductors (doping type, charge carrier lifetime, luminescence efficiency)[66,86,94,95]. It was shown, that the most favorable native defects for the discussed ZnO surfaces are O and Zn vacancies[90,96]. Moreover, oxygen vacancies or the formation of OH surface groups obtain the lowest formation energy and therefore are more energetically favorable. Formations of Zn-O dimers are predominant point defects for non-polar surfaces. The presence of surface defects must be considered during the preparation of molecular thin films on single crystalline surfaces. Their influence will be discussed in the course of this thesis.
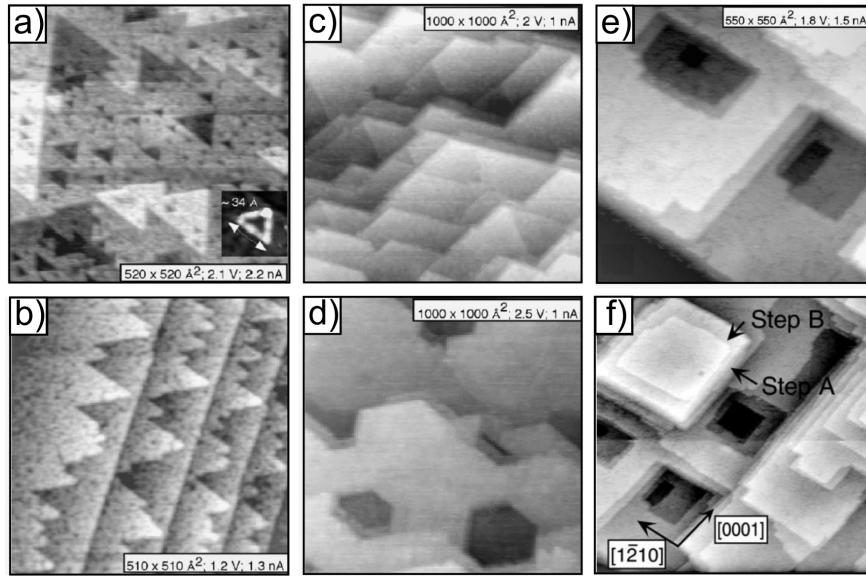
Figure 2.2: STM micrographs of the Zn-terminated ZnO (a) flat and (b) vicinal surface with the typical surface island structure on the inset. (c), (d) $ZnO(000\bar{1})$-O surface with characteristic monoatomic terraces and hexagonal holes. (e) $ZnO(10\bar{1}0)$ surface with large terraces separated by single-layer height steps with (f) two types of step edges: type A - along $[0001]$ direction; type B - along $[1\bar{2}10]$ direction (1000×1000 Å^2, +2.1 V, 0.8 nA). ZnO samples have been prepared under UHV conditions.[81]

ZnO materials have been utilized in many different fields with regard to different technological applications. Next to rubber industry, pharmaceutical and cosmetic industry, textile industry, miscellaneous application, diluted ferromagnets and acoustic wave devices some of the most relevant areas of potential ZnO applications with reference to the topic of this thesis are:[97–103]

- Optoelectronics. As an available and cheap wide band gap compound with high exciton binding energy (60 meV), ZnO can be used as a material for the fabrication of light emitting diods or laser diods covering the blue and ultraviolet (UV) spectral range especially by the realization of band gap engineering, e.g. reliable p-type doping.

- Transparent electronics. High optical transmittivity and high conductivity as well as the possibility to introduce n-type dopants into ZnO allows, for example the fabrication of transparent thin film transistors.

- Photovoltaics. High bulk electron mobility and high variety of ZnO based nanostructures make it a successful candidate for the fabrication of electron transport layers in DSSCs.

- Biosensing. Biosensors based on the utilization of ZnO materials have advantages such as nontoxicity, stability in air, chemical stability, electrochemical activity, ease of synthesis and bio-safe characteristics.

2.1.2 Titanium Dioxide (TiO$_2$)

Titanium dioxide (TiO$_2$) is naturally occurring in three common polymorph structures, which are rutile, anatase and brookite.[63,104] Under certain conditions such as high pressure, additional crystal structures of TiO$_2$ can be found[105,106], though the most stable phase is rutile[107]. Unlike the brookite structure, rutile and anatase can be synthesized in laboratory conditions and, therefore, play a significant role in industrial applications. These three structures hold different properties and consequently different photocatalytic performances,[108,109] however they all can be represented by two complementary building-blocks: Ti$_3$O blocks and TiO$_6$ polyhedra.[110] Anatase usually shows a higher photocatalytic activity than rutile and brookite,[111–113] but its metastable character at room temperature limits the versatility of anatase application. It was found that the anatase TiO$_2$ can be transformed irreversibly to rutile upon heating above a certain temperature.[114] The kinetics of this transformation is driven by the oxygen defect levels, when oxygen vacancies enhance the transformation. The amount of oxygen defect sites is strongly affected by atmospheric

conditions, reduction or oxidation reactions, grain size of nanostructured TiO_2, unintentional impurities and intentional dopants.[115–117] In the current study the focus is on the rutile TiO_2.

Rutile TiO_2 has a flat tetragonal unit cell with two Ti atoms and four O atoms (cf. Fig. 2.3 (a)). Titanium atoms are surrounded by six O atoms and the geometric structure is determined by the relative size of the ions and the coordination, which is represented in many ionic crystals.[118] In order to accomodate all the ions, the octahedral configuration of O atoms around the Ti atom is slightly distorted. Typical lengths for the four-fold symmetric and two-fold symmetric bonds between Ti and O atoms in the rutile TiO_2 crystal are 1.946 Å and 1.983 Å respectively. In the crystal, the octahedra are stacked with their long axis alternating by 90° resulting in three-fold coordinated O atoms.[119] Moreover, Ti interstitials diffuse relatively fast through the open channels of the crystal along the (001) direction, while oxygen in the bulk diffuses by site exchange with other oxygen atoms giving rise to an effective diffusion of bulk oxygen vacancies.
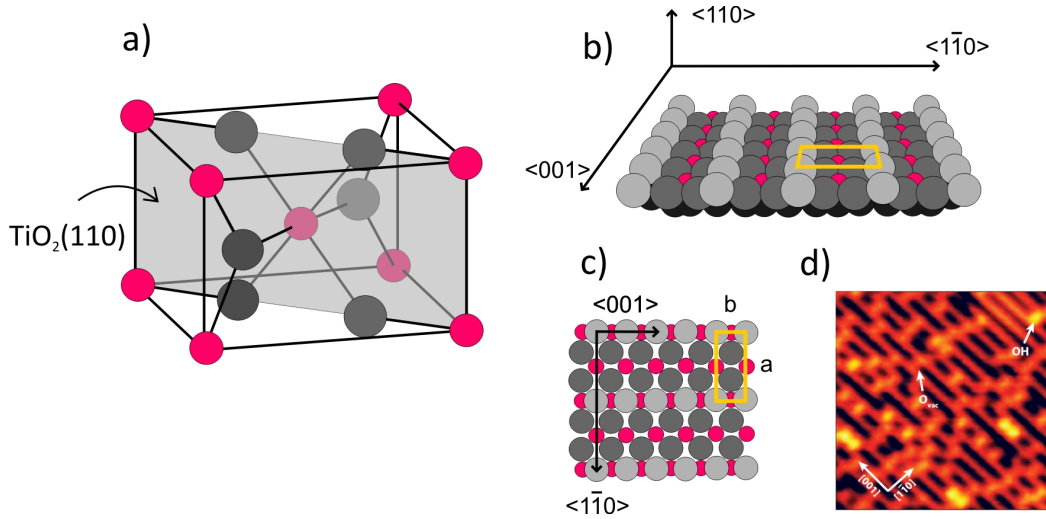
Figure 2.3: (a) Schematic illustration of the rutile TiO_2 crystal structure. Gray and red spheres represent Ti and O atoms respectively. Panels (b) and (c) represent the side and the top view of the $TiO_2(110)$ surface. STM micrograph (d) shows the (110) surface with O vacancies (O_{vac}) and OH groups (100×100 Å^2, +1.48 V, 0.08 nA).

The stoichiometric TiO_2 is a wide gap semiconductor with a band gap of $E_{gap} \approx 3$ eV and holds insulating behavior.[120] It was demonstrated, that the conductivity of titanium dioxide can be enhanced by creating bulk defects. This can be achieved by either doping crystals with metals or upon reduction.[121–126] Donor dopants like Nb can improve conducting properties in the range of 10-15 %. Due to the large ionic radii compared with donors acceptor

dopants, like Al and Ga, introduced in the crystal bulk typically change the conducting properties insignificantly, only up to 1 % or less.[127–130] Besides, TiO_2 can be easily reduced, meaning this metal oxide can exist in different oxidation states.[131] Crystal annealing in UHV conditions or introducing O vacancies and removing Ti interstitials by sputtering gives a rise to significant changes in crystal properties. Such reduction and formation of donor states in the bulk lead to the oxide behave as if it was n-type doped with enhanced conductivity.[126,132–138] In titanium dioxide, oxygen vacancies form color centers which trap electrons 0.76 eV below the conduction band. They contribute to the change in the color of the crystal from transparent through light to dark blue during the UHV annealing.[126,133]

The most stable of the low-index rutile TiO_2 surfaces is the bulk-terminated $(1\,1\,0)$ surface (with a slight surface relaxation), which is shown on Figure 2.3 (b,c). It can be obtained by cleavage of bulk material providing the equal surface termination of two opposite sites. The top-most layer is charge neutral, since it contains twice as many O^{2-} as Ti^{4+} ions. The upper-top Ti and O atoms have a different coordination. At the surface plane rows of five-fold coordinated (5f) Ti atoms alternate with rows of six-fold coordinated (6f) Ti atoms separated by rows of O atoms. All rows are aligned in the $[0\,0\,1]$ direction. Deep lying Ti atoms are covered by rows of two-fold coordinated O atoms positioned in bridge sites.[139] These so-called bridging oxygen atoms can be easily removed from the surface due to their coordinative undersaturation which results in the surface reduction. Also, these surface defects are more reactive than surface step edges and play a major role in defect-related surface chemistry. The (1×1) surface unit cell has a size of 2.96 Å in the $[0\,0\,1]$ direction and 6.5 Å in the $[1\,\overline{1}\,0]$ direction (cf. Fig. 2.3 (c), yellow box).[140] Next to other research groups,[141,142] the $TiO_2(1\,1\,0)$ surface has been intensively studied in the group of Diebold.[119,126,143,144] Since poor conductivity of the metal oxide can be suppressed by its reduction, only crystals with oxygen vacancies as defect can be applied for the STM investigation. Figure 2.3 (d) visualizes the $(1\,1\,0)$ surface with defects (O vacancies and surface hydroxyl groups), where bright rows correspond to rows of fivefold-coordinated Ti atoms and bridging oxygen atoms are imaged black.[125]

TiO_2 finds a wide application especially in environmental and energy-related fields,[145–151] some of which are:

- White pigment. Due to brightness, very high refractive index and resistance to discoloration under ultraviolet light TiO_2 is widely used as a pigment in industrial coatings and cosmetics.

- Photovoltaics and photocatalytics. Photovoltaic properties of TiO_2 are derived from the formation of photogenerated charge carriers. for the reason of good oxidative

and hydrolysis properties titanuim dioxide is widely used in DSSCs and hybrid solar cell as an antireflection coating, as a scattering layer or an interlayer in organic solar cells (a part of the active layer of the device acting as the electron transport element). Furthermore, the Grätzel Cell is based on the usage of the titanium dioxide. TiO_2 applications also include OLEDs, LCDs and electrodes for plasma displays.

- Sensors. By loosing oxygen the oxide becomes a semiconductor. The electrical resistivity in the material correlates to the oxygen content of the atmosphere. Therefore, the oxide can be used as an oxygen sensor.

- Passivating layer. The passivating effect of TiO_2 causes high chemical resistance against corrosive environments which allows its use on, for instance surface of titanium implants for orthopedic and dental applications.

2.1.3 Self-Assembled Monolayers (SAMs)

The concept of *self-assembled monolayer (SAM)* has been widely used in different scientific works during the lasts years.[152–157] SAMs can be defined as ordered assemblies of organic molecules, which can adsorb on the surface and spontaneously rearrange into distinct structures.[158] Such molecular layers typically exhibit a high degree of orientation, molecular order and packing. Such molecular behavior is a result of the structure of molecules, which consist of anchoring units (head group), an aliphatic or aromatic spacer (backbone) and the reactive tail group (functional head group) as depicted in Figure 2.4. The affinity of the active head group toward a specific substrate results in a spontaneous chemical reaction at the interface, as the system reaches the equilibrium. The spacer connects the head group and the tail group and influences the intermolecular interaction and molecular orientation as well as electronic conductivity. The tail group defines the functionality of the SAM. Many parameters, including molecular structure (aliphatic chain length), the choice of substrate as well as the preparation conditions play significant role on the quality of assembly into the two-dimensional system. The anchoring units bind chemically to the sample surface, while the interactions between molecular backbones are non-covalent and is driven by hydrogen bonds, electrostatic or via van der Waals forces. SAMs find many potential applications because of their low cost, ease of preparation by immersion, availability of a variety of functionalities and different structural properties. SAMs provide a simple, convenient and versatile system for tuning the interfacial electronic properties of a wide range of surfaces.[159–172] Wide application was found in catalysis, protective coatings, biological sensors, optoelectronic devices, adhesion promoters and nanolithography.[173–178]
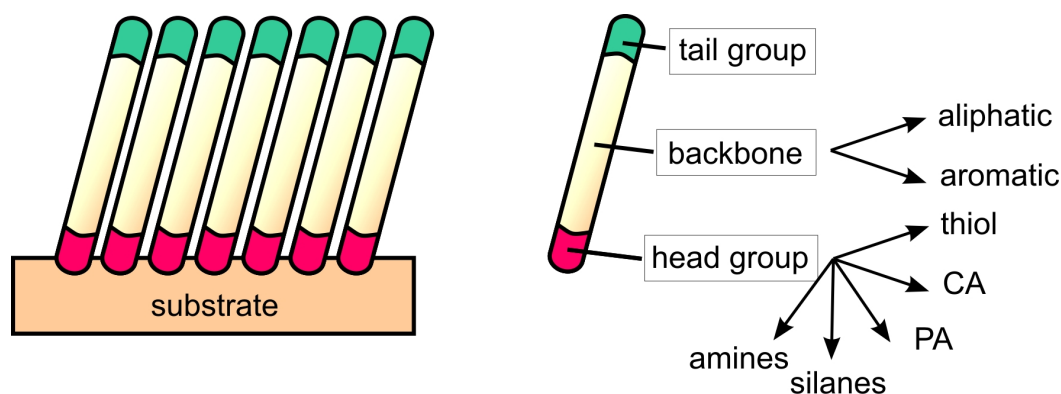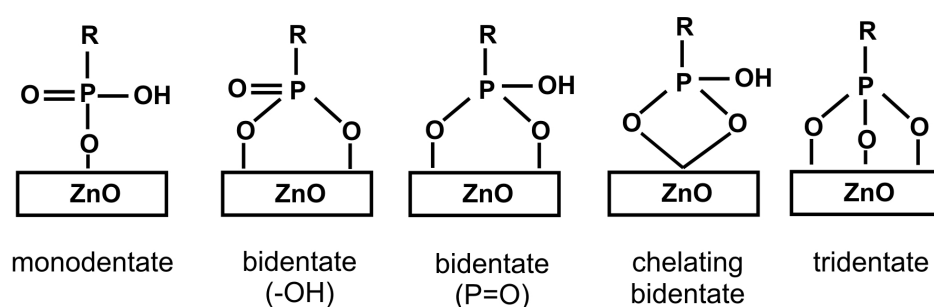
**Figure 2.4:** Schematic illustration of self-assembled molecules with the most common structural units.

The process of self-assembly has been studied most frequently for the system of thiols on gold.[179–181] However, to functionalize metal oxides, SAMs with other structural units are utilized. Next to thiols,[182,183] silanes,[184] amines[185] and other anchoring units, two main molecular classes are mainly applied, and in particular, molecules with carboxylic acid (CA)[186–189] and phosphonic acid (PA)[190–194] groups. The limitation of silanes is that the formation of stable monolayers can proceed only under very restricted conditions for the hydrolysis of silane species and is very sensitive to the water content, pH and temperature.[194–196] Carboxylic acid allows the formation of dense monolayer films of high coverage, however the stability of films was found to be very low or the film quality can be hampered by the presence of polar sites within CA-based molecules.[194,197,198] In contrast, phosphonic acid binds strongly to the oxidic surface and favors formation of robust monolayers.[194,196]

Phosphonate or phosphonic acid consists of a phosphorus atom in the +5 oxidation state in the tetra coordination that is connected to two alkoxy groups with P-O single bond and a formally double–bonded oxygen (phosphoryl group). This molecular unit can be chemically modified through the rest group of the phosphorous atom or two alkoxy groups.[194] Phosphonic acid features good solubility in most polar organic solvents and is stable at high temperatures. Its properties can be tuned by variation of the molecular backbone. It is proposed, that phosphonic acid binds to metal oxide surfaces by the first coordination of the phosphoryl oxygen to Lewis acidic sites on the surface and subsequent condensation of the P–OH groups with surface hydroxyl groups or other surface oxygen species.[194] Opposed to silanes, the multilayer formation for the phosphonic is less likely, since the homocondensation of P-OH and P-O bonds does not occur at mild conditions or in aqueous solution.[194] However, being a strong acid, PA can partially damage oxidic surfaces.

Different research groups have been studying the anchoring mechanism of PA to oxidic surfaces.[194,199–202] However, the question about how the PA bonds to the surface of ZnO is still not fully understood. Mono-, bi- and tri-dentate binding modes have been proposed on metal oxide surfaces (cf. Fig. 2.5). The formation of a particular binding mode depends on the nature of the organic material, substrate surface structure and the formation procedure. Additionally, various degrees of chemisorption and hydrogen bonding have been found. The complexity of the binding mechanism increases due to the possibility to form bridging bonds (each acid oxygen binds to a different metal atom) or chelating bonds (two or three of the acid oxygen atoms bind to the same metal atom).[199]

Figure 2.5: Schematic illustration of bonding mechanisms reported for the attachment of PA on metal oxides.
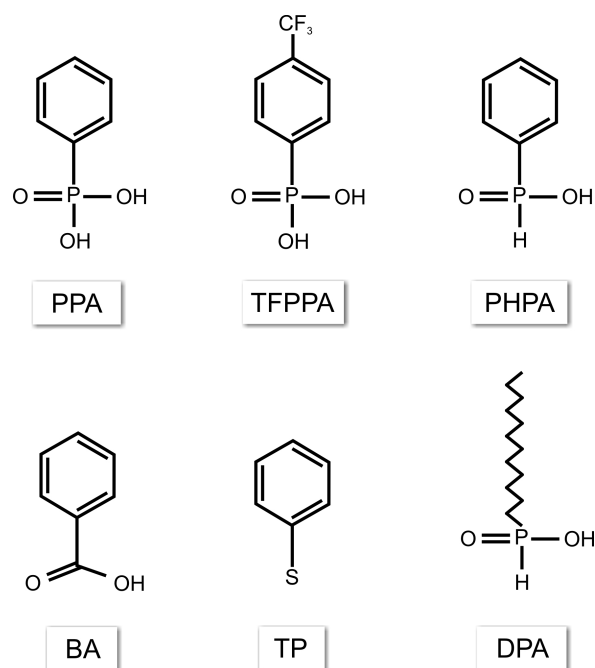
Figure 2.6: Schematic structure of organic molecules studied in this work.

In the course of this work organic molecules with phosphonic acid head groups and different functional groups have been used. A part of the study is focused on analyzing the structure and stability of CA and thiol-based SAMs compared to the PA-based SAMs. Molecular compounds involved in this thesis are listed in Figure 2.6 and introduced below:

- Phenylphosphonic acid, **PPA**. $C_6H_7O_3P$. Purity 98%, obtained from Sigma Aldrich.

- Para-trifluoromethylphenylphosphonic acid, **TFPPA**. $C_7H_6F_3O_3P$. Synthesized in the group of Prof. Dr. Stefanie Dehnen (Marburg).

- Phenylphosphinic acid, **PHPA**. $C_6H_7PO_2$. Purity 99%, obtained from Sigma Aldrich.

- Benzoic acid, **BA**. $C_7H_6O_2$. Purity 99.5%, obtained from Sigma Aldrich.

- Thiophenol, **TP**. C_6H_5SH. Purity 99.7%, obtained from Sigma Aldrich.

- *n*-Dodecylphosphonic acid, **DPA**. $C_{12}H_{27}O_3P$. Purity 99%, obtained from Sigma Aldrich.

2.2   Preparation Techniques for Metal Oxides

As it was briefly discussed in previous sections, the structure of sample surfaces strongly influences the resulting quality of molecular films. This is especially crucial for monolayer films, since the molecular attachment in the first layer may influence the resulting film structure.[203] A commonly used preparation procedure for metal oxide substrates includes repeating cycles of Ar^+ ion sputtering at 800 eV for 3 hours and sample annealing up to 850 K in UHV conditions (cf. Fig. 2.7, pathway A). Sample sputtering removes surface impurities by knocking out contaminating surface atoms as well as atoms of the sample material. Light atoms, like oxygen, can be easily removed by ion bombardment, making the residual surface rough and depleted. The surface stoichiometry can be restored by annealing. Depending on the material, different temperatures and times are needed in order to achieve a smooth surface. It was shown recently, that in case of TiO_2 crystals such preparation leads to severe oxide reduction, which is indicated by its color change to dark blue.[115–117] This happens due to the sample annealing in the UHV chamber when excessive thermal energy induces oxygen desorption from the surface. However, the oxygen depletion can be ruled out combining UHV cleaning steps with sample annealing in a muffle furnace (cf. Fig. 2.7, pathway B).[204] Next to the high oxygen concentration in the air, the main advantage of annealing is the applicability of higher temperatures (1200 K) compared to conventional annealing under

UHV conditions (850 K), which yields enhanced surface diffusion and leads to an improved surface smoothness with larger terraces and sharp low energy diffraction pattern patterns. The application of this preparation method has been successfully demonstrated on ZnO crystals of different surface terminations.[204] Nonetheless this method is not fully suitable for TiO$_2$ samples. Being highly reactive titanium, when taking the sample out of the UHV set-up after sputtering, can easily react to impurities in the air, like carbon, which highly contaminate the surface forming stable titanium carbide. Therefore, this method was modified and an additional UHV heating chamber was constructed. This allows UHV direct stepwise annealing of oxidic samples in oxygen atmosphere, usually carried out at partial oxygen pressure around 100 mbar at 950 K for 60 minutes. This method leads to the formation of atomically flat and microscopically well ordered metal oxidic crystal surfaces, which is confirmed by morphological and structural analysis of the surface. (cf. Fig. 2.7, pathway C).

2.3 Molecular Film Preparation Techniques

Molecular films which were analyzed throughout this work have been prepared by means of two different preparation techniques: wet-chemically by immersion and under UHV conditions by means of organic molecular beam deposition (OMBD).

2.3.1 Immersion

The most common *ex-situ* procedure for the formation of SAMs is to immerse the clean substrate into dilute solution of the material leading to the formation of a monolayer film with molecules chemically bound to the substrate surface (cf. Fig. 2.8). Immersion is a good alternative to the OMBD method, since there is no need for ultrahigh vacuum and expensive laboratory equipment and it allows parallel production of several samples as well as the coverage of a large sample area or after some modifications selective microcontact printing. However, this is only possible if the compound can be dissolved in the solution and, therefore, is widely used for attachment of organic molecules to substrates by means of reactive anchoring units. By providing enough time and energy to the process under right conditions, molecules can reorganize and form chemical bonds with surface atoms resulting in the covalently attached well-defined monolayer films.[158,206,207] The growth rate is proportional to the number of available sites and in a first approximation a simple Langmuir growth takes place.[205] However, many studies have shown that the monolayer
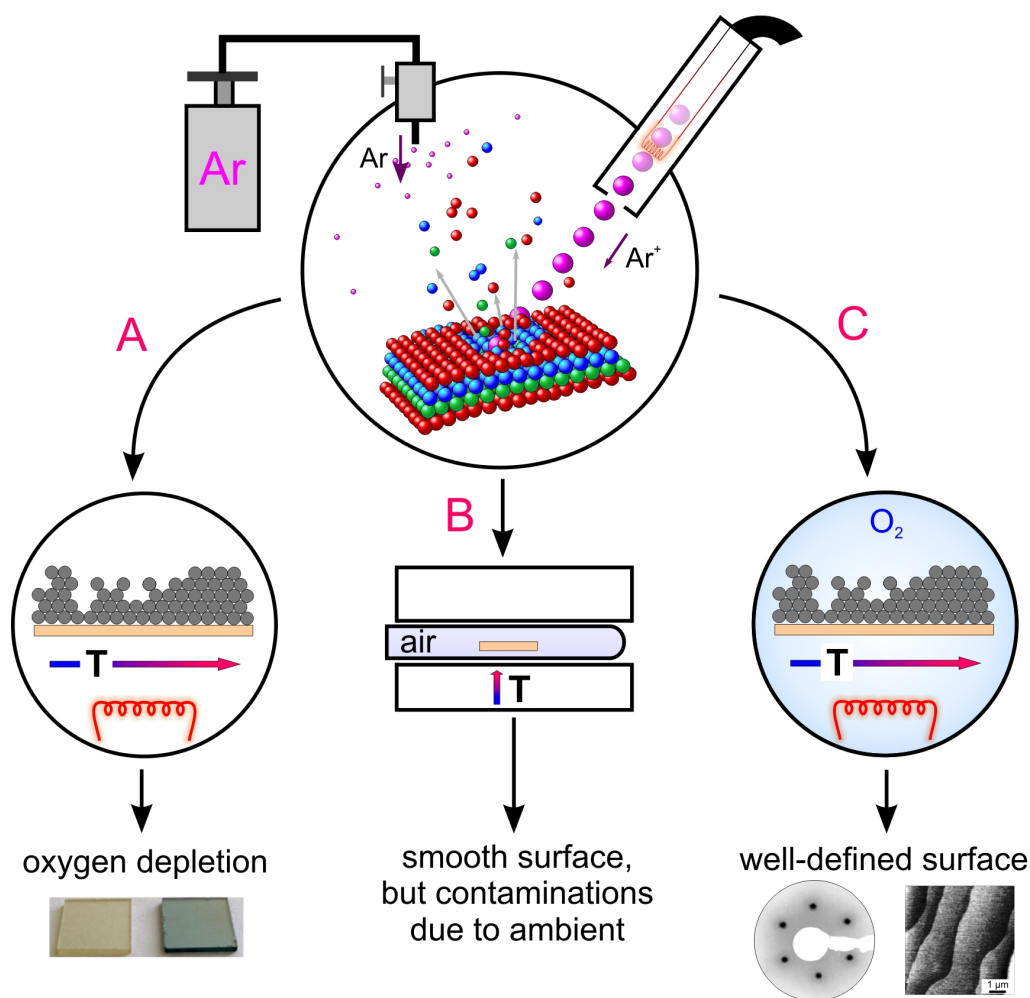
Figure 2.7: Schematic illustration of different preparation procedures for metal oxide samples. After removing surface contaminations by sputtering, three different ways to restore surface crystallinity are introduced: pathway A - annealing in the UHV (leads to oxygen depletion which is demonstrated by a color change of TiO_2 crystals); pathway B - samples annealing in a the muffle furnace (sputtered surfaces can be contaminated after contact to ambient); pathway C - annealing in the UHV chamber in oxygen gas (low energy electron diffractogram and atomic force microscopy image show formation of well-defined surfaces).

formation happens very fast whereas the reorganization of this layer in order to obtain a densely packed film requires several hours.[205]

The general simplicity of this fabrication method is often overestimated, since a number of process parameters like concentration, choice of a solvent, temperature and immersion time are critical for the quality of resulting molecular films and have to be considered carefully. Some studies report the influence of solvent-substrate interaction on the film formation of thiols or lower adsorption rate for long-chain aliphatic SAMs.[158,179,208–212] Additionally, some preparation conditions as well as properties of molecular materials can lead to surface damage by etching, which is conscientiously discussed in Chapter 4. Another important parameter is the cleanliness of the substrate. Due to the sample having contact with air, its cleanliness is not easy to control, which can influence the growth behavior.[179,205] This issue is addressed in more detail in Chapter 5.

Some modifications of sample preparation by immersion have been recently introduced in the literature, like tethering by aggregation and growth or T-BAG.[213–215] SAMs for this study have been prepared using classical immersion principles. Samples have been horizontally placed in a glass vessel filled with the solution and hermetically closed with a cap to avoid evaporation and as a consequence changes in the concentration. If not specified, the ethanolic solutions with a 0.1 mM concentration of the organic material have been used. Immersion has been performed at the temperature of 75° C for typically 24 hours. A removal of loosely attached residues after extracting samples from the solution has been realized by rinsing them with pure ethanol and blowing dry with nitrogen.

2.3.2 Organic Molecular Beam Deposition (OMBD)

The second preparation method that was used is the *organic molecular beam deposition (OMBD)*. The basic principle of the gas phase deposition includes the formation of the molecular film in the UHV chamber through the adsorption from the molecular gas phase (cf. Fig. 2.8).[216] This *in-situ* method allows to utilize clean sample surfaces for the deposition, which have been prepared directly in the same UHV apparatus, and conduct experiments with regards to the influence of the surface morphology and structure on the film formation. Moreover, this technique is the typical method of thin film preparation for materials that obtain low solubility, for example small molecule organic semiconductors, like pentacene or C_{60} or large dye-complexes, like phthalocyanines.[217,218]

In this preparation technique, the processed compound is stored in a heatable crucible (Knudsen Cell). By providing enough temperature to the crucible, the material sublimation is
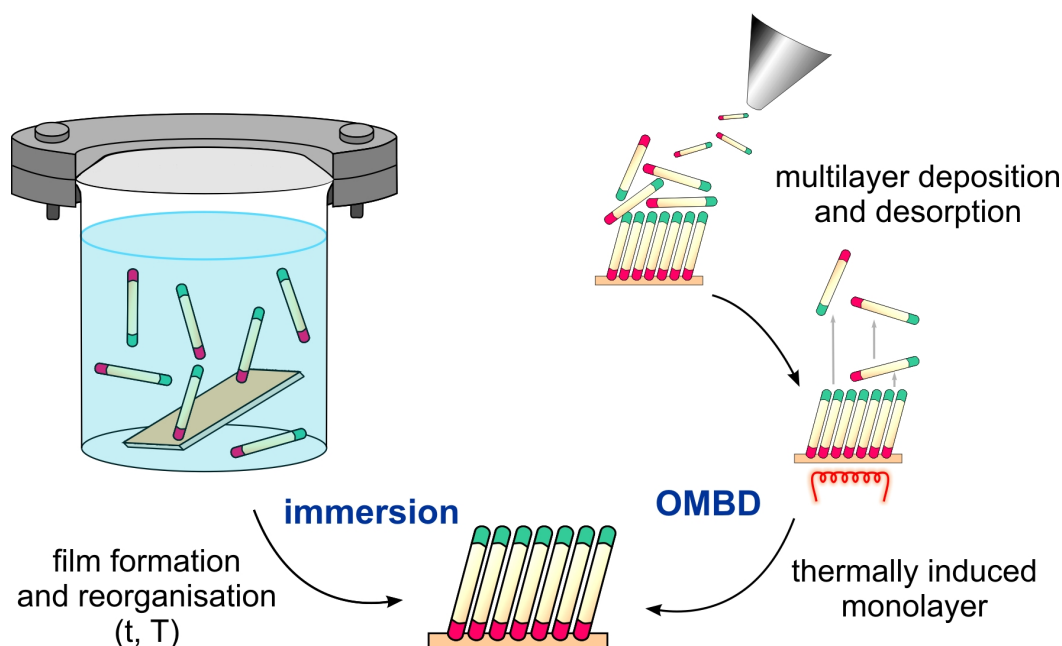
Figure 2.8: Schematic illustration of monolayer molecular film preparations wet-chemically from immersion (left pathway) and by multilayer desorption by means of OMBD (right pathway).

activated. Changing the temperature or the distance between the substrate and the molecular beam, the material flux can be adjusted to the needed value, allowing re-sublimation on these substrates and as a consequence the fabrication of molecular thin films. A quartz crystal microbalance (QCM) is utilized to monitor the flux as well as a shutter of the Knudsen Cell helps to precisely stop the flux of the molecules. From changes in frequency of a quartz-crystal resonator, the QCM analyzer measures the incoming masses and, knowing molecular density, the nominal deposition thickness per time can be calculated.[219–221] Therefore, the precise formation of thick and thin, up to sub-monolayer coverage films can be obtained. Moreover, the organic material can be purified by desorbing contaminations with lower desorption temperatures. One should note, that incorrect temperature can lead to the dissociation of molecules before coming to the sample surface. The structure and quality of formed films can depend on the substrate temperature, the substrate surface structure and flux rate during the deposition. In several studies it was shown, that the substrate temperature is a crucial parameter, and can lead either to the formation of another crystal phase or enhance the crystallinity at higher substrate temperatures.[222] In many cases in order to achieve good crystallinity of films, the precise choice of the substrate temperature and small molecular flux have to be provided during the film deposition.

Although the majority of films grown by the OMBD method are bonded by van der Waals (vdW) forces to the supporting substrate, the first molecular layer often obtains strong interaction to the surface and, therefore, is more stable. Based on this stronger interaction between the first layer and the substrate, the formation of monolayer films by multilayer desorption is allowed. In order to do that, the multilayer film is deposited onto the surface and by careful annealing will be desorbed, leaving only the monolayer film attached (cf. Fig. 2.8). The heating temperature has to be adjusted precisely to avoid partial monolayer desorption. However, the molecular attachment through reactive anchoring units in SAMs demands time and activation energy, OMBD has been also introduced for such systems.[223,224] In many cases the growth can not be simply described by the simple Langmuir asdorption model[206] and implicates many formations phases at different time scales like adsorption, re-desorption, diffusion, nucleation and growth of islands.[220]

For the current study thin films have been prepared in an UHV-chamber at a working pressure of about 10^{-9} mbar and equipped with a load lock system to enable quick sample transfers. The substrate preparation procedure has been performed in the same UHV set-up. If not specified, film deposition has been obtained at the flux of 0.5 Å/min for which the PPA was heated up to 380 K, while keeping the sample at room temperature. The precise protocol for the monolayer film formation from multilayer desorption is introduced in the corresponding chapter.

CHAPTER 3

Characterization Techniques

In this section basic principles of various characterization techniques used in the course of this work are briefly presented. Their working principles, resolution, advantages and limitations are discussed. The techniques are presented according to the sample properties they reveal: Morphological characterization (optical microscopy, SEM, AFM, contact angle), Structural characterization (LEED, XRD, NEXAFS), Elemental composition (XPS, EDX) and Thermal stability (TDS).

3.1 Morphological characterization

3.1.1 Optical microscopy

Fast visualization of surface morphology was carried out using a Leitz Metalloplan Microscope, which uses visible light and a system of lenses to magnify images of small surface area. It allows to image structures bigger than $4\,\mu$m in lateral direction by varying the magnification of the objective lens (resulting magnification available of 80 times, 160 times, 320 times or 800 times). Measurements can be carried out either in reflected-light or transmitted-light depending on the sample transparency.

3.1.2 Scanning electron microscopy (SEM)

Next to the optical microscopy the *scanning electron microscopy (SEM)* has been used to visualize surface topography of studied samples. When the electron beam with primary electron energy of around 1-10 keV, focused by a lens system into a spot of 1-10 nm in

diameter, hits the specimen, it will interact with atoms of the surface by elastic and inelastic scattering. A variety of signals can be detected, including secondary electrons, backscattered electrons, X-rays, cathodoluminesence and sample current (cf. Fig. 3.1 (a)).[225] The focused electron beam is scanned in a raster across the sample surface by a deflection coil system simultaneously to an electron beam of a video tube, which is used as an optical display.[226–228] SEM allows producing very high-resolution images of a sample surface with details less than 1 nm in size. Due to the very narrow electron beam, SEM micrographs have a large depth of field yielding a characteristic three-dimensional appearance in contrast to optical microscopy methods (cf. Fig. 3.1 (b)).[229,230]
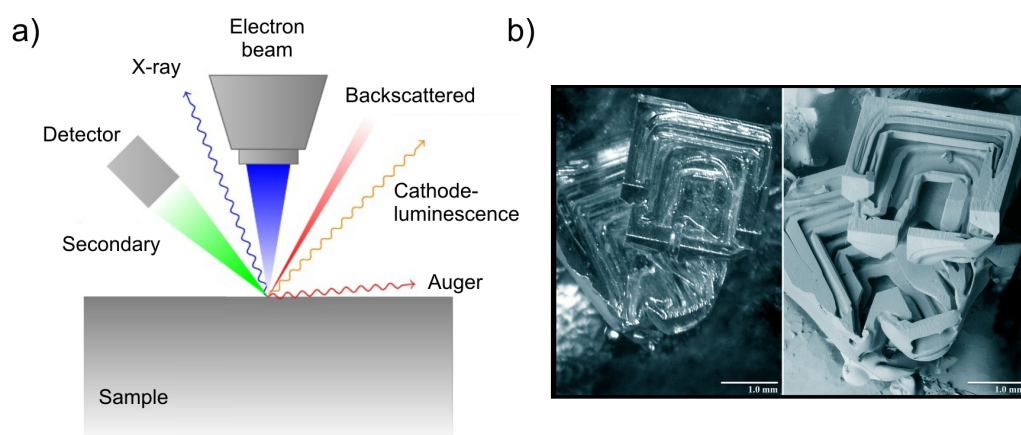
Figure 3.1: (a) Schematic illustration of the types of signals generated by irradiation of a sample by a primary electron beam. (b) Optical microscopy image (left) and SEM image (right) of a depth hoar crystal.[231]

For the measurements in this study optical images have be obtained using the REM JEOL JSM-7500F system for SEM measurements. Because of charging effects in poorly conducting samples the acceleration voltage was varied between 1 kV and 10 kV.

3.1.3   Atomic force microscopy (AFM)

Scanning probe microscopy technique is a prominent tool in surface topography analysis, covering a broad range of experimental methods. In contrast to *scanning tunneling microscopy (STM)*[232] the *atomic force microscopy (AFM)* allows to analyze the morphology of bare insulating surfaces or samples modified with molecular films on a nanoscale.[233–235]

The general set-up contains a sharp microscopic tip approximately 7 nm in diameter attached to a cantilever spring and is depicted on the Figure 3.2 (a).[236] The movement of

the cantilever can be controlled by piezo scanners. By scanning a sample in the lateral to the cantilever direction the interatomic forces between the tip and the sample surface cause bending of the cantilever. The detection of the cantilever displacement is measured by a laser beam, focused on the back of the cantilever and reflected towards a photodetector. Variation in the position of the reflected laser beam causes relative intensity changes in four quadrants of the position-sensitive photodetector. By this the repulsive force between the sample and the tip at every individual point converts in an electrical signal, which illustrates the surface morphology.
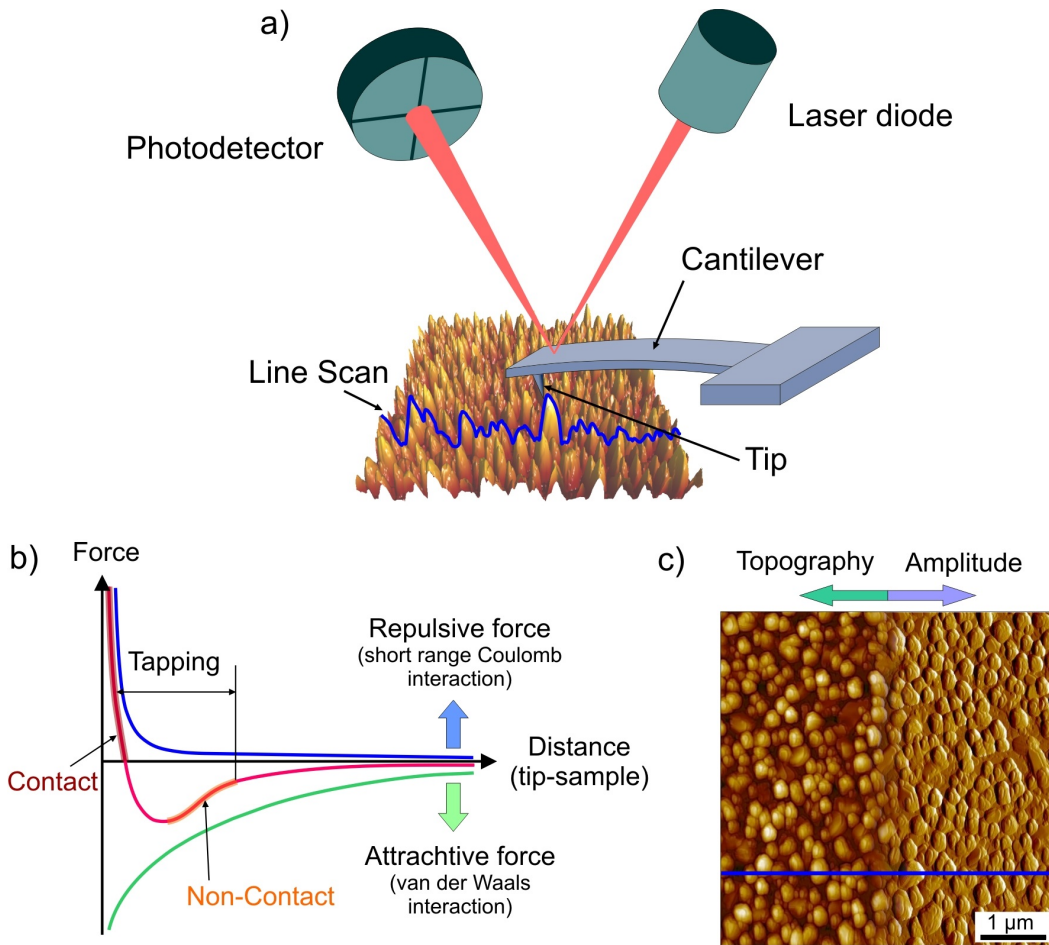
Figure 3.2: (a) Schematic illustration of working principles of AFM with (c) an example of an AFM topography and amplitude image of 30 nm PPA film deposited on ZnO. (b) Force-distance curve for different acquisition modes.

AFM measurements can be operated in two regimes: static regime (Contact mode) and dynamic regime (Non-Contact and Tapping modes) as the cantilever oscillates in the last case. [237,238] Contact mode is the most common method of operation. During the operation the AFM tip is in a close contact to the surface, which reflects the repulsive force of the

inter-molecular force curve (cf. Fig. 3.2 (b)). The surface mapping can be conducted with or without a feedback loop. If the relative spacing between the tip and the sample is adjusted by the electronic feedback, the tip-sample force is kept constant, which refers to the Constant Force mode. In the Constant Height mode the feedback is switched off and the distance between the tip and the surface remains constant. The laser beam deflection in this case leads to the difference in mutual forces, which can be translated into the surface topography image. AFM measurements in Constant Force mode have been carried out in this work to obtain topographical information. The static operation allows conducting AFM measurements at high scan speed with good resolution in topography and amplitude image (cf. Fig. 3.2 (c)). However, high lateral forces can be destructive and can damage the sample, especially in case of organic materials.

In the dynamic mode (tapping), the cantilever oscillates close to its resonance frequency and its changes in amplitude and frequency during the movement across the surface are monitored. In amplitude imaging the feedback loop adjusts the z-position of the cantilever to keep the amplitude constant. The position of corresponding piezo actuator gives the information about the surface topography and is highly sensitive to surface features (domain borders, steps). Oscillations in phase signal can be attributed to different material properties (e.g. different chemical composition, adhesion). Tapping mode is suitable for samples with weakly bound surface top layers or soft materials (polymers, thin films).

High atomic resolution in AFM can be achieved by conducting measurements in Non-Contact mode. The cantilever oscillates at a close to resonance frequency near the surface but does not contact it. In contrast to tapping mode, where tip oscillations belong the attractive force regime (van der Waals forces) as well as the repulsive force regime (Pauli repulsion) and the AFM tip touches the sample, in Non-Contact measurements the oscillations are solely in the attractive regime of the inter-molecular force curve. The decrease of resonance frequency at the surface under the influence of the van der Waals and other long-range order forces leads to the decrease in the oscillation amplitude. Therefore, the operation in this mode in most cases requires UHV conditions to circumvent acquisition problems due to adsorbed water layer on the tip and sample surface. The Non-Contact AFM measurements allow to obtain morphological information on insulating surfaces like ZnO or TiO_2 with an atomic resolution, which can be troublesome by means of STM technique.

All AFM data have been acquired with an Agilent 5500 AFM operated in Tapping Mode at ambient conditions. The AFM micrographs have been further processed and analyzed by means of $SPIP^{TM}$ software.

3.1.4   Contact angle measurements

Fast indication of chemical surface modification by SAMs has been realized performing contact angle analysis. This method allows to quantify changes in the surface wettability, which can be correlated to a surface energy of a solid surface according to the Young's Equation[239]

$$\gamma_L \cos\theta = \gamma_S - \gamma_{SL}, \tag{3.1}$$

where θ is the contact angle, γ_L, γ_S and γ_{SL} represent the liquid-vapor, solid-vapor and solid-liquid interfacial tensions. For this purpose a drop of distilled water of $1\,\mu$m has been placed on the surface and immediately imaged by a digital camera form a side. The contact angle is defined as the angle of the water droplet formed at the liquid-solid interface in the droplet profile. When the liquid spreads on the surface a small contact angle is observed, meaning a hydrophilic surface character. The contact angle greater than 90° generally means that wetting of the surface is unfavorable.[240,241]

3.2   Structural characterization

3.2.1   Low energy electron diffraction (LEED)

Low energy electron diffraction (LEED) is a diffraction technique which utilizes a beam of low energetic electrons (typically 30-250 eV) and is widely used as a standard technique to check the crystallographic quality of a surface (either clean surfaces or surfaces with ordered adsorbate overlayers). During the operation a beam of electrons from an electron gun is sent to the surface of the sample. The de Broglie wavelength of an electron is given by[234]

$$\lambda = \frac{h}{\sqrt{2mE}}, \qquad \lambda_e[\text{Å}] = \sqrt{\frac{150}{E_{kin}}}, \tag{3.2}$$

yielding the electrons with the wavelength of about 0.5–2 Å for the typical range of energies used in LEED. This corresponds to the atomic diffraction condition, namely, the λ is of the order of or less than the interatomic distances. In the equation h is the Planck constant, v is the velocity of an electron of the mass m_e.[233,242] Since the main free path of low energy electrons is short and has a value of the order of a few atomic layers (typically less than 10 Å), most elastic collisions occur in the top layer of a sample. In the experiment the structural information is gained from the analysis of the angular distribution (diffraction pattern) of

electrons that are elastically backscattered from the surface and detected by a fluorescent screen (cf. Fig. 3.3).[234,243]
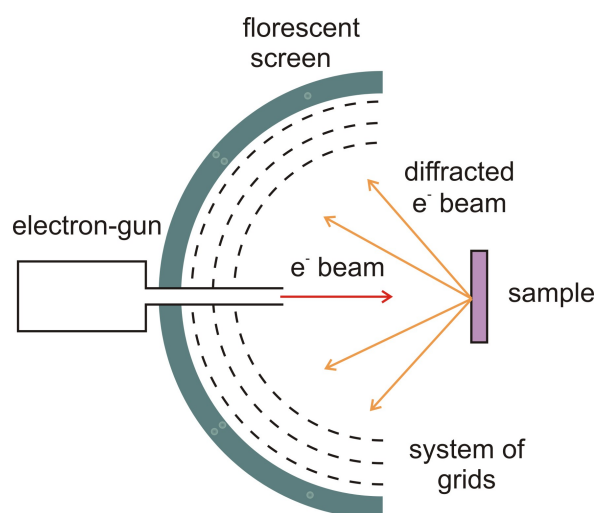

Figure 3.3: Schematic diagram of a three-grid LEED set-up.

An electron gun consists of a heated cathode at a negative potential (LaB_6 crystal) and a set of focusing lenses. The last aperture of the lens, the sample and the first grid are at earth potential, which results in the rectilinear electron beam. Electrons penetrate the surface of the sample and scatter in numerous direction depending on the surface crystallography. Scattered electrons head back towards three girds followed by a phosphor covered screen. The second and third grids screens inelastically scattered electrons. The fourth grid separates other negative grids from the fluorescent screen which carries a positive charge, resulting in the re-acceleration of the elastically scattered electrons. After passing through a system of retarding grids they land of the fluorescence screen creating a diffraction pattern.

The diffraction pattern is directly related to the reciprocal lattice of the sample - a lattice, which represents the Fourier transform of the original lattice. The information concerning the structure of sample surface or surface adsorbate can be obtained from the sharpness of a LEED pattern, spot profile and spot geometry. Samples of a good quality (long-range order) are usually characterized by sharp bright diffraction spots and low background intensity. The spot profile, namely, the intensity distribution across the width of a spot, contains information about surface imperfections like surface domains or impurities (cf. Fig. 3.4 (a)).[244] Moreover, LEED patterning can be a powerful tool to ascertain the true superstructure of self-assembled monolayers (cf. Fig. 3.4 (b)).[245]
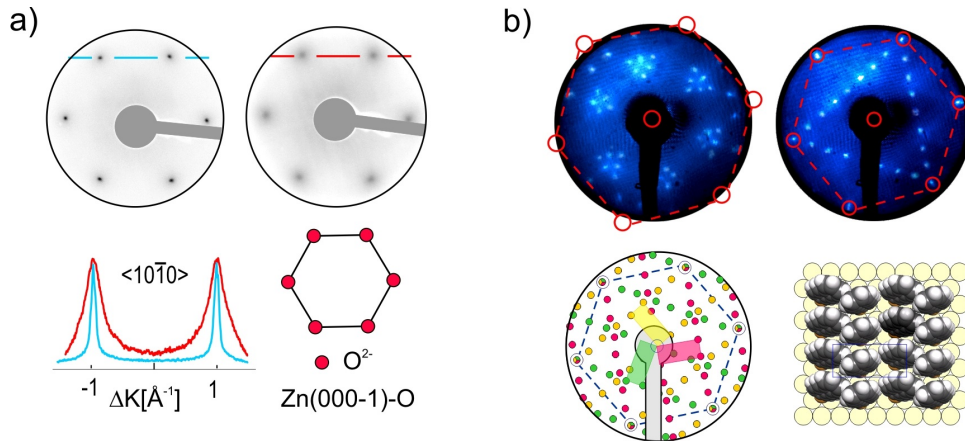
Figure 3.4: (a) Comparison of LEED patterns (58 eV) of $ZnO(000\bar{1})$-O-surfaces obtained after heating in air (left) and UHV-based cleaning cycles (right) together with corresponding profiles of the diffraction peaks and a the top view of an ideal bulk terminated ZnO-O surface.[244] (b) The measured LEED patterns with $E = 75$ eV (left) and $E = 99$ eV (right) of anthracene-2-selenolate SAMs on an Au(1 1 1) surface and the reciprocal lattice of a $(\sqrt{3} \times 4)rect.$ structure including rotational domains with a structural model.[245]

LEED diffractograms presented in this work have been measured at the UHV Omicron set-up and captured by a digital camera. The *SPIP^{TM}* software has been used to analyze the data.

## 3.2.2 X-Ray Diffraction (XRD)

One of most useful diffraction techniques for the determination of the crystal structure of molecular films, bulk or powder is the *X-ray diffraction spectroscopy (XRD)*. The basic principle of this method is the reflection of X-rays on parallel atomic planes of the sample lattice, which enables the investigation of structures on the atomic dimensions. For investigating structures of a certain dimension with the electromagnetic radiation its wavelength must be of the same order as the studied features. A typical wavelength range for the X-ray radiation is $10^{-8} - 10^{-12}$ m [234] and in the order of the lattice parameters (e.g. $a_{Zn} = 2.7 \cdot 10^{-10}$ m) [246] . This mades enables to retrieve accurate information on the interplanar spacing and atomic position in the sample. This information can be very useful for determining what material a sample consists of, to determine the interplanar spacing, or the unit cell size and lattice parameters of a specific material.[247,248]

When in the experiment a parallel wave of an incoming beam of X-rays comes into contact with the sample surface and reflects from a first lattice plane, the second wave reflects

from the second lattice plane, making the difference in the path way from the source to the detector for both waves (cf. Fig. 3.5 (a)). In the case of periodically distributed atoms as in crystals discrete peaks in this diffractogram are observed, which arise from constructive interference of X-rays scattered by atoms in equivalent lattice planes. The difference in path length between waves reflecting from parallel planes depends on the angle of incidence θ and the spacing between parallel planes d. A condition for the constructive interference states the ration between the wavelength and the path difference between two scattered waves to be integer, the Bragg law can be derived[247]

$$n\lambda = 2d\sin(\theta), \tag{3.3}$$

where n describes the diffraction order and λ is the wavelength of the X-rays. In order to find correct conditions for the constructive interference and obtain a diffraction pattern the intensity of scattered X-ray signal is monitored as a function of the angles ω between X-ray source and the sample and θ between the sample and the detector (cf. Fig. 3.5 (b)). If the experimental conditions fulfilled discrete peaks occur in the spectrum under the angle θ.
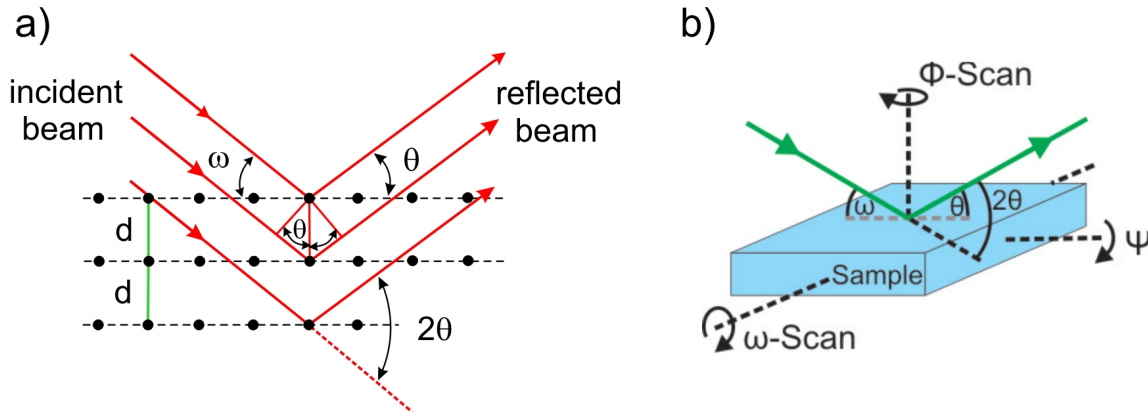
Figure 3.5: (a) Schematic representation of Braggs law and (b) the schematic illustration of the sample geometry in the experiment.[249]

Depending on the sample and type of structural information of interest four different experimental approaches can be applied:

1. **Bragg-Bretano geometry**

   It is the mostly used technique delivering diffracted signal as $\theta - 2\theta$ diffractogram (out-of-plane diffraction). The X-rays impinge the sample at an angle θ while the detectors position is set to the same angle value. Therefore, the elongation of the incoming beam and the exiting beam have a 2θ separation. Continuous symmetric

variation of ω and θ during the scan leads to the scattering vector being always parallel to the surface normal. Therefore the Bragg reflection occurs only from the planes (hkl) which are parallel to the surface plane of the sample.

2. **Grazing incidence**

The penetration depth of the X-rays mostly exceeds the thickness of the molecular film, giving intense signals from the supporting substrate in the spectrum. The way of X-rays in the sample can be increased and, as a sequence, surface sensitivity by setting the angle between the X-ray source and the sample is very small, about $\alpha = 0.2°$ (in-plane diffraction). Moreover, this allows to investigate lattice planes perpendicular to the sample surface by tilting a sample of $90°$.

3. **Rocking curve**

The detection of crystalline phases on a substrate that are slightly tilted from the parallel to surface planes can be obtained when scanning along the ω angle at fixed detector position. The tilt distribution of the crystallites as well as the sample quality is represented by the broadness of measured peaks.

4. **Φ-scan**

Determination of crystalline azimuthal orientations on the surface (epitaxial films) is enabled when the angles θ and ψ are fixed to certain values for the lattice plane of interest and the sample is rotated along its surface normal. The presence of discrete peaks on the diffractogram (fulfilled Bragg conditions) is the indication for the presence of specific orientation of crystalline phases on the surface (non isotropic distribution). Otherwise crystallites have isotropic distribution and constant intensity in the spectra.

XRD measurements for this work have been carried out with a Bruker AXS Discover D8 diffractometer using monochromatized CuK$_\alpha$ radiation ($\lambda = 1.54056$ Å) and a LynxEye silicon strip detector. In addition, single crystalline analysis with subsequent unit cell determination has been performed with a single-crystal diffractometer (Bruker AXS, Quest D8) equipped with a micro-focused Mo anode and a PHOTON 100 CMOS detector as in the collaborative group of Prof. Dr. Stefanie Dehnen.

3.2.3 Near-Edge X-Ray Absorption Fine Structure Spectroscopy (NEX-AFS)

Near-edge X-ray absorption fine structure (NEXAFS) spectroscopy is a useful and effective analytic method that provides information on the electronic structure and allows to identify the geometrical alignment of molecules at surface and interfaces. This method probes the fine-structure arising at near atomic absorption edges, especially K-edges of so-called low-Z atoms (Z is the atomic number). The interaction between X-rays and a sample (solids or liquids) lead to resonant excitation of core electrons into higher unoccupied molecular states (cf. Fig. 3.6 (a)).[250]
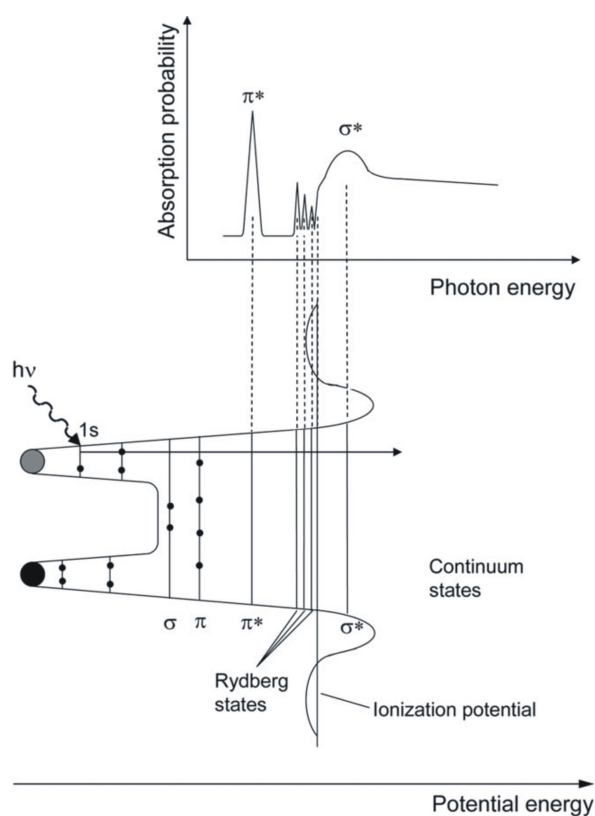
Figure 3.6: Typical excitation process monitored by NEXAFS.[251]

Most materials obtain a high absorption coefficient for soft X-rays, which limit transmission measurements of relatively thin molecular films deposited on a supporting substrate. Instead, different detection modes are used, which are all based on the detection of secondary processes to quantify the absorption.[252] After the resonant excitation of core electrons the remaining hole is refilled by an electron of a higher energetic level. The resulting energy difference has to be compensated by either fluorescence or the emission of Auger electrons,

which depends on the atomic number of the involved elements (high Auger electron yield for light elements and high fluorescence yield for heavy elements). The actual detection of the absorption spectrum is based on these processes and can be monitored by appropriate detectors. Since the organic compounds mainly consist of light elements like carbon, oxygen or nitrogen, the emission of Auger electrons is the predominant mechanism in such materials. Auger electrons, in particular currents, in a certain energy window are measured by using an electron analyzer (*Auger electron yield, AEY*). Another detection mode is based on counting electrons with kinetic energies above a certain threshold (*partial electron yield, PEY*) by a channel-plate detector with a retarding field in front of it. The retarding field blocks secondary electrons and enhances the sensitivity of the method. The electron current can also be detected by measuring the sample current (*total electron yield, TEY*). Therefore, the probe depth (d) in the experiment depends on the detection mode applied and follow $d_{TEY} > d_{PEY} > d_{AEY}$. The mean free path of electrons in common organic materials at excitation energies around 280 eV equals ∼8 Å which makes the AEY mode the most surface sensitive.[253,254]

Typical NEXAFS spectrum features discrete peaks, since the X-ray absorption due to the resonant excitation does not occur at higher energies than the resonant energy as well as characteristic edge jump for energies larger than the ionization potential (cf. Fig. 3.7 (c)).[254] Figure 3.7 (b) provides a NEXAFS spectrum of benzene and corresponding energy scheme in panel (a). In aromatic molecular systems the lowest unoccupied molecular orbitals (*LUMO*, *LUMO+1* etc.) have symmetry and excitations into these final orbitals are denoted as π^*-resonances, while excitations into σ^*-orbitals happen at higher energies (so called σ^*-resonances or Rydberg resonances R^*). Various NEXAFS resonances differ in their spectral width, which is influenced by the vibrational fine-structure as well as by the lifetime of certain resonance. Very short lifetime of σ^*-states leads to wide peaks of several eV, whereas π^*-resonances appear generally sharper.

The difference in chemical shift of the individual atoms in a molecule results in a high number of resonances in the adsorption spectra. Due to the different positions of the core holes, which leads to the difference in each ground state level and each final state, individual core atoms of different chemical surrounding are characterized by different excitation energies. This is illustrated on the example of pyrazine molecule (cf. Fig. 3.7 (b)). The substitution of two carbon atoms in the benzene molecule by nitrogen in the pyrazine results in the appearance of additional spectral resonances for each fundamental transition present in non-symmetrically equivalent carbon atoms.
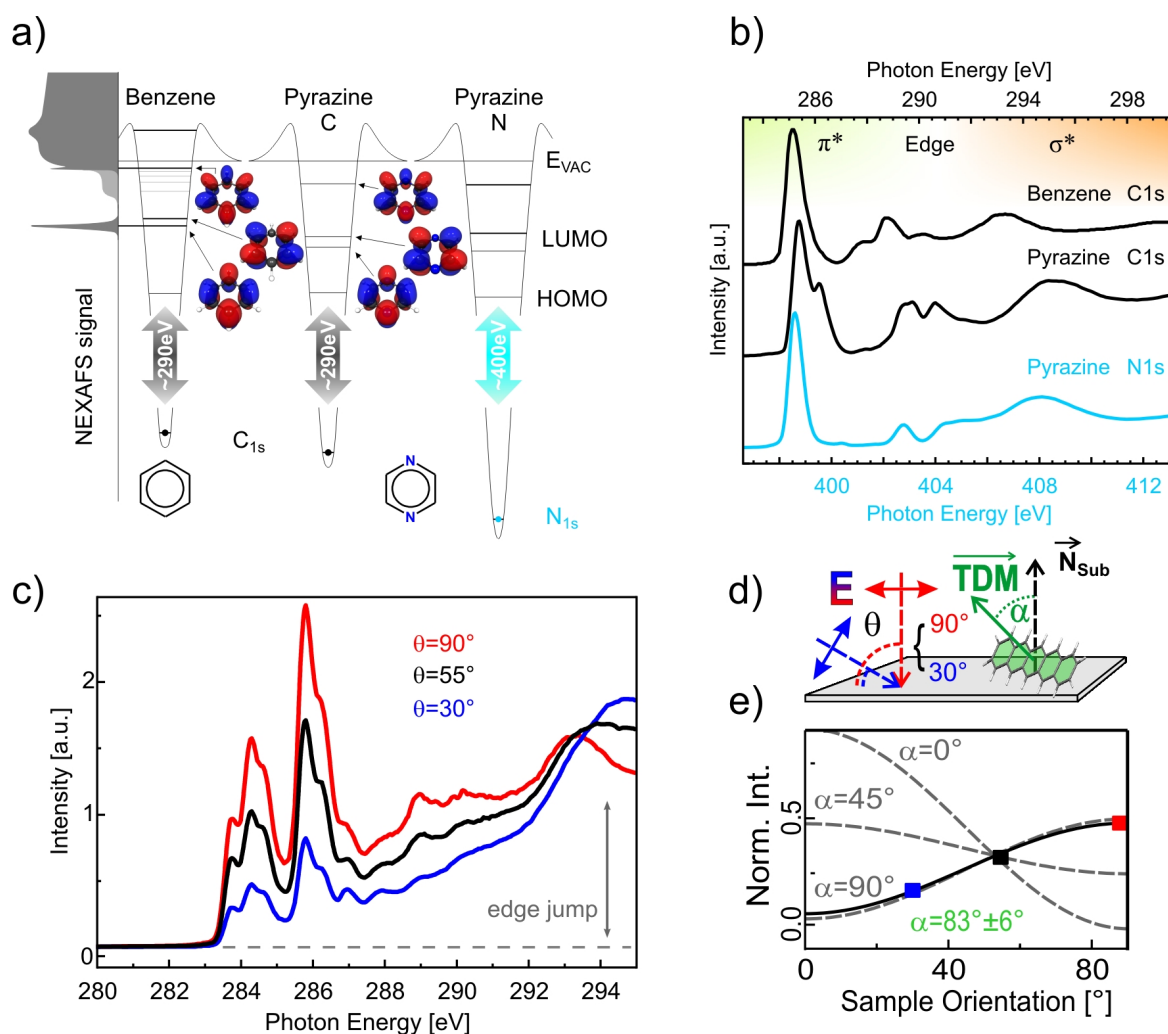
Figure 3.7: (a) Energy schemes calculated using the StoBe code of some simple aromatic molecules (C*1s* for benzene and C*1s*, N*1s* for pyrazine) with (b) corresponding experimental NEXAFS measurements. (c) C*1s* NEXAFS spectra of PEN multilayer on SiO$_2$ substrate recorded at different sample orientations θ. (d) Scheme of experimental geometry and TDM orientation and (e) evaluation of dichroism. [254]

In addition to the information on the electronic structure of molecules this technique can be used to determine their orientation. Since transitions from core levels into unoccupied molecular orbitals are governed by dipole selection rules the relative orientation between the electrical field vector $\vec{E}$ of the incoming photon beam and the corresponding transition dipole moment $\overrightarrow{TDM}$ or $\vec{T}$ of the molecule influence intensities of spectral features. A strong dependence of the signal intensity of characteristic absorption peaks on the angle between the sample and the incident beam is called dichroism and can be experimentally obtained by using the linearly polarized synchrotron beam. In the current work the incidence angle and polarization direction of the linearly polarized beam are defined according to the sketch in the Figure 3.7 (d). The incident angle θ describes the orientation of the sample normal relative to the orientation of the $\vec{E}$-vector of the X-ray beam, while the angle α describes the average orientation of the $\overrightarrow{TDM}$-vector relative to the sample normal.

According to the quantum mechanical description the excitation of an electron from an initial state into a final state happens to a certain extent, so that the probability is given by Fermi's golden rule:

$$I \propto |\left\langle \psi_{final}|\overrightarrow{\mathbf{E}} \cdot \mathbf{p}|\psi_{initial} \right\rangle|^2 \rho_f(E), \qquad (3.4)$$

where $\mathbf{p}$ is the dipole transition operator and the $\rho_f(E)$ the density of final states. Since the light is linearly polarized, this simplifies to

$$I \propto |\overrightarrow{\mathbf{E}} \cdot \overrightarrow{\mathbf{TDM}}|^2, \qquad (3.5)$$

where the transition dipole moment is given by $\overrightarrow{\mathbf{TDM}} = \left\langle \psi_{final}|\mathbf{p}|\psi_{initial} \right\rangle$. For linear PAHs $\overrightarrow{TDM}$ the transition into π^* orbitals lies parallel to the direction of the final state orbital as it is schematically shown in case of pentacene (PEN) molecule (cf. Fig. 3.6 (d)). Therefore the transition intensity is given by

$$I_{\pi^*} \propto P\cos^2\theta \left(\cos^2\alpha + \frac{1}{2P}\tan^2\theta \sin^2\alpha \right), \qquad (3.6)$$

where $\mathbf{P}$ is the degree of polarization. A multilayer of PEN on SiO_2 substrate is characterized by standing PEN molecules within surface layers. The highest intensity of a resonance is obtained when the electric field vector $\vec{E}$ lies along the direction of the final state molecular orbital and is observed under normal incidence ($\theta = 90°$). Under the grazing incidence ($\theta = 30°$) vectors are close to perpendicular to each other and the intensity of the signal decreases. The effective orientation of the $\overrightarrow{TDM}$ can be derived from approximation to the plots (cf. Fig. 3.7 (e)) and yields $\alpha = 83° \pm 6°$ for this film. One should note that the errors slightly depend on the extracted angle value due to the non-linear character

of individual resonances and obtain higher values for angles above 70°. Moreover, the determined molecular tilt angle gives only preferred averaged orientation and does not directly indicate the crystalline nature of the probed material. The sample crystallinity has to be verified by additional experimental method, for example XRD.

a)   b)
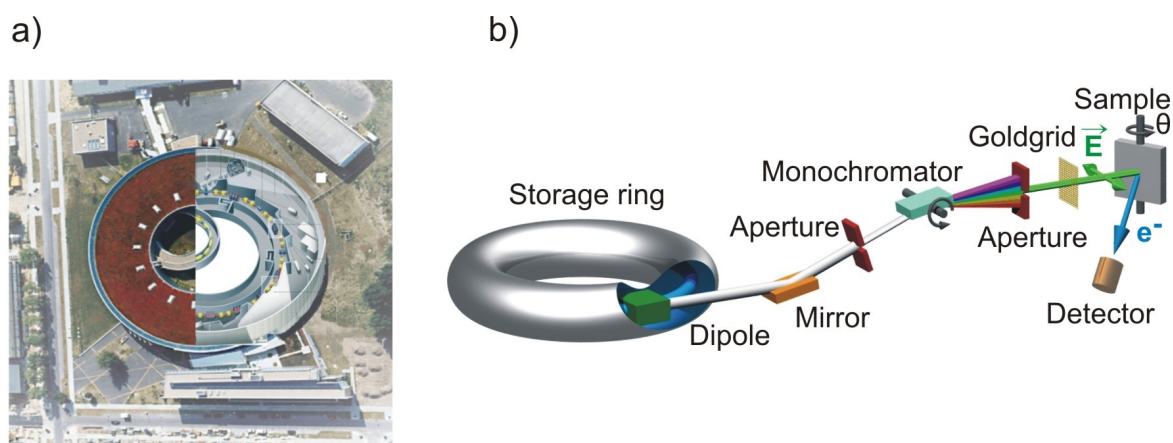
Figure 3.8: (a) Top view of the synchrotron facility BESSY II adapted from the Helmholtz-Zentrum Berlin website [256] and (b) scheme of a dipole beam-line showing the essential optical and detection elements relevant for NEXAFS measurements. [254]

This technique requires a linearly polarized adjustable X-ray beam, which is not easy to realize in home-laboratories but available at synchrotron radiation sources. The NEX-AFS experiments for this work have been conducted at the HE-SGM dipole beamline at the synchrotron storage ring BESSY II (Berlin) facilitated by the Helmholtz-Gesellschaft Deutschland. [255] A schematic illustration of the beamline is given in Figure 3.8. The synchrotron radiation, originated from the emission of electromagnetic radiation of angular accelerated electrons kept in the storage ring, is deflected onto a monochromator grating in the separated beamline. This allows selecting a certain energetic region of the X-ray beam.

If not specified, a retarding field of -150 V was applied to obtain NEXAFS spectra presented in this work. The polarization factor of the synchrotron beam was 0.91. All spectra were recorded with a spectral width of the monochromatized light of 300 meV. To calibrate the absolute energy scale of the NEXAFS spectra, a simultaneously recorded signal of the photocurrent from a carbon coated gold grid in the incident beam was used which exhibits a sharp resonance at 284.9 eV. All NEXAFS raw data have been normalized with respect to the incident photon flux, and the transmission characteristics of the clean substrates were considered.

3.3   Elemental composition

3.3.1   X-ray photoelectron spectroscopy (XPS)

To probe the electronic structure of occupied states at the surface and near surface region a commonly used photoelectron spectroscopy analytical technique, in particular *X-ray photoelectron spectroscopy (XPS)*, which is also called *electron spectroscopy for chemical analysis (ESCA)*, has been used. If the photon energy of the X-ray beam is large enough the core level electrons of surface atoms absorb photons with the energy $\hbar\omega$ and leave the surface with a kinetic energy[234]

$$E_{Kin} = \hbar\omega - E_{Bin} - \phi, \qquad (3.7)$$

where E_{Bin} is the binding energy of core level electrons and ϕ is the spectrometer work function (material-dependent factor). This excitation process in known as the photoelectric effect and the photoemission can be schematically illustrated according to Figure 3.9 (a).[257,258] Generally, X-rays with electron energies around 1-2 keV will penetrate several hundred nanometers into a surface ionizing atoms to that depth. To be detected photoelectrons have to leave the surface without interacting with overlaying atoms, which may lead to loss of E_{Kin} (inelastic scattering). The probability that a photoelectron will reach the surface without losing any of its kinetic energy can be approximated using the Beer-Lambert Law:

$$I_d = I_0 e^{-d/\lambda}, \qquad (3.8)$$

where I_d is the photoelectron intensity originating from atoms at depth d, I_0 is the signal emanating from the surface atoms, and in the first approximation λ is the electron inelastic mean free path (IMFP).[259–261] The IMFP represents the average distance a photoelectron can travel before undergoing inelastic scattering and is dependent on the material properties (i.e. density). In case of metal oxides the IMFP of metal 2p core electrons is calculated to be in the order of 10–18 Å using the AlK$_\alpha$ radiation ($hv = 1486.6$ eV) which allows to probe the sample at the depth between 3–6 nm for these systems.[231,253,262]

Photoelectrons ejected from a sample surface are focused towards the entrance slit of a combined concentric hemispherical (CHA) and spherical mirror (SMA) energy analyzer (cf. Fig. 3.9 (b)). Prior to entering the analyzer the energies of the photoelectrons are retarded to a fixed pass energy (PE). To monitor the photoelectron counts as a function of BE (spectrum mode) the CHA is used. The absolute resolution of the instrument increases with decreasing
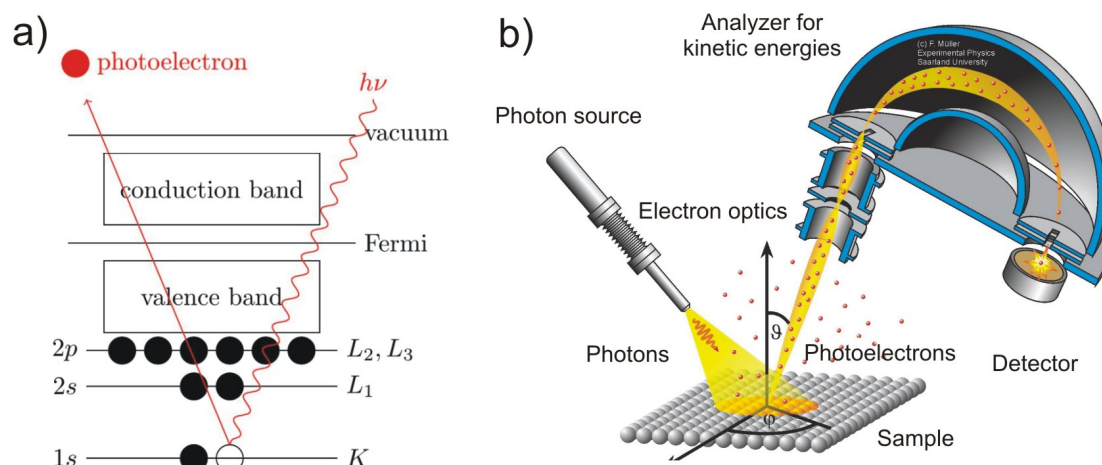
Figure 3.9: (a) Schematic illustration of the energy diagram for the photoelectric effect[257] and (b) XPS detection principles.[263]

pass energy. Any increase in spectral resolution results in a loss of photoelectron signal due to a higher dispersion of the electrons around the exit slit.
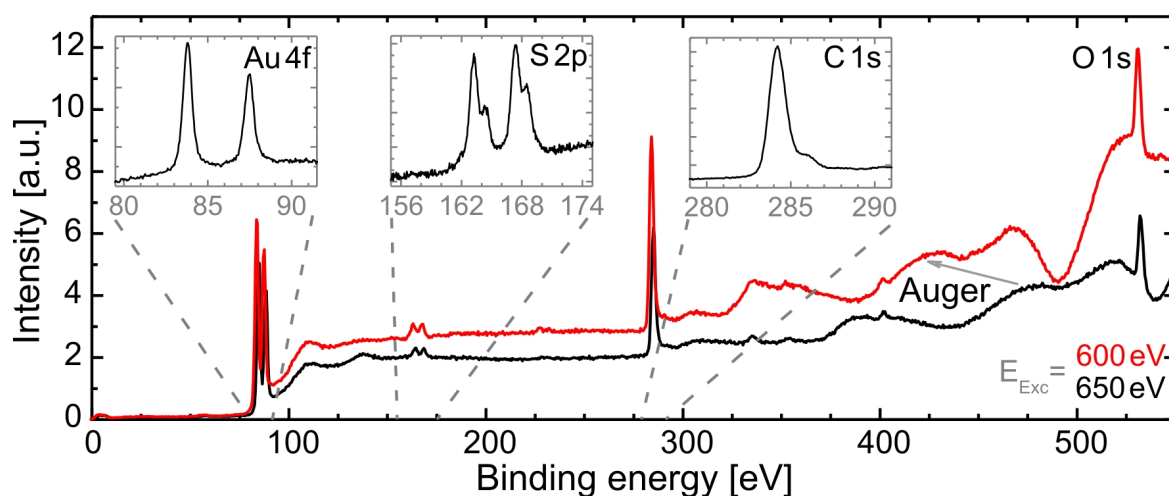
Figure 3.10: XP-spectra of stilbenedithiol on gold measured at different excitation energies and panels with high resolution spectra for selected elements.[264]

An exemplary XP-spectrum is shown in Figure 3.10.[264] Besides the peaks due to elastic photoelectrons, they exhibit a number of additional features, like the continuous background, Auger peaks and peaks due to the plasmon losses which can be featured in the spectral line. Emitted core level electrons show up as sharp peaks in the spectra. Each peak is defined by certain electron binding energy which, in turn, is essentially characteristic of atomic species.[266] In other words, the presence of peaks at definite energies is an indication of the presence of a particular elemental species at the surface region. As a consequence, the
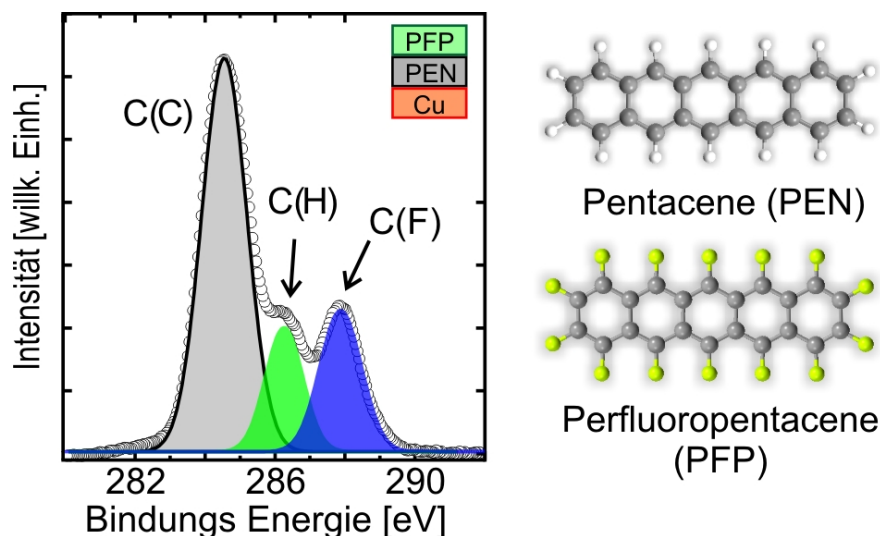
Figure 3.11: XP-spectra of heteromolecular bilayer PFP/PEN system on Cu illustrating different C*1s* signals from different carbon atoms the molecule.[265]

XP-spectrum contains information on the surface composition. By comparing the binding energies on the experimental spectrum with values from a database the chemical composition of the sample can be distinguished. Moreover, the high-energy resolution XPS measurements allow visualizing the fine structure of core levels, which binding energy varies depending on the chemical surrounding, so-called *chemical shift* (cf. Fig. 3.11).

It should be noted, that for samples of insulating character, like TiO_2, the XPS measurements can be hampered by the sample charging effect, especially when one is intended to study the relatively small shifts in core electron binding energies. Accumulated surface charge can easily shift a photoelectron energy peak by several tens of electron volts, and typically has a nonuniform character. The general approach to overcome this problem is to use a flood gun to compensate the surface charge. This method, however, can severely damage organic materials and, therefore, is not applicable for samples with SAMs.[267]

All XPS analysis completed as part of this work was performed at the HE-SGM dipole beamline, located at the synchrotron storage ring BESSY II (Berlin), Germany. The X-ray photoemission spectra were recorded at an incident angle of 45° and at normal emission using a hemispherical electron energy analyzer (Scienta R3000), typical pass energies of 100 eV and photon energies between 350 and 750 eV depending on the substrate and the studied region, chosen such that parasitic contributions by, for example, Auger lines were omitted. To provide a precise energy calibration, the XPS binding energies have been referenced to characteristic substrate peaks of the various samples which have been measured simultaneously. The spectra have been corrected by subtracting a Shirley background and

dividing by the intensity of the corresponding substrate signals to compensate variations of the photon flux.[268] After that, spectra have been normalized to the maximum intensity of each series to enable comparability.

3.3.2   Energy-dispersive X-ray spectroscopy (EDX)

Energy-dispersive X-ray spectroscopy (EDX) is an analytical technique used for the elemental analysis or chemical characterization of samples.[269] To provide elemental identification a high energy beam of electrons penetrates a sample and excites core electrons to high energy states, creating a low-energy vacancy in the electronic structures of the atom. This leads to a cascade of electrons releasing from higher energy levels until the atom regains a minimum-energy state. Due to conservation of the energy, electrons emit X-rays at their transition to lower energy states. The number and energy of the X-rays emitted from a specimen can be measured by an energy-dispersive spectrometer. Each element has a unique atomic structure as the energies of the X-rays are characteristic of the difference in energy between the two shells of the emitting element. Quantitative analysis (determination of the concentrations of the elements present) entails measuring line intensities for each element in the sample. The accuracy of EDX can be affected by many parameters. For example, EDX detectors cannot detect presence of elements with atomic number less than 5 (H, He, Li, Be). The nature of the sample may influence the accuracy as well (inhomogeneous or rough samples), since the likelihood of an X-ray to escape the specimen and be detected depends on the energy of the X-ray and the amount and density of material in has to pass through.[270–272]

EDX data presented in the present work have been carried out using scanning electron microscope CamScan 4DV equipped with an EDX microanalysis system (Noran Instruments Voyager 4.0) in collaboration with the group of Prof. Dr. Stefanie Dehnen.

3.4   Thermal stability

3.4.1   Thermal desorption spectroscopy (TDS)

Thermal desorption spectroscopy (TDS), which is also referred to as *temperature programmed desorption (TPD)*, allows the characterization of thermal stability of a compound adsorbed on a surface.[273–275] This method incorporates the monitoring of the desorption process as a function of substrate temperature with mass-sensitive detection, thus allowing chemical

sensitivity. If the adsorbed species within a multilayer or a monolayer gains enough energy from thermal vibrations of surface atoms during the sample annealing they can leave the sample, nevertheless they are chemisorbed or physisorbed.

In the experiment it is realized by a filament heating a sample with a linear heating ramp under UHV conditions (cf. Fig. 4.5). Activated species leave the surface, which leads to a rise in pressure in the measurements chamber. Desorbed species can be directly detected by a quadrupole mass spectrometer or partially re-adsorbed on cold components with subsequent desorption after some time. If the pumping speed of the used UHV setup is large compared to the partial pressure increase of the desorption the measured partial pressure is proportional to the desorption rate. Then the area under the measured TDS curves is generally proportional to the number of desorbing molecules.[276] Since the TDS measurements are carried our under UHV conditions, even small pressure changes induced by adsorbate desorption or parasitic effects, like temperature oscillations, can affect measurements. A quadrupole mass spectrometer (QMS) is used to detect different m/z (mass-to-charge-ratio) signals, which correspond to molecules or their fragments. To enable this the incoming molecules have to be ionized by a filament in the mass spectrometer. Consequently, the ions, which are afterwards accelerated, interact differently with electrical fields, depending on their actual m/z value. By tuning the voltage between two rod pairs in the quadroupol mass spectrometer only ions with a certain ratio have a stable trajectory and can reach a detector.
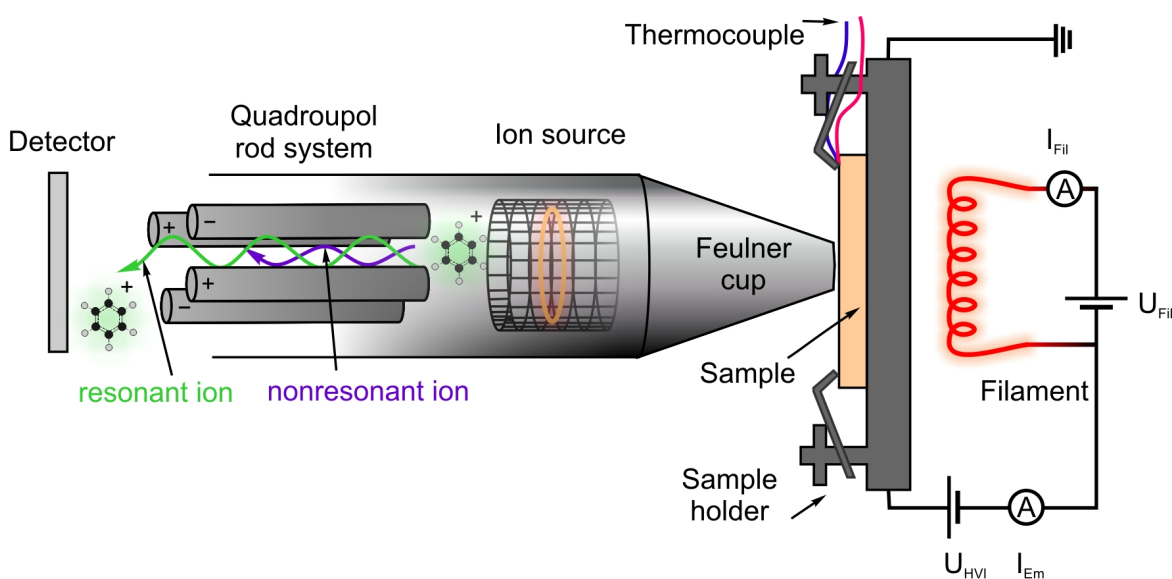
Figure 3.12: Operation scheme for the TDS measurement with the schematic illustration of the working principle of a quadroupol mass analyzer.

Adsorption takes place when an attractive interaction between a particle and a surface is strong enough to overcome the disordering effect of thermal motion.[234,277,278] Depending on the strength of the interaction between an adsorbate and a substrate physisorption (weak interaction) or chemisorption (strong interaction) takes place. Weak adsorbate-substrate interaction for physisorbed species is characterized by van der Waals forces and intact desorption. The typical binding energies are on the order of 10-100 meV. Chemisorption occurs when the overlap between the molecular orbitals of the adsorbed particle and the surface atoms permit the formation of chemical bonds, which are characterized by dissociation energies on the order of 1-10 eV. In this case the activation barrier must be overcome. A common feature of molecular chemisorption is the weakening of intramolecular bonds that often lead to the dissociative desorption character. Therefore, several surface processes may occur when providing thermal energy to a sample with an adsorbate layer: adsorbed molecule can decompose to either gas phase products or other surface species (dissociative desorption); an atomic adsorbate may react with the substrate to yield a specific surface compound, or diffuse into the bulk of the underlying solid or by gaining enough energy complete adsorbate molecule can escape from a surface (intact desorption).[279] An exemplary TD-spectra are shown in Figure 4.6 (a) and demonstrate desorption of multilayer films of different thickness and a monolayer desorption preak.[286]

Generally, the desorption rate of the adsorbate from the surface r is described by the Polanyi-Wigner equation[280]:

$$r = -\frac{d\Theta}{dt} = v(n)\Theta^n e^{-\frac{E_{des}}{RT_{des}(t)}}, \tag{3.9}$$

where Θ is the surface coverage (molecules per cm^2), v the pre-exponential factor and n the desorption order. R stands for the universal gas constant and T_{des} for the temperature of desorption peak maximum.[280,281] This equation is a helpful tool to understand, describe and simulate the desorption spectrum of a system[282]. This theoretical description allows us to get information about the population and energetics of adsorbates on a certain surface. For a linear temperature ramp $\beta = dT/dt$ the activation energy of desorption can be estimated according to the Redhead equation[283]

$$E_{des} = RT_{des}\left[\log\left(\frac{v_0 T_{des}}{\beta}\right) - 3.46\right], \tag{3.10}$$

where the pre-exponential factor is typically given by $v_0 = 10^{13}\,s^{-1}$ [284] However, this value is only valid for small molecules like CO.[284,285] For precise calculations the pre-exponential

factor can be experimentally determined for a certain substrate-adsorbate system from a set
of TDS spectra of different linear heating rates.
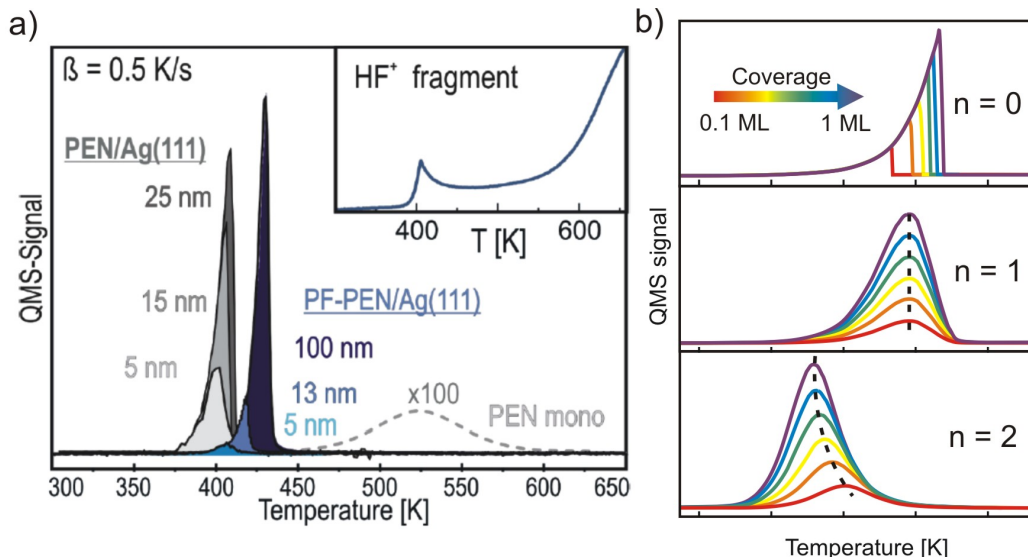
Figure 3.13: (a) TDS spectra of perfluoro-pentacene PFP-PEN on Ag(111)
reordered for different film thicknesses. [286] (b) Schematic simulation of TD-
spectra for different desorption kinetics.

The nature of the actual microscopic desorption process has a big impact on the desorption
process. [234] Zero-order desorption ($n = 0$) describes the desorption of physisorbed molecules
(cf. Fig. 4.6 (b)). The corresponding QMS signals exhibit an exponential increase with
temperature until the complete layer has desorbed. At that point, the signal instantly drops
giving the tearing edge of the spectra. The position of the tearing edge depends strongly
on the coverage such that it shifts to higher temperatures with increasing coverages. For
first ($n = 1$) and second ($n = 2$) order desorption TDS data exhibit another behavior. The
first describes chemisorbed monolayers and is characterized by a symmetric peak shape, of
which center position does not change with the coverage. Second order desorption kinetics is
assigned to recombinative desorption; in this case the peak is symmetric but its broadness
as well as its center shift with coverage such that it becomes sharper and shifts to lower
temperatures with increasing coverage.

For the current study all TD-spectra were reordered using a Pfeiffer QMG 220 M3 with
detection range of $m/z \in (1 - 300)$ amu. To provide reliable temperature measurements, K-
type thermocouples were attached directly to the sample surfaces. The spectra were acquired
during a linear increase of the substrate temperature with a heating rate of $\beta = 0.5$ K/min
using a self-implemented computer-controlled PID-feedback control if not specified. To

avoid parasitic contributions from the sample holder and the manipulator, a movable Feulner cup was positioned close to the sample surface[287].

CHAPTER 4

ZnO surface etching upon formation of phosphonic-acid SAMs

4.1 Introduction

Functionalization of metal oxides by means of SAMs has been studied with attention to its promising perspective in photovoltaic and photocatalytical technological application. Of particular interest for such applications are TCOs which are widely used as transparent electrodes in light emission and display devices or solar cells.[288] Among these materials ZnO has gained special interest since its large charge carrier mobility and low temperature processability also offer an alternative to amorphous silicon for the fabrication of thin film transistors also on flexible substrates.[289,290] In addition, ZnO based organic/inorganic structures have been demonstrated to enable the fabrication of hybrid diodes.[291] Mostly common prototypical systems for tailoring interfacial properties are organothiol-based SAMs adsorbed on noble metal surfaces which can be easily prepared by immersion, and therefore have been widely studied.[292] Similarly, covalently fixated SAMs have also been reported for metal oxides. Among the available anchoring units (thiols, silanes, amines, carboxylic or phosphonic acid) phosphonic acid based SAMs exhibit the highest stability.[293–295] Aside from its ease, the preparation of organothiol-SAMs on gold substrates by dint of immersion provides the advantage of being a self-terminating process which ensures the formation of exact monolayer films with exclusion of additional multilayers being formed. When providing sufficient thermal energy and time during preparation this yields exceptionally well ordered SAMs of one exclusive phase.[207] By contrast, on oxidic substrates undesirable side reactions such as partial dissolution of the substrate surfaces have been reported[294,296–300] which are made responsible for failure and improper behavior of electronic devices.[301–303]

Therefore, a closer analysis of the immersion chemistry of such hybrid systems is mandatory. Understanding the chemical robustness of ZnO surfaces is also of interest in the field of corrosion since Zn/ZnO coatings are commonly used as protection layers for steel sheets, hence raising questions about their chemical stability and possible delamination. [304]

Here we have studied the formation of phenylphosphonic acid SAMs on differently oriented, well-defined ZnO single crystals with particular emphasis on the substrate integrity upon adsorption. Beside the formation of monolayer films also a notable dissolution of all ZnO substrates was found, which leads to the growth of crystalline precipitations during prolonged immersion. Combining EDX, TDS, AFM, XRD the structure, composition and stability of these precipitations have been thoughtfully investigated. The influence of reaction conditions for the SAM formation like surface roughness and pH value of a solvent has been studied as well. Additionally, the energetics of this surface-etching process was analyzed in the group of Prof. Dr. Bernd Meyer (Erlangen) using density functional theory (DFT) method to identify potential microscopic pathways of this reaction.

## 4.2 ZnO surface etching and Formation of surface precipitations

Previous studies reported a notable etching of ZnO surfaces upon PPA-SAM formation by immersion in the presence of remaining water in the solutions. [297,294] Therefore, particular attention was paid to use carefully dried ethanolic solutions for our film preparation. PPA films have been prepared on the ZnO-O surface from immersion in dry ethanol for 1 day at 75°. Though after 1 day of immersion no deposits are visible by the naked eye, thorough AFM measurements reveal the presence of small precipitations which steadily grow with increasing immersion time. Figure 4.1 (a) depicts an AFM micrograph of a ZnO-O sample that had been immersed for 4 days in water-free ethanolic PPA solution. It reveals a large density of precipitations with a height of 10-20 nm and diameters of about 50-80 nm yielding an increased surface roughness as compared to the bare ZnO-surfaces. Occasionally, also larger particles with lateral extensions of more than 200 nm are found. Although the surface etching is supposed to be reduced in water-free solutions, the dynamic process of the phosphonic acid etching the ZnO is still conceivable on a time scale of days. For comparison, SAMs were also prepared from PPA solution using absolute ethanol without extra drying. In that case the formation of noticeable grainy structures was found already after 9 h (cf. Fig. 4.1 (b)) hence showing a faster precipitation formation which might be attributed to remaining water. A closer inspection of the AFM micrograph shows furthermore that some particles are

located at step edges of the ZnO surface - typical monoatomic steps of the ZnO-O surface (cf. Fig. 4.1, (c)) - while others nucleate at terraces where also holes with a depth corresponding to one ZnO layer are present.
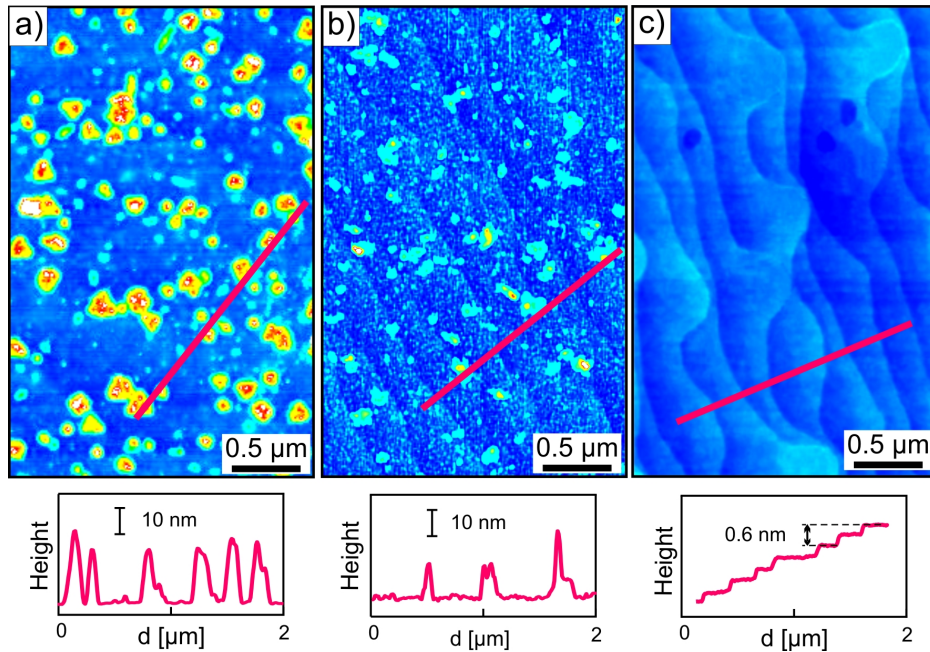
Figure 4.1: Comparison of AFM micrographs (phase image) showing the morphology of ZnO-O samples immersed in ethanolic PPA-solutions (a) using dried ethanol (immersion time: 4 days) and (b) absolute ethanol (without drying, immersion time: 9 hours) and (c) a bare ZnO-O surface, together with corresponding topographic line-scans (red curves). Note, that the line profile for a bare sample is tilted for better visualization of the substrate surface steps.

To enable a more detailed analysis of the nature of precipitations, larger structures are required as they are obtained by immersion of ZnO crystals in (absolute) ethanolic PPA solution for several days. After that prolonged immersion time ZnO samples revealed a mat adlayer of milky color, thus indicating a distinct surface conversion. Similar grown structures have been obtained for both polar ZnO surfaces as well as the non-polar, mixed terminated surface (cf. Fig. 4.2 (a-c)). Corresponding optical and scanning electron micrographs reveal the presence of distinct three-dimensional star-shaped precipitations consisting of individual needles. The lateral diameter of a single precipitation is about 10-20 μm and the typical height is up to 15 μm (cf. Fig. 4.2 (f)). A majority of needles is not planar but tilted with angles of between 0° and 90° relative to the surface plane without any indications of a preferential lateral orientation. The size of the formed precipitations strongly depends on the immersion time which allows growing even larger structures. To complement the
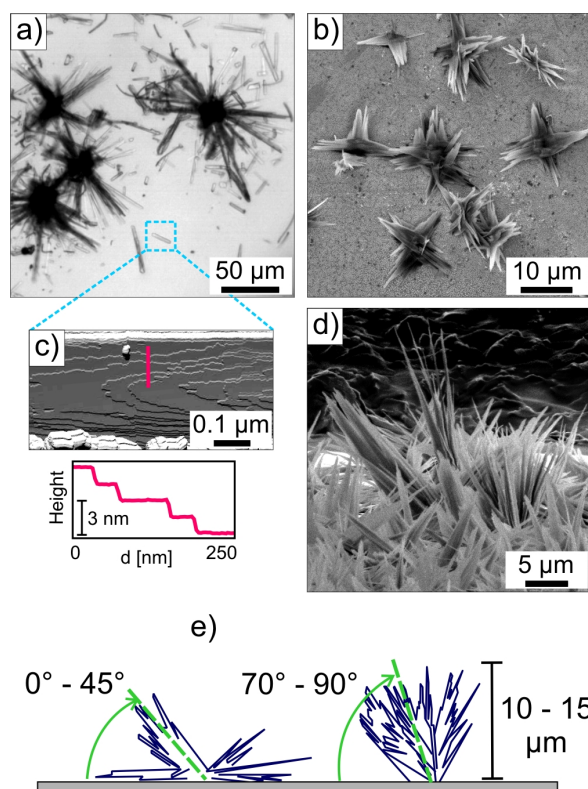
Figure 4.2: Morphology of surface precipitations formed on various ZnO surfaces upon immersion in PPA-solutions using (absolute) ethanol: (a) on mixed terminated ZnO-M after 4 days of immersion (optical micrograph), (b) for ZnO-O and (d) for ZnO-Zn in each case after 2 days of immersion (SEM micrographs, top and side view). Panel c) depicts an AFM phase image of an individual recumbent needle with corresponding topographic line-scan.

morphological study AFM measurements have been carried out. Since the dimensionality of the surface aggregates limits the AFM applicability, only isolated needles oriented parallel to the surface can be characterized. As shown exemplarily in Figure 4.2 (d,e) the corresponding AFM data reveal a characteristic step height of 1.4 nm between flat terraces which suggests a crystalline nature of the precipitations.

In addition, longer immersion is accompanied by the formation of a dense adlayer on the sample surface between the large star-shaped precipitation, so that the morphology of bare ZnO surface can not be further visualized (cf. Fig. 4.3 (a,b)). Next to grainy structures formed after 2 days, planar needles, flakes and later small agglomerations of needles were found. Large precipitations are weakly bound to the surface and can be partially removed in ultrasonic bath in acetone and propanol for 15 minutes in each solution. This, however, leads to a highly damaged remaining surface (cf. Fig. 4.3 (c)), of which microscopic structure can not be easily restored. In this case, the usual preparation procedure by sputtering and
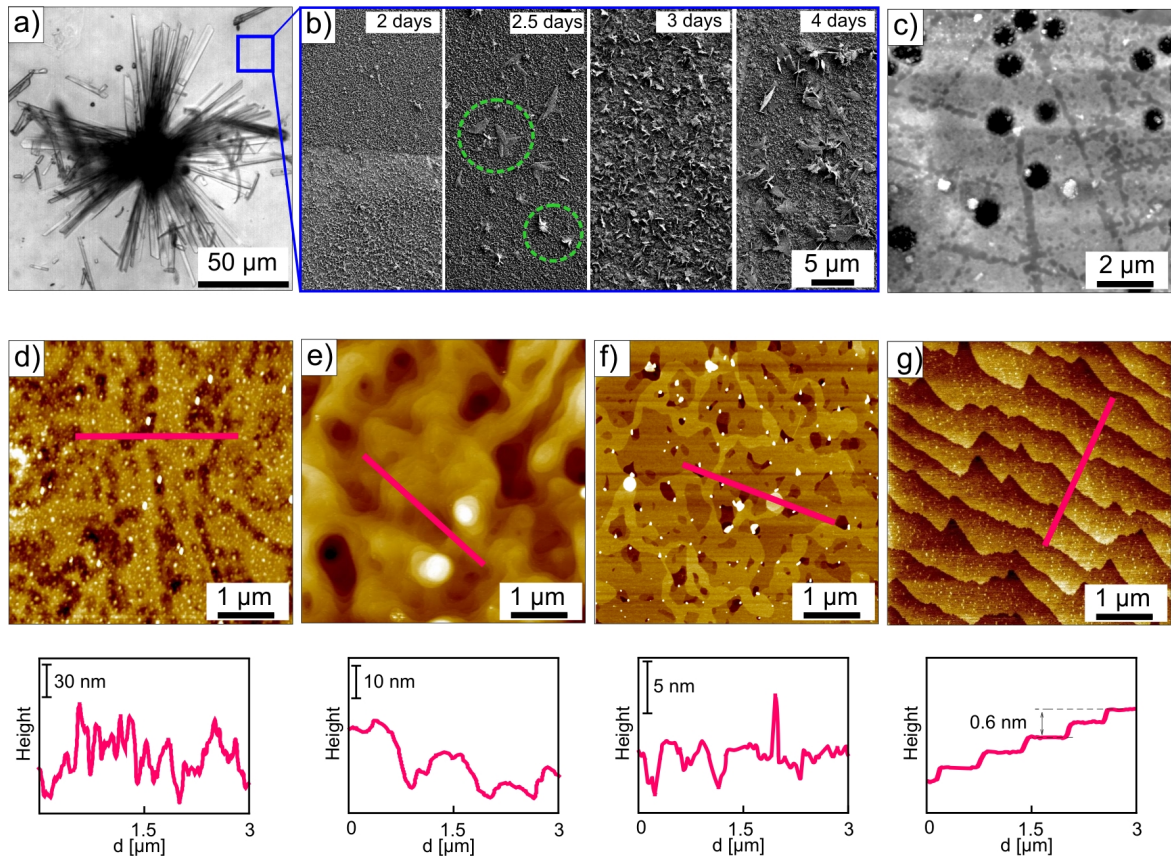
Figure 4.3: (a) Optical image of grown precipitations on the ZnO-O surface after 4 days of immersions with (b) a set of SEM micrographs, depicting the area of the sample surface between large star-shaped aggregation after: 2 days, 2.5 days, 3 days, 4 days. (c), (d) The remaining ZnO-O surface after removing the precipitations by sonication in acetone and propanol solutions. Figure (e) visualizes the surface on the panel (d) after general preparation procedure (sputtering and annealing in oxygen gas for 1 hour in UHV chamber) and (f) after additional annealing in the muffle furnace in air for 3 hours and (g) the surface prepared combining the UHV method and annealing in an muffle furnace for 12 hours with corresponding line profiles.

stepwise annealing in the vacuum chamber in the oxygen atmosphere for an hour does not result in a clean and atomically flat surface, but instead only repeated cycles of Ar^+ ion bombardment and excessive annealing for more than 12 hours at 1200 K in the muffle furnace under ambient conditions allows repairing surface crystallinity and results in smooth atomically flat surfaces with large terraces (cf. Fig. 4.3 (d-g)).

Complementary contact angle measurements have been carried out on ZnO single crystals to study surface tension. The measurements have been performed immediately after placing a droplet of distilled water on the surface. To increase the reliability of the analysis, contact
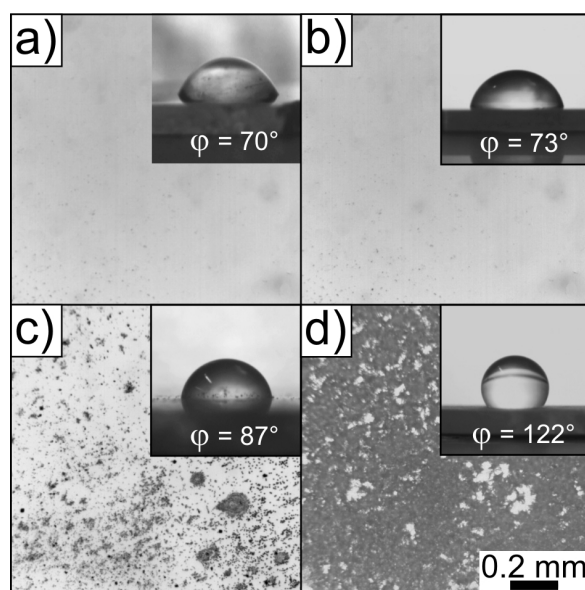
Figure 4.4: Optical microscopy image of temporal evolution of surface precipita-
tions formation on ZnO-O sample together with corresponding measurements of
water contact angles as a function of immersion time in ethanolic PPA solution:
(a) 12 hours; (b) 1 day; (c) 2 days; (d) 1 week.

angle values were averaged over several different locations. Data were obtained for different
immersion times up to one week and exhibit a decrease of the wettability of ZnO surfaces by
water (cf. Fig. 4.4). The unmodified ZnO-O shows an average contact angle of $40° \pm 4°$. PPA
modification after 12 hours of immersion increases the contact angle up to $70° \pm 4°$, which
remains nearly constant also after a day of immersion. The formation of visible surface
precipitations further influences the surface wettability and results in a much higher contact
angle of $122° \pm 4°$ after a week of immersion. However, this highly hydrophobic behavior is
not solely caused by a chemical surface functionalization by means of the SAM but also due
to the Lotus effect as a consequence of the formation of non-planar precipitations. Similar
hydrophobic character with the comparable contact angle values was previously reported for
nanostructured ZnO layers.[305,306]

4.3   Thermal stability of surface precipitations

Apparently, immersing ZnO samples in PPA solution leads not only to the surface modifica-
tion by SAM but also to an additional reaction leading to the formation of surface aggregates.
From morphological analysis these surface precipitations consist of needles which at first
sight have a crystalline structure. Though the covalent attachment of PPA to the ZnO surface

is the primary process during immersion, the possibility for PPA to crystallize from solution might be also taken into account. In order to verify that assumption the thermal stability of the surface precipitations was examined by comparing it to the stability of crystalline PPA powder.
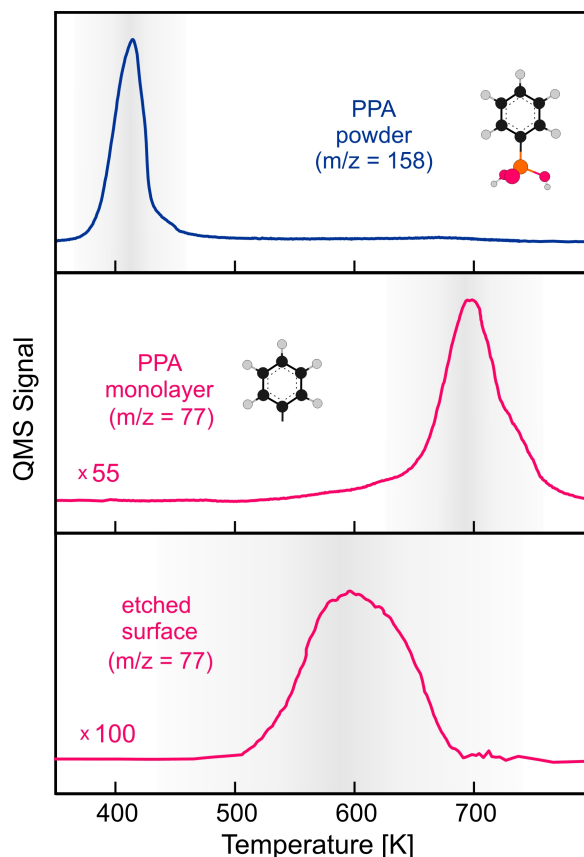
Figure 4.5: (a) Series of thermal desorption spectra recorded for (a) PPA powder (blue curve, detected mass signal $m/z = 158$ amu), (b) PPA-SAM (red curve, mass signal $m/z = 77$ amu) and (c) etched ZnO-O samples during a linear heating rate of 0.5 K/s. Spectra were obtained with the heating ramp $\beta = 0.5$ K/s.

In this experiment a small amount of PPA powder was reamed onto the oxide sample surface and heated with a constant heating ramp ($\beta = 0.5$ K/s) up to 850 K in UHV. Simultaneously, TDS measurements have been used to track the desorption of PPA (cf. Fig. 4.5 (a)). PPA starts to desorb from the surface at 380 K and the maxima intensity of the desorption signal was found at around 420 K. The largest contribution was recorded for the mass of the molecule ion ($m/z = 158$ amu) which is indicative for an intact desorption as expected for van der Waals bound PPA solids. By contrast, PPA-SAM prepared by immersion remains rather stable even at temperature higher than 600 K and eventually desorbs dissociatively causing a distinct desorption peak at the mass of the phenyl ring ($m/z = 77$ amu) at around

690 K (cf. Fig. 4.5 (b)). The sample with a dense layer of surface precipitations grown after a week of immersion was annealed under vacuum conditions as well (cf. Fig. 4.5 (c)). No signal at the mass of the molecule ion was registered. Furthermore, the absence of the desorption peak at around 400 K in the signal of the phenyl ring mass, which is referred to the desorption of the pure PPA compound, indicates the origin of these precipitation as not the crystallized PPA. The rather broad peak of small intensity from 500 K up to 700 K is related to the dissociative desorption of PPA monolayer, which formation is not suppressed by the surface etching, or partial desorption of the newly formed compound. Detailed investigation of PPA monolayer desorption from ZnO surfaces will be discussed in the next Chapter 5.
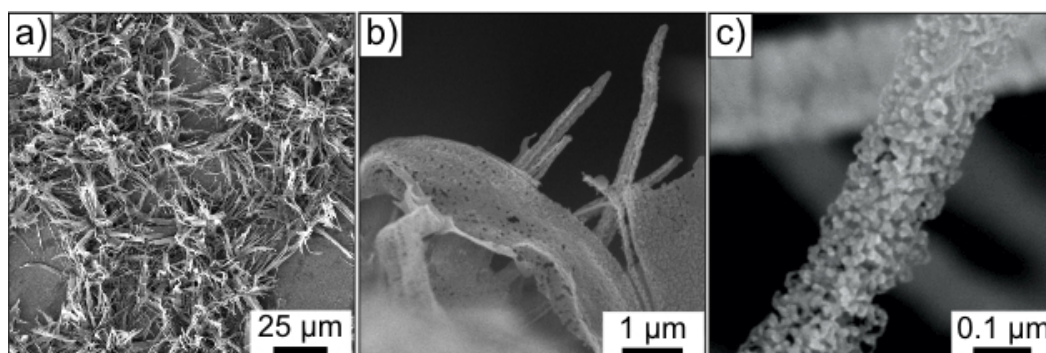

Figure 4.6: SEM image of surface precipitations grown on the ZnO-O sample after a week of immersion and annealing up to 900 K in vacuum: (a) top view; (b) side view and (c) magnified image of a needle. The contrast image (white/black) indicates the porous structure of annealed precipitations.

Interestingly, the grown precipitations are thermally rather stable and still can be found on the surface even after extensive heating up to 900 K in UHV (cf. Fig. 4.6 (a)) as revealed by SEM. However, the sample annealing leads to the color change of the adlayer from white to black, which can be attributed to some structural changes. A closer inspection shows further that their macroscopic structure is preserved upon extensive heating while the needles become porous (cf. Fig. 4.6 (b,c)). The majority of organic materials in a condensed phase sublimes at temperatures below 500 K and completely decompose up to 820 K.[307–309] Therefore, the observed high thermal stability of the precipitations directly excludes crystalline PPA or any pure organic compound as a material in the obtained precipitations especially in view of the rather low thermal stability of PPA powder which is completely desorbed at ∼450 K.

4.4 Structural investigation and composition analysis of surface precipitations

In the previous section it was shown, that precipitations exhibit unexpected high thermal stability for pure organic compounds. To finally understand their exact nature, the precise analysis of their chemical composition is needed. This is enabled here by conducting EDX measurements. Since the penetration depth of the electron beam, which is utilized for this techniques, is relatively high and can result in strong signal from the underlying ZnO crystal, individual precipitations have been peeled off from the supporting substrate and measured separately. These measurements of several precipitations fragments reveal a content of zinc, phosphorus, oxygen and carbon (cf. Fig. 4.7). The detected Zn cannot originate from the ZnO and, therefore, is incorporated in the precipitation material, hence showing the formation of a metal-organic compound. Because of the low EDX cross section of light elements a quantitative analysis was restricted to zinc and phosphorus only, yielding a stoichiometric ratio of $P : Zn \approx 1 : 1$. From these considerations a possible origin of the etching products as a result of a dissolution-precipitation reaction during immersion is the formation of zinc-phosphonate.
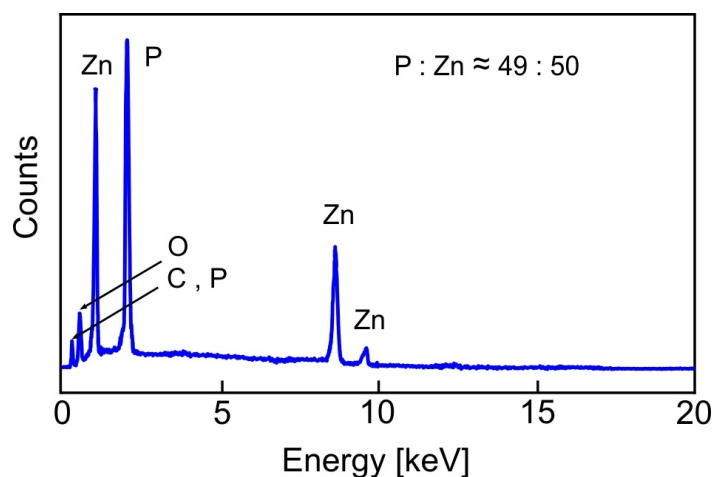

Figure 4.7: EDX analysis of precipitations grown on the ZnO-O sample after a week of immersion reveal a content of zinc, phosphorus, oxygen and carbon.

To derive further information on the precipitations and to identify the type of the zinc-phosphonate compound, X-ray diffraction measurements were performed. The size of the formed aggregates is rather small and limits the single crystal analysis, as well as the XRD powder measurements due to the small amount of the material. However, since the precipitations exhibit rather isotropically distributed character, out-of-plane measurements

in Bragg-Brentano geometry were carried out to mimic powder spectra. First, the surface precipitations grown after 4 days of immersion in water-free ethanolic PPA solution have been analyzed (cf. Fig. 4.8 (a)). The corresponding diffractogram reveals in addition to the substrate reflex at $2\theta = 34.9°$ for ZnO(0001) planes weak but distinct signatures of another crystalline material, thus corresponding to the precipitations (cf. Fig. 4.8 (b)). The presence of distinct diffraction peaks confirms the crystalline nature of the precipitations and enables a comparison of the peak positions with powder diffraction patterns of known zinc-phosphonates. To enhance the intensity of the diffraction signals further measurements have been performed on precipitations formed after immersion in ethanolic PPA solution for 2 days, 1 week and 1 month as depicted in panel (c) in Figure 4.8. Although the size of the formed needles was certainly increased, the performance of an adequate single crystal analysis was still challenging. From out-of-plane measurements it was found, that diffraction peaks of the precipitations grown in the ethanolic solution agree well with these formed in dry solution and the powder spectrum of zinc-phenylphosphonate ($C_6H_5O_3PZn$, ZnPP)[310] thus allowing for their tentative identification (cf. Fig. 4.8 (d)). Based on this assignment, the peaks found at $2\theta = 6.2°$ and $2\theta = 16.9°$ are attributed to (010) and (110) planes in the crystal consequently. The peaks at $12.4°$ and $18.6°$ correspond to the second and the third order of the (010) plane.

In addition, a characteristic temporal evolution of the relative intensity of the various diffraction peaks with the immersion time was observed. The initially formed (110) peak almost disappeared with the prolonged immersion time while the (010) diffraction peak of ZnPP becomes dominating. This change is accompanied by a morphological transformation from the initially formed star-shaped precipitations towards lamellar, rhombic-shaped crystallites as shown by optical micrographs (cf. Fig. 4.8 (e)) and schematically depicted in Figure 4.8 (f). Metal phenylphosphonates such as ZnPP feature a layered structure of (010) planes where metal cations are coordinated by the oxygen atoms from phosphonic acid PO_3 groups while the phenyl units act as interlayer spacer (cf. Fig. 4.9). The rhombic crystallites that are formed upon prolonged immersion adopt an (010) orientation indicating that this is the thermodynamic most stable surface. Moreover, the (010) interlayer spacing of ZnPP equals 14.3 Å which is in excellent agreement with the step height of 1.4 nm obtained in the AFM micrographs for vertically oriented crystalline precipitation fibers (cf. Fig. 4.2 (c)).

The formation of surface precipitations was also simulated by chemical reaction between ZnCl and PPA under different conditions, like reaction time, temperature and concentration of compounds (collaborative work with the group of Prof. Dr. S. Dehnen). Since ZnO is hardly soluble in ethanol, ZnCl was utilized. All reactions result in the formation of a solid phase material, which was extracted, dried on a hot plate and rimmed onto a glass
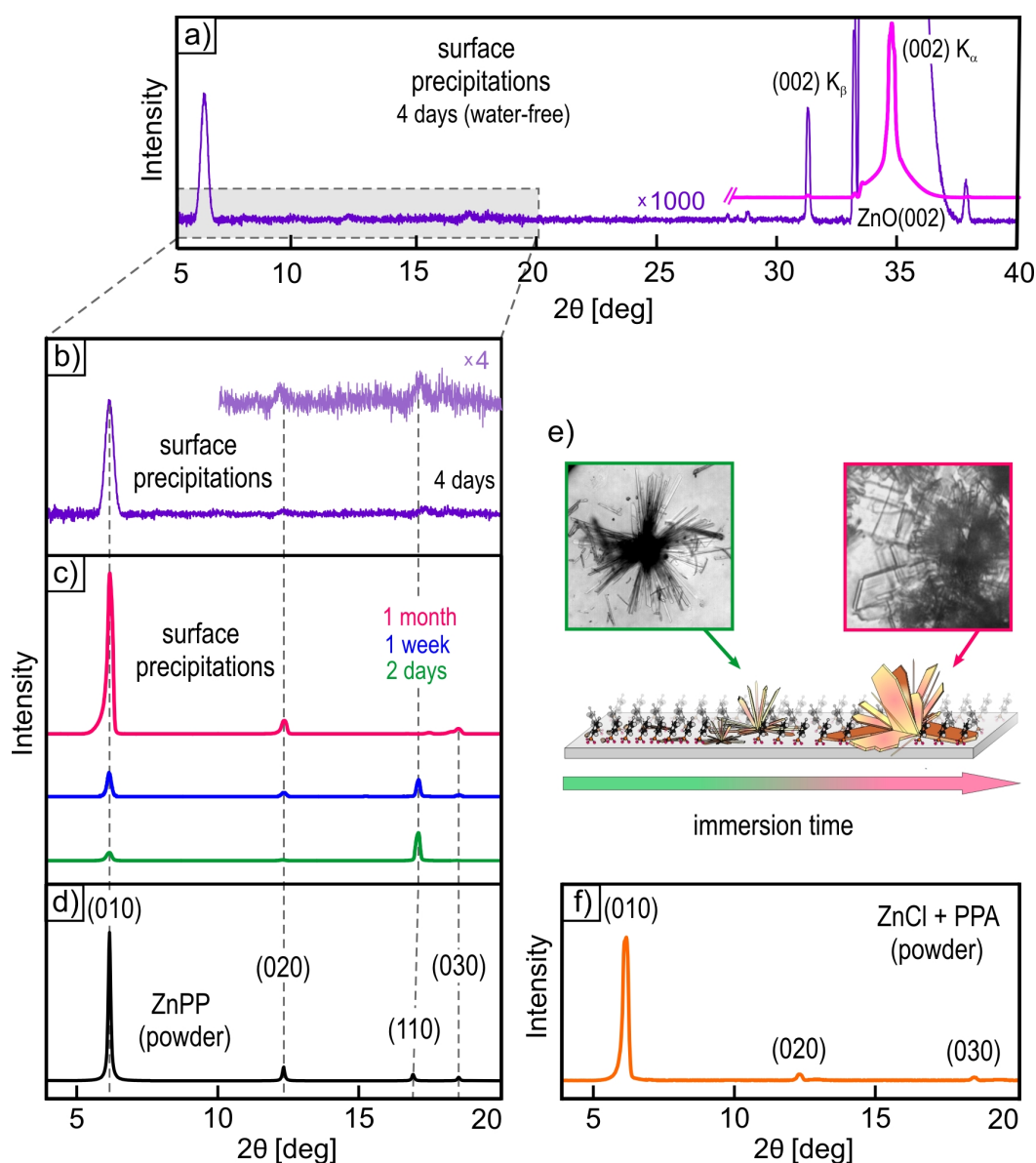
Figure 4.8: Comparison of XRD $\theta - 2\theta$-scans of precipitations formed after immersion of ZnO samples in PPA solution: (a) ZnO-O sample after immersion in water-free ethanolic PPA solution for 4 days with (b) a magnified spectral part revealing signal from the grown precipitations. (c) Diffraction patterns for ZnO-M oriented crystal after different immersion times in (absolute) ethanolic PPA solution: 2 days, 1 week, 1 month. Diffractogram (c) give a comparison with powder spectrum of zinc-phenylphosphonate ($C_6H_5O_3PZn$, ZnPP).[310] The optical micrographs in (e) and the corresponding scheme show the morphological change of the precipitations with increased immersion time. Panel (f) shows a diffraction pattern for products of reaction between ZnCl and PPA, which simulates the formation of ZnPP.
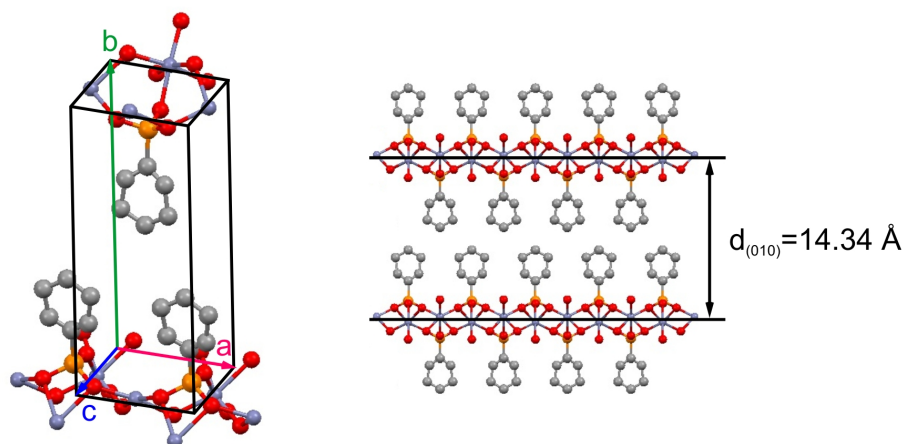
Figure 4.9: Unit cell and crystal structure of ZnPP.[310]

Table 4.1: Crystallographic data for the grown precipitations and ZnPP single crystal

Unit cell parameters	Precipitations	ZnPP single crystal	Theory: PBE+D3
a	5.58 Å	5.63 Å	5.72 Å
b	14.10 Å	14.34 Å	14.80 Å
c	4.78 Å	4.83 Å	4.73 Å
$\alpha/\beta/\gamma$	90°/90°/90°	90°/90°/90°	90°/90°/90°
Crystal system	orthorhombic	orthorhombic	orthorhombic
Space group	$Pmn2_1$	$Pmn2_1$	-
Z	2	2	2
Cell volume	376.7 Å^3	390.4 Å^3	400.2 Å^3

substrate. From numerous XRD measurements in $\theta - 2\theta$ geometry, exemplary depicted in Figure 4.8 (f), we can see that the product of these reactions is ZnPP. Giving consideration to the presence of only $(0n0)$ reflexes in the diffractogram, we conclude fast recrystallization of the material, which confirms the (010) orientation to be the most thermodynamically favored.

This structural identification was also corroborated by a refined XRD single crystal analysis. By extending immersion time further large precipitations of the dimension even more than $300\,\mu$m have been obtained. This enabled the separation of crystalline lamellas from the ZnO support in an ultrasonic bath. Measurements were performed by K. Harms (Uni Marburg). The analysis yielded an orthorhombic crystal structure and unit cell parameters

which are in close agreement with those reported for zinc-phenylphosphonate[310] and listed in Table 4.1. A closer inspection reveals actually somewhat smaller lattice parameters and a slightly reduced cell volume for the precipitations as compared to the ZnPP bulk crystal structure. We attribute this difference to the presence of crystal water which was reported for ZnPP bulk crystals[310–312] while it is essentially absent in the presently observed precipitations.

4.5 Theoretical study on the surface precipitation formation

Density-functional theory calculations were performed to analyze why the precipitates are formed. The DFT calculations were carried out with the PWscf code of the Quantum Espresso software package,[313] using the Perdew-Burke-Ernzerhof PBE exchange-correlation functional,[314] Grimme D3 dispersion corrections,[315] Vanderbilt ultrasoft pseudopotentials,[316] and a plane-wave basis set with kinetic energy cutoff of $30\,\mathrm{Ry}$. With this setup the ZnO bulk lattice constants of $a = 3.266\,\mathrm{Å}$ and $rmc = 5.272\,\mathrm{Å}$ was obtained, which deviate only by $+0.5\%$ and $+1.2\%$ from the respective experimental values of $a = 3.250\,\mathrm{Å}$ and $c = 5.207\,\mathrm{Å}$. Optimized lattice parameters for the ZnPP crystal structure are given in Table 4.1.

At first the theoretical analysis was performed for the nonpolar, mixed-terminated ZnO-M surface and then the obtained results were generalized to the two polar ZnO-O and ZnO-Zn terminations. The most favorable binding mode of single PPA molecules on the ZnO-M surface is a bidentate configuration. The large distance between the Zn surface ions on ZnO-M prevents the formation of tridentate species. The interaction of the PPA molecules with the ZnO-M surface is very strong. From the PBE+D3 calculations a binding energy of $3.04\,\mathrm{eV}$ was obtained. Since each PPA molecule blocks two Zn surface sites, the highest coverage, which can be achieved based on the most favorable PPA binding mode, is 0.5 ML. The structure of this configuration is shown in Figure 4.10 (a). The binding energy per PPA molecule has increased to $3.52\,\mathrm{eV}$. Note that the same structure would have been obtained if a fully hydroxylated and water covered ZnO-M surface was considered[317,318] and had adsorbed the PPA molecules via condensation reactions and displacement of water molecules. At 0.5 ML surface coverage all PPA molecules are deprotonated and all surface O ions are converted to OH groups. Two O atoms of the PO_3 unit are bound to surface Zn, the third O atom is oriented across the trench of the ZnO-M surface and forms H-bonds with the adjacent OH-groups. Furthermore, this O atom sits right above a subsurface Zn ion, but no bond can form since this subsurface Zn ion is already 4-fold coordinated.
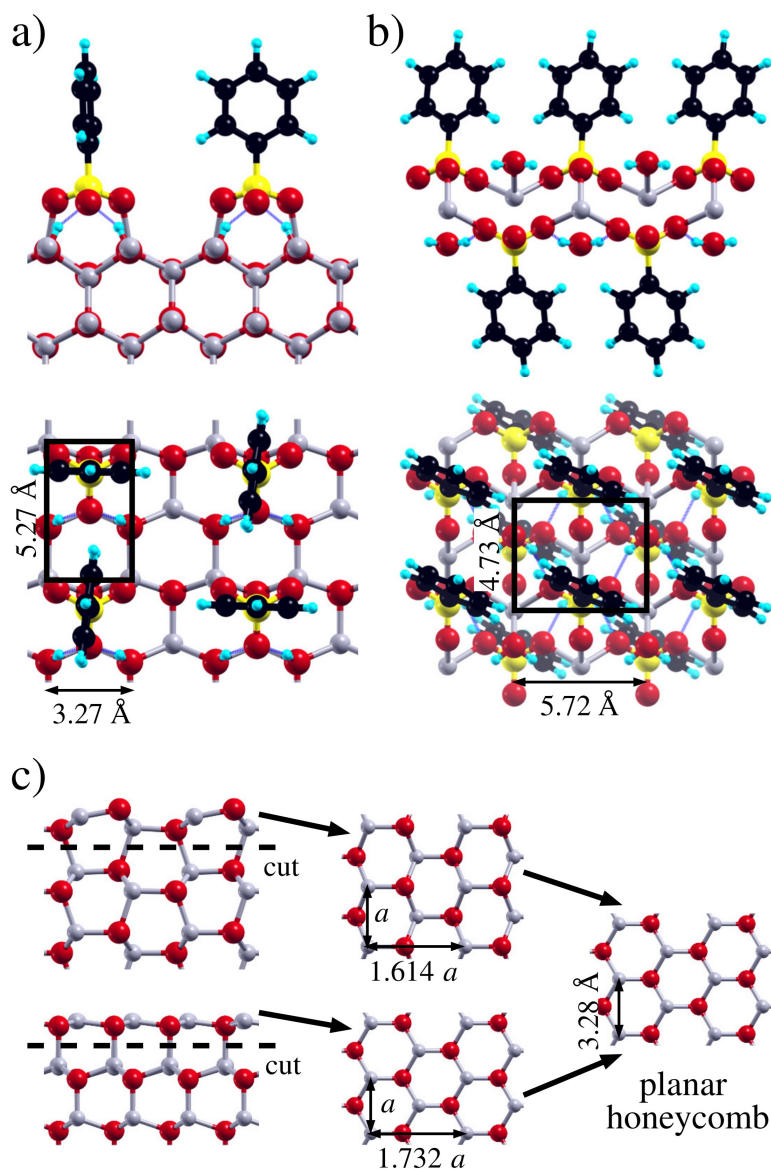
Figure 4.10: Top and side view of (a) a 0.5 ML of adsorbed PPA on the nonpolar ZnO-M surface and (b) a single layer of the ZnPP crystal. (c) Side view of the nonpolar (top) and polar (bottom) surfaces and a top view of a detached ZnO bilayer before and after relaxation of the lattice parameters

If the structure of the ZnO-M surface with the adsorbed PPA molecules is compared with those with a layer of the ZnPP crystal (cf. Fig. 4.10 (b)), some similarities can be identified: the Zn ions form a centered rectangular lattice in both, the ZnPP layer and the ZnO bilayers, the basic building block of the ZnO-M surface structure (cf. Fig. 4.10 (c)). Only the distances between the Zn ions differ. Thus, if a ZnO bilayer with the adsorbed PPA molecules is detached from the ZnO-M surface and PPA molecules are adsorbed at the bottom in the same

configuration as at the top (thereby introducing a mirror glide plane as it is present in the ZnPP layer), then a structure is obtained which is already quite similar to the layers in the ZnPP crystal.

The most important difference is, however, the PPA coverage. While the ZnO:PPA ratio is 1:1 in ZnPP layers, it is 2:1 in the ZnO bilayer structure with adsorbed bidentate PPA molecules. Thus, to obtain a layer of the ZnPP crystal, the short Zn-Zn distance has to expand from the ZnO bulk lattice constant a = 3.27 Å to 5.72 Å (the long Zn-Zn distance slightly shrinks from the ZnO bulk lattice constant c = 5.27 Å to 4.73 Å) and an additional PPA molecule has to be inserted between neighboring PPA adsorbates. Simultaneously, deprotonation of the added PPA molecules converts the OH groups of the ZnO bilayer to water molecules as they are present in the ZnPP crystal.

Are some of the additional PPA molecules already present at the ZnO-M surface? In the 0.5 ML structure of PPA on ZnO-M the available area for each PPA molecule is two surface unit cells (34.4 Å^2). In the ZnPP crystal it is 27.0 Å^2 and in the PPA crystal it is only 21.9 Å^2. Thus, the packing density of the PPA molecules in the 0.5 ML structure is much lower than in the ZnPP crystal. So the 0.5 ML of PPA molecules on ZnO-M exhibits a certain degree of frustration: the phenyl rings prefer to be closer packed, however, as long as the topmost ZnO bilayer is not detached from the ZnO surface, a higher PPA coverage can only be achieved if some of the PPA molecules forfeit their preferred bidentate binding mode and adopt a monodentate configuration.

In the next step the thermodynamic stability of such closer-packed adsorbate layers was investigated. By using surface unit cells of size (4×2), (5×2), (6×2) and (7×2) low-energy structures of PPA layers with 0.57, 0.6, 0.66, 0.71, 0.8 and 1 ML surface coverage were determined. Indeed, the binding energy per molecule E_b decreases to 3.42, 3.38, 3.18, 3.11, 2.80 and 1.44 eV, respectively. All structures contain a certain fraction of monodentate-bound PPA molecules. These molecules are still protonated and the OH-groups form very stable H-bonds to neighboring O atoms (cf. Fig. 4.11). The thermodynamic stability of the PPA layers is analyzed by converting the binding energy E_b to the interface energy $\triangle \gamma$ and the energy gain per surface area is given by:[318,319]

$$\triangle \gamma = N(E_b + \triangle \mu_{PPA})/nA, \tag{4.1}$$

where n denotes the number of surface unit cells (i.e., N/n is the surface coverage) and A is the area of one surface unit cell. $\triangle \gamma$ is zero for the adsorbate-free surface, and the most stable surface coverage at a given PPA chemical potential can be identified as the one with the lowest interface energy. Figure 4.11 demonstrates a plot of $\triangle \gamma$ as function of the PPA

chemical potential $\triangle\mu_{PPA}$. At the chemical potential of $\triangle\mu_{PPA} = -1.7\,\text{eV}$, which reflects the conditions in the immersion experiments, the thermodynamically most favorable surface coverage is 0.6-0.7 ML. At this coverage, the packing density of the phenyl rings is almost the same as in the ZnPP crystal. Higher coverages become unfavorable because the phenyl groups start to repel each other. In order to be able to accommodate a full PPA monolayer, as it would be required for a ZnPP crystal, the lattice constant a of the ZnO-M surface would have to expand from 3.27 Å to 5.72 Å as in the ZnPP crystal (cf. Fig. 4.10). However, this can only happen if the upper ZnO bilayer detaches from the ZnO-M surface.
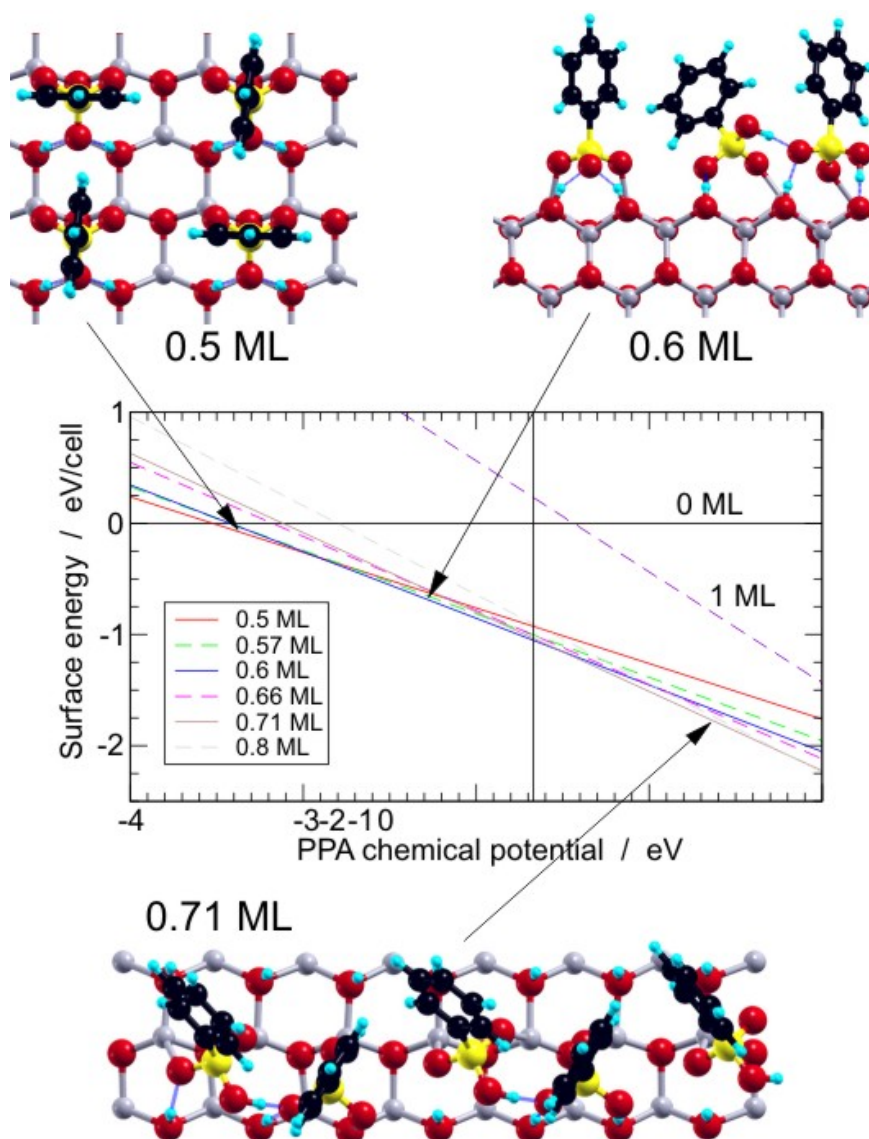
Figure 4.11: Surface phase diagram for the adsorption of PPA on ZnO-M. The chemical potential of $\triangle\mu_{PPA} = -1.7\,\text{eV}$ is indicated by the vertical solid line.

The energy cost for cleaving a ZnO bilayer from the ZnO-M surface in vacuum is +1.59 eV per surface unit cell. In vacuum the detached ZnO bilayer structure is not stable. After relaxation of the lattice parameters the bilayer adopts a planar hexagonal honeycomb structure with lattice constant 3.28 Å, thereby lowering the energy by 0.14 eV per initial unit cell (two ZnO units, cf. Fig. 4.10 (c)). However, if we first saturate the ZnO-M surface with 0.6 ML of PPA molecules and then detach the topmost ZnO bilayer, saturating simultaneously its bottom and the newly created ZnO-M surface with PPA molecules as it would occur in immersion or in a PPA vapor, the energy cost reduces to +0.36 eV per surface unit cell (cf. Fig. 4.12). To determine this energy difference, a ZnO bilayer with a (5×2) unit cell and 12 adsorbed PPA molecules (6 on each side) was relaxed and the energies of the PPA molecules and a bilayer in vacuum was subtracted, thereby assuming a PPA chemical potential of $\triangle \mu_{PPA} = -1.7$ eV. While the energy for detaching a ZnO bilayer in a PPA environment is still slightly positive, it is much smaller than in vacuum and also significantly smaller than in liquid water. Repeating the same procedure for adsorbed monolayers of water instead of 0.6 ML of PPA yields an energy cost for detachment of +0.80 eV per ZnO-M surface unit cell. More important, the detached PPA/ZnO bilayers can now expand to the ZnPPA lattice constant and can increase their PPA coverage to 1 ML, thereby lowering the energy by -0.82 eV per initial ZnO-M surface unit cell (cf. Fig. 4.12). Finally, vertical stacking of the ZnPP layers to form the ZnPP crystal gives an additional energy gain of -0.25 eV per unit cell (cf. Fig. 4.12). Overall, the schematic energy diagram of Figure 4.12 illustrates that the formation of the ZnPP crystal is a thermodynamically favorable process and that the ZnPP crystal is the thermodynamic ground state and not the PPA/ZnO-M self-assembled monolayer. The PPA-saturated bilayer can be regarded as a fictitious, idealized transition structure which only serves to demonstrate that no high activation barriers have to be overcome when PPA/ZnO is detached from the surface and transformed into ZnPP crystals.

On the basis of these calculations two driving forces that are responsible for the transformation of the PPA-SAMs to the ZnPP crystals can be identified. First, the frustration in the adsorbed PPA layer. The most favorable binding mode of the PPA molecules on ZnO is a bidentate or tridentate configuration. However, to achieve the preferred packing density of the phenyl rings, PPA molecules have to adsorb in a monodentate geometry since not enough Zn sites are available. The PPA molecules can only recover their preferred bidentate and tridentate binding mode if the surface bilayer restructures by detaching from the substrate. The second driving force is the very strong interaction of PPA with ZnO. The binding energy for PPA is much larger than for water.[317] Even at coverages below 0.5 ML the PPA molecules stabilize the ZnO-M surfaces as well or better than a monolayer of

water. This strong interaction makes the detachment of the ZnO layers thermodynamically favorable.

These arguments are not specific for the nonpolar, mixed-terminated ZnO-M surface. Also the polar O- and Zn-terminated surfaces ZnO-O and ZnO-Zn are composed of ZnO bilayer building blocks (cf. Fig. 4.10 (c)). The only difference is that the bilayers from the polar surfaces consist of a Zn and an O layer and the unit cell is hexagonal with lattice constant a, whereas the bilayer from the nonpolar ZnO-M surface contains an equal number of Zn and O atoms in both layers and the unit cell is rectangular with lattice constants a and $c = 1.614\,a$ (cf. Fig. 4.10 (c)). A hexagonal lattice, however, can also be described by a rectangular unit cell with lattice constants a and $\sqrt{3}a = 1.732a$. After structural relaxation and relaxation of the lattice constants, the bilayers from the polar surfaces adopt exactly the same planar honeycomb structures as the relaxed bilayers from the nonpolar ZnO-M surface (cf. Fig. 4.10 (c)). Thus, all arguments given above on the stabilization of the bilayers by PPA adsorption and their transformation to ZnPP can be applied to the bilayers stemming from the polar surfaces as well.
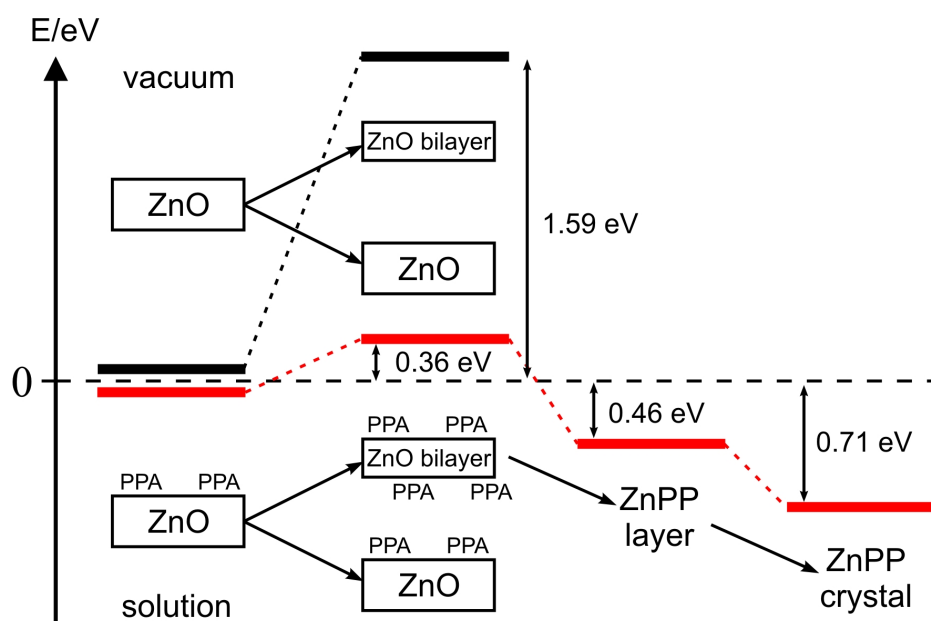
Figure 4.12: Schematic energy diagram for the transformation of a PPA-SAM on ZnO-M into a ZnPP crystal.

4.6 Influence of surface roughness on precipitation formation

Surface defects like step edges are typically suggested as active nucleation sites for the formation of the ZnPP precipitations. Therefore, we have also investigated the influence of the surface morphology on the etching efficiency by comparing the density of surface precipitations formed on well-defined and intentionally roughened ZnO samples. As it was discussed earlier in the section 2.2 the single crystal preparation yields smooth surfaces consisting of extended terraces separated by monatomic steps (cf. Fig. 4.1 (c)), while significant surface roughness and increased amount of defects can be induced by extensive Ar^+ ion beam bombardment at $800\,eV$ for 2 hours. Figure 4.13 compares the density of precipitations that are formed at the differently prepared ZnO samples after immersion in PPA solution for 2 days under equivalent conditions. The amount of formed ZnPP precipitations on the damaged surface clearly exceeds the number of precipitations observed on the well-defined ZnO surface and thus corroborates the idea that precipitations nucleate at surface defects.
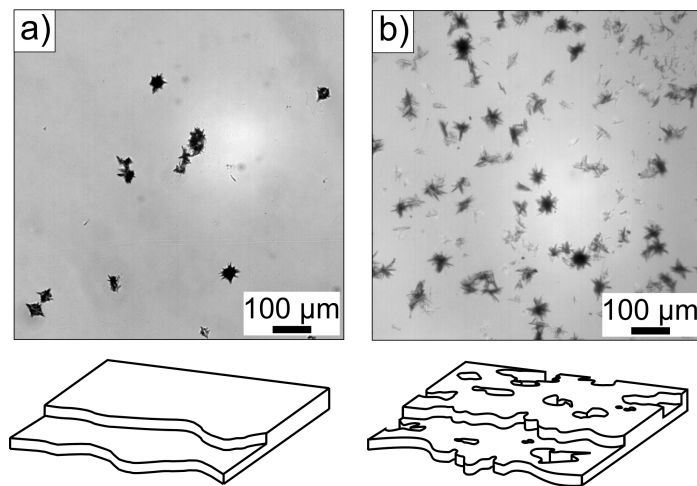

Figure 4.13: Optical micrographs of surface precipitations formed upon immersion of (a) smooth and (b) intentionally roughened ZnO-O surfaces for 2 days together with corresponding schemes of the primary surface morphologies.

4.7   Influence of pH value on etching

Another important factor that has been reported to affect the ZnO stability and its surface etching upon immersion is the pH value of the immersion solution which has been mentioned in previous studies. Being a strong acid PPA has the ability to partially dissolve metal oxides.[320–322] Based on previous studies the following pH regimes have been reported for ZnO[322,323] pH < 3.8 - severe etching; 3.8 < pH < 5.5 – slow surface dissolution; 5.5 < pH < 10 – no evidence of etching. In our experiments a pH value of 4.5 was measured for a 0.1 mM ethanolic PPA solution. Therefore, additional SAMs were prepared from solution whose pH value had been adjusted to 5.75 by using an acetic acid/sodium acetate aqueous buffer system to address the influence of pH value on ZnO etching. Acetic acid $C_2H_4O_2$ of the purity 99.8% has been obtained from AnalaR NORMAPUR ACS, sodium acetate $C_2H_3NaO_2$ of the purity 99.5% from Grüssing GmbH and the water was distillated in the RiOs-DI-System. Unlike the predicted behavior we observe that immersing ZnO-O in such a buffer solution does not suppress surface etching. As opposite, dense layer of large crystalline lamellar precipitations is observed already after 6 hours of immersion as depicted in Figure 4.14 (a-c) while lamellas of similar size have been found only for samples which were kept for a month in ethanolic PPA solution. In addition, this preparation strategy leads to even more severe surface damages with a large number of etching pits on the surface (cf. Fig. 4.14 (c)). Moreover, large unattached crystalline fragments were formed directly in the solution, which obtain similar layered structure (cf. Fig. 4.14 (d,e)). However, due to the extreme formation conditions (large concentration of water in the solution) the step heights observed in AFM lies between 1 and 3 nm which is larger than previously found (cf. Fig 4.2, (c)), thus indicating formation of multisteps. Additional XRD measurements have proved that also these precipitations originate from ZnPP.

This severe surface etching is attributed to the presence of water in the solution which expedites the formation of precipitations as reported in previous studies[297,298] and will be discussed in more details in the next section. The influence of water on the formation of surface precipitations was also confirmed by a simple experiment, where the formation efficiency of zinc-phenylphosphonates on a bare and water precoated ZnO surface was compared. For this purpose a droplet of distilled water was placed on the ZnO-O surface as depicted in Figure 4.15. After drying the sample was immersed for 4 days in ethanolic PPA solution. Indeed, the surface area of a ZnO sample intentionally marked with a droplet of distilled water in advance exhibits a distinctly higher density of surface precipitations than the untreated surface after immersion in PPA solution. Based on these findings also different
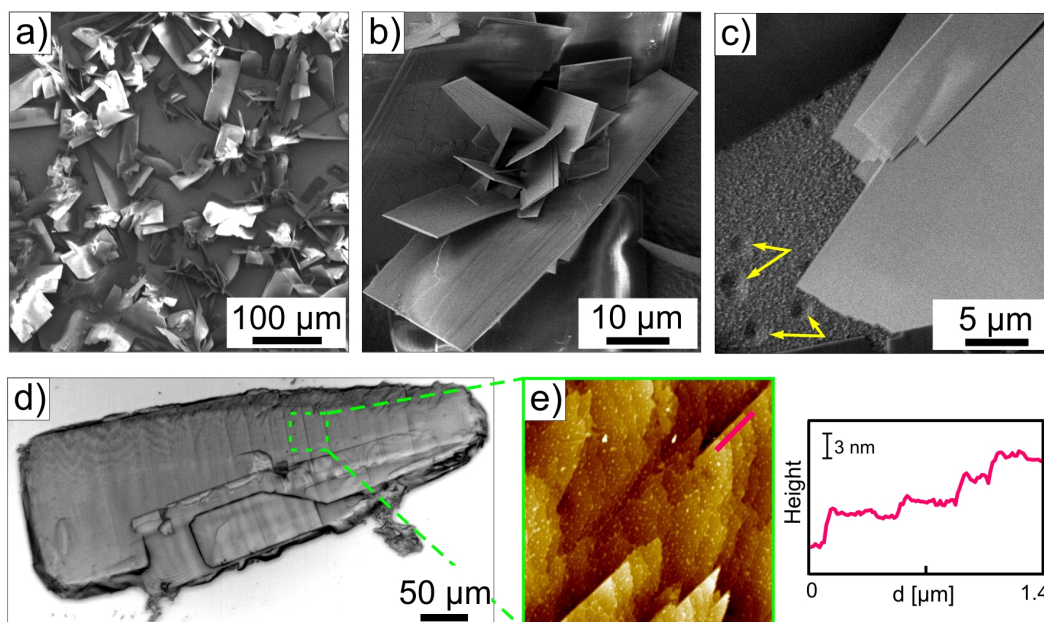
Figure 4.14: SEM micrographs of (a-c) ZnO-O after immersing for 6 hours in an aqueous acetic acid/sodium acetate buffer solution (pH = 5.75) revealing severe surface damage of supporting ZnO sample with the formation of many etching pits marked by yellow arrows. (d) Optical micrograph of free crystals found directly in the solution with (e) corresponding AFM micrograph, which reveals layered structure.
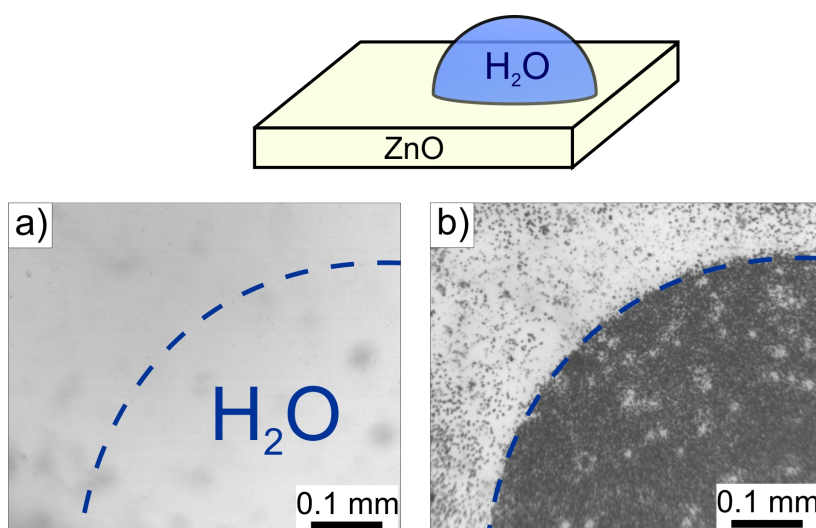
Figure 4.15: Optical microscopy image of (a) bare ZnO-O surface with the hydroxylated area marked by the dashed blue line and (b) after 4 days of immersion in the PPA solution. Clearly a higher density of precipitations was found on hydroxylated surface area.

solvents (isopropyl alcohol, acetonitrile) have been tested. In all cases the respective samples showed etching behavior similar to one observed after using ethanolic solutions.

4.8 Discussion of metal oxide etching mechanism and analysis of experimental results

To enable the preparation of well-defined SAMs on ZnO, the discussed etching has to be prevented. For this purpose, an understanding of underlying mechanisms and parameters that affect this surface instability is mandatory.

The general concept of ZnO dissolution is described for aqueous solutions and is explained by the following steps: the first process is the protonation of surface oxo groups of the solid; secondly, the rupture of metal bonds to oxide and, finally, the transfer of metal ions into the solution.[194] ZnO as an amphoteric oxide can react with both, strong acids and bases to form salts and water. Depending on the pH value of the solution the surface hydroxyl groups can act as proton donors or acceptors. The dissolution chemistry can be described by the following reactions: $ZnO + 2H^+ (sol) \longrightarrow Zn^{2+} (sol) + H_2O$.[322,323] Hence Zn^{2+} ions chemically react with organic molecules from the solution and can form complexes, which subsequently precipitate on the surface.[194,320,324,325] The formed molecules can accelerate the surface dissolution further.[326]

In previous work it has been reported, that the O-terminated ZnO surface is less stable against etching in oxidizing solvents than Zn- or mixed-terminated surfaces.[327] The difference in the etching efficiency has been attributed to the presence of a dangling bond with two electrons at the oxygen surface atoms. The existence of dangling electrons results in the more severe distortion from tetrahedral sp^3 symmetry for O than Zn atomic bonds. Therefore, the O-terminated surface is expected to be more prone to etching reactions, since dangling electrons are more susceptible to chemical interactions with electron-seeking ligands in the solution. However, this dependence has not been directly observed in our experiments. Instead, we find similar precipitation formation for both polar and the non-polar ZnO surface terminations on a time scale of several days, thus obtaining this simple explanation.

Typically, surface reactions like dissolution and growth are initiated at surface defects like steps, kinks or vacancies[329,330], which can be rationalized by the reduced coordination of the respective sites. In a first approximation the dissolution rate is proportional to the concentration of active surface sites and the probability for the anchoring group to find a specific adsorption site in the coordinative arrangement.[328] Dissolution of metal atom

means that their bonds to the lattice have to be broken and replaced by bonds to functional phosphonic groups. In chemical dissolution the adsorption of acids changes the Zn-O bond length.[331] The break of one hydrolytic bond between adsorption active atoms of the kink site and neighboring atoms in the remaining lattice triggers the dissolution by weakening the remaining bonds. The sputtered surface has a larger concentration of such surface defects and is therefore etched more effectively. Though the used single crystalline ZnO samples exhibit rather smooth surfaces with several steps due to a slight miscut (cf. Fig. 4.1 (c)), they may exhibit additional defects that are not resolved by AFM. Previous STM studies by the Diebold group revealed the presence of characteristic surface vacancies/depressions on differently oriented ZnO surfaces.[81,85]
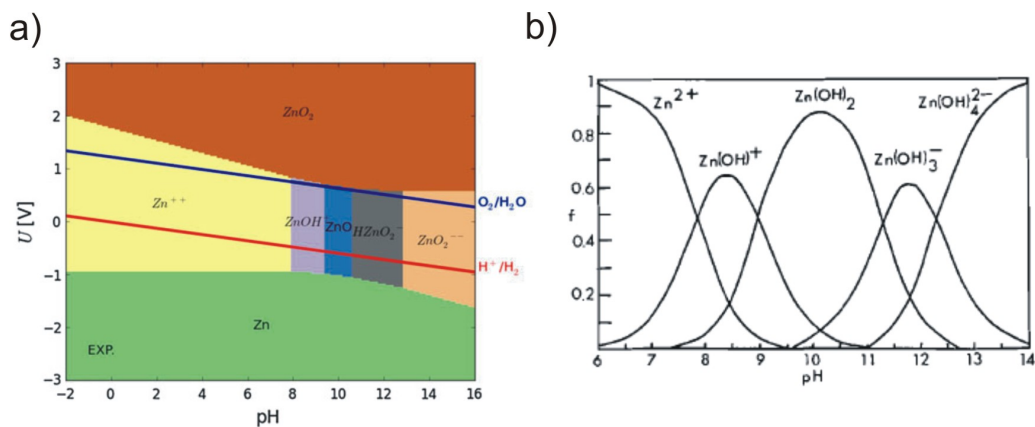
Figure 4.16: (a) Experimental Pourbaix diagrams for ZnO drawn for a concentration of 10^{-6} M at $25°$ C. The Pourbaix diagram consists of regions defined by straight lines which represent different equilibrium reactions. (b) Fractions of Zn which exist in an aqueous solution as a function of the pH value at $25°$ C.[333]

The phase stability of metal oxides as a function of the pH value of a solution is generally described in Pourbaix diagrams (cf. Fig. 4.16 (a)).[332] Moreover, due to the amphoteric nature of ZnO the formation of different ions, such as $Zn^{2+}, Zn(OH)^+, Zn(OH)_4^{2-}$ and others, depending on the solution acidity has been reported (cf. Fig. 4.16 (b)).[322,333] In addition the dissolution behavior of the various organic solvents depends also on their concentration. PPA is a strong acid (dissociation constant $pK_a = 2.2$) and, therefore, dissolves ZnO on a shorter time scale and in lower concentrations compared to a weak acid.[294,295] The point of zero charge (PZC) of ZnO equals 9 and indicates the pH value of a solution where the concentration of protonated and deprotonated groups on a surface equal.[334,335] Lower pH values than PZC leads to a positively charged surface, since the bare or hydroxylated oxide surface adsorb protons. At high pH values they lose protons to produce a negatively charged surface. According to this consumption the dissolution of ZnO can be suppressed by varying

the pH-value of the PPA solution. However, as discussed before, we instead observe an increased etching. This is attributed to the use of aqueous solvent which is required for the buffer systems. Previous studies have shown, that many metal oxides are not stable in the presence of water and may recrystallize in the near-surface region.[326,335,336] Moreover, the solubility of zinc hydroxide in aqueous solutions exhibits slight changes depending on the temperature and may be thermodynamically induced.

To summarize, in all these processes aqueous solution plays a vital role. In fact it was pointed out by Lange *et al.*[298] that the concentration of residual water in the immersion solution is crucial for the efficiency of precipitation formation which is also corroborated by our present findings for immersion in aqueous buffer solutions. In previous work it was further found that the O-terminated ZnO surface is less stable against etching in oxidizing solvents than Zn- or mixed-terminated surfaces which enables a clear distinction of both polar surfaces.[327] Surprisingly, however, such a dependence has not been observed in our experiments. Instead, rather similar precipitation formation is found for both polar and the non-polar ZnO surface terminations on a time scale of several days when using water free immersion solutions, hence evidencing another transformation mechanism. Indeed the present theoretical analysis shows that the structural transformation can be well explained by a dry solid state reaction without any ion dissolution which is energetically driven by the lattice energy of the formed zinc-phosphonates.

4.9 Conclusions

Here we demonstrate, that functionalization of ZnO samples via self-assembled monolayer films anchored by phosphonic acids is accompanied by a chemical side reaction leading to a marked surface degradation and formation of surface precipitations which have been identified as zinc-phosphonate. Such a surface etching was observed for both polar and the mixed-terminated ZnO surface as well as for PA molecules with different backbone. Initial substrate surface roughness and the presence of remaining water in the solution are critical parameters and accelerate the precipitation formation. Remarkably, such phosphonate precipitations are also formed upon immersion in carefully dried (i.e. water-free) PPA solutions on a time scale of days. This shows that the formation of PA-based SAMs on ZnO is not a self-terminating process like for the organothiol-based SAMs on gold substrates. In fact a DFT-based energy analysis reveals that PA-anchored SAMs on ZnO represent rather a metastable configuration while zinc-phosphonate is the energetically more stable configuration. The theoretical analysis yields further a microscopic reaction path leading to the

structural transformation without addition of water. Therefore, prolonged immersion times should be avoided upon SAM formation and a slow electrochemically driven precipitation formation might be considered during long time operation of devices utilizing such interfaces. Interestingly, a reduced surface etching efficiency was found upon SAM formation when replacing phosphonic acid by phosphinic acid anchoring units which might be related to differences in acidity for the second deprotonation of both acids or the lattice energies of phosphonates and phosphinates. In previous work the usage of Al-doped ZnO was proposed to avoid the etching effect, [337] though a surface degradation still has been found in case of doped samples and raises the question about the resulting film quality. Therefore, an alternative SAM preparation based on organic molecular beam deposition (OMBD) by first depositing thin multilayer films and subsequently thermally desorbing the multilayer excess in order to obtain a monolayer film at the surface appears as interesting alternative. Corresponding results will be discussed in the next Chapter 5.

Formation and Stability of Phenylphosphonic Acid Monolayers on ZnO: Comparison of *in-situ* and *ex-situ* SAM Preparation

5.1 Introduction

Self-assembled monolayers of covalently bound molecules offer a versatile approach to modify physico-chemical surface properties.[292,338,339] As it was discussed in previous chapters SAMs have also attracted interest in the field of organic electronics because they enable tuning of electronic interfacial properties, for instance, the work function of metal oxide electrodes which is decisive for the charge carrier injection.[340–343] Using adequate anchoring units SAMs can also be formed on metal oxides. This is of particular interest as it also allows to control the work function of conductive transparent metal oxides such as ZnO or ITO, which are considered as alternative transparent electrodes in optoelectronic devices.[36,344,345] Initially, various anchoring units have been proposed for metal oxides, such as carboxylic acids, phosphonic acids or thiols, while phosphonic acids yield the most stable SAMs.[348–355] However, detailed information about the structure and thermal stability of such SAMs on metal oxides is by far not as complete as for organothiol-SAMs on metals. In part this is due to the common use of polycrystalline or sputtered oxide substrates, which exhibit a notable roughness and low conductivity that hampers, for example, the routinely use of scanning tunneling microscopy. Among the metal oxides, ZnO is a particular interesting model substrate as it permits the preparation of highly ordered single crystalline surfaces of different orientation and termination. In fact, several studies have recently become available for the formation of phosphonic acid-based SAMs on ZnO.[199,297,298,293,351–355] Generally,

it is found that phosphonic acids are bound to ZnO by formation of coexisting bi- and tri-dentate species. Despite the growing body of available data, some aspects such as a comparison of the binding situation of the differently oriented ZnO surfaces or the influence of surface hydroxylation on the SAM formation have not yet been addressed experimentally. Though an improved ordering by post deposition annealing has been reported for phosphonic acid-based SAMs[356,357] limits of their thermal stability are still unknown. In addition, a competing etching reaction has been observed upon immersion of ZnO in phosphonic acid solutions, which leads to increasing surface roughness and formation of zinc-phosphonate precipitations as discussed in the previous chapter.[297,298,351]

In this chapter the thermal stability and molecular orientation of phenylphosphonic acid SAMs formed on differently oriented single crystals, including both polar $ZnO(000\overline{1})$ and $ZnO(0001)$ surfaces as well as the mixed-terminated $ZnO(10\overline{1}0)$ surface were analyzed by using TDS, XPS, NEXAFS and DFT calculations. DFT calculations were performed in the collaboration group of Bernd Meyer to assist in the assignment of the peaks in TD-spectra.

The DFT calculations were carried out in the group of Prof. Dr. B. Meyer from Erlangen with the PWscf code of the Quantum Espresso software package,[313] using the Perdew-Burke-Ernzerhof PBE exchange-correlation functional,[314] Grimme D3 dispersion corrections,[315] Vanderbilt ultrasoft pseudopotentials,[316] and a plane-wave basis set with kinetic energy cutoff of 30 Ry. The ZnO surfaces were represented by periodically repeated slabs consisting of four ZnO double-layers, which are separated by a vacuum region of more than 20 Å.[358] The oxygen atoms at the bottom of the polar slab for the ZnO-Zn surface were passivated by hydrogen-like atoms with nuclear charge of $+1/2$.[359] A series of PPA adsorbate structures on different ZnO surfaces was considered for the theoretical analysis. Our set of model adsorbate structures consists of mono-, bi- and tridentate configurations of PPA molecules bound to the mixed-terminated ZnO-M and the polar Zn-terminated ZnO-Zn surface. In addition, different surface coverages were considered, ranging from quasi-isolated molecules to densely-packed molecular layers. For each PPA molecule in our set of model structures the strength of the C-P interaction was determined by cleaving the C-P bond. The energy of the two fragments was calculated using spin-polarized DFT and subtracted from the energy of the initial structure.

Since SAM preparation by immersion usually is accompanied by contact to humidity, at least a partial surface pre-coating by water or hydroxyl species cannot be ruled out. To study also the influence of surface hydroxylation on the PPA-SAM formation, an alternative monolayer preparation method is introduced which is based on organic molecular beam deposition in combination with the controlled desorption of excess multilayers. Together

with the UHV preparation of the ZnO single crystals, this enables a detailed comparison of SAMs formed on bare and OH-precoated ZnO surfaces, which is obtained by dipping samples in ethanolic NaOH solution before SAMs deposition. The TDS measurements were complemented by angular resolved NEXAFS measurements to determine the molecular orientation adopted by PPA molecules in the various SAMs on the different surfaces.

5.2 Thermal stability of PPA-SAMs prepared by immersion

Thermal desorption spectroscopy was used to characterize and compare the thermal stability of PPA monolayer films on the differently oriented ZnO crystal surfaces. The films were prepared by immersing the samples in water-free ethanolic solution and limiting the immersion time to 24h in order to minimize surface damage by etching. In this way no visible layer of precipitations was found on the samples. Figure 5.1 compares TD-spectra of PPA monolayer films on ZnO-O, ZnO-Zn and ZnO-M single crystal surfaces. All films show a remarkable high thermal stability and start to desorb only above 600 K. For all three surfaces two distinct desorption peaks (denoted as γ_1 and γ_2) were observed at 690 and 730 K respectively. Though various mass signals were simultaneously recorded, distinct signals were only observed for the mass of the phenyl unit (C_6H_5, $m/z = 77$ amu) and related fragments (e.g. C_4H_3, $m/z = 51$ amu). In particular, no phosphorus or oxygen containing fragments were found which suggests a dissociative desorption mechanism. The presence of two desorption channels is generally indicative for different binding configurations at the surface. Interestingly, essentially the same desorption temperatures were found for all three ZnO surfaces despite their different termination. It must be noted that intensities of measured signals do not define the resulting film density and quality and do not necessarily match for films prepared on different samples. Nevertheless, analysis of desorption signals within one measurement provides reliable data.

Additional information on thermally induced desorption of PPA films was obtained from temperature-dependent XPS measurements. Figure 5.2 displays a series of XPS measurements for high-resolution O*1s* and C*1s* (recorded at $E_{ph} = 650$ eV) and Zn*3s* and P*2p* (recorded at $E_{ph} = 350$ eV) core level regions at different temperatures. The corresponding XP-spectra were recorded during cooling after the sample had reached the given annealing temperature. The binding energy is calibrated to the the position of the substrate Zn*3s* peak (139.3 eV).[360] After subtracting a background relative changes in the shape and constituents of the O*1s* core level peak compared to the corresponding peak of a bare ZnO surface are
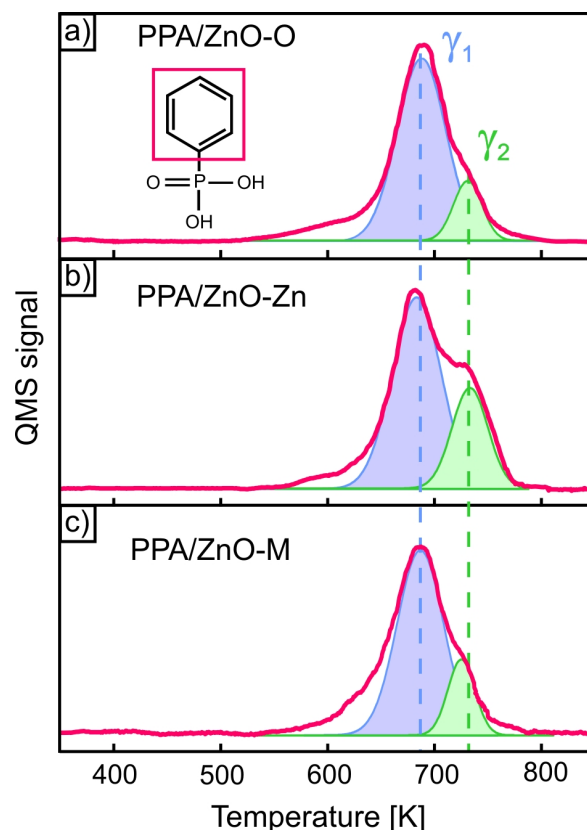
Figure 5.1: Series of TD-spectra for PPA films on (a) ZnO-O, (b) ZnO-Zn and (c) ZnO-M single crystals prepared by immersion. All spectra were recorded for the mass $m/z = 77$ amu and a heating rate of 0.5 K/s. Fits indicate the two desorption peaks that are attributed to dissociative desorption of tridentate (blue) and bidentate (green) species. The inset in (a) depicts the schematic structure of PPA together with the phenyl fragment (red box).

usually considered for the analysis of PA binding modes.[297,352] The oxygen of the bare ZnO surface exhibit a main peak at around 531 eV. The shoulder at 532.4 eV is typically attributed to oxygen incorporated into surface hydroxyl groups. The binding energy shifts for the bi- and tridentate modes were reported at 533.1 and 532.1 eV respectively.[297,199,201] Alterations in the O$1s$ peak shape up to 600 K are ascribed to desorption of surface water layer or hydroxyl groups, which are included in all films prepared by immersion. However, small contributions from the actual reorganization in the binding character can be considered, since the partial PPA desorption at these temperatures cannot be completely excluded. Along with the increasing intensity for the O$1s$ ZnO substrate peak due to the desorption of adlayer which was blocking photoelectrons the intensity of the C$1s$ peak decreases (cf. Fig. 5.2 (b)). The main contribution to this peak is given by carbon atoms of the phenyl ring. Small changes in the peak position are assigned to characteristic carbon species, like C-C or

C-P, which are revealed during annealing. Panel (c) on the Figure 5.2 shows a series of temperature dependent XP-spectra for Zn*3s* and P*2s* regions recorded at 350 eV. Note, that at higher photon energies the relative peak intensities of phosphorous and zinc signals are reversed. This is caused by a generally higher penetration depth of photons at higher energies, which gives larger signal from the substrate material than the adsorbate. The intensity of the C*1s* and P*2p* photoelectron peaks measured for PPA SAM on ZnO-O as a function of the annealing temperature is given in Figure 5.3. In order to study relative correlations of different contributions, peak intensities were normalized to the respective RT values before heating. A distinct reduction of the carbon signal starts above $\sim$650 K and drops even stronger above 710 K while the phosphorous signal increases oppositely. This behavior is caused by a reduced attenuation of the P*2p* photoelectron signal due to desorbing phenyl units while the phosphorus anchor units mostly remains at the surface even for temperatures up to 850 K. A similar behavior had been reported before for n-hexanephosphonic acid layers adsorbed onto polycrystalline ZnO films.[293] The intensity of emitted photoelectrons at a certain depth below the surface can be quantitatively described by the Beer-Lambert law (cf. Eq. 3.8). Based on the intermolecular distances and considering the phenyl tilt angle obtained by our NEXAFS data, an effective thickness of the phenyl layer was derived to be d=5.6 Å. Moreover, under the assumption that the variation between the density of the phenlyl ring and the benzene is not significant and utilizing the Gries formula[253] the IMFP for P*2p* electrons recorded with a photon energy of 350 eV was estimated as 12.6 Å. An approximated P*2p* signal attenuation of 1.6 was derived, which is in close agreement with the experimentally observed value of 1.7. Thus confirming an exclusive dissociative desorption that was also indicated before on the basis of the TDS data.

Due to the dissociative desorption the desorption peak temperatures cannot be used directly to determine adsorption energies for the phosphonic acids on ZnO. Instead, they rather represent activation energies of the C-P bond breaking for the different adsorption states. To assist in the assignment of two desorption peaks in the TD-spectra, a series of DFT calculations for a set of model structures of PPA adsorbed on ZnO was performed. Representative structures of the most favorable PPA configuration in tridentate and bidentate binding modes are shown in Figure 5.4. As a general rule we find that tridentate PPA species are more tightly bound to the ZnO substrate than bidentate configurations. For the strength of the C-P bond typical values of 4.1-4.2 eV in the case of tridentate binding and 4.4-4.5 eV for bidentate species were obtained. A lower value for the C-P bond strength for tridentate configurations is in line with the expectation that a stronger binding to the substrate leads to a weakening of the intramolecular C-P bond. A similar situation has been found for organothiol-SAMs adsorbed on copper surfaces. As a consequence of the
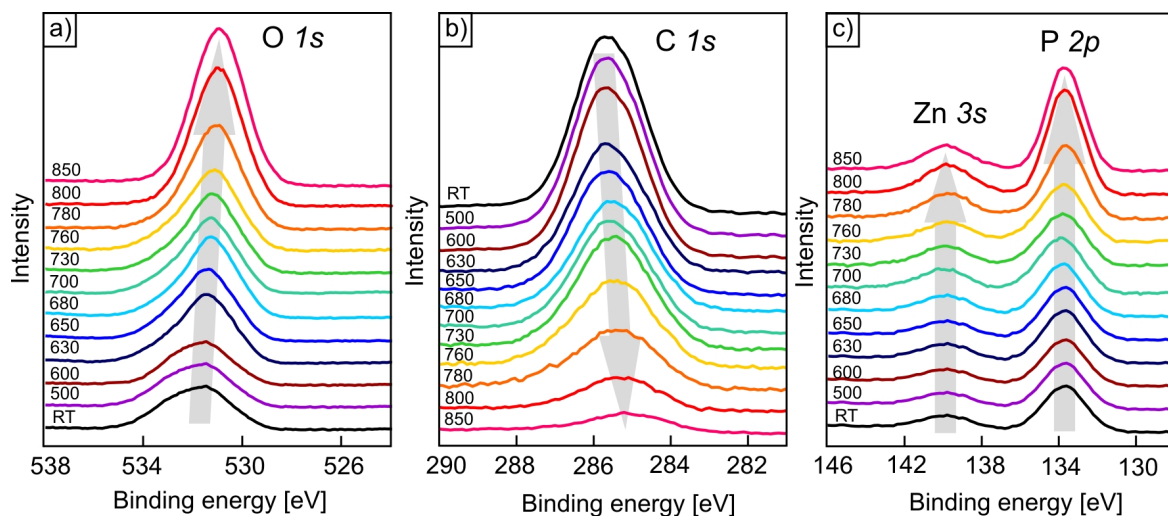
Figure 5.2: XPS spectra of the (a) O 1s, (b) C*1s* and (c) Zn*3s* and P*2p* regions for PPA SAM on ZnO-O annealed to different temperatures in UHV.
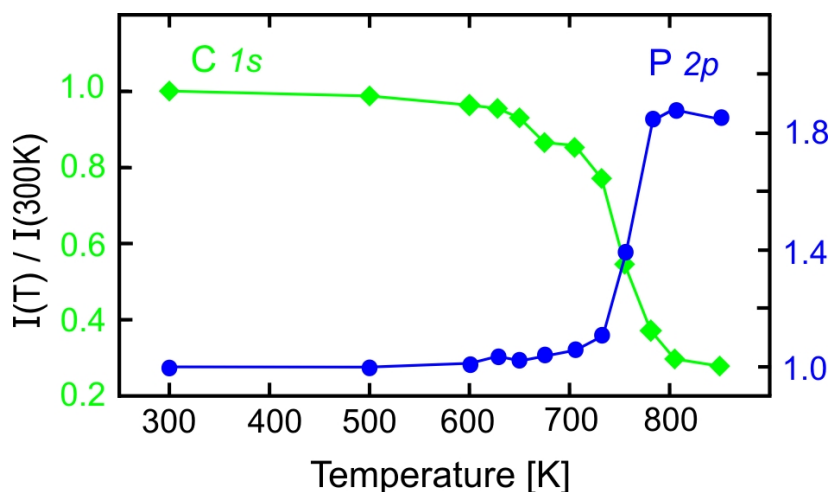
Figure 5.3: Evolution of C*1s* and P*2p* photoelectron signals as a function of the annealing temperature under vacuum conditions of a PPA SAM on a ZnO-O surface.

strong S-Cu interaction the internal S-C bond is weakened and the dissociation depends on the coordination of the adsorption site of the thiolate anchor.[361] Therefore, we attribute the lower temperature signal (γ_1) to the dissociation of tridentate species and the higher temperature peak (γ_2) to PPA molecules bound in a bidentate configuration. Using this assignment we derive from the relative intensity of the two desorption peaks in TDS tri- to bidentate ratios of 3.0, 1.9 and 2.4 for the PPA SAMs on the ZnO-O, ZnO-Zn and ZnO-M surfaces, respectively.
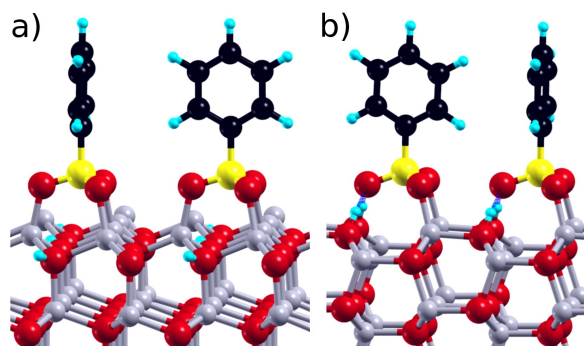
Figure 5.4: Side view of the most favorable configuration of (a) tridentate PPA on ZnO-Zn and (b) bidentate PPA on ZnO-M.

5.3   Thermal stability of PPA-SAMs preparation by OMBD

Though all ZnO surfaces have been prepared thoroughly under UHV-conditions, samples were exposed to air during the immersion process which might affect the film formation by uncontrolled adsorption of hydrogen, hydroxyl or water on the bare ZnO surfaces. Therefore, an alternative SAM preparation was tested that is based on organic molecular beam deposition of PPA to enable a rigorous UHV preparation. This strategy was established before for the preparation of monolayer films of organic semiconductors, such as pentacene on metal surfaces, and utilizes the different adsorption energy of van der Waals bound multilayers and chemisorbed monolayers.[362] We note that PPA films were already prepared in previous studies by evaporating of small amounts onto alumina or anatase substrates,[363–365] however, without analyzing the thermal stability of the films. To develop a reliable preparation method, at first thin PPA multilayer films (about 5 nm) were evaporated from a Knudsen cell onto the before cleaned bare ZnO surfaces and then their thermal stability was analyzed.

The subsequently recorded TD spectrum (cf. Fig. 5.5) reveals a distinct desorption peak (γ_0) around 390 K also at the mass of the molecular ion (m/z=158 amu) beside the prominent phenyl fragment. At higher temperatures again a desorption doublet occurs at the mass of the phenyl fragment with peak maxima at 690 K and 715 K, hence indicating a successful SAM formation. A closer inspection reveals in addition to the multilayer desorption signal also a further but weak desorption peak at about 440 K (denoted as γ_3). Interestingly, this peak was not observed if a 5 nm PPA film was evaporated onto a PPA-SAM prepared before by immersion (cf. dark blue curve in Fig. 5.5 (a)). Note that for mono-dentates a desorption signal is expected for the mass signal 157 amu, but can also observed at mass 158 amu due to isotopomers or crosstalk from neighboring masses. Therefore, this signal is tentatively
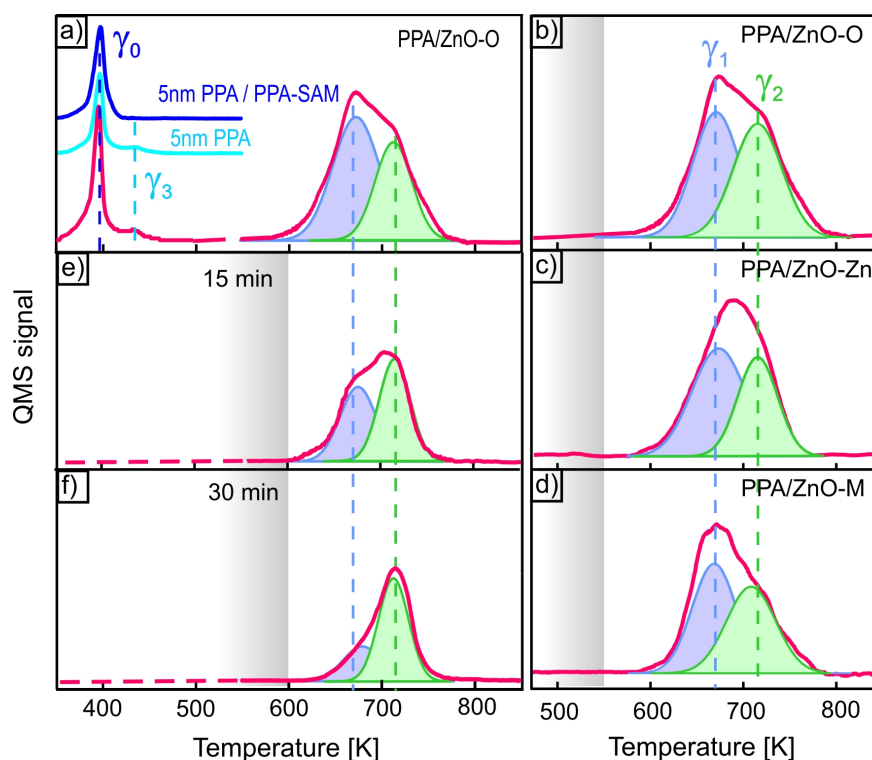
Figure 5.5: Series of TD-spectra for PPA films prepared by OMBD on (a,b,e,f) ZnO-O, (c) ZnO-Zn and (d) ZnO-M single crystals recorded for the mass m/z=77 amu (red curves) during a heating rate of 0.5 K/s. Blue curves in (a) show additionally the molecular ion signal (m/z=158 amu) for a 5 nm PPA film deposited on ZnO-O which exhibit a distinct multilayer peak (γ_0) as well as weak signal (γ_3) that is attributed to monodentate species. The latter was not observed if the PPA film was grown onto a PPA-SAM prepared before by immersion (dark blue curve). The TD-spectra (b-d) were recorded after the multilayer films had been heated at 550 K for 5 min to remove excess multilayers. Spectra (e,f) demonstrate a selective depopulation of the first adsorption state by extended heating of the samples at 600 K for 15 and 30 min prior to the acquisition of the TD-spectra.

attributed to mono-dentate species whose formation might be related to steric hindrance due to the multilayer film. Using the OMBD preparation method comprising first a deposition of 5 nm PPA followed by annealing at 550 K to thermally desorb multilayer excess, SAMs were also prepared on the differently oriented ZnO surfaces. The corresponding TD-spectra reveal a rather similar situation: again, two distinct desorption peaks around 690 K (γ_1) and 715 K (γ_2) were observed for all surfaces. The quantitative analysis of both desorption signals yields tri- to bidentate ratios of 1.2, 1.1, and 1.3 for PPA-SAMs on the ZnO-O, ZnO-Zn and ZnO-M surfaces, respectively, which are significantly smaller than for immersion preparation. The lower tridentate fraction in OMBD prepared films might be explained by a lower barrier for

deprotonation of the hydroxyl unit of PA as a result of the surrounding (dielectric) solution, the longer immersion time or steric hindrance in the solid adlayer.

Precisely knowing the dissociation energetics of the two adsorption states also enables to change their relative ratio by selective thermal desorption of the tridentate species. This is demonstrated in Figure 5.5 (e) and (f) which shows a series of TD-spectra for PPA-SAMs prepared by OMBD and heating at 600 K for different times (15 and 30 min) before acquisition of the spectra. The resulting peak ratio γ_1/γ_2 decreases to 0.7 and 0.3 with increasing heating time. Although this reflects a partial decomposition of the SAM, it might be beneficial to control the relative bi- to tridentate ratio within the film as it offers a route for a spectroscopic characterization of the individual dentate species.

## 5.4 Influence of hydroxylation and surface roughness on SAM formation

Though the OMBD preparation of PPA-SAMs yields a larger bidentate proportion than the immersion, it rigorously excludes a sample contact to humidity. Thus, a comparison with ZnO samples that have been intentionally pre-dosed to water or its constituents allows studying their influence on the SAM formation. To this end, at first the uptake of H_2O and OH during exposure to air has been characterized. For this purpose, UHV-prepared ZnO crystals were exposed to air for various periods (1 and 10 min) before they are loaded back into the vacuum system. For comparison additional samples were also dip-coated in ethanolic NaOH solution for 1 min. Figure 5.6 summarizes the corresponding TD-spectra for the mass signal m/z=17 amu that were obtained for the differently oriented ZnO crystals after the various treatments. We note that very similar curves were also observed for the mass m/z=18 amu. This is attributed to the difficulty to distinguish between both masses because of protonation reactions during the ionization. The corresponding TD-spectra reveal in each case rather broad signals, but two main desorption bands at temperatures of 350-345 K and around 550 K can be identified. Previous TDS experiments for water adsorption on a single crystalline ZnO-M surface[317,366] and on Mn-doped polycrystalline ZnO[367] also revealed a distinct desorption peak around 370 K and 420 K as well as weaker signals above 550 K, which were assigned to the desorption of water and OH. The desorption signals are largest after NaOH dip, which indicates a fully hydroxylated surface. On the other hand, the data also show that already after exposure to air for 1 minute a notable water/OH uptake takes place. We further note that for samples which had been heated to 750 K in vacuum for a few minutes, no desorption signals at the mass of OH or water were found in the subsequently

recorded TD-spectrum (light blue curves in Fig. 5.6), hence indicating that the heating results in water free surfaces.
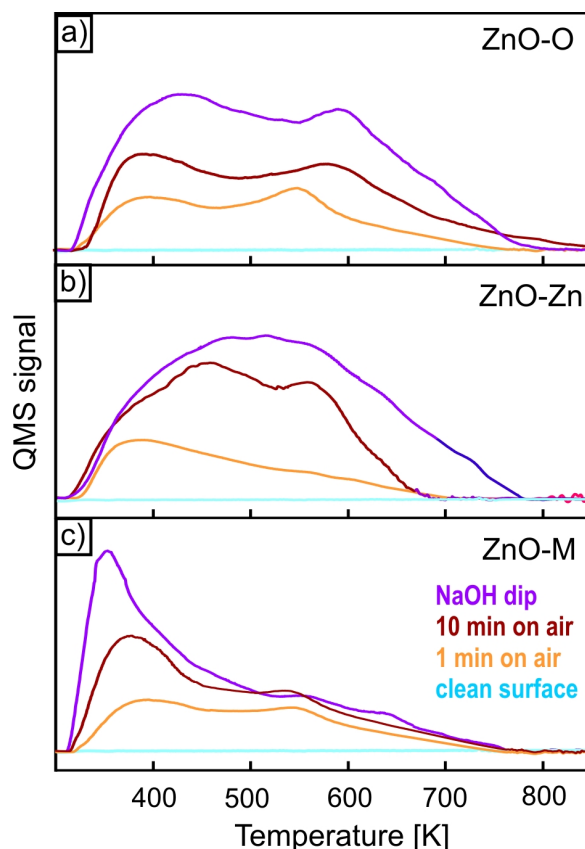
Figure 5.6: Series of thermal desorption spectra recorded for the hydroxyl mass (OH, m/z=17 amu) during a heating rate of 0.5 K/s for (a) ZnO-O, (b) ZnO-Zn and (c) ZnO-M samples after different surface treatments: exposure to air for 1 minute (orange curve), for 10 minutes (brown curve) and after NaOH dip for 1 minute (purple curve). The light blue curve corresponds to spectra of the bare surface (after heating to 750 K).

To study the influence of hydroxylation on the dentate formation on the various ZnO surfaces, additional samples were initially hydroxylated by means of NaOH dip before immersion in PPA solution. As depicted in Figure 5.7 (a-c), the subsequently recorded TD-spectra reveal again two distinct desorption peaks with tri- to bidentate ratios of 3.6 for ZnO-O, 2.6 for ZnO-Zn and 4.8 for ZnO-M, which is a noticeable increase as compared to the non-hydroxylated surfaces (cf. Fig. 5.1). Remarkably, this pretreatment enhances also the tridentate fraction for films prepared by OMBD as shown exemplarily in Figure 5.7 (d) for ZnO-O, which yields a peak ratio of 1.7 (as compared to 1.2 for the non-treated surface
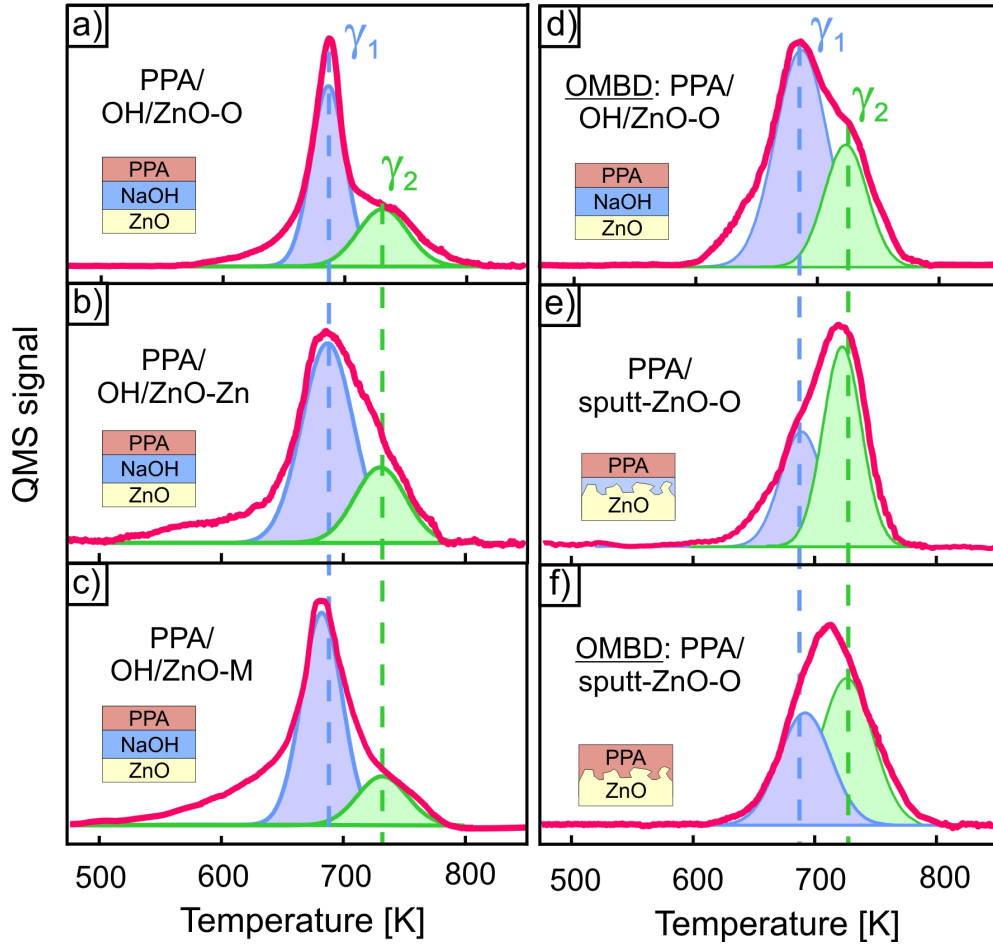
Figure 5.7: Series of TD-spectra for PPA-SAMs prepared on pretreated ZnO surfaces acquired for the mass m/z=77 amu (red curves) during a heating rate of 0.5 K/s. TD-spectra on the left column were recorded for (a) ZnO-O, (b) ZnO-Zn and (c) ZnO-M single crystals which had been hydroxylated by NaOH dip before immersion, while TDS data corresponding to PPA-SAMs prepared by OMBD on a hydroxylated ZnO-O and by immersion of a sputtered ZnO-O surface are shown in (d) and (e) respectively.(f) PPA monolayer desorption prepared by OMBD on bare roughened by sputtering ZnO-O surface.

(cf. Fig. 5.5 (b)). This data clearly indicate that a tridentate formation on ZnO surfaces is promoted by former hydroxylation.

For the sake of completeness we have also studied the influence of surface roughness on the dentate formation. For this purpose a ZnO-O surface had been intentionally roughened by Ar$^+$ sputtering for 30 min without any further annealing before immersion in PPA-solution. As shown in Figure 5.7 (e) the corresponding TD-spectrum for samples prepared by immersion reveals a tri- to bidentate ratio of 0.6, thus demonstrating that the preferential tridentate formation found for a smooth single crystalline ZnO-O surface (cf. Fig. 5.1 (a))

is reversed. In this case a partial water layer is formed on the ZnO substrate surface, which should induce the formation of the tridentate mode. Nonetheless, because roughened substrates tendentiously possess an even higher number of disturbed sites than the originally smooth ZnO surface the possibility to form tridentate is limited by the reduced number of adsorption sites and the distance to the underlying metal ions. These indicates that in such systems rather than surface hydroxylation the surface defects define the film formation. Similar tendency to bidentate was found for PPA films on roughned ZnO prepared by OMBD (cf. Fig. 5.7 (e)). These findings emphasize the influence of surface defects on the interface chemistry and SAM anchoring.

5.5   Molecular orientation

Finally, also the molecular orientation of PPA molecules in saturated monolayer films has been determined by analyzing the dichroism observed in NEXAFS measurements for samples prepared by immersion and OMBD on differently terminated ZnO surfaces. The corresponding data set of carbon K-edge NEXAFS spectra for the system of PPA on ZnO-O is presented in Figure 5.8. A typical carbon edge NEXAFS spectrum (cf. Fig. 5.8 (a)) reveals a sharp resonance at around 285.1 eV (denoted as π_1^*) due to the excitation of C$1s$ electrons into unoccupied π^* orbitals of the aromatic phenyl ring and rather broad resonances at higher energies that are attributed to excitation into σ^* orbitals. A more detailed analysis reveals an additional sub-resonance at 285.6 eV (π_2^*) that results from a slightly different chemical coordination of the carbon atoms attached to the phosphonic anchoring group. Such an initial state effect has been reported before also for the case of benzenethiol.[361] Additional weak resonances appear at 287.5, 288.7 and 290 eV, which have been assigned to several overlapping π^* and σ^* resonances in previous NEXAFS studies of PPA films adsorbed on ITO and indium zinc oxide (IZO) substrates.[202,367]

NEXAFS spectra that were recorded for different orientations of the electrical field vector $\overrightarrow{E}$ of the incident synchrotron light relative to the surface normal (cf. blue and red curves in Figure 5.8 (a) reveal a pronounced intensity variation of the π^* resonances (linear dichroism), which reflects distinct orientational ordering within the SAM. The theoretical analysis shows that this intensity of the π^* resonance, I_{π^*}, depends on the orientation of the electrical field vector $\overrightarrow{E}$ of the incident synchrotron light and the transition dipole moment of the excitation, $\overrightarrow{T}$, according to the equation 3.5. For linearly polarized light with a polarization factor, P, a substrate of 3-fold symmetry and vector-type π^* orbitals present in the aromatic ring system,

this yields the dependency (rearranged equation 3.6):

$$I_{\pi^*} \propto P\cos^2\theta \left(3\frac{\cos^2\alpha}{2} - \frac{1}{2}\right) + \frac{\sin^2\alpha}{2}, \tag{5.1}$$

where α denotes the angle between $\overrightarrow{T}$ that is oriented normal to the phenyl ring plane and the surface normal as depicted in the inset in Figure 5.8 (a) and discussed in more details Chapter "Characterization techniques". The strongest absorption efficiency is found for normal incidence (θ=90°, red curve), while rather weak absorption is present under gracing incidence (θ=30°, blue curve). Interestingly, the PPA-SAMs that were prepared by immersion reveal a somewhat larger dichroism than films prepared by OMBD as depicted in Figures 5.8 (b)and (c). Considering the intensity of the leading π_1^* resonance (which was separated from the π_2^* signal by careful curve fitting) for different incident angles of θ=30°, 55°, 70°, and 90° enables a more precise analysis of the dichroism (cf. Fig. 5.8 (d)). This yields an orientation of the aromatic moiety relative to the sample surface of $\alpha_{imm} = 82°\pm5°$ and $\alpha_{OMBD} = 71°\pm4°$ for films prepared by immersion and OMBD respectively. One should note that the defined orientational order in the SAM does not designate the resulting film density and does not provide information about the lateral molecular order.

Corresponding NEXAFS measurements for PPA monolayer films adsorbed on the other ZnO surfaces yield rather similar molecular orientations, irrespective on the actual surface termination that are depicted on the Figure 5.9 and summarized in the Table 5.1. The analysis indicates an almost upright orientation of the phenyl ring plane in the immersed films, while it appears somewhat inclined in films that have been prepared by OMBD. The DFT calculations for our set of model PPA adsorbate structures show that bidentate PPA molecules are more flexible in their orientation than tridentates and show larger tiltings in some configurations. Therefore, the inclination for the OMBD prepared films can be explained by the preferential bidentate formation and lower tridentate to bidentate ratio as it is evidenced by our TDS data. The outcome of our orientational analysis is also in a good agreement with recent experimental results reported by Gliboff *et al.* for PPA-SAMs prepared by immersion on other oxidic substrates yielding values of $\alpha = 71°\pm4°$ and $77°\pm5°$ for indium tin oxide and indium zinc oxide, respectively.[202,368] At this point we would like to note, that frequently not the orientation of the transition dipole moment $\overrightarrow{T}$ relative to the sample normal, α, but the complementary angle between the ring plane and the surface normal, ϕ, is denoted as tilt angle which are related by $\alpha = 90°-\phi$ (cf. inset in Fig. 5.8 (a)). The slightly smaller α values (i.e. larger tilt angles ϕ) obtained by Gliboff *et al.* can be attributed to the surface roughness of the used polycrystalline oxide substrates.
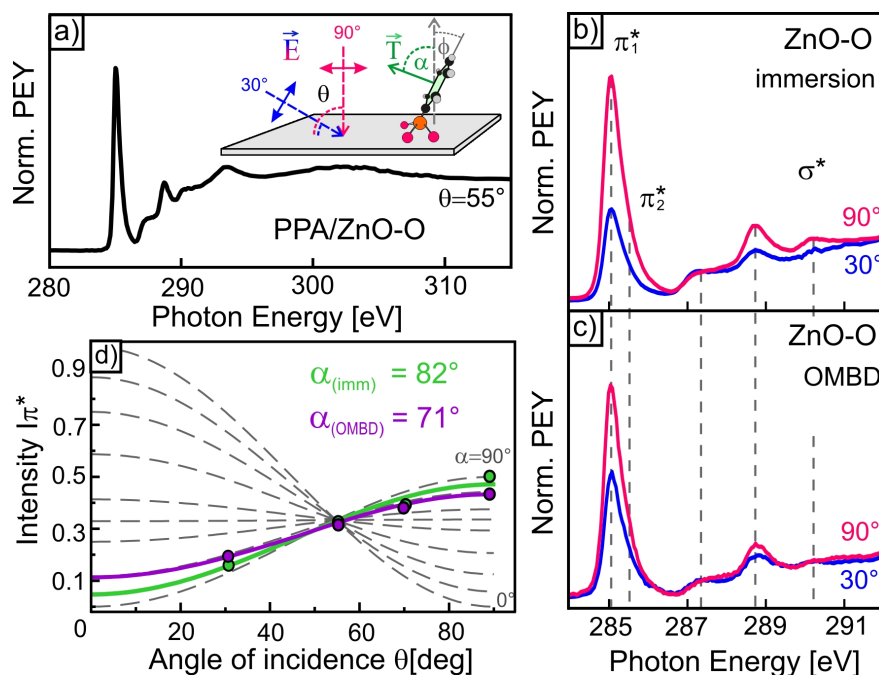
Figure 5.8: Summary of C 1s NEXAFS data of PPA monolayer films on ZnO-O. (a) Full spectrum recorded at an incident angle of 55° together with a scheme of the experimental geometry. (b,c) Angular dependency of the magnified π^* region of PPA SAMs prepared (b) from immersion and (c) by OMBD. The π_1^* resonance intensity as a function of the angle of incidence is shown in (d) together with a best fit to the data.

Moreover, a rather similar molecular orientation ($\alpha = 72°$) was reported for trifluoromethyl substituted PPA-SAMs formed on the single crystalline ZnO-Zn surface.[297] Interestingly, a distinctly larger downward tilting of the phenyl ring is observed in monolayers if the phenyl ring is separated from the phosphonic acid anchoring unit by an additional methylene unit. For such PA-SAMs prepared on a ZnO-Zn surface a substantially lower tilt angle of $\alpha = 45°$ has been obtained[298] which indicates that the intermediate alkyl spacer has a severe influence on the molecular orientation. This parallels the situation of oligophenylenethiol-SAMs on gold where the orientation of the phenylene backbone depends decisively on the length of alkyl chains separating the aromatic moiety from the anchor unit showing a distinct odd/even effect.[369,370]

Complementary measurements dealing with the influence of substrate roughness and hydroxylation on the molecular orientation were performed and summarized in Figure 5.10 and Table 5.2. Consistent with the TDS data, where the surface hydroxylation results to dominating tridentate mode, the increased value of the tilt angle obtained from the NEXAFS dichroism can be assigned to the PPA attachment mainly driven by the tridentate bonding.
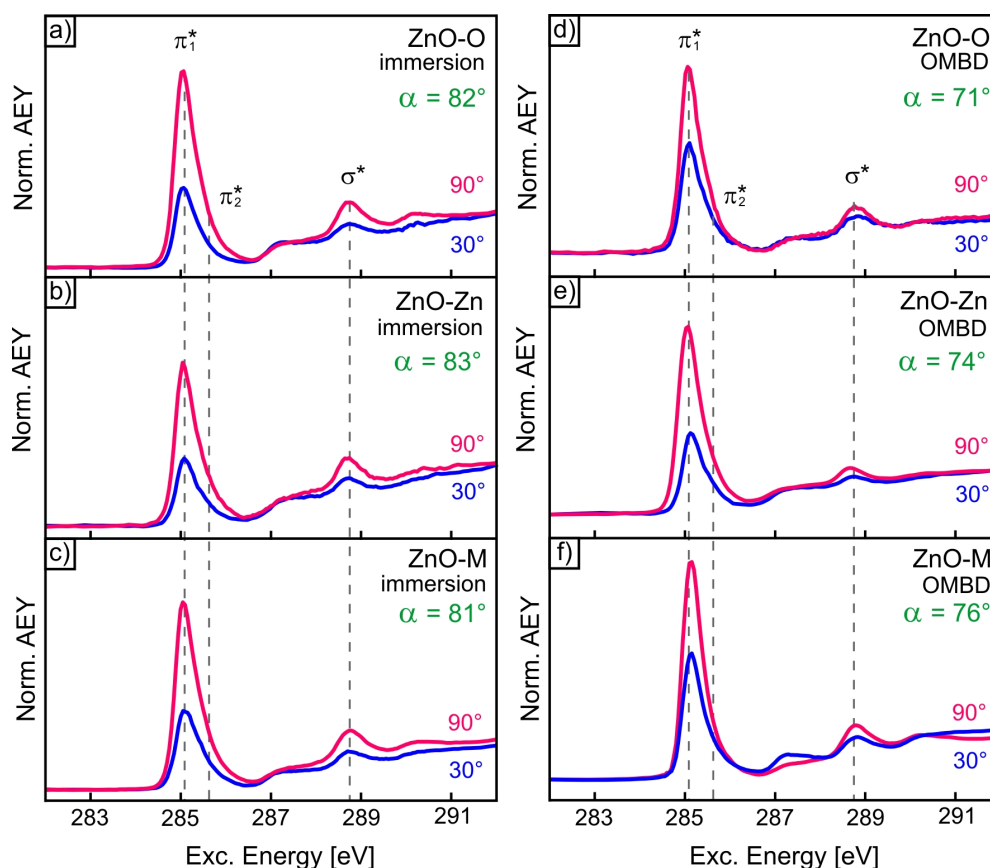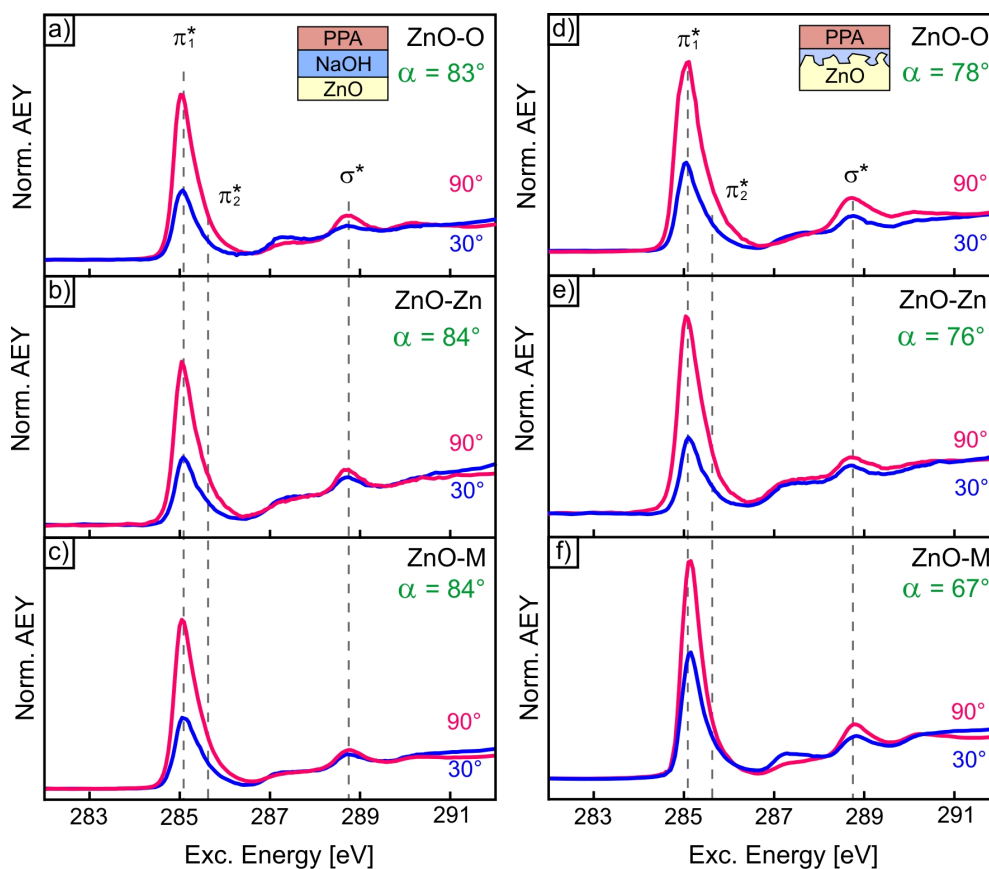
Figure 5.9: A series of C 1s NEXAFS measurements in the PEY mode for PPA monolayer films on ZnO-O, ZnO-Zn and ZnO-M prepared by (a) immersion and (b) OMBD.

Although the experimental variations are not significant and can be attributed to the accuracy range. Previous DFT studies for the methyl phenylsphosphonic acid on ZnO-Zn also report relatively small changes in the inclination, in particular, $\alpha = 43.4°$ for the bidentate and $\alpha = 45.5°$ for the tridentate.[201] The dominant bidentate attachment on rough ZnO is attributed to the decrease in the phenyl ring inclination. Molecules which adsorb onto samples with rough surface morphology typically also obtain disordered character due to a large number of surface domain boundaries for the adsorption. The obtained tilt angle for such films is the average tilt angle because the beam spot is macroscopic. If SAMs are not equally distributed on the surface NEXAFS experiments do not provide a reliable directional preference. Similar analysis for films prepared by OMBD could provide valuable data about the mechanism of PPA attachment on ZnO, in particular after the sample surface pretreatment by NaOH.

Table 5.1: Effective orientation of the phenyl ring determined from NEXAFS dichroisms of PPA-SAMs prepared on various ZnO surfaces by immersion and OMBD.

Molecular tilt angle	ZnO-O	ZnO-Zn	ZnO-M
α_{imm}	82°	83°	81°
α_{OMBD}	71°	74°	76°

Figure 5.10: A series of C 1s NEXAFS measurements in the PEY mode for PPA monolayer films prepared by immersion on (a) hydroxylated by the NaOH dip and (b) roughened by Ar^+ sputtering on ZnO-O, ZnO-Zn and ZnO-M samples.

5.6 Conclusions

Using thermal desorption spectroscopy we demonstrate that phenylphosphonic acid SAMs formed on crystalline ZnO surfaces desorb dissociatively and exhibit two distinct desorption channels. These desorption signals are related to bi- and tridendate species because they reveal

Table 5.2: Effective orientation of PPA-SAMs prepared on various hydroxylated and roughened ZnO surfaces by immersion.

Molecular tilt angle	ZnO-O	ZnO-Zn	ZnO-M
Surface hydroxylation	83°	84°	84°
Surface roughening	78°	76°	67°

different internal C-P bond strengths. The analysis of the corresponding peak intensities observed for SAMs prepared on the differently oriented ZnO surfaces enables to quantify the relative abundance of both species. We note that SAM preparation by immersion is generally accompanied by uncontrolled pre-coating of the substrate by adsorption of water and/or hydroxyl species as demonstrated by our complementary TDS experiments. To exclude such parasitic effects we have established an alternative monolayer preparation which is based on UHV deposition in combination with subsequent desorption of excessing multilayer material. This enables in particular to compare the stability and formation of PPA SAMs on bare and intentionally hydroxylated ZnO surfaces achieved by NaOH dip-coating before the PPA deposition. The corresponding analysis of the desorption signals indicates that hydroxylation favors the tridentate formation.

A comparison of our TDS data obtained for the differently oriented single crystalline ZnO surfaces indicates that tridentate species are found on all ZnO surfaces. This is rather surprising since such a binding geometry is hardly possible on ideal oxygen- or mixed-terminated ZnO surfaces. Therefore, it rather suggests a local surface relaxation or reconstruction upon PPA-SAM formation leading to a microscopic surface roughness which renders a tridentate formation possible. This would also explain our mistrials to obtain LEED patterns for the SAMs on the single-crystalline ZnO surfaces as well as the notable surface roughness obtained in the AFM data after thermal desorption of the SAMs. This is an important aspect as it challenges the assumption that ZnO surfaces remain intact upon adsorption of phosphonic acids. To clarify this point further, structural studies are needed which will hopefully be available in future work.

CHAPTER 6

Structure and Stability of SAMs with Different Anchoring Units on ZnO

6.1 Introduction

As it was discussed in previous chapters that self-assembled monolayers find a wide range of application since they provide a versatile possibility of tailoring surface properties like wetting behavior, adhesion, lubrication, and corrosion.[371] Among this, SAMs have been widely introduced in organic electronic devices, for example OLEDs or organic field-effect transistors.[371–374] Especially, this is allowed by the variety of available dipolar SAMs, which are used to tailor the work function of inorganic semiconductors. Such energy level alignment is described by changes of the interface dipole.[375–380] The formed interface dipole shifts the molecular levels by a large amount relative to the Fermi energy and substantially modifies the work function of the electrode material. In the literature several contributions have been proposed for the interface dipole.[381–383] Six possible contributions were listed by Ishii *et al.* including: charge transfer across the interface; image potential induced polarization of the organic material; pushing back the electron cloud tail out of the inorganic material surface by the organic material; chemical reactions; formation of interface states and alignment of the permanent dipole of the organic material.[52,342] However, among these factors usually contributions from the chemical interaction between the semiconductor and the SAM, interface surface states and permanent molecular dipole are considered.[57,377,384,385] The change of the work function can be also described in terms of an effective dipole moment. The total effective dipole can be explained by a double layer of dipoles, which correspond to the intrinsic molecular dipole moment and the dipole moment induced by the electronic reorganization at the interface which can be caused by the chemisorption or the weak surface

restructuring. The effective dipole moment is a vector perpendicular to the surface plane. Therefore, the molecular orientation within the adsorbed layer, which is generally sensitive to the molecular structure and chemical composition, can influence the dipole vector and as a sequence the work function modulation.[56,386–388] For example, for alkanethiol-based SAMs changes in the chain length can lead to pronounced changes in the resulting film structure and stability.[389–393] Moreover, regarding future applications SAMs can be used as the contact primer layer. While fully π-conjugated SAMs reveal high electrical conductivity, aliphatic SAMs having a large band gap and thus are rather good insulators.[394–396] Therefore, it is important and helpful to investigate the structure of molecular films for different organic molecules.

In this chapter the earlier study of PPA SAMs on ZnO is expand to organic molecules with different substitutions in the molecular backbone and the anchoring group. First the monolayer film formation and its stability for TFPPA and DPA on O-terminated ZnO substrates is discussed. The partially fluorinated TFPPA has an intrinsic dipole moment, which makes this material intersting for the tailoring of electronic interface properties. The influence of the insulating alkyl-chain of the DPA on the SAMs formation and ZnO surface stability will be discussed as well. Next the structure and stability of PPA monolayer films is compared to the SAMs formation for the less studied PHPA on differently terminated ZnO samples. Additionally the analysis of the stability of molecular films on ZnO attached through the carboxylic acid anchoring and thiol is presented in this chapter. Here the thermal stability of TFPPA, DPA, PHPA, BA and TP on single crystalline ZnO surfaces is studied by means of TDS. The information about the molecular orientation is obtained from NEXAFS studies. Optical microscopy, AFM and SEM as well as XRD methods are used to analyze ZnO etching by PA-based SAMs and identify products of the dissolution-precipitation reaction.

Some of the earlier works have alluded to TPPA and similar to DPA molecular layers on metal oxides, but concentrated mostly on the work function modification. Recently Koch N. *et al.* reported about the modification of single crystalline ZnO substrates by means of TFPPA and DPA or analogous molecules.[297,352] They report formation of well-defined, dense ($\sim 2\,\mathrm{molecule/nm^2}$ for aliphatic and $\sim 4\,\mathrm{molecule/nm^2}$ for aromatic SAMs) and robust monolayer films prepared by wet chemical methods. By that the work function of ZnO was modified of more that $1.7\,\mathrm{eV}$ depending on the SAM composition. They find different offsets between the molecular frontier levels and those of the substrate leading to the variations of the ionization potential up to $0.7\,\mathrm{eV}$. While the non-fluorinated PAs do not significantly change the WF, the adsorption of TFPPA, which owns the largest dipole moment compared to PPA and DPA, results in the most effective work function tuning. For the majority of studied systems the molecular attachment via bidentate mode was found to be

dominant. However, in some works the attachment of aliphatic SAMs proceeds mostly by the formation of the tridentate mode. The orientation of PA-based SAMs has been investigated in the group of D.S. Ginger by conducting NEXAFS measurements.[368] For PAs on ITO they find that introducing the fluorine atoms direct to the aliphatic chain leads to the more upright oriented molecules, when the fluorinated PPA was found to be less upright oriented. This was explained by differences in the binding character for these molecules, since molecules bound by the bidentate mode obtain slightly smaller tilt angle. Similar results were obtained for fluorinated octylphosphonic acid and benzyl phosphonic acid on ITO from the polarization modulation-infrared reflection–absorption spectroscopy (PM-IRRAS) measurements by Sang L. *et al.*.[397] Although DFT calculations conducted by the group of C. Wood[201] point to only small structural changes between fluorinated and not fluorinated SAMs, the difference in molecular tilt angle for two binding motifs was shown to be around $10°$ in the experiment. Later Hotchkiss P. J. *et al.* showed, that the aliphatic SAMs form stable densely packed films on ZnO films with the coverage up to $5\,molecule/nm^2$.[199] The monolayer assembly stabilization is explained by the van der Waals interaction between alkyl chains in a fully *anti*-conformation.[199,294] Moreover, it was found that the longer alkyl chain is the stronger the vdW interaction between molecular backbones is. The decomposition temperature of alkanethiol SAMs on gold was shown to increase with increasing chain length of the alkane backbone as well.[398,399] Observed changes in the packing density for PA-based SAMs in different studies can explained by the choice of metal oxide substrates varying from single crystalline to polycrystalline ZnO or ITO and IZO. Sputter-deposited zinc oxide films used by P. J. Hotchkiss more likely have higher degree of surface defects than single crystalline ZnO substrates and, therefore, obtain a larger number of active sites for molecular attachment. The preferential tridentate anchoring for aliphatic PAs as well as their high stability was reported for single crystalline ZnO as well as for the nanostructured substrates.[293,400] Although experimental data about the thermal stability connected to film structure for TFPPA and DPA is lacking.

As opposed to the PA the usage of phenylphosphinic acid based SAMs as a contact primer layer or reactive group for the dye attachment is still limited. The majority of scientific works so far is dealing with the phosphinic acid bonding to TiO_2 substrates. First phosphininc acid as a part of a new class of molecular insulators, particularity amphiphiles, has been introduced by M. Wang *et al.*.[401] The dineohexyl phosphinic acid (DINHOP) has been used for the interface engineering of the nanocrystalline TiO_2/electrolyte junction. DSSCs based on the co-adsorption of the DINHOP and a dye sensitizer exhibit increasing power output of the cell and exceptional stability under prolonged light soaking. Later study showed, that the DPA, containing phosphonic acid group, bound more efficiently to the surface of titania in

comparison to DINHOP, containing the phosphonic acid group, when adsorbed from similar ethanol solutions.[402] This, however, can be attributed to the difference in the molecular structure. Another study showed, that after introducing diphenylphosphonic acid into the dye system of DSCs, the total energy conversion efficiency was significantly improved.[403] Likewise usage of phosphinic acid treatment agents for the porphyrin-sensitised titania films improves the efficiency of DSSC devices as well.[404] The direct dye attachment to oxidic surface by means of HPA was discussed in the work of I. Lòpez-Durante *et al.*.[405] Apparently, the level of Zn-phthanolyanine dye adsorption on TiO$_2$ films was found to be higher for dyes with carboxylic acid functional group, thus giving a slightly higher solar conversion efficiency. Nonetheless the phosphinic acid dye attachment was shown to have stronger binding properties than the carboxylic anchoring group improving the durability of the system. The bonding of phosphinic acid to metal oxide surfaces on a microscopic level can proceed through mono- or bidentate modes. The only available study where this topic was addressed refers the anchoring of diphenylphosphinic acid and its derivatives to TiO$_2$ particles and finds the molecular attachment mainly in the bidentate mode.[406] Besides phosphinic acid and its derivatives find wide application in biochemical, biological and medical fields[407] as well as in synthesis of hybrid materials by sol-gel methods[408–410]. HPAs are also good extractant for extraction and separation of rare earth metals from a solution.[411,412] Despite several studies mention the relative stability of such films this issue remains unclear, especially regarding the influence of molecular construction and backbone composition.

Many studies agree on the fact, that in spite of better adsorptions and good electric coupling provided by CA-based SAMs their stability is much lower compared to PA.[294–296,413] The difference in binding strengths was demonstrated experimentally by T. Lenz *et al.*, when the aliphatic CA on the AlO$_x$ was fully substituted by fluorinated aliphatic PA.[430] This was later confirmed by theoretical DFT calculations on the similar model system.[416] Among the available binding modes of CA to metal oxide surfaces, which are the attachment by means of an uncoordinated anion, a monodentate ligand, a bidentate chelate or a bridging bidentate, the monodentate adsorption was found to be always energetically more favorable at all experimental conditions.[197,416] Not much is known about thermal stablity of CA SAMs on ZnO. According to several studies simple CA molecules are stable only up to 380 K on metal oxides. Next to that 40% of carboxylate species recombine with the surface hydroxyl groups at 400 K and the rest desorption proceeds through unimolecular dehydration reaction resulting in the formation of different molecular fractions at the temperature about 525 K.[417] This, however, was found for the CA films on powder pellets on anatase TiO$_2$. Next to extensive studies for the thiol/Au systems metal oxide surfaces can be

also modified by thiols.[292,350,418] Generally thiols on metal oxides exhibit lower thermal stability than PAs and CAs.[293,350] However, the desorption temperatures of thioles attached to metal oxides reported in the literature are rather contradictory and varies from 370 K up to 600 K.[293,350,419]

## 6.2   Trifluorophenylphosphonic acid (TFPPA) and Dodecylphosphonic acid (DPA)

Monolayers of TFPPA with the -CF$_3$ side group attached to the top of the phenyl ring and DPA with the aliphatic backbone were prepared on single crystalline ZnO-O substrates by immersion to determine how the backbone substitution influence the film formation and stability. ZnO crystals have been soaked in 0.1 μM ethanolic solutions of listed compounds for 24 hours. Figure 6.1 (a) and (b) represent the TD-spectra for TFPPA and DPA respectively. Both films were found to exhibit similar to PPA stability and start to desorb at around 600 K. The information about the TFPPA desorption behavior can be obtained by tracking two of the most intense signals corresponding to the phenyl ring ($m/z = 77$ amu, red curve) and the -CF$_3$ molecular fragment ($m/z = 69$ amu, gray curve). The most intense signal at the mass $m/z = 51$ amu corresponding to the C$_4$H$_3$ alkyl chain fragment was found for DPA. This indicates the dissociative desorption for both molecular systems. The presence of the intense -CF$_3$ signal for TFPPA and the C$_4$H$_3$ fragments points to the molecular decomposition which is more likely caused by the molecular ionization in the QMS. Although, when analyzing relative peak intensities for both recorded signals and their position relative to each other on the temperature axis it can not be excluded, that first some C-C(F) binds break and contribute to the signal and the cleavage of C-P bond occurs next. At around 600 K the C-C bond between the phenyl ring and the -CF$_3$ side group breaks giving the rise for the corresponding TDS signal. Next to this process partial cleavage of the C-P bond happens and is indicated by the first less intense peak in the spectral line for the aromatic ring desorption. At higher temperatures the second process dominates and the intensity of this molecule fragment peak increases. Two desorption channels marked with blue and green fits at γ_1=690 K and $\gamma_2 = 730$ K have been identified for TFPPA. Slightly changed desorption temperatures were found for DPA and yield γ_1=680 K and γ_2=700 K for the first and the second desorption channels respectively. Non-homogeneous desorption components in both spectra indicated by weak shoulders at around 600 K, result from molecules differently bound to the ZnO surface. Analogous to PPA two spectral features have been attributed to bi- and tridentate binding motifs. Since the peak at the lower temperature was attributed to the tridentate mode

and the second peak to the bidentate mode the analysis of their relative intensities yields nearly similar number of bi- and tridentate modes for TFPPA and dominanting tridentate bond for DPA. For aromatic TFPPA this correlates to previous findings, that the fluorination results in more bidentate molecular attachment.[368] In case of DPA the dominant tridentate was also found for aliphatic PA-based SAMs of shorter chain lengths.[297,352]
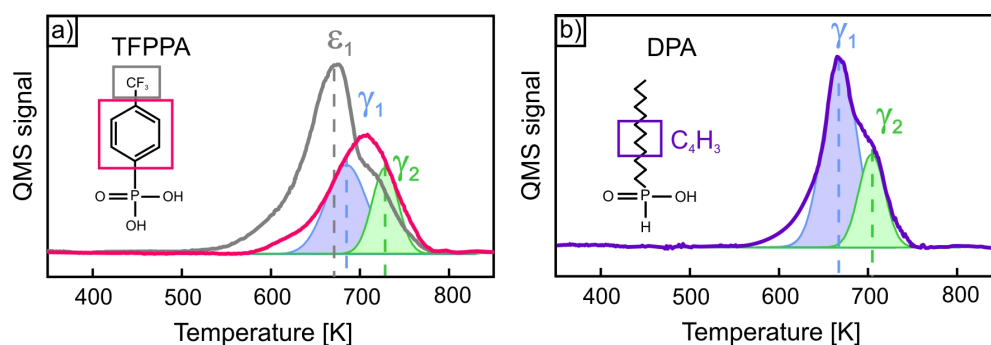

Figure 6.1: A series of the TD-spectra for(a) TFPPA and (b) DPA monolayers on the ZnO-O sample prepared by immersion. TFPPA desorption is given for the mass signal of the -CF$_3$ fragment (gray curve) and the mass signal of the phenyl ring (red curve). Desorption spectra for the DPA have been recorded for the mass signal of the C$_4$H$_3$ fragment of the aliphatic chain. Fits indicate two different desorption channels for the bidentate (green) and the tridentate (blue).

In addition the molecular orientation of both SAMs was investigated, since changes in the molecule structure can influence its coordination within the film. The molecular orientation of TFPPA and DPA molecules in saturated monolayer films has been determined by analyzing the dichroism observed in PEY NEXAFS measurements (cf. Fig. 6.2). Panels (a) and (c) represent the carbon K-edge NEXAFS spectra for TFPPA and DPA molecules respectively for the $\theta = 55°$ angle of incidence. In TFPPA spectra the strong angular dependence in the transition to the C=C π^* resonance, located at 285.1 eV with a π_2^* shoulder peak caused by the C-P bond are observed. Other notable features between include C-H, C-C(F) signatures and C-C σ^* signatures and their overlap at 287-300 eV. The introduction of fluorine atoms does not result in the appearance of additional spectral features, since it directly affects only broad σ^* resonance. The dichroism analysis of π_1^* peak intensities yields the orientation of molecular aromatic part $\alpha = 66° \pm 4°$ which means, that compared to PPA the addition of -CF$_3$ side group leads to more tilted backbone. Similar tendency was found for PPA with directly fluorinated phenyl ring.[368] The broad peak on the DPA NEXAFS spectra at 289-290 eV corresponds to the C-C σ^* transition. The second rather broad beak with the maximum at 287.8 eV is caused by the C-H bond and the small spectral feature at ~285 eV is caused by the carbon surface contaminations or beam radiation in the experiment. The molecular tilt angle was determined from the corresponding dichroism for the C-C σ^* transition. Fitting the
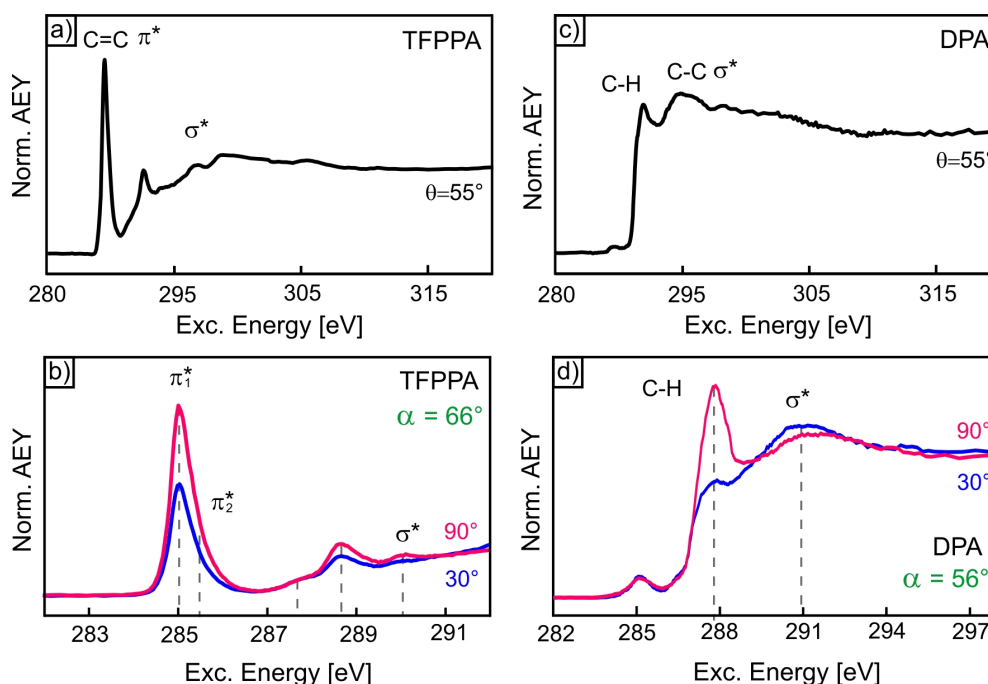
Figure 6.2: C1s NEXAFS data of (a,b) TFPPA and (c,d) DPA monolayer films on ZnO-O prepared from immersion. (a,c) Full spectra recorded at an incident angle of 55°. (b) Angular dependency of the magnified π^* and σ^* regions of TFPPA SAMs and (d) of the σ^* region of DPA.

normalized peak intensities to the dichroism model yields an orientation of the axis of alkyl chain $\alpha = 56° \pm 4°$. The self-assembled structures do not leave a distinctive mark in the σ^* region and the tilt angle value coincides with the magic angle, which equals 54.7° in case of ideally linear polarized radiation. Generally two possible explanations for the films structure at such tilt angle arise. This indicates that either the alkyl-chains renders exactly this tilt angle to the surface plane and the absorption signal in these particular molecular conformation is independent from the average molecular TDM orientation or DPA molecules are randomly oriented.[250] The aliphatic PA-based molecules are supposed to form well-defined dense films on oxidic surfaces. This, however, was reported for systems mainly based on the usage of polycrystalline ZnO or ITO and SAMs with shorter aliphatic spacer.[293,368] Without additional experiments the distinction between an uniformly tilted layer and a loosely packed and disordered film can not be established. Although DPA layers exhibit similar to PPA high thermal stability the direct conclusion about the adsorption efficiency of these SAMs can not be derived. The correct comparison of thermal stability requires similar backbones to elucidate the role of intramolecular forces and films with similar molecular packing. Since the packing of aliphatic PA-based SAMs was shown to be lower than for aromatic the direct correspondence becomes therefore troublesome for both systems.[297,352] It is known, that
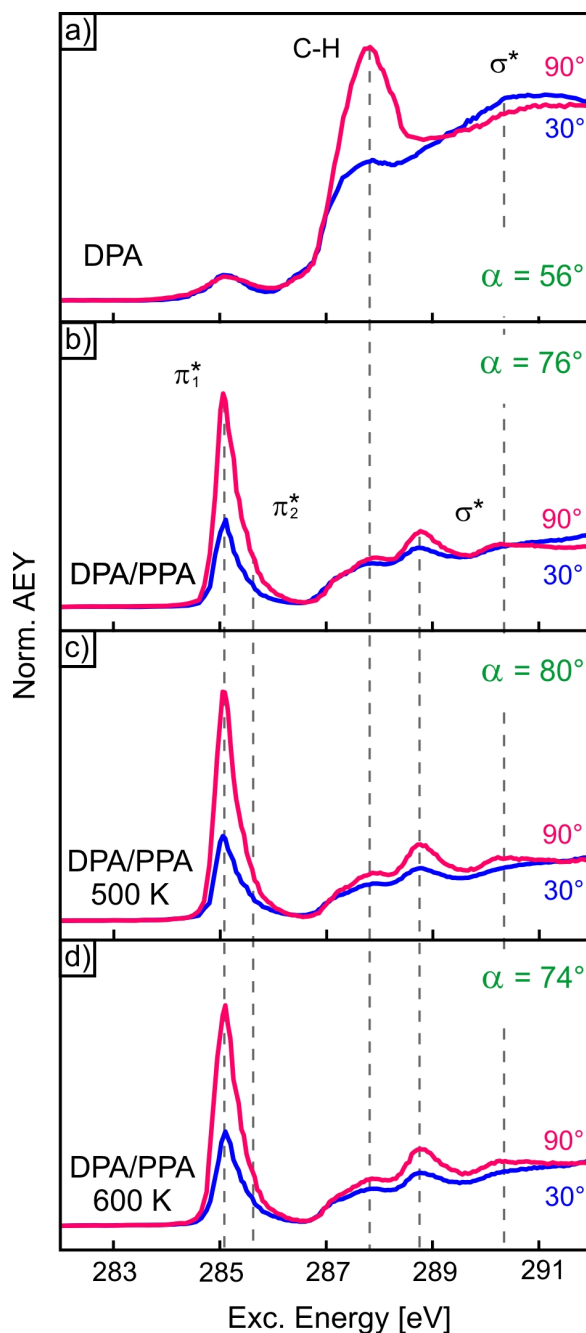
Figure 6.3: A series of NEXAFS spectra of (a) DPA monolayer on ZnO-O prepared by immersion and substituted by (b) PPA monolayer. The exchange reaction is indicated by the presence of the π^* resonant peak on the spectra after PPA postdepositon. Similar signatures and comparable molecular orientation were found after annealing samples up to (c) 500 K and (d) 600 K.

disordered films are more susceptible to degradation or exchange with other SAMs obtaining more reactive towards substrate material anchoring groups.[420,421] Therefore the degree of

orientational order for DPA films has been investigated by means of NEXAFS in an exchange reaction. ZnO-O samples with DPA monolayers have been re-immerssed for 12 hours in 0.1 mM PPA solution and analyzed. The presence of C=C bond in aromatic SAMs produce an increase in the spectral peak at 285.1 eV corresponding to the π^* resonance, which is absent at non-aromatic material (cf. Fig. 6.3 (a,b)). This gives a clear indication to the poor packing of the aliphatic chains and as a sequence the adsorption of PPA. We interpreted these results as a proof for the DPA film disorder. Re-immersed PPA molecules obtain upright orientation of aromatic units and comparable molecular tilt angle. Small variations in the tilt angle value are attributed to the formation of surface defects after earlier DPA adsorption, which partially effect PPA attachment. Moreover, the prominent angle-dependence of the π^* state in newly formed PPA layers remains stable after annealing up to 600 K (cf. Fig. 6.3 (c,d)) indicating strong surface-adsorbate interaction. These results demonstrate that the amount of SAMs disorder can be correlated with the structure of molecular backbone.

To complement the study also the influence of other backbone units on the etching of the ZnO surface and the resulting structure of precipitation has been addressed. Also for this case, we found the formation of distinct, star-shaped precipitations after immersion of a ZnO-O crystal in ethanolic TFPPA-solution (for 1 week) as depicted in Figure 6.4 (a). Although large area of the oxide substrate is covered by precipitations only small needles are formed (even after prolonged immersion time) which hampered a single crystal analysis. However, $\theta/2\theta$-measurements have been possible and confirmed the crystalline nature of formed structures. Based on a comparison of the acquired diffractogram with a powder spectrum of ZnPP (calculated from the single crystal data[310]) a tentative assignment of the observed reflexes was made (cf. Fig. 6.4 (c)). This enabled us to identify the leading diffraction peaks as $(0n0)$ reflexes with a corresponding interlayer distance of $d_{(010)}$=18.6 Å. Compared to the non-fluorinated ZnPP precipitations this means an increased layer separation, which can be rationalized by the extended fluorinated phenyl spacer as depicted schematically on the Figure 6.4 (b). The results indicate the formation of zinc-trifluorophenylphosphonate phase (ZnTFPP). Interestingly, when using phosphonic acid molecules with aliphatic backbone such as DPA for SAM preparation, no visible precipitations were found - even after immersion for one week. At first glance this suggests an absence of etching. However, on a microscopic level an increased surface roughness was observed by means of AFM, again showing an etching of the ZnO surface. The absence of sizeable precipitations indicates that alkane chains reduce the stability (i.e. lattice energy) of crystalline zinc-dodecyl-phosponate precipitations.
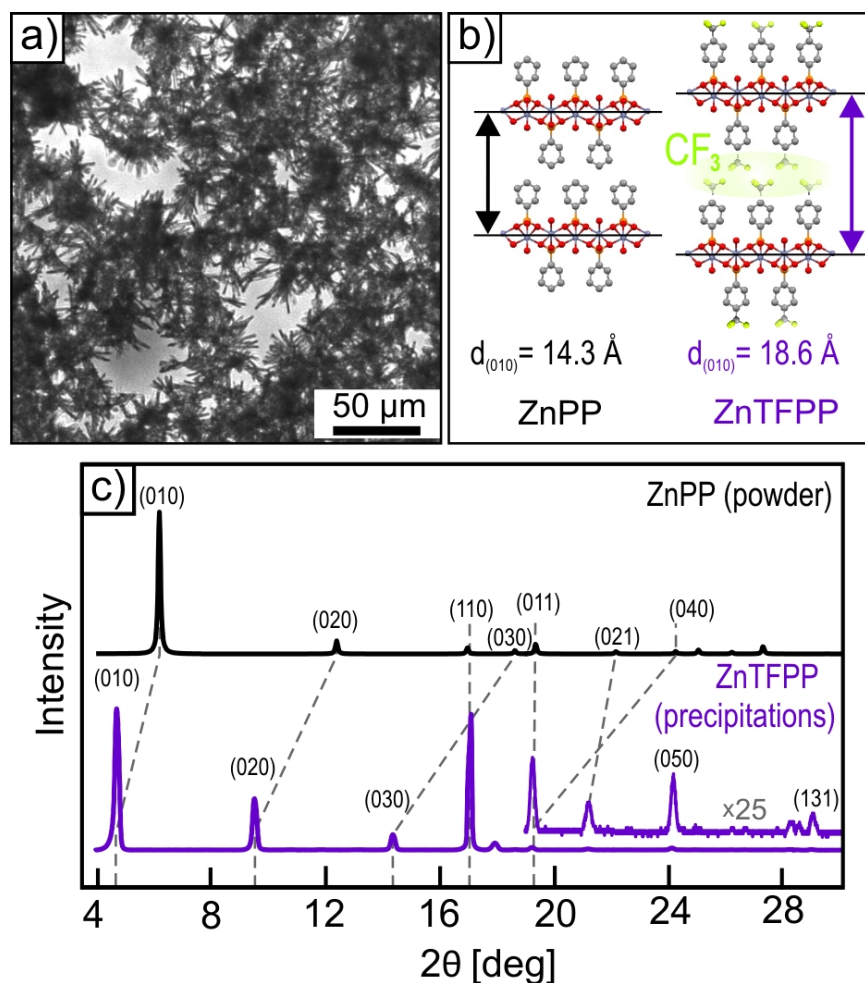
Figure 6.4: (a) Optical micrographs and (c) $\theta/2\theta$-scan of surface precipitation formed after immersing ZnO-O samples in TFPPA solution for one week. A comparison with the XRD powder spectrum of ZnPP[194] allows a tentative assignment of the diffraction peaks which suggests an enhanced interlayer distance $d_{(0n0)}$ due to the substitution of -CF$_3$ groups to the backbone as shown in (b).

6.3 Phenylphosphinic acid (PHPA)

Replacement of phosphonic acid with phosphinic acid is expected to lead to different results, as both are chemically different, regarding stability, reducing power and acidity. We find, that PHPA forms monolayer films on differently terminated ZnO samples from immersion. Besides, the thermal stability of molecular films resembles the film stability obtained for PPA, though with slightly different TD signatures. Owing to the dissociative desorption character the mass signal $m/z = 77$ amu of the phenyl ring was monitored. Films were found to be stable up tp 500 K and start to desorb with further temperature increase (cf. Fig. 6.5 (a-c)).

TD-spectra contain rather broad resonances. The desorption maximum for PHPA on ZnO-O and ZnO-M was found at around ξ_1=615 K and on ZnO-Zn at ξ_1=690 K. This variation is ascribed to different binding modes. However, unlike PPA, the formation of the tridentate is not possible for HPA. The available pathways for the HPA attachment on oxidic surfaces can be monodentate through P-OH or P=O bonds, bidentate or chelating bidentate, though the chelating mode is considered to be inconceivable (cf. Fig. 6.6). Clearly, the precise determination of two experimentally obtained binding modes for these systems demands additional verification like infrared spectroscopy (IRs) and additional DFT calculations. Despite the fact that the theoretical approach can be challenging due to a possible surface reconstruction during the SAM formation which has to be considered, the PHPA monolayers on single crystalline ZnO surfaces can be good "bench mark" systems for revealing the molecular attachment. The comparative analysis of PPA and PHPA adsorbed on well-defined single crystalline ZnO samples is allowed by the HPA limitation of the tridentate.
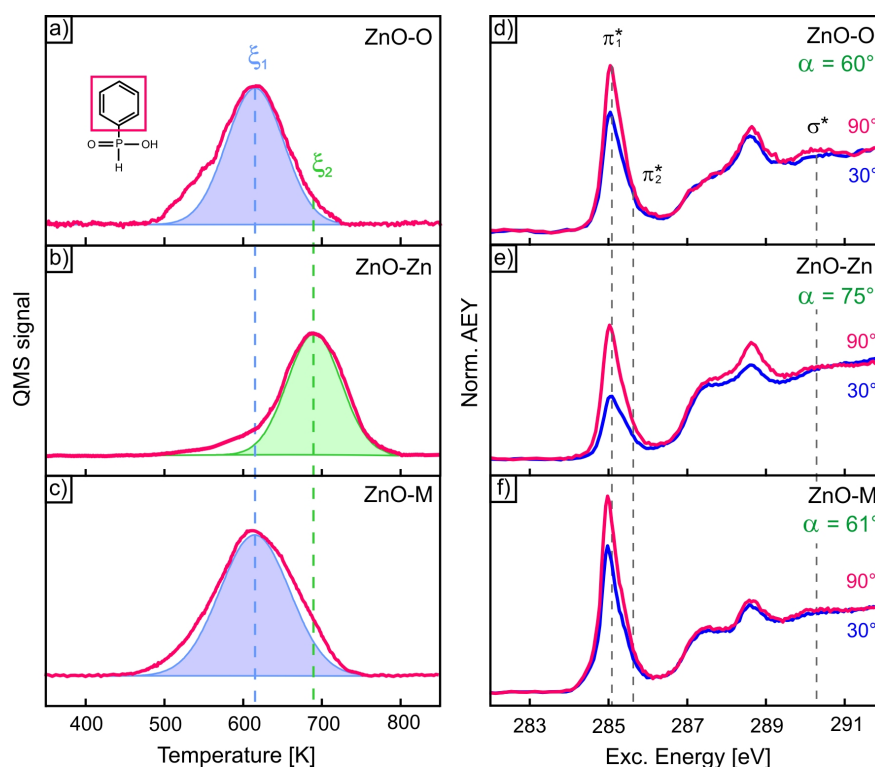
Figure 6.5: (a-c) A series of TD-spectra and (d-e) a series of NEXAFS spectra for the PHPA on single crystalline ZnO of different surface orientations: ZnO-O, ZnO-Zn and ZnO-M (from top to the bottom).

The measured NEXAFS spectra were recorded in order to reveal the information about the molecular orientation of PHPA films. NEXAFS signatures are identical to those obtained for PPA and exhibit π^* resonances of the C=C(H) and the C=C(P) bonds, broad σ^* features
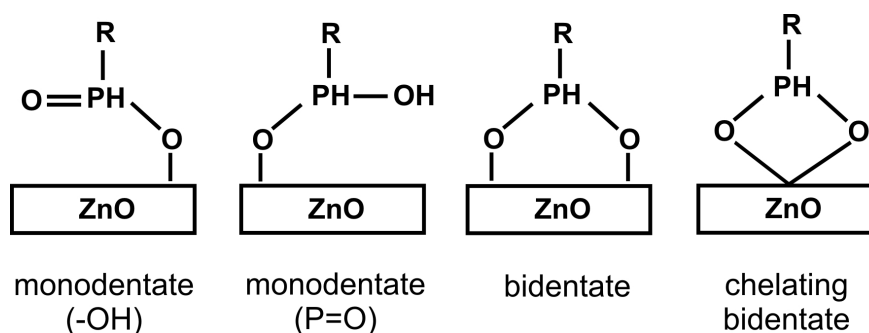
Figure 6.6: Available binding modes for molecules with phosphinic anchoring group.

and their overlap (cf. Fig. 6.5 (d-e)). From explicit dichroism of π_1^* resonances we deduce a pronounced orientational order for these SAMs. Best fit yields an orientation of the phenyl ring as $\alpha = 60° \pm 4°$, $\alpha = 75° \pm 4°$ and $\alpha = 61° \pm 4°$ for films on ZnO-O , ZnO-Zn and ZnO-M respectively. The inclination to smaller angle values is related to different binding models and consistent with the tendency for molecules bound by bidentate to obtain less upright orientation than molecules attached by tridentate .[297,352,201]
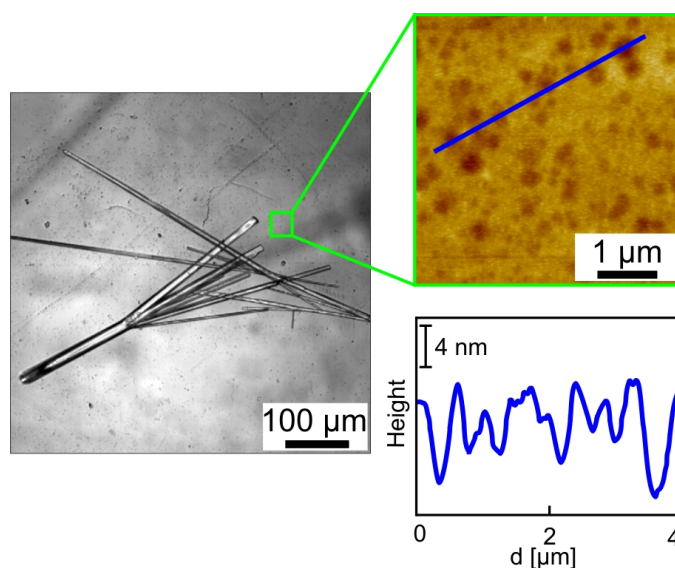
Figure 6.7: Optical micrographs of grown ZnPHP surface precipitation on ZnO-O with an AFM micrograph of the remaining ZnO surface with corresponding line scan.

Apart from the high thermal stability and pronounces molecular orientation the chief asset of PHPA is the reduced etching damage of ZnO, which was observed in this work for ZnO-O crystal systems immersed in (absolute) ethanolic PHPA solution. In contrast to the thermally more stable triprotic phosphoric acid, phosphonic and phosphinic acid are both
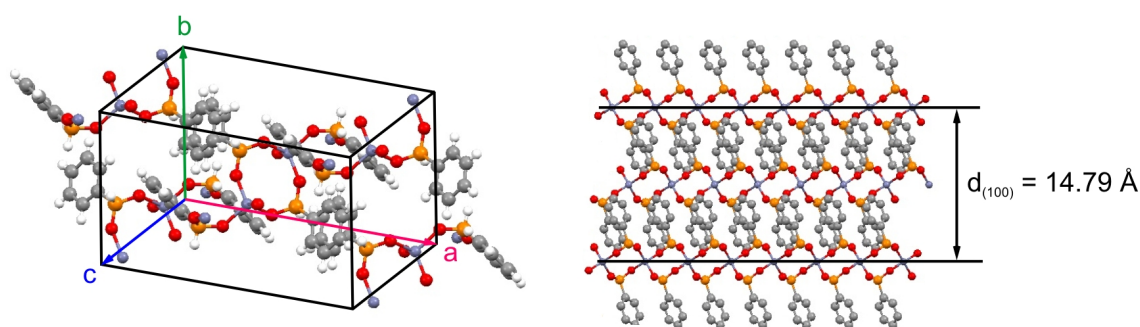
Figure 6.8: Unit cell and crystal structure of ZnPHP.[424]

Table 6.1: Unit cell parameter derived from a single crystal XRD analysis of isolated precipitations and literature data of zinc-phenylphosphinate (ZnPHP) single crystal.[424]

Unit cell parameters	Precipitations	ZnPHP single crystal
a	15.56 Å	15.61 Å
b	10.96 Å	10.95 Å
c	8.21 Å	8.23 Å
$\alpha/\beta/\gamma$	90°/108.96°/90°	90°/108.62°/90°
Crystal system	monoclinic	monoclinic
Space group	C2/c	C2/c
Z	4	4
Cell volume	1332 Å^3	1332 Å^3

diprotic compounds. While the acidity for the first deprotonation step is very similar for both acids (with a pKs value of 2.0), phosphinic acid is particular in that is shows roughly the same acidity for the second deprotonation with $pK_s = 2.2$, thus favoring the cleavage of a P-H bond, whereas for phosphonic acid the pKs value for the second deprotonation increases to 6.6.[422] Organic derivatives of phosphinic acid are formed by replacing one, two, or all three H atoms with organic groups (alkyl, aryl), with the H atoms bonded directly to the P atom being replaced first. The properties of the organo-phosphinic acids develop similarly as those of the inorganic free acid.

Indeed, even after one week treatment formation of only few but extended crystalline needles was detected (cf. Fig. 6.7). Precipitations consist of well separated individual large crystalline needles in contrast to ZnPP and ZnTFPP complexes, which form densely packed

layers of star-shaped crystalline structures. Apparently the etching of ZnO in PHPA solution proceeds to a less degree. Corresponding AFM data reveal also some etch pits on the ZnO-O surface at regions between the formed crystalline needles. However, the depth of these etching pits and the overall degree of surface degradation is much lower than after immersing ZnO in PPA solution for the same time. This can be also attributed to slow recrystallization from water for HPA.[423] Based on a single crystal XRD-analysis this precipitations are identified as zinc-phenylphosphinate (ZnPHP). The analysis yielded a monoclinic crystal structure of ZnPHPP and unit cell parameters which are in close agreement with those reported previously in the literature (cf. Tab. 6.1).[424] The zinc-phenylphosphinate compound also exhibits a layered structure but reveals a different crystal structure represented in the Figure 6.8. The interlayer spacing $d_{(100)}$ gives the surface steps height of $d_{(100)}/2$=7.4 Å.

6.4   Benzoic acid (BA) and Thiophenol (TP)

In this section a comparison is given between carboxylic acid and thiole anchoring and attachment of phosphonic acid to ZnO. BA and TP compounds have been chosen, since they have a structure similar to PPA and contain the phenyl ring as the backbone. Films have been prepared by immersion for 24 hours on ZnO-O substrates from a 0.1 mM ethanolic solutions. First their thermal stability was analyzed by means of TDS. Figure 6.9 illustrates TD-spectra for the studied systems. BT desorption has been monitored at different mass signals, though the most intence was recordered for the signal at the m/z=45 amu, which corresponds to CHO_2 or C_2H_5O molecular fragments (cf. Fig. 6.9, (a), blue curve). The next most intense signal though relatively weak compared to the first one corresponds to the C_4H_3 fraction of the aromatic ring (m/z=51 amu) (cf. Fig. 6.9 (a), violet curve). Even though the C_4H_3 fraction represents approximately 35% of all detected BA fragments in the mass spectra for the pure compound[414] its small intensity is surprising. It is attributed to phenyl ring decomposition during the ionization in the QMS and different propapility for detection of mass signals. In addition, another fragment of the phenyl ring decomposition is C_3H_8 and obtains the mass to change ration of 44 amu. Since it is difficult to separate this mass from the signal recorded for 45 amu signal mass because of protonation reactions during the ionization its contribution can be included in the blue curve. For the TP the mass signal of the sulfur (m/z=32 amu, orange curve) and the C_4H_3 fragment supplement the TD-spectra (cf. Fig. 6.9 (b)). Both molecules are less stable than PPA and fully desorb from the ZnO-O surface till 600 K, which is consistent with previous results.[350,417,419] This accentuates prior affinity of PAs towards metal oxides. Recorded signals of anchoring unit fragments point to intact

desorption for both films. However, simultaneous detection of signals representing backbone and anchoring unit for BA can be possible if molecules desorb dissociatively and decompose in the QMS. TP first loses the aromatic ring around ζ=415 K and following that sulfur atoms start to desorb from the ZnO surface giving the rise to the desorption peak with the maximum at $\sim$425 K. In contrast to TP, where only one bonding mode is available BA spectra exhibit two desorption channels at τ_1=490 K and τ_2=540 K. These peaks are attributed to different absorption modes, which are presumably monodentate coordination for the first signature peak and the bidentate for the second peak.
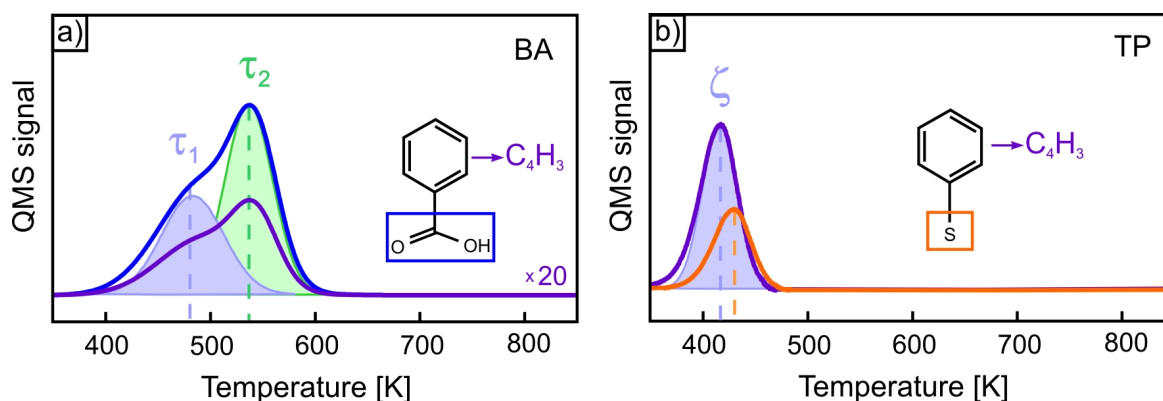
Figure 6.9: Desorption spectra of (a) BA and (b) TP monolayers on ZnO-O samples monitored for the mass signal of C_4H3 molecular fragments (blue curves) for both molecules, CHO_2 fragment for BA (blue curve) and sulfur for TP (orange curve).

The BA and TP structural arrangement on the surface of ZnO generally resembles the resulting film quality and stability. To elucidate the orientational order NEXAFS measurements in PEY mode were carried out for monolayer films. NEXAFS curves are represented in Figure 6.10 (a-d) and dominated by spectral features, which are typical for molecules containing unsaturated functional groups such as phenyl rings. Similar to PPA spectra the prominent resonance at 285 eV represents the $1s \rightarrow \pi^*$ transition and is characteristic for the aromatic C=C carbon bonds. Transitions driven by atoms bound to aromatic carbons though the electron-withdrawing, like sulfur or the phenolic group, contribute to π_2^* shoulder peaks. Broad features beyond 290 eV represent excitations into σ^* orbitals. Due to overlap of π^* C-C electronic transitions and such C-H σ^* multi-electron excitations peak at $\sim$288.7 eV show a sharp rise. The absorption band of characteristic for carboxyl carbon group C=O transition also exhibits additional structure near 288.6 eV and therefore can not be directly divided from other resonances. This also makes the determination of BA binding mode from NEXAFS spectra, in particular, the detection of free C=O anchoring sites for the monodentate attachment via -OH group not reliable. In addition to these pronounced absorption bands,
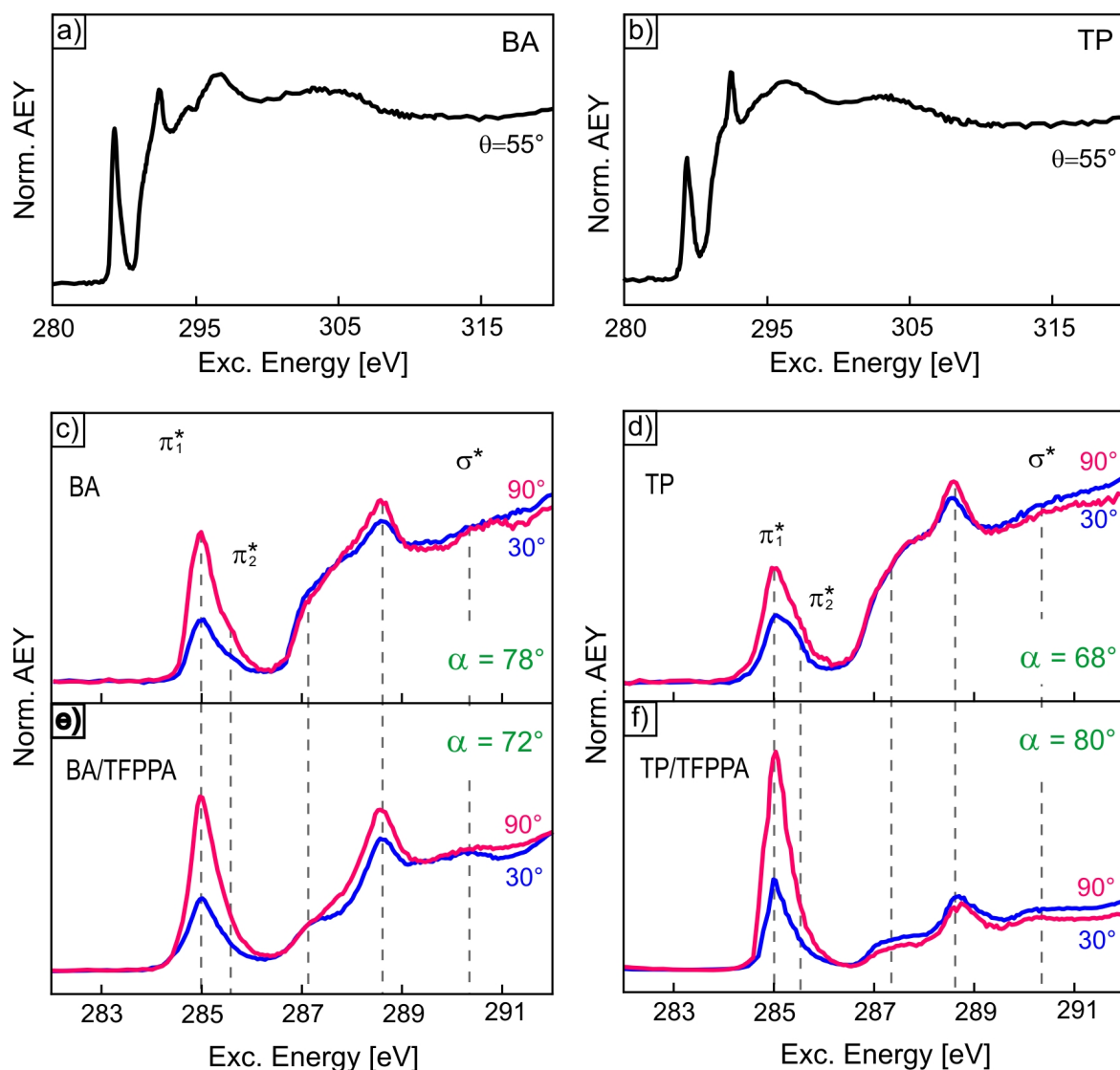
Figure 6.10: A series of full NEXAFS spectra of (a) BA monolayer on ZnO-O prepared by immersion and (b) TP recordered at an incident angle of 55°. Panels (c) and (d) represent angular dependency of the magnified π^* region of BA and TP respectively. Resulting spectra after the SAMs exchange reactions for BA and TP by TFPPA are given in panels (e) and (f).

several more spectral features and their overlap can be observed in C 1s NEXAFS spectra. The detected signals are in a good agreement with NEXAFS spectra reported in the literature for CA and thiols.[425–429]

The pronounced anisotropy of low-energetic π^* resonances for both systems point to the molecular assembly with the preferential orientational order. Aromatic rings of BA and TP were found to be tilted relative to the surface plane at $\alpha = 78° \pm 5°$ and $\alpha = 68° \pm 4°$ angles

respectively. Since obtaining orientational order by SAMs does not represent the lateral packing arrangement a correspondence between film characteristics and film quality without additional experiments can not be concluded. Similar to DPS the stability of the chemical bonding between the molecule and the substrate can be tested by the exchange reaction. Reduced packing in molecular attachment by active anchoring groups as well as at the upper top layer of head groups is expected to have the subsequent effect of reducing the overall SAM quality and depletion towards the exchange reaction. For the exchange experiments single-component BA and TP SAMs were prepared by immersion discussed earlier in this work and subsequently re-immersed in TFPPA solution for 6 hours. Assuming that the exchange process does not result in chemical reaction between components the relative changes in spectral characteristics can be monitored. Except the increasing intensity of the π^* resonant states NEXAFS spectra do not provide enough evidence for the molecular substitution by reason of similarity in spectral signatures for BA and TP and PPA (cf. Fig. 6.10 (e,f)).

In order to evaluate changes in the film composition XPS has been applied. Partial TFPPA fluorination gives a distinct signature in XPS spectra and provides direct test for the molecular exchange. Figure 6.11 and figure 6.12 exhibit XP spectra for different regions, like F$1s$, O$1s$, C$1s$, Zn$3s$ and P$2p$ for BA and S$2p$ additional for TP. The photon beam at the energy of 730 eV was directly pointed toward a sample in the experiment. To obtain more intensity S$2p$, Zn$3s$ and P$2p$ regions were measured additionally by the photon flux with 350 eV energy. All spectra were energy calibrated to the surface Zn$3s$ peak and their position was verified with previously reported energies in the literature.[297,294,352] First original BA and TP films were measured (green curves). Changes in the organization of the endgroups of SAMs have been indicated by appearance of distinct phosphorous and fluorine peaks found after the exchange reaction (blue curves). This indicates that SAMs consisting of carboxylic acid molecules can be partially or fully substituted by phosphonic acid molecules on account of higher reactivity and affinity of PAs. T. Lenz *et al.* also finds, that PA anchor groups tend to substitute carboxylic acid molecules on aluminum oxide surfaces and thus allow the formation of mixed or fully exchanged monolayers.[430] Moreover, recent DFT calculations in the group of T. Clark for the system of acetic acid and phosphonic acid on AlO$_x$ yield that exchange of carboxylates with phosphonates is thermodynamically possible.[431]

6.5   Conclusions

With these findings, we conclude that suitable molecules with PA anchoring groups tend to self-assemble on ZnO-O surfaces. The backbone substitution and the modification of PA
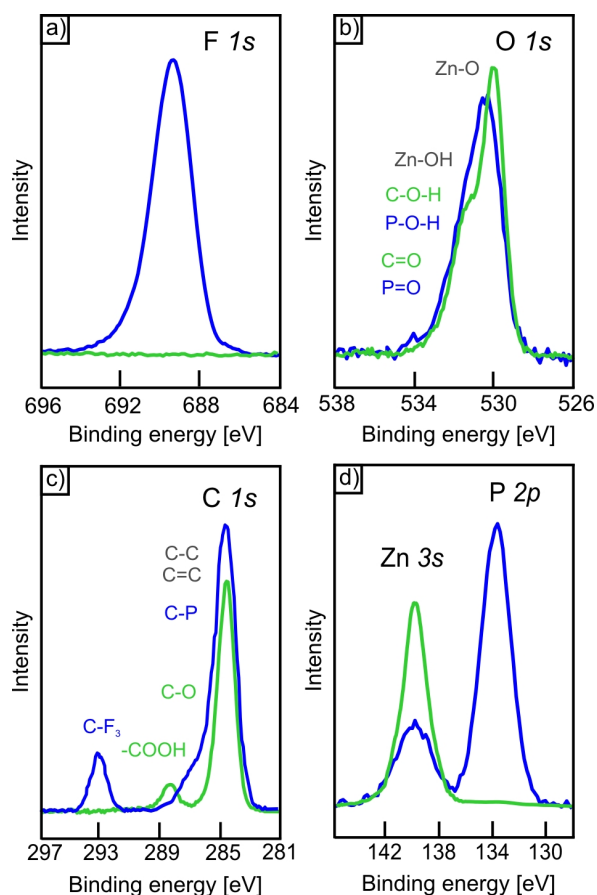
Figure 6.11: XPS spectra of different regions for BA on ZnO-O before (green curve) and after (red curve) exchange reaction by TFPPA for the following regions: (a) F*1s*, (b) O1*1s*, (c) C*1s*, (d) Zn*3s* and (e) P*2p*. Characteristic contributions to XPS peaks from different materials are marked by different colors: ZnO substrate - gray, BA - green and TFPPA - blue.

group to HPA leads to no significant changes in the resulting film structure and stability compared to PPA. However, SAMs with aromatic backbones tent to form more densely packed films than aliphatic. Analogous to PPA two molecular coordinations have been found for TFPPA and DPA. SAMs based on molecules with different structures show variations in binding modes, with preferential bitentate in case of partial fluorination and preferential tridentate for molecules with alkyl-chains. Apart from general correspondence of PHPA to PPA the precise determination of binding mechanism for phosphinic acid on oxidic surfaces demands additional experimental and theoretical verification making PHPA on single crystalline ZnO a good model system for the understanding of PA binding mechanisms. According to the results of the exchange reaction, the package density and stability of CA and thiols is much lower than for PA. This indicates the superior binding strength of PA on metal oxides compared to other linkers. Besides, surface etching was investigated for
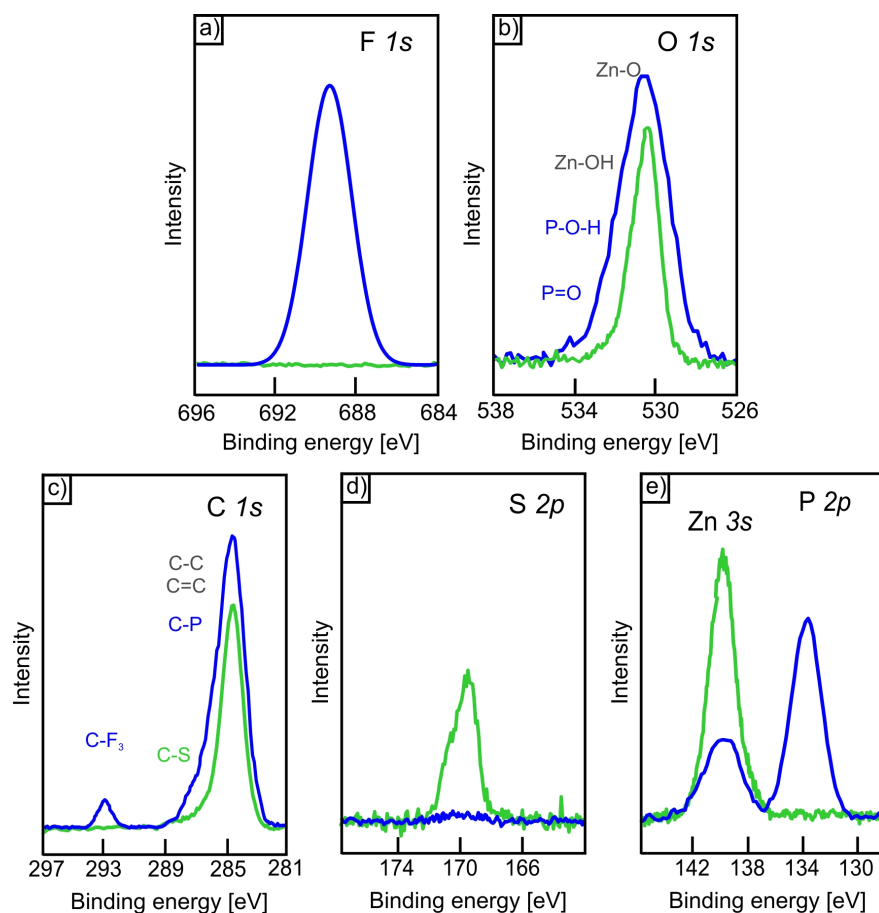
Figure 6.12: XPS spectra of different regions for TP on ZnO-O before (green curve) and after (red curve) exchange reaction by TFPPA for the following regions: (a)F*1s*, (b) O1*1s*,(c) C*1s*, (d) S*2p*, (e) Zn*3s* and (f) P*2p*. Characteristic contributions to XPS peaks from different materials are marked by different colors: ZnO substrate - gray, TP - green and TFPPA - blue.

different molecular systems and observed for PA molecules with different backbone while a reduced etching efficiency was found for SAMs with phosphinic acid anchoring units.

CHAPTER 7

Formation of Phenylphosphonic acid SAMs on rutile TiO$_2$: Structure and Stability

7.1 Introduction

When modified with covalently attached functional organic molecules TiO$_2$ plays an important role as an electron transfer layer in hybrid devices and finds wide application in photovoltaic and photocatalytic systems.[46,108,437–439]. In dye-sensitized solar cells titania surfaces are coated with various dyes which are mainly conjugated organic molecules like phthalocyanines with substitutes, allowing covalent attachment of a dye.[440–445] In order to achive such dye fixations, reactive anchoring units which enable self-assembly are used. For the improvement of the device performance the choice of anchoring units which serve as an electron bridge is important.[446,447] The most commonly used CA retrieves good electronic coupling with the Ti$3d$ conduction band orbital mainfold, thought CA-modified dyes demonstrate poor solubility in common organic solvents and low stability.[448–452] In contrast, PA binds more strongly to TiO$_2$ indicating its high affinity toward metal oxide surfaces, therefore promises a good alternative to CA for the dye attachment.[452,165,453,454] Generally PA shows three binding modes, including mono-, bi- and tridentate which can be also realized on TiO$_2$. Even though several studies agree on the bidentate PA attachment to be the most energetically favorable for rutile and anatase surfaces, some studies claim the monodentate binding mode as the predominant.[455–458] In addition, conflicting data about the formation of remaining two modes on anatase are given in the literature.[459] Luschtinetz *et. al* demonstrated from DFT calculations that PA attachment on anatase and rutile proceeds mainly through bidentate and monodentate with a strong tendency of monodentate adsorption geometry relaxing toward the bidentate configuration.[455] However, some experiments demonstrate in

addition to the bidentate mode simultaneous formation of the dominant monodentate mode for aliphatic and the tridentate mode for aromatic SAMs.[455,460–462] Information about PA anchoring to rutie TiO$_2$ is still lacking also due to its insulating character. Besides, not much is known about the thermal stability of such attachment. Aliphatic PAs start to decompose at temperatures above 650 K from amorphous titania surfaces.[463] Lower stability was found for poly(vinylphosphonic acid) on TiO$_2$ nanoparticles functionalized with was stable only up to 470 K.[464]

To clarify addressed issues well-defined model systems are required. The current study is focused on the adsorption of PAs on single crystalline rutile TiO$_2$(1 1 0). However, a detailed analysis of such systems is hampered by TiO$_2$ charging which makes the application of electron based analytical techniques such as XPS, NEXAFS or LEED troublesome. To overcome this problem doped crystals can be used. Advantages of using such doped samples and its limitations are demonstrated and discussed in this chapter as well.

7.2   Stability of PPA monolayers on TiO$_2$

Information about thermal stability of PPA films on (1 1 0) rutile TiO$_2$ surfaces was obtained from TDS measurements. First PPA monolayer films were deposited onto metal oxide surfaces by immersion (0.1 mM PPA ethanolic solution for 24 h. at 75°). As one can see from the desorption spectrum a signal of the phenyl mass fragment in Figure 7.1 PPA desorbs dissociatively after the cleavage of the C-P bond. Two features have been identified and visualized with a peak τ_1 and a peak τ_2 at temperatures around 670 and 720 K respectively. Since the tridentate PPA attachment was found to be less stable than the bidentate the most intense peak around 670 K can be attributed to the bidentate mode. However, this assignment is rather tentative and requires additional experimental verification. Therefore, in the following discussion these biding modes will be denoted as the binding mode 1 (for τ_1 peak) and the mode 2 (for τ_2). PPA films can be also prepared by OMBD according to the previously established for the PPA/ZnO system procedure. PPA multilayer films of the approximate thickness of 5 nm were evaporated from a Knudsen cell onto before cleaned bare TiO$_2$ surfaces. A multilayer desorption was achieved by sample annealing at 550 K for 5 minutes and is indicated by a desorption peak τ_0 around 390 K (cf. Fig. 7.2 (a)). The recorded mass signal correspond to the C$_4$H$_3$ fragment of the molecule phenyl ring (m/z=51 amu) and was found to be the most intense. An additional peak τ_3 at ∼450 K represents desorption of weakly bound PPA. At higher temperatures remaining monolayer films also desorb through

two channels with peak maxima at 685 K and 715 K, hence indicating similar stability to films prepared from immersion.
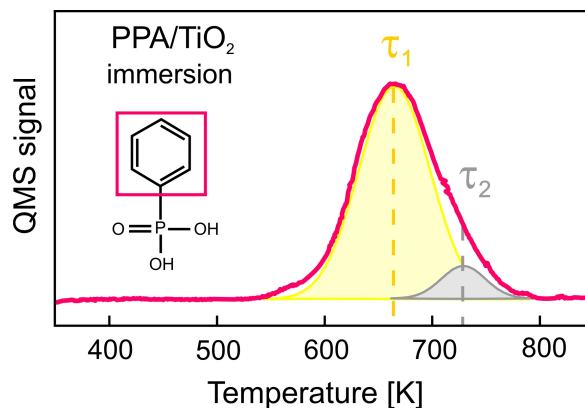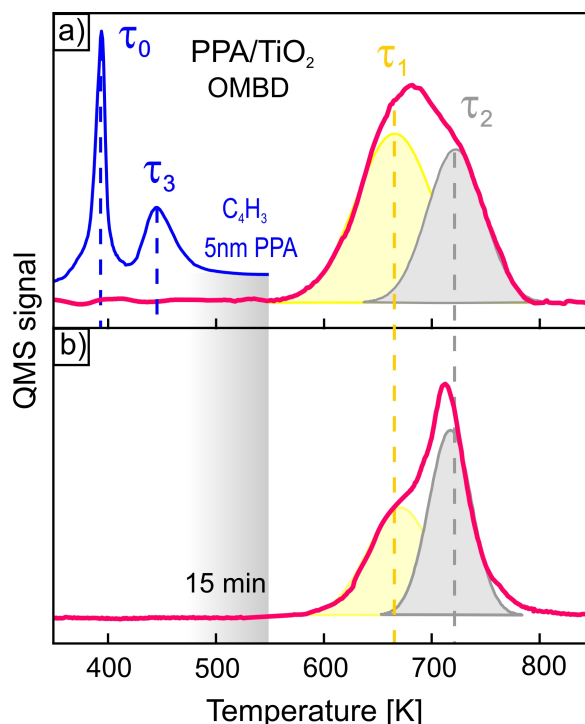

Figure 7.1: TD-spectra for PPA on TiO$_2$ prepared by immersion and recorded for the mass signal of the phenyl ring. Fits indicate two different desorption channels: mode 1 (yellow) and mode 2 (gray).

Obtained temperatures for both systems are in a good agreement with corresponding PPA stabilies on ZnO, thought their origin regarding different binding modes can contrast. The quantitative analysis reveal the differences in relative intensities of two desorption channels for immersion and OMBD and yields mode 1 to mode 2 ratios of 2.6 and 1.2 respectively. More prone formation of the first mode from immersion can be explained by more favorable formation conditions of the most stable phase, like time for molecular rearrangement and external thermal energy. Moreover, this effect can be attributed to the presence of hydroxy species in the solution as it was found in case of PPA on ZnO.

In regard to controlling the relative fraction of a less stable binding mode to a more stable mode by choosing annealing time, supplementary experiments have been performed. In Figure 7.2 (b) a TD-spectrum for PPA SAM prepared by OMBD and heated at 550 K for 10 min is shown. Though similar thermal stability for the monolayer is obtained, intensity of the first mode slightly decreases giving a peak ratio τ_1/τ_2 as 0.6. This provides a way to tune a relative number of a specific binding mode.

7.3 Surface charging of TiO$_2$. Nb-doped TiO$_2$

Further investigations of molecular order and orientation by spectroscopic methods, like XPS, NEXAFS or LEED are largely hindered by the poor conductivity of TiO$_2$. When an X-ray beam penetrates an insulating sample and activate the loss of photo-emitted electrons, charge

Figure 7.2: TD-spectra for PPA on TiO_2 prepared by OMBD and subsequent multilayer desorption. Blue curve in (a) shows 5 nm PPA multilayer desorption reordered for a molecular ion signal for C_4H_3 (m/z=51 amu) molecule fragment. A distinct multilayer peak (τ_0) and an additional signal (τ_3) from weakly bounded molecules. Red curves are given for the phenyl ring signal for samples which have been heated at 550 K for (a) 5 min and (b) 15 min to remove excess multilayers also causing partial depopulation of state τ_1. Fits indicate two different desorption channels for τ_1 (yellow) and τ_2 (gray).

depletion or excess sample areas can be created leading to nonhomogeneous surface charging. For example in XPS measurements formed surface charge can easily shift photoelectron energy peaks by several tens of eV. This energy shift typically has a nonuniform character in time and on a sample surface as one can see in Figure 7.3 (a). XP spectra are presented "*as measured*" without additional energy calibration. The blue and light blue spectra were measured on the same TiO_2 sample with a time difference of 10 minutes. The position of Ti2p peaks retrieved from Ti^{4+} electron configuration in a fully oxidized sample lies at 459.3 eV and 465.1 eV for Ti2$p_{3/2}$ and Ti2$p_{1/2}$ respectively.[465] An oxygen O1s peak, representing O^{2-} valence states in TiO_2 has a binding energy of 540.4 eV. Carbon surface contaminations are indicated by a C1s peak at around 284.8 eV.[466] These spectral peaks are either absent (blue curve) or shifted (light blue curve). It is belied, that the formation of Ti^{3+} species, so-called "Ti^{3+} *centers*" is responsible for conducting behavior of titania.[467,468] Their formation can be induced by a chemical reduction or an introduction of donor species

into the oxide bulk. As it was briefly discussed earlier in this work the conductivity of titanium dioxide can be transformed to *n*-type by annealing in reducing environments or by shallow donor impurities (e.g., Nb, F, and H).[119,126,125,108] The p-type conducting properties can be achieved by incorporating Cr doping into the TiO$_2$ bulk. Black curve in Figure 7.3 (a) represents a XP-spectra for oxygen-depleted crystal, where all spectral lines correspond to their initial position on the energy axis. Note, that different photon energy chosen for the black curve *hv*=650 eV instead of *hv*=600 eV excitation energy for remaining measurements results only in the Auger peak position shift. Unfortunately, Cr doping does not improve spectral characteristics of TiO$_2$ and exhibit time dependent surface charging (cf. Fig. 7.3 (b)). As opposed to p-type doping, Nb doping improves oxide conductivity, which allows further spectroscopic analysis.

Based on these findings TiO$_2$ 0.25%wt. Nb-doped (denoted as TiO$_2$:Nb) samples obtained from SurfaceNet GmbH have been used for the study. Since the ionic radius of Nb^{5+} equals 0.64 Å and very close to that of Ti^{4+} which is 0.61 Å, Nb substitute Ti atoms in the bulk (cf. Appendix 1).[469] However, an attempt to continue investigations ran into difficulties related to universality of utilizing Nb-doped samples. When applying the typical substrate preparation consisting of repeated cycles of Ar$^+$ ion sputtering and sample annealing in the oxygen atmosphere up to 1000 K for 1 hour the formation of distinct surface defects demonstrated on the optical image (a) in Figure 7.4 was found. Surfaces of TiO$_2$:Nb samples were fully or locally covered by multiple furrows distributed along directions, which lie within 55-65° (+/- 180°) relative to the $\langle 001 \rangle$ direction as it is schematically illustrated in panel (b). The morphology of damaged samples was analyzed in more details using AFM. From 3D AFM surface profile in Figure 7.4 (c) one can see increased roughness of annealed samples indicating formation of narrow elevations.

Apparently, similar though much smaller in size elevations were found directly on new TiO$_2$:Nb samples which have not been utilized in any experiments yet (cf. Fig 7.4 (a)). This finding provides some evidence for a metastable character of (110) rutile surface in doped titania crystals. Defect structures grew after one preparation cycle and sharp elevations about 4 nm in height were obtained (cf. Fig. 7.5 (b)). Repeated cycles of sputtering and extend annealing in the oxygen result in even more increased roughness as represented in panel (c). A sample surface prepared once and left in ambient for 3 months is somewhat smoother and shows formation of potholes about 35 nm in height (cf. Fig. 7.5 (d)). Some samples exhibit formation of ~10 nm high surface clusters visualized in Figure 7.6 (a-c) by SEM and AFM. One can note that relatively large clusters form at surface step edges. Besides large pothols and clusters some surface areas exhibit formations of rows (cf. Fig. 7.6 (d-f)). Surface stoichiometry has been further analyzed by LEED method. Reduced sharpness of
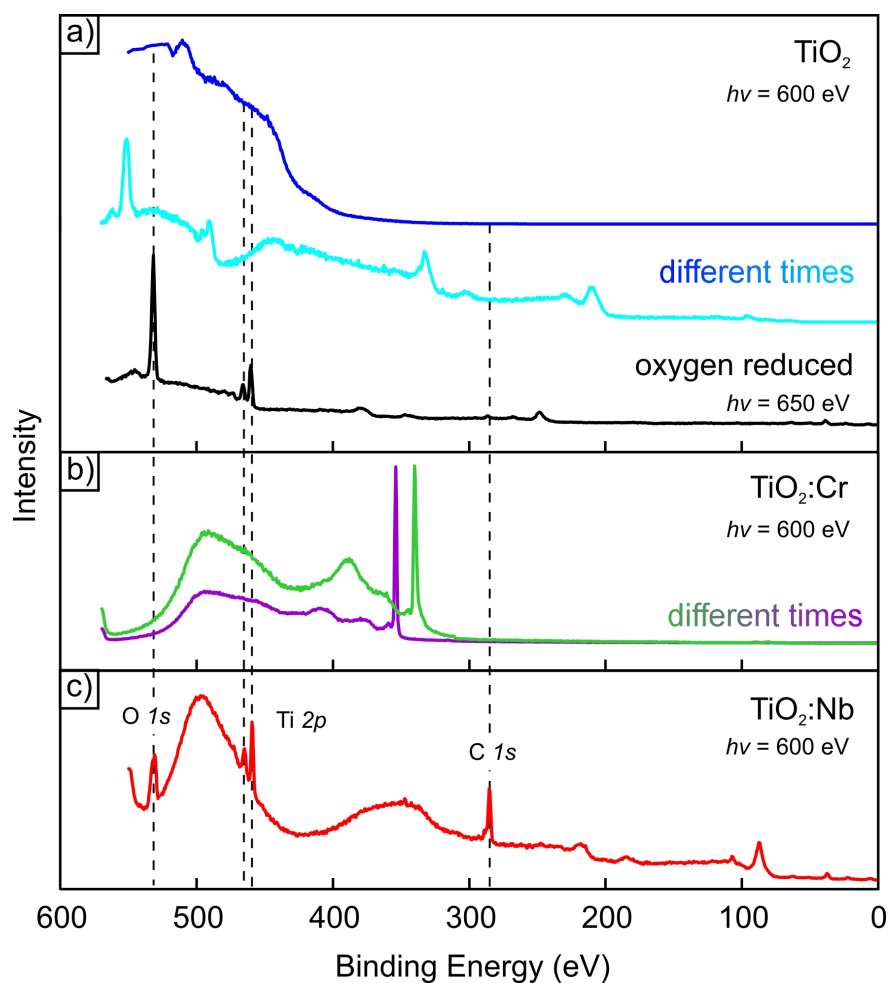
Figure 7.3: XP-spectra for (a) TiO$_2$ recorded at different times (t=0 - blue curve and t=10 min - light blue curve) and oxygen-depleted TiO$_2$ after repeated cycles of Ar$^+$ sputtering and extensive annealing (black curve). Sample charging is indicated by shifted peaks. Panel (b) illustrates charging effect for Cr-doped TiO$_2$ recordered at different times (t=0 - green and t=10 min - violet curve). (b) Nb-doped samples show good conductivity and an accurate peak position in the XPS signature.

LEED reflexes on diffraction patterns for the Nb-doped oxide compared to pure TiO$_2$ yields slightly reduced surface crystallinity (cf. Fig. 7.7). However, no additional to pure TiO$_2$ reflexes on the diffractogram were identified.

Several possible mechanisms which could lead to the formation of such line-shaped pattern on the surface of oxide can be derived from the literature. Listed below effects are partially illustrated in Appendix 2. Depending on temperature, oxygen pressure, type of a doping and its concentration following processes are proposed:
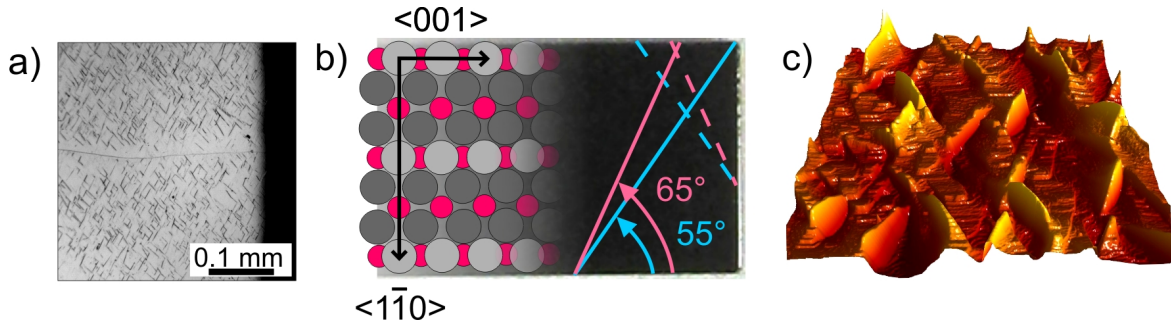
Figure 7.4: (a) Optical micrograph of surface defects formed on Nb-doped rutil TiO$_2$(110) samples after annealing in oxygen and (b) a schematic illustration of their distribution relative to crystallographic directions. (c) 3D AFM image of a damaged surface.
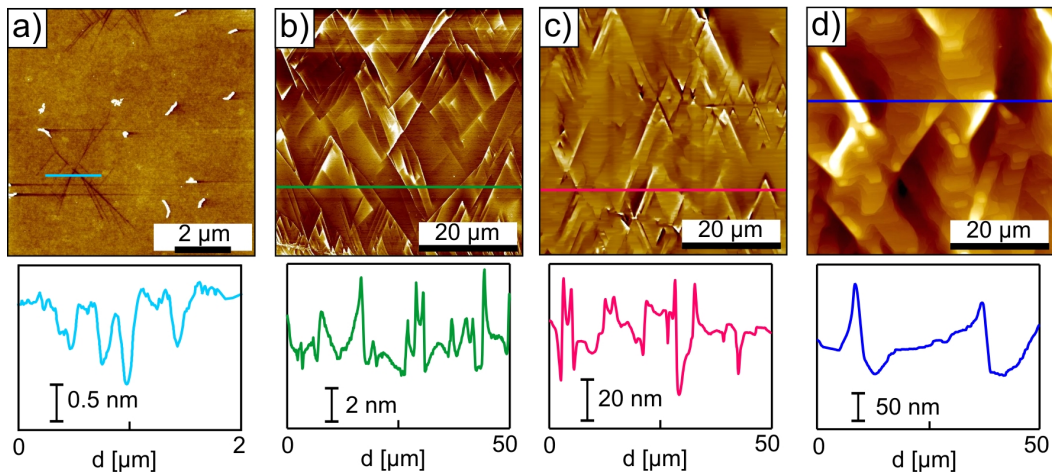
Figure 7.5: A series of AFM micrographs for (a) a new "*as obtained*" TiO$_2$:Nb sample, (b) a surface obtained after 1 preparation cycle, (c) a surface obtained after 5 preparation cycles, (c) a surface obtained after several preparation cycles and contact to ambient for 3 months with corresponding line profiles.

- Thermally induced phase separation and formation of titanium alloys, which can show Ti microsctuctures in compact hexagonal crystal structure (α), body-centered cubic (β) and mixed phase ($\alpha + \beta$).[470–472]

- Ti and O self-diffusion in the bulk leading to a surface reconstruction during annealing.[473–479]

- Phase transitions from rutile to anatase induced by doping and annealing.[480,481]

- Segregation of bulk impurities including a doping material at domain boundaries and a sample surface.[481–487] However, some studies find no evidences of doping segregation on the surface.[478,488,489]
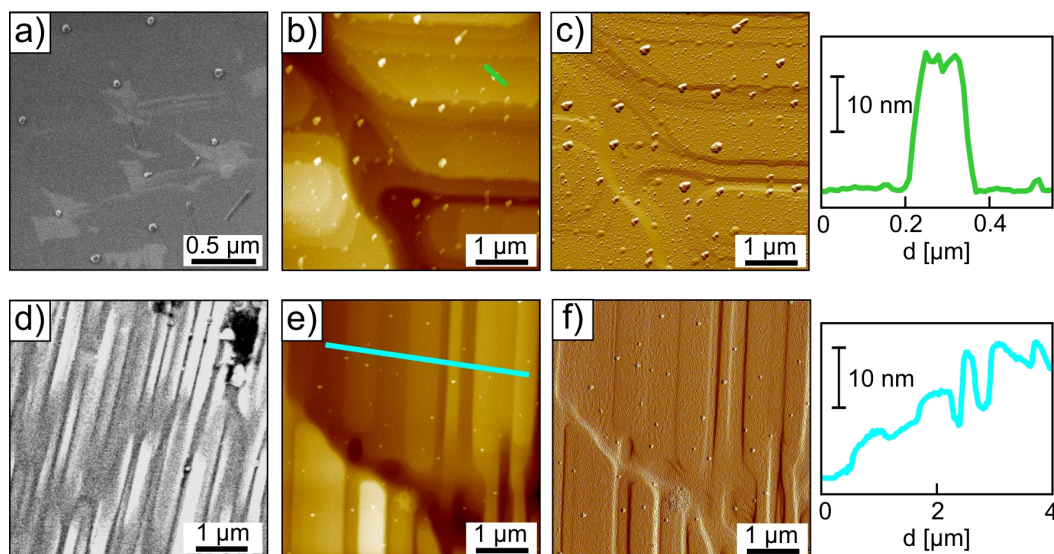
Figure 7.6: (a),(d) SEM and AFM (b),(e) amplitude and (c),(f) phase micrographs of formed surface clusters and rows respectively. In addition, corresponding line profiles are given. Note, that AFM micrographs (a) and (c) recorded with a double-tip. SEM micrograph (d) is provided by Katharina Gries (Uni Marburg).
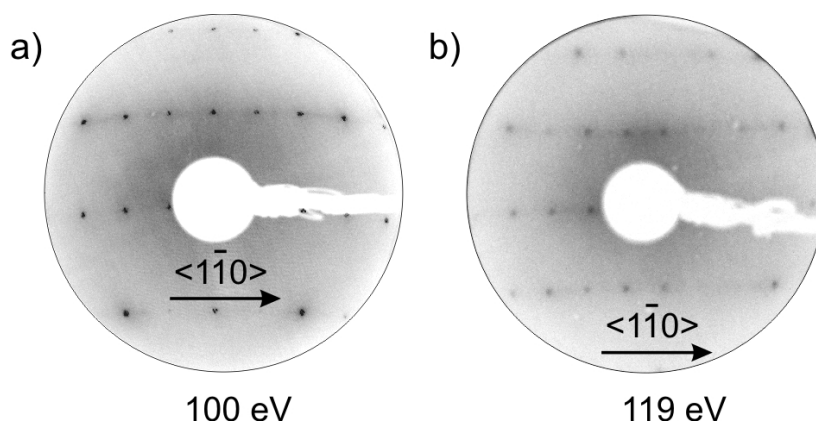
Figure 7.7: LEED diffractograms for (a) pure Tio$_2$ (100 eV) and Nb-doped TiO$_2$ (119 eV) after similar preparation, which includes one sputtering/annealing cycle.

In addition, a combination of several processes can be a reason for the observed surface transformation.

In order to understand mechanisms leading to the surface transformation and critical parameters during the sample preparation supplementary expertise is necessary. So far, a distinct proof of Nb excess on the surface, which could corresponds to the line-shaped pattern, by means of EDX, XPS or XRD was not successful (cf. Appendix 3).

7.4 PPA monolayers on Nb-doped TiO$_2$

It is important to check whether surface defects found on Nb-doped TiO$_2$ crystals are reflected in the PPA film stability. In order to analyze that test TDS measurements have been carried out. Ar$^+$ sputtered and annealed in oxygen TiO$_2$:Nb samples which show small density of surface defects were selected. This means that only a part of a sample surface was covered with structures observed with a naked eye. One should note that the remaining sample area could still exhibit microscopic defects. Apparently, Nb doping and its possible segregation at
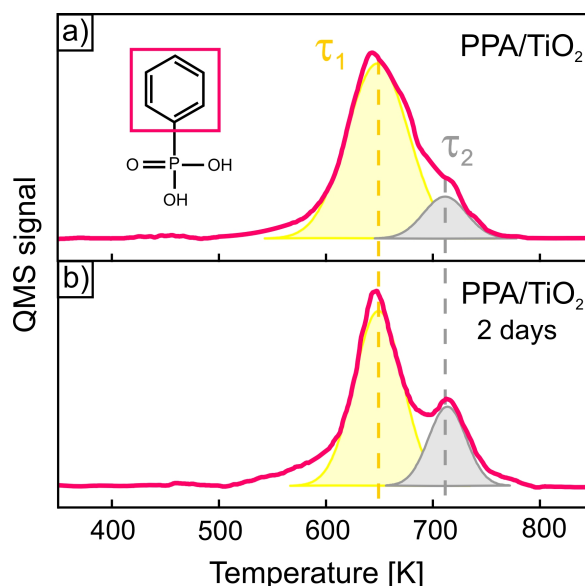
Figure 7.8: TD-spectra for PPA on damaged TiO$_2$:Nb $(1\,1\,0)$ surfaces prepared by immersing samples for (a) 1 day and (b) 2 days. Fits indicate two different desorption channels: mode 1 (yellow) and mode 2 (gray).

the surface of TiO$_2$ does not significantly influence PPA SAMs thermal stability. Equivalent to previously found desorption modes at $\tau_1 \approx 650\,\text{K}$ and $\tau 2 \approx 710\,\text{K}$ were identified (cf. Fig. 7.8 (a)). First desorption mode was also found to be more favorable and the relative ratio τ_1/τ_2 was obtained as 2.4. After longer immersion time of 2 days in similar PPA solution, which is allowed by advanced stability of TiO$_2$ upon dissolution in acidic conditions, somewhat different ratio of 2.9 was obtained (cf. Fig. 7.8 (b)). Increased intensity of the τ_2 peak and sharp TDS signatures indicate that PPA self-assembly on the TiO$_2$ surface is characterized by a rather slow kinetics, and extended time is needed to improve molecular reorganization.

7.5   Conclusions

The experiments presented above clearly demonstrate that monolayers of PA-based SAMs can be formed on rutile TiO$_2$(1 1 0) surface from immersion and OMBD. The analysis of PPA stability on titania enables to determine two biding modes with different binding strength toward substrate. In thermally induced monolayers an additional binding mode at lower temperatures was found. PA stability on TiO$_2$ is comparable to its stability on ZnO indicating good PA affinity towards metal oxides. Charging effect of TiO$_2$ samples due to their poor conducting properties was illustrated, and ways to its reduction were discussed and tested. Metal oxide doping with Nb improves its conductivity and allows spectroscopic investigation. However, metastable character of doped samples upon annealing results in formation of irreversible surface defects and hampers model studies. Several explanations are given, although additional analysis must be performed to reveal nature and formation mechanism of surface defects.

CHAPTER 8

Summary and Outlook

In this thesis a detailed investigation of self-assembling organic molecules covalently attached to metal oxide surfaces is presented. Although nowadays commercial inorganic materials still outperform organic materials, hybrid systems have the advantage of low cost device manufacturing with large area coverage even on flexible substrates. Since the resulting device performance is governed to a larger extent by interface layers, it is important to find a well matching material combination and analyze structure and stability of SAMs at such heterojunctions. A rather high affinity of PA anchoring compared with that expected from CA and thiol groups has been established on the basis of thermal stability analysis in the course of this work, which makes PA-based SAMs a promising candidate for tailoring interfacial properties of transparent conductive oxides or for selective attachment of organic dyes. Therefore, model systems of PA-based SAMs on single crystalline metal oxides (ZnO and TiO_2) were investigated in greater detail.

In the first place, the importance of PA-based SAMs preparation is highlighted. It was demonstrated that attachment of organic molecules with PA anchoring units on ZnO is not a self-terminating process like for the organothiols on gold substrates. The common preparation by immersion is accompanied by a chemical side reaction leading to severe surface degradation and formation of surface precipitations which have been identified as zinc-phosphonate. DFT analysis revealed that a monolayer formation is rather a metastable configuration while zinc-phosphonate is the energetically more stable configuration. An increased surface roughness and an excess of water content in the reaction were found to induce ZnO etching. Moreover, this structural transformation can be well explained even by a dry solid state reaction without any ion dissolution.

Giving consideration to these findings, an alternative SAM preparation based on OMBD by first depositing thin multilayer films and subsequently thermally desorbing the multilayer excess in order to obtain a monolayer film at the surface was implemented. The resulting monolayer films were investigated and their properties were compared to SAMs prepared by immersion. It was demonstrated that PPA thin films used for this study desorb dissociatively and exhibit two distinct desorption channels which were attributed to bi- and tridentate species. These experimental results were further supported by DFT calculations. Furthermore, UHV deposition enables in particular a comparison of PPA SAMs stability and structure on bare and intentionally roughened and hydroxylated ZnO surfaces, which was found to influence the relative abundance of two binding species. In addition, both preparation methods result in PPA films with preferential orientational order.

An interesting model system for more detailed investigation of PA anchoring on ZnO surfaces was found to be phenylphosphinic acid SAM. Such monolayer films exhibit similar thermal stability as in PA-based SAMs, though the tridentate formation is not allowed. Moreover, it was established that ZnO surface etching by PHPA is less efficient. Therefore, additional experiments and computational studies for HPA-based SAMs on metal oxides can reveal additional details in the binding mechanism for both systems.

PA attachment on TiO_2 was investigated as well. It was found that PA-based SAMs exhibit similar thermal stability as thin films on ZnO and can be prepared by immersion and by OMBD methods. However, the self-assembly process on TiO_2 is characterized by a rather slow kinetics and allows prolonged immersion times without formation of surface precipitations. Unfortunately, spectroscopical investigation by XPS or NEXAFS is challenging due to the poor conductivity of titania. There are essentially two approaches to overcome the sample charging problem, which are using oxygen reduced samples or samples with a doping. Oxygen depleting results in surface defects (oxygen vacancies) and is not suitable for model studies. Therefore, Nb-doped TiO_2 samples were utilized and were found to improve conducting properties. However, a surface reconstruction of Nb-doped titanium dioxide was observed after the sample annealing at sufficiently high temperatures. First morphological and structural studies concerning the identification of surface defects are obtained and presented in this work. It is necessary though, that this phenomenon is studied more thoroughly in further studies.

Overall, the study presented in this thesis constitutes a comprehensive investigation of SAMs formation on oxidic surfaces with the main focus on PA-based thin films. Some open questions within the field of organic semiconductors and molecular thin films still remain. However, a better understanding of some fundamental and practical questions that are relevant

for processes which occur at various organic/inorganic interfaces helps in improving the performance of hybrid systems.

Bibliography

[1] The nobel prize in chemistry 2000.
http://www.nobelprize.org/nobelprizes/chemistry/laureates/2000/

[2] Shirakawa, H.; Louis, E. J.; MacDiarmid, A. G.; Chiang, C. K.; Heeger, A. J. Synthesis of electrically conducting organic polymers: halogen derivatives of polyacetylene, $(CH)_x$. *J. Chem. Soc. Chem. Commun.* **1977**, *24*, 578–580. DOI 10.1039/C39770000578

[3] Spanggaard, H.; Krebs, F. C. A brief history of the development of organic and polymeric photovoltaics. *Sol. Energy Mater. Sol. Cells* **2004**, *83*, 125–146 . DOI 10.1016/j.solmat.2004.02.021

[4] Wehlus, T.; Körner, T.; Nowy, S.; Frischeisen; J., Karl, H.; Stritzker, B.; Brütting, W. Hybrid organic–inorganic materials for integrated optoelectronic devices Hybrid organic–inorganic materials for integrated optoelectronic devices. *Phys. Status Solidi A* **2011**, *208*, 264–275 . DOI 10.1002/pssa.201026524

[5] Chiang, C. K.; Fincher, C. R., Jr.; Park, Y. W.; Heeger, A. J.; Shirakawa, H.; Louis, E. J.; Gau, S. C.; MacDiarmid, A. G. Electrical Conductivity in Doped Polyacetylene. *Phys. Rev. Lett.* **1977**, *39*(17), 1098-1101. DOI http://dx.doi.org/10.1103/PhysRevLett.39.1098

[6] Aviram, A.; Ratner, M. A. Molecular rectifiers. *Chem. Phys. Lett.* **1974**, *29*(2), 277-283. DOI 10.1016/0009-2614(74)85031-1

[7] Mann, B.; Kuhn, H. Tunneling through fatty acid salt monolayers. *J. Appl. Phys.* **1971**, *42*(11), 4398-4405. DOI http://dx.doi.org/10.1063/1.1659785

[8] Das, R.; Harrop, P. Printed, Organic & Flexible Electronics Forecasts, Players & Opportunities 2016-2026. *IDTechEx* **2015**. Report

[9] Dediu, V.A.; Hueso, L. E.; Bergenti, I.; Taliani, C. Spin routes in organic semiconductors. *Nat. Mater.* **2009**, *8*, 707–716. DOI 10.1038/nmat2510

[10] Groves, C. Organic light-emitting diodes: Bright design. *Nat. Mater.* **2013**, *12*, 597–598. DOI 10.1038/nmat3688

[11] Facchetti, A. Organic semiconductors: Made to order. *Nat. Mater.* **2013**, *12*, 598–600. DOI 10.1038/nmat3686

[12] Greiner, M. T.; Lu, Z.-H. Thin-film metal oxides in organic semiconductor devices: their electronic structures, work functions and interfaces. *NPG Asia Mater.* **2013**, *5*, 55. DOI 10.1038/am.2013.29

[13] Newman, C. R.; Frisbie, C. D.; da Silva Filho, D. A.; Brédas, J.-L.; Ewbank, P. C.; Mann, K. R. Introduction to Organic Thin Film Transistors and Design of n-Channel Organic Semiconductors. *Chem. Mater.* **2004**, *16*, 4436. DOI 10.1021/cm049391x

[14] Facchetti, A.; Letizia, J.; Yoon, M.-H.; Mushrush, M.; Katz, H. E.; Marks, T. J. Synthesis and Characterization of Diperfluorooctyl-Substituted Phenylene- Thiophene Oligomers and n-Type Semiconductors. Molecular Structure-Film Microstructure-Mobility Relationships, Organic Field-Effect Transistors, and Transistor Nonvolatile Memory Elements. *Chem. Mater.* **2004**, *16*, 4715. DOI 10.1021/cm0495008

[15] Crone, B.; Dodabalapur, A.; Lin, Y. Y.; Filas, R. W.; Bao, Z.; LaDuca, A.; Sarpeshkar, R.; Katz, H. E.; Li, W. Large-scale complementary integrated circuits based on organic transistors. *Nature* **2000**, *403*, 521. DOI 10.1038/35000530

[16] Diao, Y.; Tee, B. C.-K.; Giri, G.; Xu, J.; Kim, D. H.; Becerril, H. A.; Stoltenberg, R. M.; Lee, T. H.; Xue, G.; Mannsfeld, S. C. B.; Bao, Z. Solution coating of large-area organic semiconductor thin films with aligned single-crystalline domains. *Nat. Mater.* **2013**, *12*, 665–671. DOI 10.1038/nmat3650

[17] Burghartz. J. N. You can't be too thin or too flexible. *IEEE Spectr.* **2013**, *50*(3), 38–61.

[18] Burghartz, J. N.; Appel, W.; Rempp, H. D.; Zimmermann, M. A new fabrication and assembly process for ultrathin chips. *IEEE Trans. Electron Devices* **2009**, *56*(2), 321–327. DOI 10.1109/TED.2009.2010581

[19] Munck, K. D; Chiarella, T.; Moor, P. D.; Swinnen, B.; Van, H. C. Influence of extreme thinning on 130-nm standard CMOS devices for 3-D integration. *IEEE Electron Device Lett.* **2008**, *29*(4), 322–324. DOI 10.1109/LED.2008.917940

[20] Chen, C.-C., Chang, W.-H.; Yoshimura, K.; Ohya, K.; You, J.; Gao, J.; Hong, Z.; Yang, Y. An Efficient Triple-Junction Polymer Solar Cell Having a Power Conversion Efficiency Exceeding 11%. *Adv. Mater.* **2014**, *26*, 5670-5677. DOI 10.1002/adma.201402072

[21] Liu, Y.; Zhao, J.; Li, Z.; Mu, C.; My, W.; hu, H.; Jiang, K.; Lin, H.; Ade, H.; Yan, H. Aggregation and morphology control enables multiple cases of high-efficiency polymer solar cells. *Nat. Commun.* **2014**, *5*, 5293. DOI 10.1038/ncomms6293

[22] Mirletz, H. M.; Peterson, K. A.; Martin, I. T.; French, R. H. Degradation of transparent conductive oxides: Interfacial engineering and mechanistic insights. *Sol. Energy Mater. Sol. Cells* **2015**, *143*, 529–538. DOI 10.1016/j.solmat.2015.07.030

[23] Dennler, G.; Scharber, M. C.; Brabec, C. J. Polymer-Fullerene Bulk-Heterojunction Solar Cells. *Adv. Mat.* **2009**, *21*(13), 1323–1338. DOI 10.1002/adma.200801283

[24] Hu, Q.; Wu, J.; Jiang, C.; Liu, T.; Que, X.; Zhu, R.; Gong, Q. Engineering of Electron-Selective Contact for Perovskite Solar Cells with Efficiency Exceeding 15%. *ACS Nano* **2014**, *8*(10), 10161–10167. DOI 10.1021/nn5029828

[25] Albrecht, S.; Grootoonk, B.; Neubert, S.; Roland, S.; Wördenweber, J.; Meier, M.; Schlatmann, R.; Gordijn, A.; Neher, D. Efficient hybrid inorganic/organic tandem solar cells with tailored recombination contacts. *Sol. Energy Mater. Sol. Cells* **2014**, *127*, 157–162. DOI 10.1016/j.solmat.2014.04.02010.1016/j.solmat.2014.04.020

[26] Klauk, H. Organic thin-film transistors. *Chem. Soc. Rev.* **2010**, *39*(7), 2643–2666 . DOI 10.1039/b909902f

[27] Ginley, D. S.; Bright, C. (Ed.) Transparent Conducting Oxides. *MRS Bulletin* **2000**, *25*, 15-18. http://dx.doi.org/10.1557/mrs2000.256

[28] Stadler, A. Transparent Conducting Oxides—An Up-To-Date Overview. *Materials* **2012**, *5*, 661-683. DOI 10.3390/ma5040661

[29] Coutts, T. J.; Perkins, J. D.; Ginley, D. S.; Mason, T. O. Transparent Conducting Oxides: Status and Opportunities in Basic Research. *National Renewable Energy Laboratory. Washington* **1999**.

[30] Aphale, A.; Maisuria, K.; Mahapatra, M. K.; Santiago, A.; Singh, P.; Patra, P. Hybrid Electrodes by *In-Situ* Integration of Graphene and Carbon-Nanotubes in Polypyrrole for Supercapacitors. *Sci. Rep.* **2015**, *5*, 14445. DOI 10.1038/srep14445

[31] Bonaccorso, F.; Sun, Z.; Hasan, T.; Ferrari, A. C. Graphene photonics and optoelectronics. *Nat. Photonics* **2010**, *4*, 611-622. DOI 10.1038/NPHOTON.2010.186

[32] Park, H.; Rowehl, J. A.; Kim, K. K.; Bulovic, V.; Kong, J. Doped graphene electrodes for organic solar cells. *Nanotechnol.* **2010**, *21*, 505204. DOI http://dx.doi.org/10.1088/0957-4484/21/50/505204

[33] Ellmer, K.; Mientus, R. Carrier transport in polycrystalline transparent conductive oxides: A comparative study of zinc oxide and indium oxide. *Thin Solid Films* **2008**, *516*(14), 4620–4627. DOI 10.1016/j.tsf.2007.05.084

[34] Major, S.; Chopra, K. L. Indium-doped zinc oxide films as transparent electrodes for solar cells. *Sol. Energy Mater.* **1988**, *17*(5), 319-327. DOI 10.1016/0165-1633(88)90014-7

[35] Ellmer, K.; Klein, A.; Rech, B. Transparent Conductive Zinc Oxide: Basics and Applications in Thin Film Solar Cells. *Springer-Verlag* **2007**.

[36] Minami, T. Transparent conducting oxide semiconductors for transparent electrodes. *Semicond. Sci. Technol.* **2005**, *20*, 35–44. DOI 10.1088/0268-1242/20/4/004

[37] Dawar, A. L.; Joshi, J. C. Semiconducting transparent thin films: their properties and applications. *J. Mater. Sci.* **1984**, *19*, 1-23. DOI 10.1007/BF00552989

[38] Dosmailov, M.; Leonat, L. N.; Patek, J.; Roth, D.; Bauer, P.; Scharber, M. C.; Sariciftci, N. S.; Pedarnig, J. D. Transparent conductive ZnO layers on polymer substrates: Thin film deposition and application in organic solar cells. *Thin Solid Films* **2015**, *591*, 97-104. DOI 0.1016/j.tsf.2015.08.015

[39] Godlewski, M.; Guziewicz, E.; Luka, G.; Krajewski, T.; Lukasiewicz, M.; Wachnicki, L.; Wachnicka, A.; Kopalko, K.; Sarem, A.; Dalati, B. ZnO layers grown by Atomic Layer Deposition: A new material for transparent conductive oxide. *Thin Solid Films* **2009**, *518*, 1145–1148. DOI 10.1016/j.tsf.2009.04.066

[40] Keis, K.; Bauer, C.; Boschloo, G.; Hagfeldt, A.; Westermark, K.; Rensmo, H.; Siegbahn, H. Nanostructured ZnO electrodes for dye-sensitized solar cell applications. *J. Photochem. Photobiol., A* **1999**, *12*, 487-490. DOI 10.1016/S0965-9773(99)00165-8

[41] Galstyann, V.; Comini, E.; Baratto, C.; Faglia, G.; Sberveglier, G. Nanostructured ZnO chemical gas sensors. *Ceram. Int.* **2015**, *41*, 14239–14244. DOI 10.1016/j.ceramint.2015.07.052

[42] Sung, S.; Park, S.; Lee, W.-J.; Son, J.; Kim, C.-H.; Kim, Y.; Noh, D. Y.; Yoon M.-H. Low-Voltage Flexible Organic Electronics Based on High Performance Sol-Gel Titanium Dioxide Dielectric. *ACS Appl. Mater. Interfaces.* **2015**, *7*, 7456-7461. DOI 10.1021/acsami.5b00281

[43] Benedix, R.; Dehn, F.; Quaas, J.; Orgass, M. Application of Titanium Dioxide Photocatalysis to Create Self-Cleaning Building Materials. *Lacer* **2000**, *5*, 158-168. http://www.mchnanosolutions.com/references/Selfcleaning.pdf

[44] Roy, P.; Berger, S.; Schmuki, P. TiO$_2$ Nanotubes: Synthesis and Applications. *Angew. Chem. Int. Ed.* **2011**, *50*, 2904 – 2939. DOI 10.1002/anie.201001374

[45] Fujishima, A.; Zhang, X.; Tryk, D. A. TiO$_2$ photocatalysis and related surface phenomena. *Surf. Sci. Rep.* **2008**, *63*, 515–582. DOI 10.1016/j.surfrep.2008.10.001

[46] Nakata, K.; Ochiai, T.; Murakami, T.; Fujishimaa, A. Photoenergy conversion with TiO$_2$ photocatalysis: New materials and recent applications. *Electrochim. Acta.* **2012**, *84*, 103-111. DOI 10.1016/j.electacta.2012.03.035

[47] Henderson, M. A. A surface science perspective on TiO$_2$ photocatalysis. *Surf. Sci. Rep.* **2011**, *66*, 185-297. DOI 10.1016/j.surfrep.2011.01.001

[48] Vallejo L., W. A.; Quinones S., C. A.; Hernandez S., J. A. The Chemistry and Physics of Dye-Sensitized Solar Cells, Solar Cells - Dye-Sensitized. Kosyachenko, L. D. (Ed.), *InTech* **2011**, ISBN: 978-953-307-735-2. http://www.intechopen.com/books/solar-cells-dye-sensitizeddevices/the-chemistry-and-physics-of-dye-sensitized-solar-cells

[49] Klauk, H. Organic Electronics: Materials, Manufacturing, and Applications. *WILEY-VCH Verlag GmbH & Co. KGaA*, Weinheim, **2006**.

[50] van Woudenbergh, T.; Blom, P. W. M.; Vissenberg, M. C. J. M.; Huiberts, J. N. Temperature dependence of the charge injection in poly-dialkoxy-pp-phenylene vinylene. *Appl. Phys. Lett.* **2001**, *79*, 1697. DOI http://dx.doi.org/10.1063/1.1395515

[51] van Woudenbergh, T.; Blom, P. W. M.; Huiberts, J. N. Electro-optical properties of a polymer light-emitting diode with an injection-limited hole contact. *Appl. Phys. Lett.* **2003**, *82*, 985. DOI http://dx.doi.org/10.1063/1.1543255

[52] Ishii, H.; Sugiyama, K.; Ito, E.; Seki, K. Energy Level Alignment and Interfacial Electronic Structures at Organic/Metal and Organic/Organic Interfaces. *Adv. Mater.* **1999**, *11*, 605-625. DOI 10.1002/(SICI)1521-4095(199906)11:8<605::AID-ADMA605>3.0.CO;2-Q

[53] Koch, N. Organic Electronic Devices and Their Functional Interfaces. *ChemPhysChem* **2007**, *8*, 1438-1455. DOI 10.1002/cphc.200700177

[54] Braun, S.; Salaneck, W. R.; Fahlman, M. Energy-Level Alignment at Organic/Metal and Organic/Organic Interfaces. *Adv. Mater.* **2009**, *21*, 1450-1472. DOI 10.1002/adma.200802893

[55] Heimel, G.; Romanerb, L.; Zojerc, E.; Brédas, J.-L. A theoretical view on self-assembled monolayers in organic electronic devices. Organic Optoelectronics and Photonics III. Heremans, P. L. (ed.) **2008**. DOI 10.1117/12.785122

[56] de Boer, B.; Hadipour, A.; Mandoc, M. M.; van Woudenbergh, T.; Blom, P. W. M. Tuning of Metal Work Function with Self-Assembled Monolayers. *Adv. Mater.* **2005**, *17*, 621-625. DOI 10.1002/adma.200401216

[57] Wang, M.; Hill, I. G. Fluorinated Alkyl Phosphonic Acid SAMs Replace PE-DOT:PSS in Polymer Semiconductor Devices. *Org. Electron.* **2012**, *13*, 498-505. DOI 10.1016/j.orgel.2011.12.008

[58] Morana, M.; Wegscheider, M.; Bonanni, A.; Kopidakis, N.; Shaheen, S.; Scharber, M.; Zhu, Z.; Waller, D.; Gaudiana, R.; Brabec, C. Bipolar Charge Transport in PCPDTBT-PCBM Bulk-Heterojunctions for Photovoltaic Applications. *Adv. Funct. Mater.* **2008**, *18*, 1757-1766. DOI 10.1002/adfm.200701428

[59] White, M. S.; Olson, D. C.; Shaheen, S. E.; Kopidakis, N.; Ginley, D. S. Inverted Bulk-Heterojunction Organic Photovoltaic Device Using a Solution-Derived ZnO Underlayer. *Appl. Phys. Lett.* **2006**, *89*, 143517. DOI http://dx.doi.org/10.1063/1.2359579

[60] Chen, W.; Chen, S.; Chen Qi, D.; Gao, X. Y.; Wee, A. T. S. Molecular Orientation and Energy Level Alignment at the CuPc/SAMs Interface. *Adv. Syn. Rad.* **2008**, *01*, 33. DOI 10.1142/S1793617908000094

[61] Kim, J. S.; Park, J. H.; Lee, J. H.; Jo, J.; Kim, D.-Y.; Cho, K. Control of the electrode work function and active layer morphology via surface modification of indium tin oxide for high efficiency organic photovoltaics. *Appl. Phys. Lett.* **2007**, *91*, 112111. DOI 10.1063/1.2778548

[62] Novak, M.; Jäger, C. M.; Rumpel, A.; Kropp, H.; Peukert, W.; Clark, T.; Halik, M. The morphology of integrated self-assembled monolayers and their impact on devices – A computational and experimental approach. *Org. Electron.* **2010**, *11*, 1476–1482. DOI 10.1016/j.orgel.2010.05.009

[63] Henrich, V. E.; Cox, P. A.; Vioux, A. The Surface Science of Metal Oxides. *Cambridge University Press* **1994**.

[64] Janotti, A.; Van de Walle, C. G. Fundamentals of zinc oxide as a semiconductor. *Rep. Prog. Phys.* **2009**, *72*, 126501. DOI 10.1088/0034-4885/72/12/126501.

[65] Srikant, V.; Clarke, D. R. On the optical band gap of zinc oxide. *J. Appl. Phys.* **1998**, *83*, 5447. DOI 10.1063/1.367375.

[66] Morkoc, H.; Ozgur, U. Zinc Oxide: Fundamentals, Materials and Device Technology. *WILEY-VCH Verlag GmbH & Co. KGaA* **2009**.

[67] Landolt, H.; Börnstein, R. Landolt-Börnstein: Numerical Data and Functional Relationships in Science and Technology - New Series. *Springer-Verlag* **1999**.

[68] Wander, A.; Schedin, F.; Steadman, P.; Norris, A.; McGrath, R.; Turner, T. S.; Thornton, G.; Harrison, N. M. Stability of Polar Oxide Surfaces. *Phys. Rev. Lett.* **2001**, *86*, 3811. DOI 10.1103/PhysRevLett.86.3811.

[69] Noguera, C. Polar oxide surfaces. *J. Phys.: Condens. Matter* **2000**, *12*, 367. DOI 10.1088/0953-8984/12/31/201.

[70] Dulub, O.; Diebold, U.; Kresse, G. Novel Stabilization Mechanism on Polar Surfaces: ZnO(0001)-Zn. *Phys. Rev. Lett.* **2003**, *90*, 6102. DOI 10.1103/PhysRevLett.90.016102.

[71] Ostendorf, F.; Torbrügge, S.; Reichling, M. Atomic scale evidence for faceting stabilization of a polar oxide surface. *Phys. Rev. Lett. B* **2008**, *77*, 041405. DOI 10.1103/PhysRevB.77.041405.

[72] Torbrügge, S.; Ostendorf, F.; Reichling, M. Stabilization of Zinc-Terminated ZnO(0001) by a Modified Surface Stoichiometry. *J. Phys. Chem. C* **2009**, *113*, 4909-4914. DOI 10.1021/jp804026v.

[73] Valtiner, M.; Todorova, M.; Grundmeier, G.; Neugebauer, J. Temperature Stabilized Surface Reconstructions at Polar ZnO(0001). *Phys. Rev. Lett.* **2009**, *103*, 065502. DOI 10.1103/PhysRevLett.103.065502.

[74] Jedrecy, N.; Sauvage-Simkin, M.; Pinchaux, R. S. The hexagonal polar ZnO(0001) − (1 × 1) surfaces: structural features as stemming from X-ray diffraction. *Appl. Surf. Sci.* **2000**, *162-163*, 69-73. DOI 10.1016/S0169-4332(00)00172-0.

[75] Allen, M. W.; Swartz, C. H.; Myers, T. H.; Veal, T. D.; McConville, C. F.; Surbin, S. M. Bulk transport measurements in ZnO: The effect of surface electron layers. *Phys. Rev. B.* **2010**, *81*, 075211. DOI 10.1103/PhysRevB.81.075211.

[76] Becker, T.; Hovel, S.; Kunat, M.; Boas, C.; Burghaus, U.; Wöll, C. Interaction of hydrogen with metal oxides: the case of the polar ZnO(0001) surface. *Surf. Sci.* **2001**, *486*, 502–506. DOI 10.1016/S0039-6028(01)01120-7.

[77] Kunat, M.; Girol, S. G.; Becker, T.; Burghaus, U.; Wöll, C. Stability of the polar surfaces of ZnO: A reinvestigation using He-atom scattering. *Phys. Rev. B.* **2002**, *66*, 081402. DOI 10.1103/PhysRevB.66.081402.

[78] Lyle, M. J.; Warschkow, O.; Delley, B.; Stampfl C. Coverage and charge-state dependent adsorption of carbon monoxide on the zinc oxide (0001) surface. *Phys. Rev. B.* **2010**, *82*, 165401. DOI 10.1103/PhysRevB.82.165401.

[79] Valtiner, M.; Borodin, S.; Grundmeier, G. Preparation and characterisation of hydroxide stabilised $ZnO(0001)$–Zn–OH surfaces. *Phys. Chem. Chem. Phys.* **2007**, *9*, 2406-2412. DOI 10.1039/B617600C.

[80] Kresse, G.; Dulub, O.; Diebold, U. Competing stabilization mechanism for the polar $ZnO(0001)$-Zn surface. *Phys. Rev. B* **2003**, *68*, 245409. DOI 10.1103/PhysRevB.68.245409.

[81] Dulub, O.; Boatner, L. A.; Diebold, U. STM study of the geometric and electronic structure of $ZnO(0001)$-Zn, $(000\bar{1})$-O, $(10\bar{1}0)$, and $(11\bar{2}0)$ surfaces. *Surface Science* **2002**, *519*, 201-217. DOI 0.1016/S0039-6028(02)02211-2.

[82] Koplitz, L. V.; Dulub, O.; Diebold, U. STM study of Copper Growth on $ZnO(0001)$-Zn and $ZnO(000\bar{1})$-O Surfaces. *J. Phys. Chem. B* **2003**, *1017*, 10583-10590. DOI 10.1021/jp0352175.

[83] Parker, T. M.; Condon, N. G.; Lindsay, R.; Leibsle, F. M.; Thornton, G. Imaging the polar $(000\bar{1})$ and non-polar $(10\bar{1}0)$ surfaces of ZnO with STM. *Surf. Sci.* **1998**, *415*, 5, L1046–L1050. DOI doi:10.1016/S0039-6028(98)00563-9.

[84] Diebold, U.; Koplitz, L. V.; Dulub, O. Atomic-scale properties of low-index ZnO surfaces. *Appl. Surf. Sci.* **2004**, *237*, 336-342. DOI 10.1016/j.apsusc.2004.06.040.

[85] Dulub, O.; Boatner, L. A.; Diebold, U. STM study of Cu growth on the $ZnO(10\bar{1}0)$ surface. *Surf. Sci.* **2004**, *504*, 271-281. DOI 10.1016/S0039-6028(02)01107-X.

[86] Polarz, S.; Strunk, J.; Ischenko, V.; Van den Berg, M. W. E.; Hinrichsen, O.; Muhler, M.; Driess, M. On the Role of Oxygen Defects in the Catalytic Performance of Zinc Oxide. *Angew. Chem. Int. Ed.* **2006**, *45*, 2965-2969. DOI 10.1002/anie.200503068.

[87] Ischenko, V.; Polarz, S.; Grote, D.; Stavarache, V.; Fink, K.; Driess, M. Zinc Oxide Nanoparticles with Defects. *Adv. Funvt. Mater.* **2005**, *15*, 1945-1954. DOI 10.1002/adfm.200500087

[88] Özgür, Ü.; Alivov, Ya. I.; Liu, C.; Teke, A.; Reshchikov, M. A.; Doğan, S.; Avrutin, V.; Cho, S.-J.; Morko, H. A comprehensive review of ZnO materials and devices. *J. Appl. Phys.* **2005**, *98*, 041301. DOI 10.1063/1.1992666

[89] Meyer, B. First-principles study of the polar O-terminated ZnO surface in thermodynamic equilibrium with oxygen and hydrogen. *Phys. Rev. B* **2004**, *69*, 045416. DOI 10.1103/PhysRevB.69.045416

[90] Kováčik, R.; Meyer, B.; Marx, D. F. Centers versus Dimer Vacancies on ZnO Surfaces: Characterization by STM and STS Calculations. *Angew. Chem. Int. Ed.* **2007**, *46*, 4894–4897. DOI 10.1002/anie.200604399

[91] Oba, F.; Choi, M.; Togo, A.; Tanaka, I. Point defects in ZnO: an approach from first principles. *Sci. Technol. Adv. Mater.* **2011**, *12*, 034302. DOI 10.1088/1468-6996/12/3/034302

[92] Erhart, P.; Albe, K.; Klein, A. First-principles study of intrinsic point defects in ZnO: Role of band structure, volume relaxation, and finite-size effects. *Phys. Rev. B* **2006**, *73*, 205203. DOI 10.1103/PhysRevB.73.205203

[93] Kohan, A. F.; Ceder, G.; Morgan, D.; Van de Walle, C. G. First-principles study of native point defects in ZnO. *Phys. Rev. B* **2000**, *61*, 15019. DOI http://dx.doi.org/10.1103/PhysRevB.61.15019

[94] Liu, M.; Kitai, A. H.; Mascher, P. Point defects and luminescence centres in zinc oxide and zinc oxide doped with manganese. *J. of Lum.* **1992**, *54*, 35-42. DOI 10.1016/0022-2313(92)90047-D.

[95] Janotti, A.; Van de Walle, C. G. New insights into the role of native point defects in ZnO. *J. Cryst. Growth* **2006**, *287*, 58-65. DOI 10.1016/j.jcrysgro.2005.10.043

[96] Janotti, A.; Van de Walle, C. G. Native point defects in ZnO. *Phys. Rev. B* **2007**, *76*, 165202. DOI 10.1103/PhysRevB.76.165202

[97] Wang, Z. L. Zinc oxide nanostructures: growth, properties and applications. *J. Phys.: Condens. Matter* **2004**, *16*, 829–858. DOI 10.1088/0953-8984/16/25/R01

[98] Radzimska, A. K.; Jesionowski, T. Zinc Oxide—From Synthesis to Application: A Review. *Materials* **2014**, *7*, 2833-2881. DOI 10.3390/ma7042833

[99] Ozgur, U.; Hofstetter, D.; Morkoc, H. ZnO Devices and Applications: A Review of Current Status and Future Prospects. *Proceedings of the IEEE 98* **2010**, *7*, 1255-1268. DOI 10.1109/JPROC.2010.2044550

[100] Kumar, S. S.; Venkateswarlu, P.; Rao, V. R.; Rao, G. N. Synthesis, characterization and optical properties of zinc oxide nanoparticles. *Int. Nano Lett.* **2013**, *3*, 30. DOI 10.1186/2228-5326-3-30

[101] Anta, J. A.; Guillén, E.; Tena-Zaera, R. ZnO-Based Dye-Sensitized Solar Cells. *J. Phys. Chem. C* **2012**, *116*(21), 11413–11425. DOI 10.1021/jp3010025

[102] Fan, J. C.; Chang, S. L.; Xie, Z. ZnO-Based Light-Emitting Diodes. "Optoelectronics - Advanced Materials and Devices", Pyshkin, S. L. ed. *CC BY 3.0 license* **2013**, ISBN 978-953-51-0922-8 . DOI 10.5772/51181

[103] Abbasi, M. A.; Ibupoto, Z. H.; Hussain, M.; Nur, O.; Willander, M. The fabrication of white light-emitting diodes using the n-ZnO/NiO/p-GaN heterojunction with enhanced luminescence. *Nanoscale Res. Lett.* **2013**, *8*, 320. DOI 10.1186/1556-276X-8-320

[104] Banfield, J. F.; Bischoff, B. L.; Anderson, M. A. TiO_2 accessory minerals: coarsening, and transformation kinetics in pure and doped synthetic nanocrystalline materials. *Chem. Geol.* **1993**, *110*, 211. DOI 10.1016/0009-2541(93)90255-H

[105] Alemany, L. J.; Baares, M. A.; Pardo, E.; Martín-Jiménez, F.; Blasco, J. M. Morphological and Structural Characterization of a Titanium Dioxide System Materials Characterization. *Mater. Charact.* **2000**, *44*(3), 271-275. DOI 10.1016/S1044-5803(99)00066-2

[106] Liu, Q.-J.; Ran, Z.; Liu, F.-S.; Liu, Z.-T. Phase transitions and mechanical stability of TiO_2 polymorphs under high pressure. *J. Alloys Compd.* **2015**, *631*(15), 192-201. DOI :10.1016/j.jallcom.2015.01.085

[107] Haines, J.; Leger, J. M. X-ray diffraction study of TiO_2 up to 49 GPa. *Phys. B (Amsterdam, Neth.)* **1993**, *192*, 233-237. DOI 10.1016/0921-4526(93)90025-2

[108] Linsebigler, A. L.; Lu, G.; Yates, J. T. Photocatalysis on TiO_2 Surfaces: Principles, Mechanisms, and Selected Results. *Chem. Rev.* **1995**, *95*, 735-758. DOI 10.1021/cr00035a013

[109] Schneider, J.; Matsuoka, M.; Takeuchi, M.; Zhang, J.; Horiuchi, Y.; Anpo, M.; Bahnemann, D. W. Understanding TiO_2 Photocatalysis: Mechanisms and Materials. *Chem. Rev.* **2014**, *114*, 9919-9986. DOI dx.doi.org/10.1021/cr5001892

[110] Landmann, M.; Rauls, E.; Schmidt, W. G. The electronic structure and optical response of rutile, anatase and brookite TiO_2. *J. Phys.: Condens. Matter* **2012**, *24*, 195503-195509. DOI 10.1088/0953-8984/24/19/195503

[111] Sun, Q.; Xu, Y. Evaluating Intrinsic Photocatalytic Activities of Anatase and Rutile TiO_2 for Organic Degradation in Water. *J. Phys. Chem. C* **2010**, *114*(44), 18911–18918. DOI 10.1021/jp104762h

[112] Luttrell, T.; Halpegamage, S.; Tao, J.; Kramer, A.; Sutter, E.; Batzill, M. Why is anatase a better photocatalyst than rutile? - Model studies on epitaxial TiO_2 films. *Scientific Reports* **2014**, *4*, 4043. DOI 10.1038/srep04043

[113] Zhang, J.; Zhou, P.; Liu, J.; Yu, J. New understanding of the difference of photocatalytic activity among anatase, rutile and brookite TiO_2. *Phys. Chem. Chem. Phys.* **2014**, *16*, 20382-20386. DOI 10.1039/C4CP02201G

[114] Horn, M.; Schwerdtfeger, C. F.; Meagher, E. P. Refinement of the structure of anatase at several temperatures. *Zeitschrift für Kristallographie* **1972**, *136*, 273. DOI 10.1524/zkri.1972.136.3-4.273

[115] Hanaor, D. A. H.; Sorrell, C. H. Review of the anatase to rutile phase transformation. *J. Mater. Sci.* **2011**, *46*, 855–874. DOI 10.1007/s10853-010-5113-0

[116] Satoh, N.; Nakashima, T.; Yamamoto, K. Metastability of anatase: size dependent and irreversible anatase-rutile phase transition in atomic-level precise titania. *Scientific Report* **2013**, *3*, 1959. DOI 10.1038/srep01959

[117] Arbiol, J.; Cerdá, J.; Dezanneau, G.; Cirera, A.; Peir, F.; Cornet, A.; Morante, J. R. Effects of Nb doping on the TiO_2 anatase-to-rutile phase transition. *J. Appl. Phys.* **2002**, *92*, 853. DOI dx.doi.org/10.1063/1.1487915

[118] Wyckoff, R. W. G. Crystal Structure Descriptions, 2 ed. *John Wiley and Sons Ltd.* , Chichester, New York, **1963**.

[119] Diebold, U. The surface science of titanium dioxide. *Surf. Sci. Rep.* **2003**, *48*, 53. DOI 10.1016/S0167-5729(02)00100-0

[120] Scanlon, D. O.; Dunnill, C. W.; Buckeridge, J.; Shevlin, S. A.; Logsdail, A. J.; Woodley, S. M.; Catlow, C. R. A.; Powell, M. J.; Palgrave, R. G.; Parkin, I. P.; Watson, G. W.; Keal, T. W.; Sherwood, P.; Walsh, A.; Sokol, A. A. Band alignment of rutile and anatase TiO_2.*Nat. Mater.* **2013**, *12*, 798-801. DOI 10.1038/nmat3697

[121] Nowotny , M. K.; Bak , T.; Nowotny, J. Electrical Properties and Defect Chemistry of TiO_2 Single Crystal. *J. Phys. Chem. B* **2006**, *110*(33), 16270–16282. DOI 10.1021/jp0606210

[122] Baumard, J. F.; Tani, E. Electrical conductivity and charge compensation in Nb doped TiO_2 rutile. *J. Chem. Phys.* **1977**, *67*, 857. DOI http://dx.doi.org/10.1063/1.434952

[123] Zhao, X. P.; Yin, J. B. Preparation and Electrorheological Characteristics of Rare-Earth-Doped TiO_2 Suspensions. *Chem. Mater.* **2002**, *14*(5), 2258–2263. DOI 10.1021/cm011522w

[124] Janisch, R.; Gopal, P.; Spaldin, N. A. Transition metal-doped TiO_2 and ZnO—present status of the field. *J. Phys.: Condens. Matter* **2005**, *17*, 657-689. DOI 10.1088/0953-8984/17/27/R01

[125] Diebold, U.; Li, S.-C.; Schmidt, M. Oxide Surface Science. *Annu. Rev. Phys. Chem.* **2010**, *61*, 129–148. DOI 10.1146/annurev.physchem.012809.103254

[126] Diebold, U.; Li, M.; Dulub, O.; Hebenstreit, E. L. D.; Hebenstreit, W. The relationship between bulk and surface properties of $TiO_2(1\,1\,0)$. *Surf. Rev. Lett.* **2000**, *7*, 613-617. DOI 10.1142/S0218625X0000052X

[127] Trenczek-Zajac, A.; Rekas, M. Electrical properties of Nb-doped titanium dioxide TiO_2at room temperature. *Mater. Sci.-Pol.* **2006**, *24*(1), 53. http://www.materialsscience.pwr.wroc.pl/bi/vol24no1/articles/ms-2006-007.pdf

[128] Xu, L.; Garrett, M. P.; Hu, B. Doping effects on internally coupled seebeck coefficient, electrical, and thermal conductivities in aluminum-doped TiO_2 . *J. Phys. Chem. C* **2012**, *116*(24), 13020. DOI 10.1021/jp302652c

[129] Lee, D. K.; Yoo, H. I. Electrical conductivity and oxygen nonstoichiometry of acceptor (Ga)-doped titania. *Phys. Chem. Chem. Phys.* **2008**, *10*, 6890. DOI 10.1039/B811319J

[130] Wang, Q. L.; Lian, G.; Dickey, E. C. Grain boundary segregation in yttrium doped polycrystalline TiO_2. *Acta Mater.* **2004**, *52*(4), 809. DOI 10.1016/j.actamat.2003.10.016

[131] Samsonov, G. V. The Oxide Handbook. *IFI/Plenum* **1982**, New York.

[132] Cronemeyer, D. C. Infrared Absorption of Reduced Rutile TiO_2 Single Crystals. *Phys. Rev.* **1956**, *113*, 1222. DOI http://dx.doi.org/10.1103/PhysRev.113.1222

[133] Cronemeyer, D. C. Electrical and Optical Properties of Rutile Single Crystals. *Phys. Rev.* **1952**, *87*, 876. DOI http://dx.doi.org/10.1103/PhysRev.87.876

[134] Breckenridge, R. B.; Hosler, W. R. Electrical properties of titanium dioxide semiconductors. *Phys. Rev.* **1953**, *91*, 793. DOI http://dx.doi.org/10.1103/PhysRev.91.793

Bibliography 141

[135] Becker, J. H.; Hosler, W. R. Multiple-Band Conduction in n-type rutile (TiO_2). *Phys. Rev.* **1965**, *137*, 1972-1965. DOI 10.1103/PhysRev.137.A1872

[136] Ashcroft, N. W.; Mermin, N. D. Solid State Physics. *Saunders College Publishing* **1976**, New York.

[137] Yagi, E.; Hasiguti, R. R.; Aono, M. Electronic conductivity above 4 K of slightly reduced oxygen deficient rutile TiO_{2-x}. *Phys. Rev. B* **1996**, *54*, 7945. DOI http://dx.doi.org/10.1103/PhysRevB.54.7945

[138] Yu, N. C.; Halley, J. W. Electronic-Structure of Point-Defects in Rutile TiO_2. *Phys. Rev. B* **1995**, *51*, 4768. DOI http://dx.doi.org/10.1103/PhysRevB.51.4768

[139] Hameeuw, K. J.; Cantele, G.; Ninno, D.; Trani, F.; Iadonisi, G. The rutile $TiO_2(1\,1\,0)$ surface: Obtaining converged structural properties from firstprinciples calculations. *J. Chem. Phys.* **2006** , *124* , 024708. DOI http://dx.doi.org/10.1063/1.2136158

[140] Ramamoorthy, M.; King-Smith, R. D.; Vanderbilt, D. Defects on $TiO_2(1\,1\,0)$ surfaces. *Phys. Rev. B* **1994**, *49*, 7709. DOI http://dx.doi.org/10.1103/PhysRevB.49.7709

[141] Onishi, H.; Fukui, K.; Iwasawa, Y. Atomic-Scale Surface Structures of $TiO_2(1\,1\,0)$ Determined by Scanning Tunneling Microscopy: A New Surface-Limited Phase of Titanium Oxide. *Bull. Chem. Soc. Jpn.* **1995**, *68*, 2447-2458. DOI 10.1021/jz5004704

[142] Rohrer, G. S.; Henrich, V. E.; Bonnell, D. A. Structure of the Reduced $TiO_2(1\,1\,0)$ Surface Determined by Scanning Tunneling Microscopy. *Science* **1990**, *250*, 1239-1241. DOI 10.1126/science.250.4985.1239

[143] Diebold, U.; Lehman, J.; Mahmoud, T.; Kuhn, M.; Leonardelli, G.; Hebenstreit, W.; Schmid, M.; Varga, P. Intrinsic defects on a $TiO_2(1\,1\,0)(1 \times 1)$ surface and their reaction with oxygen: a scanning tunneling microscopy study. *Surf. Sci.* **1998**, *411*, 137–153. DOI 10.1016/S0039-6028(98)00356-2

[144] Diebold, U. Structure and properties of TiO_2 surfaces: a brief review. *Appl. Phys. A* **2003**,*76*, 681–687. DOI 10.1007/s00339-002-2004-5

[145] Chen, X.; Mao, S. Titanium Dioxide Nanomaterials: Synthesis, Properties, Modifications, and Applications. *Chem. Rev.* **2007** , *107*, 2891-2959. DOI 10.1021/cr0500535

[146] Gupta, S. M.; Tripathi, M. A review of TiO_2 nanoparticles. *Phys. Chem.* **2011**, *56*, 1639–1657. DOI 10.1007/s11434-011-4476-1

[147] Nakataa, K.; Fujishimaa, A. TiO_2 photocatalysis: Design and applications. *J. Photochem. Photobiol., C* **2012**, *13*, 169–189. DOI 10.1016/j.jphotochemrev.2012.06.001

[148] Kasemo, B.; Gold, J. Implant surfaces and interface processes. *Advances in dental research* **1999**, *13*, 8-20. DOI 10.1177/08959374990130011901

[149] El-Sherbiny, S.; Morsy, F.; Samir, M.; Fouad, O. A. Synthesis, characterization and application of TiO_2 nanopowders as special paper coating pigment. *Appl. Nanosci.* **2014**, *4*, 305–313. DOI 10.1007/s13204-013-0196-y

[150] Zhang, T.-H.; Ling-Yu, P.; Su-Ling, Z.; Zheng, X.; Qian, W.; Chao, K. Application of TiO_2 with different structures in solar cells. *Chin. Phys. B* **2012**, *21*, 118401. DOI 10.1088/1674-1056/21/11/118401

[151] Bai, Y.; Mora-Sero, I.; Angelis, F. D.; Bisquert, J.; Wang, P. Titanium Dioxide Nanomaterials for Photovoltaic Applications. *Chem. Rev.* **2014**, *114*(19), 10095–10130. DOI 10.1021/cr400606n SAMs

[152] Fenwick, O.; Dyck, C. V.; Murugavel, K.; Cornil, D.; Reinders, F.; Haar, S.; Mayor, M.; Cornil, J.; Samorí, P. Modulating the charge injection in organic field-effect transistors: fluorinated oligophenyl self-assembled monolayers for high work function electrodes. *J. Mater. Chem. C* **2015**, *3*, 3007-3015. DOI 10.1039/C5TC00243E

[153] Kato, H. S.; Murakami, Y.; Kiriyama, Y.; Saitoh, R.; Ueba, T.; Yamada, T.; Ie, Y.; Aso, Y.; Munakata, T. Decay of the Exciton in Quaterthiophene-Terminated Alkanethiolate Self-Assembled Monolayers on Au(1 1 1). *J. Phys. Chem. C* **2015**, *119*(13), 7400–7407. DOI 10.1021/acs.jpcc.5b02105

[154] Gholamrezaie, F.; Vijayaraghavan, R. K.; Meskers, S. C. J. Photovoltaic action in a self-assembled monolayer of hemicyanine dyes on gold from dissociation of surface plasmons. *Appl. Phys. Lett.* **2015**, *106*, 183303. DOI http://dx.doi.org/10.1063/1.4919900

[155] Shen, X.; Wei, X.; Tan, P.; Yu, Y.; Yang, B.; Gong, Z.; Zhang, H.; Lin, H.; Li, Y.; Li, Q.; Xie, Y.; Chi, L. Phase Transitions: Concentration-Controlled Reversible Phase Transitions in Self-Assembled Monolayers on HOPG Surfaces. *Small* **2015**, *11*(19), 2222. DOI 10.1002/smll.201570108

[156] Jacquelín, D. K.; Pérez, M. A.; Euti, E. M.; Arisnabarreta, N.; Cometto, F. P.; Paredes-Olivera, P.; Patrito, E. M. A pH-Sensitive Supramolecular Switch Based on Mixed Carboxylic Acid Terminated Self-Assembled Monolayers on Au(1 1 1). *Langmuir* **2016**, *32* (4), 947–953. DOI 10.1021/acs.langmuir.5b03807

[157] Gao , W.; Dickinson , L.; Grozinger, C.; Morin, F. G.; Reven, L. Self-Assembled Monolayers of Alkylphosphonic Acids on Metal Oxides. *Langmuir* **1996**, *12*(26), 6429–6435. DOI 10.1021/la9607621

[158] Love, J. C.; Estroff, L. A.; Kriebel, J. K.; Nuzzo, R. G.; Whitesides, G. M. Self-Assembled Monolayers of Thiolates on Metals as a Form of Nanotechnology. *Chem. Rev.* **2005**, *105*, 1103–1170. DOI 10.1021/cr0300789

[159] Chidsey, C. E. D.; Loiacono, D. N. Chemical Functionality in Self -Assembled Monolayers: Structural and Electrochemical Properties. *Langmuir* **1990**, *6*, 682-691. DOI 10.1021/la00093a026

[160] Gooding, J. J.; Mearns, F.; Yang, W.; Liu, J. Self-Assembled Monolayers into the 21st Century: Recent Advances and Applications. *Electroanalysis* **2003**, *15*, 2. DOI 10.1002/elan.200390017

[161] Lin, W. C; Lee, S. H.; Karakachian, M.; Yu B.Y, Chen Y.Y, Lin Y.C, Kuo, C. H.; Shyue, J. J. Tuning the surface potential of gold substrates arbitrarily with self-assembled monolayers with mixed functional groups. *Phys. Chem. Chem. Phys.* **2009**, *11*(29), 6199-204. DOI 10.1039/b902044f

[162] Novak, M.; Jäger, C. M.; Rumpel, A.; Kropp, H.; Peukert, W.; Clark, T.; Halik, M. Influence of self-assembled monolayer dielectrics on the morphology and performance of α, ω-dihexylquaterthiophene in thin film transistors. *Org. Electron.* **2010**, *11*, 1476. DOI http://dx.doi.org/10.1063/1.3560454

[163] Halik, M.; Klauk, H.; Zschieschang, U.; Schmid, G.; Dehm, C.; Schutz, M.; Maisch, S.; Effenberger, F.; Brunnbauer, M.; Stellacci, F. Low-voltage organic transistors with an amorphous molecular gate dielectric. *Nature* **2004**, *431*, 963. DOI 10.1038/nature02987

[164] Arita, T.; Moriya, K.; Yoshimura, T.; Minami, K.; Naka, T.; Adschiri, T. Dispersion of Fatty Acid Surface Modified Ceria Nanocrystals in Various Organic Solvents. *Ind. Eng. Chem. Res.* **2010**, *49*, 9815. DOI 10.1021/ie901319c

[165] Ganbold, E. O.; Lee, Y.; Lee, K.; Kwon, O.; Joo, S. W. Interfacial Behavior of Benzoic Acid andPhenylphosphonic Acid on Nanocrystalline TiO_2 Surfaces. *Chem. Asian. J.* **2010**, *5*, 852. DOI 10.1002/asia.200900414

[166] Arita, T.; Moriya, K.; Minami, K.; Naka, T.; Adschiri, T. Supercritical Hydrothermal Synthesis of Carboxylic Acid-surface-functionalized TiO_2 Nanocrystals: pH Sensitive Dispersion and Hybridization with Organic Compounds. *Chem. Lett.* **2010**, *39*, 961. DOI http://doi.org/10.1246/cl.2010.961

[167] Luschtinetz, R.; Frenzel, J.; Milek, T.; Seifert, G. Adsorption of Phosphonic Acid at the TiO_2 Anatase (101) and Rutile (110) Surfaces. *J. Phys. Chem. C* **2009**, *113*, 5730. DOI 10.1021/jp8110343

[168] Jedaa, A.; Burkhardt, M.; Zschieschang, U.; Klauk, H.; Habich, D.; Schmid, G.; Halik, M. The Impact of Self-Assembled Monolayer Thickness in Hybrid Gate Dielectrics for Organic Thin-Film Transistors. *Org. Electron.* **2009**, *10*, 1442. DOI 10.1016/j.orgel.2009.08.006

[169] Habich, D. B.; Halik, M.; Schmid, G. Cyclic voltammetry on n-alkylphosphonic acid self-assembled monolayer modified large area indium tin oxide electrodes. *Thin Solid Films* **2011**, *519*, 7809-7812. DOI 10.1016/j.tsf.2011.05.013

[170] Hagberg, D. P.; Marinado, T.; Karlsson, K. M.; Nonomura, K.; Qin, P.; Boschloo, G.; Brinck, T.; Hagfeldt, A.; Sun, L. Tuning the HOMO and LUMO Energy Levels of Organic Chromophores for Dye Sensitized Solar Cells. *J. Org. Chem.* **2007**, *72*, 9550. DOI 10.1021/jo701592x

[171] Xu, W.; Peng, B.; Chen, J.; Liang, M.; Cai, F. New Triphenylamine-Based Dyes for Dye-Sensitized Solar Cells. *J. Phys. Chem. C* **2008**, *112*, 874. DOI 10.1021/jp076992d

[172] Whitesides, G. M.; Kriebel, J. K.; Love, J. C. Molecular engineering of surfaces using self-assembled monolayers. *Sci. Prog.* **2005**, *88*(1), 17-48. DOI http://dx.doi.org/10.3184/003685005783238462

[173] Wink, Th.; van Zuilen, S. J.; Bult, A.; van Bennekom, W. P. Self-assembled Monolayers for Biosensors. *Analyst Vol.* **1997**, *122*, 43–50. DOI 10.1039/A606964I

[174] Browne, K. P.; Grzybowski , B. A. Controlling the Properties of Self-Assembled Monolayers by Substrate. *Langmuir* **2011**, *27* (4), 1246–1250. DOI 10.1021/la103960q

[175] Colvin, V. L.; Goldstein, A. N. ; Alivisatos, A. P. Semiconductor Nanocrystals Covalently Bound to Metal Surfaces with Self-Assembled Monolayers. *J. Am. Chem. SOC* **1992**, *114*, 5221-5230. DOI 10.1021/ja00039a038

[176] Faucheux, N.; Schweiss, R.; Lutzow, K.; Werner, C.; Groth, T. Self-assembled monolayers with different terminating groups as model substrates for cell adhesion studies. *Biomaterials* **2004**, *25*, 2721–2730. DOI 10.1016/j.biomaterials.2003.09.069

[177] Chaki, N. K.; Vijayamohanan, K. Self-assembled monolayers as a tunable platform for biosensor applications. *Biosens. Bioelectron.* **2002**, *17*, 1–12. DOI 10.1016/S0956-5663(01)00277-9

[178] Kumar, A.; Biebuyck, H. A.; Whiteside, G. M. Patterning Self-Assembled Monolayers: Applications in Materials Science. *Langmuir* **1994**, *10*, 1498-1511. DOI 10.1021/la00017a030

[179] Bain, C. D.; Troughton, E. B.; Tao, Y. T.; Evall, J.; Whitesides, G. M.; Nuzzo R. G. Formation of monolayer films by the spontaneous assembly of organic thiols from solution onto gold. *J. Am. Chem. Soc.* **1989**, *111*, 321. DOI 10.1021/ja00183a049

[180] Hähner, G.; Wöll, C.; Buchk, M.; Grunze, M. Investigation of Intermediate Steps in the Self-Assembly of n-Alkanethiols on Gold Surfaces by Soft X-ray Spectroscopy. *Langmuir* **1993**, *9*, 1955. DOI 10.1021/la00032a005

[181] Poirier, G. E.; Pylant, E. D. The Self-Assembly Mechanism of Alkanethiols on Au(111). *Science* **1996**, *272*, 1145. DOI http://classic.sciencemag.org/content/272/5265/1145.long

[182] Neouze, M.-A.; Schubert, U. Surface Modification and Functionalization of Metal and Metal Oxide Nanoparticles by Organic Ligands. *Monatsh. Chem.* **2008**, *139*, 183–195. DOI 10.1007/s00706-007-0775-2

[183] Hofer, R.; Textor, M.; Spencer, N. D. Alkyl Phosphate Monolayers, Self-Assembled from Aqueous Solution onto Metal Oxide Surfaces. *Langmuir* **2001**, *17*(13), 4014–4020. DOI 10.1021/la001756e

[184] Moses, P. R.; Wier, L. M.; Lennox, J. C.; Finklea, H. O.; Lenhard, J. R.; Murray, R. W. X-ray photoelectron spectroscopy of alkylaminesilanes bound to metal oxide electrodes. *Anal. Chem.* **1978**, *50*(4), 576–585. DOI 10.1021/ac50026a010

[185] Bonhôte, P.; Gogniat, E.; Tingry, S.; Barbé, C.; Vlachopoulos , N.; Lenzmann , N.; Comte, P.; Grätzel, M. Efficient Lateral Electron Transport inside a Monolayer of Aromatic Amines Anchored on Nanocrystalline Metal Oxide Films. *J. Phys. Chem. B* **1998**, *102*(9), 1498–1507. DOI 10.1021/jp972890j

[186] Wang, J. Q.; Yang, S. R.; Chen, M.; Xue, Q. J. Optical and structural properties of aluminium oxide thin films prepared by a non-aqueous sol–gel technique. *Surf. Coat. Technol.* **2004**, *176*, 229. DOI 10.1007/s10971-011-2505-9

[187] Abelev, E.; Starosvetsky, D.; Ein-Eli, Y. Enhanced Copper Surface Protection in Aqueous Solutions Containing Short-Chain Alkanoic Acid Potassium Salts. *Langmuir* **2007**, *23*, 11281. DOI 10.1021/la701434e

[188] Foster, T. T.; Alexander, M. R.; Leggett, G. J.; McAlpine, E. Friction Force Microscopy of Alkylphosphonic Acid and Carboxylic Acids Adsorbed on the Native Oxide of Aluminum. *Langmuir* **2006**, *22*, 9254. DOI 10.1021/la061082t

[189] Pertays, K. M.; Thompson, G. E.; Alexander, M. R. Self-assembly of stearic acid on aluminium: the importance of oxide surface chemistry. *Surf. Interf. Anal.* **2004**, *36*, 1361. DOI 10.1002/sia.1919

[190] Ball, J. M.; Wobkenberg, P. H.; Colleaux, F.; Heeney, M.; Anthony, J. E.; McCulloch, I.; Bradley, D. D. C.; Anthopoulos, T. D. Solution processed low-voltage organic transistors and complementary inverters. *Appl. Phys. Lett.* **2009**, *95*. DOI http://dx.doi.org/10.1063/1.3212736

[191] Bardecker, J. A.; Ma, H.; Kim, T.; Huang, F.; Liu, M. S.; Cheng, Y. J.; Ting, G.; Jen, A. K. Y. Self-assembled Electroactive Phosphonic Acids on ITO: Maximizing Hole-Injection in Polymer Light-Emitting Diodes. *Adv. Funct. Mater.* **2008**, *18*, 3964. DOI 10.1002/adfm.200800033

[192] Liakos, I. L.; McAlpine, E.; Chen, X. Y.; Newman, R.; Alexander, M. R. Assembly of octadecyl phosphonic acid on the $\alpha - Al_2O_3(0\,0\,0\,1)$ surface of air annealed alumina: Evidence for termination dependent adsorption. *Appl. Surf. Sci.* **2008**, *255*, 3276. DOI 10.1016/j.apsusc.2008.09.037

[193] Hanson, E. L.; Guo, J.; Koch, N.; Schwartz, J.; Bernasek, S. L. Advanced Surface Modification of Indium Tin Oxide for Improved Charge Injection in Organic Devices. *J. Am. Chem. Soc.* **2005**, *127*, 10058. DOI 10.1021/ja050481s

[194] Mutin, P. H.; Guerrero, G.; Vioux, A. Hybrid materials from organophosphorus coupling molecules. *J. Mater. Chem.* **2005**, *15*, 3761-3768. DOI 10.1039/B505422B

[195] Aswal, D. K.; Lenfant, S.; Guerin, D.; Yakhmi, J. V.; Vuillaume, D. Self-assembled monolayers on silicon for molecular electronics. *Anal. Chim. Acta* **2006**, *568*(12), 84-108. DOI 10.1016/j.aca.2005.10.027

[196] Mutin, P. H.; Guerrero, G.; Vioux, A. Organic-inorganic hybrid materials based on organophosphorus coupling molecules: from metal phosphonates to surface modification of oxides. *C. R. Chim.* **2003**, *6*(10), 1153-1164. DOI 10.1016/j.crci.2003.07.006

[197] Pawsey, S.; Yach, K.; Halla, J.; Reven, L. Self-assembled monolayers of alkanoic acids: A solid-state NMR study. *Langmuir* **2000**, *16*(7), 3294-3303. DOI 10.1021/la991273e

[198] Taylor, C. E.; Schwartz, D. K. Octadecanoic acid self-assembled monolayer growth at sapphire surfaces. *Langmuir* **2003**, *19*(7), 2665-2672. DOI 10.1021/la026218b

[199] Hotchkiss, P. J.; Malicki, M.; Giordano, A. J.; Armstrong, N. R.; Marder, S. R. Characterization of phosphonic acid binding to zinc oxide. *J. Mater. Chem.* **2011**, *21*, 3107. DOI 10.1039/C0JM02829K

[200] Pujari, S. P.; Luc Scheres, Antonius T. M. Marcelis, and Han Zuilhof Covalent Surface Modification of Oxide Surfaces. *Angew. Chem. Int. Ed.* **2014**, *53*, 6322 – 6356. DOI 10.1002/anie.201306709

[201] Wood, C.; Li, H.; Winget, P.; Brédas, J.-L. Binding Modes of Fluorinated Benzylphosphonic Acids on the Polar ZnO Surface and Impact on Work Function. *J. Phys. Chem. C* **2012**, *116*(36), 19125-19113. DOI 10.1021/jp3050725

[202] Gliboff, M.; Sang, L.; Knesting, K. M.; Schalnat, M. C.; Mudalige, A.; Ratcliff, E. L.; Li, H.; Sigdel, A. K.; Giordano, A. J.; Berry, J. J; Nordlund, D.; Seidler, G. T.; Brédas, J. L.; Marder, S. R.; Pemberton, J. E.; Ginger, D. S. Orientation of Phenylphosphonic Acid Self-Assembled Monolayers on a Transparent Conductive Oxide: A Combined NEXAFS, PM-IRRAS, and DFT Study. *Langmuir* **2013**, *29*, 2166-2174. DOI 10.1021/la304594t

[203] Breuer, T.; Salzmann, I.; Götzen, J.; Oehzelt, M.; Morherr, A.; Koch, N.; Witte, G. Interrelation between Substrate Roughness and Thin-Film Structure of Functionalized Acenes on Graphite. *Cryst. Growth Des.* **2011**, *11*, 4996-5001. DOI 10.1021/cg200894y

[204] Götzen, J.; Witte, G. Rapid preparation of highly ordered ultraflat ZnO surfaces. *Appl. Surf. Sci.* **2012**, *258*(24), 10144-10147. DOI 10.1016/j.apsusc.2012.06.094

[205] Schreiber, F. Structure and growth of self-assembling monolayers. *Prog. Surf. Sci.* **2000**, *65*, 151–257. DOI 10.1016/S0079-6816(00)00024-1

[206] Langmuir, I. The mechanism of the surface phenomena of flotation. *Trans. Faraday Soc.* **1920**, *15*, 62. DOI 10.1039/TF9201500062

[207] Cyganik, P.; Buck, M.; Strunskus, T.; Shaporenko, A.; Wilton-Ely, J. D. E. T.; Zharnikov, M.; Wöll, C. Competition as a design concept: Polymorphism in self-assembled monolayers of biphenyl-based thiols. *J. Am. Chem. Soc.* **2006**, *128*(42), 13868-13878. DOI 10.1021/ja0640647

[208] Dannenberger, O.; Buck, M.; Grunze, M. J. Self-Assembly of *n*-Alkanethiols: A Kinetic Study by Second Harmonic Generation. *Phys. Chem. B* **1999**, *103*, 2202. DOI 10.1021/jp983433l

[209] Peterlinz, K. A.; Georgiadis, R. In Situ Kinetics of Self-Assembly by Surface Plasmon Resonance Spectroscopy. *Langmuir* **1996**, *12*, 4731. DOI 10.1021/la9508452

[210] Poirier, G. E.; Tarlov, M. J.; Rushmeier, H. E. Two-Dimensional Liquid Phase and the $p \times \sqrt{3}$ Phase of Alkanethiol Self-Assembled Monolayers on Au(1 1 1). *Langmuir* **1994**, *10*, 3383. DOI 10.1021/la00022a004

[211] Bensebaa, F.; Voicu, R.; Huron, L.; Ellis, T. H.; Kruus, E. Kinetics of Formation of Long-Chain *n*-Alkanethiolate Monolayers on Polycrystalline Gold. *Langmuir* **1997**, *13*, 5335. DOI 10.1021/la970052a

[212] Karpovich, D. S.; Blanchard, G. J. Direct Measurement of the Adsorption Kinetics of Alkanethiolate Self-Assembled Monolayers on a Microcrystalline Gold Surface. *Langmuir* **1994**, *10*, 3315. DOI 10.1021/la00021a066

[213] Hanson, E. L. The T-BAG: A novel method for the formation of self-assembled monolayers on metal oxide surfaces. Thesis (Ph.D.). *Princeton University* **2004**.

[214] Hanson, E. L.; Schwartz, J.; Nickel, B.; Koch, N.; Danisman, M. F. Bonding Self-Assembled, Compact Organophosphonate Monolayers to the Native Oxide Surface of Silicon. *Journal of the American Chemical Society* **2003**, *125*(51), 16074-16080. DOI 10.1021/ja035956z

[215] Vega, A.; Thissen, P.; Chabal, Y. J. Environment-Controlled Tethering by Aggregation and Growth of Phosphonic Acid Monolayers on Silicon Oxide. *Langmuir* **2012**, *28*, 8046-8051. DOI dx.doi.org/10.1021/la300709n

[216] Forrest, S. R. Ultrathin Organic Films Grown by Organic Molecular Beam Deposition and Related Techniques. *Chem. Rev.* **1997**, *97*, 1793-1896. DOI 10.1021/cr941014o

[217] Breuer, T.; Witte, G. Thermally activated intermixture in pentacene-perfluoropentacene heterostructures. *J. Chem. Phys.* **2013**, *138*, 114901. DOI http://dx.doi.org/10.1063/1.4795004

[218] Breuer, T.; Witte, G. Diffusion-controlled growth of molecular heterostructures: fabrication of two-, one-, and zero-dimensional C(60) nanostructures on pentacene substrates. *ACS Appl. Mater. Interfaces.* **2013**, *5*(19), 9740-9745. DOI 10.1021/am402868s

[219] Sauerbrey, G. Verwendung von Schwingquarzen zur Wägung dünner Schichten und zur Mikrowägung. *Angew. Chem.* **1957**, *69*, 761. DOI 10.1007/BF01337937

[220] Schreiber, F. Organic molecular beam deposition: Growth studies beyond the first monolayer. *phys. stat. sol. (a)* **2004**, *201*(6), 1037–1054. DOI 10.1002/pssa.200404334

[221] Liu, C.; Wang, S.; Hsieh, J.; Ju, Y. Gas sensing properties of vacuum-deposited titanyl phthalocyanine film. *Sens. Actuators, B* **2000**, *65*, 371–374. DOI 10.1016/S0925-4005(99)00420-7

[222] Mänz, A.; Breuer, T.; Witte, G. Epitaxial TTF-TCNQ Thin Films on KCl(100): New Preparation Methods and Observation of Interface-Mediated Thin Film Polymorph. *Cryst. Growth Des.* **2015**, *151*, 395-403. DOI 10.1021/cg501484p

[223] Budz, H. A.; Biesinger, M. C.; LaPierrea, R. R. Passivation of GaAs by octadecanethiol self-assembled monolayers deposited from liquid and vapor phases. *J. Vac. Sci. Technol. B* **2009**, *27*(2), 637-648. DOI 10.1116/1.3100266

[224] Gerstenberg, M. C.; Schreiber, F.; Leung, T. Y. B.; Bracco, G.; Forrest, S. R. and Scoles, G. Organic semiconducting thin film growth on an organic substrate: 3,4,9,10-perylenetetracarboxylic dianhydride on a monolayer of decanethiol self-assembled on Au(111). *Phys. Rev. B* **2000**, *61*, 7678. DOI http://dx.doi.org/10.1103/PhysRevB.61.7678

[225] TEXample.net http://www.texample.net/tikz/examples/area/physics/

[226] Verhoeven, J. D.; Whan, R. E. (Ed.) Scanning Electron Microscopy in Materials Characterization. *America Society for Metals*, **1986**.

[227] Reimer, L. Scanning Electron Microscopy: Physics of Image Formation and Micro-analysis. 2nd ed. *Springer-Verlag*, Berlin, **1998**.

[228] Goodhew, P. J.; Humphreys, J.; Beanlan, R. Electron Microscopy and Analysis. *Taylor & Fran*, London, **2001**.

[229] Goldstein, J.; Newbury, D. E.; Echlin, P.; Joy, D. C.; Romig Jr., A. D.; Lyman, C. E.; Fiori, C.; Lifshin, E. Scanning Electron Microscopy and X-Ray Microanalysis. *Springer Science & Business Media* **2012**.

[230] Egerton, R. F.; M. Malac, P. Li. Radiation damage in the TEM and SEM. *Micron* **2004**, *35*, 399-409. DOI doi:10.1016/j.micron.2004.02.003

[231] https://upload.wikimedia.org/wikipedia/commons/c/c9/LightLTSEM.jpg

[232] Meyer, E.; Hug, H. J.; Bennewitz, R. Scanning Probe Microscopy. *Springer*, **2003**.

[233] Bubert, H.; Jenett, H. Surface and Thin Film Analysis: A Compendium of Principles, Instrumentation, and Application. *Wiley-VCH Verlag Gmbh*, Weinheim, **2003**.

[234] Oura, K.; Lifshits, V. G.; Saranin, A. A.; Zotov, A. V.; Katayama, M. Surface Science: An introduction. *Springer*, Berlin, **2003**.

[235] Binning, G.; Quate, C. F.; Gerber, C. Atomic Force Microscope. *Physical Review Letters*, **1986**, *56*, 930. DOI http://dx.doi.org/10.1103/PhysRevLett.56.930

[236] Grütter, P.; Hofer, R.; Rosei, R. Properties of Single Organic Molecules on Crystal Surfaces. *Imperal College Press*, **2006**.

[237] http://usa.jpk.com/index.download.c46f64176d66c310620d0c4bdf4be7ef

[238] Wallace, J. M. Applications of Atomic Force Microscopy for the Assessment of Nanoscale Morphological and Mechanical Properties of Bone. *Bone*, **2012**, *50*(1), 420-427. DOI http://dx.doi.org/10.1016/j.bone.2011.11.008

[239] Young, T. An Essay on the Cohesion of Fluids. *Philos. Trans. R. Soc. Lond.* **1805**, textit95, 65-87. DOI 10.1098/rstl.1805.0005

[240] Yuan, Y.; Lee, T. R. Surface Science Techniques, Springer Series in Surface Sciences 51. *Springer-Verlag* **2013**.

[241] Butt, H.-J.; Kappl, M. Surface and interfacial forces. *WILEY-VCH*, Weinheim **2010**.

[242] Henzler, M.; Göppel, W. Oberflächenphysik des Festkörpers, 2. *Teubner Studienbücher*, Stuttgart, **1994**.

[243] Nalva, H. S. Handbook of Thin Film Materials, 2. *Akademic Press*, **2002**.

[244] Götzen, J.; Witte, G. Rapid preparation of highly ordered ultraflat ZnO surfaces. *Appl. Surf. Sci.* **2012**, *258*, 10144-10147. DOI 10.1016/j.apsusc.2012.06.094

[245] Bashir, A.; Käfer, D.; Wöll, C.; Terfort, A.; Witte, G. Selenium as a Key Element for Highly Ordered Aromatic Self-Assembled Monolayers. *Angew. Chem.* **2008**, *47*, 5250. DOI 10.1002/anie.200800883

[246] http://periodictable.com/Elements/030/data.html

[247] Birkholz, M.; Fewster, P. F.; Genzel, C.; Birkholz, M. (Hrsg.) Thin Film Analysis by X-Ray Scattering. *Wiley VHC*, Weinheim **2006**.

[248] Pietsch, U.; Holy, V.; Baumbach, T. High-Resolution X-Ray Scattering: From Thin Films to Lateral Nanostructures, 2nd Edition. *Springer*, New York **2004**.

[249] Karthäuser, A. Heterogrowth of Crystalline Organic Films: Preparation, Characterization and Interface Properties. Master thesis. *Philipps-Universität Marburg* **2015**.

[250] Stöhr, J.; Gomer, R. (Hrsg.) NEXAFS Spectroscopy. *Springer* **1992**.

[251] Hähner, G. Near edge X-ray absorption fine structure spectroscopy as a tool to probe electronic and structural properties of thin organic films and liquids. *Chem. Soc. Rev* **2006**, *35*, 1244-1255. DOI 10.1039/b509853j

[252] Nefedov, A.; Wöll, C. Surface Science Techniques: Advanced Applications of NEXAFS Spectroscopy for Functionalized Surfaces. *Springer Series in Surface Sciences* **2013**, *51*, 277-303. Chapter 10

[253] NIST Electron Inelastic Mean Free Path Database (Version 1.1) *U.S. Secretary of Commerce* **2010**. NIST Electron Inelastic-Mean-Free-Path Database

[254] Breuer, T.; Klues, M.; Witte, G. Characterization of orientational order in π-conjugated molecularthin films by NEXAFS *"flash desorption"* measurements from single crystal surfaces. *J. Electron Spectrosc. Relat. Phenom.* **2015**, *204*, 102-115. DOI http://dx.doi.org/10.1116/1.570537

[255] Helmholtz-Zentrum Berlin (HZB) http://www.helmholtz-berlin.de

[256] Electron storage ring BESSY II https://www.helmholtz-berlin.de/

[257] Energy diagram http://www.texample.net/tikz/examples/area/physics/

[258] Hähner, G. Near edge X-ray absorption fine structure spectroscopy as a tool to probe electronic and structural properties of thin organic films and liquids. *Chem. Soc. Rev.* **2006**, *11*, 1244-1255. DOI 10.1039/B509853J

[259] Moulder, J. F.; Chastain, J.; King, R. C. Handbook of x-ray photoelectron spectroscopy: A reference book of standard spectra for identification and interpretation of XPS data. *Eden Prairie and Minn: Physical Electronics* **1995**.

[260] Hufner, S., Photoelectron Spectroscopy: principles and applications, 3 ed. *Springer-Verlag* **2003**.

[261] Hofman, S. Auger- and x-ray photoelectron spectroscopy in materials science: A user-oriented guide, vol. 49 of Springer series in surface sciences. *Physics and astronomy online library*, Berlin and Heidelberg **2013**.

[262] Tanuma, S.; Powel, C. J.; Penn, D. R. Calculations of electron inelastic mean free paths for 31 materials. *Surf. Interface Anal.*, **1998**, *11*, 577. DOI 10.1002/sia.740111107

[263] XPS detection

[264] Välkner, J. Investigation of the Thermal Stability and Structure of Stilbenedithiol on Gold. Master thesis. *Philipps-Universität Marburg* **2014**.

[265] Schmidt, C. Eigenschaften fuorierter Aromaten an Metall/Organik-Grenzflächen. Dissertation. *Philipps-Universität Marburg* **2012**.

[266] Shirley, D. A. High-Resolution X-Ray Photoemission Spectrum of the Valence Bands of Gold. *Phys. Rev. B* **1982**, *5*, 4709-4714. DOI http://dx.doi.org/10.1103/PhysRevB.5.4709

[267] Baer, D. R.; Engelhard, M. H.; Gaspar, D. J.; Lea A. S.; Windisch Jr. C. F. Use and limitations of electron flood gun control of surface potential during XPS: two non-homogeneous sample types. *Surf. Interface Anal.* **2002**, *33*, 781–790 DOI 10.1002/sia.1454

[268] Schirley, D. A. High-Resolution X-Ray Photoemission Spectrum of the Valence Bands of Gold. *Phys. Rev. B* **1972**, *5*, 4709-4714. DOI http://dx.doi.org/10.1103/PhysRevB.5.4709

[269] Friel, J. J. X-ray and image analysis in electron microscopy. *Princeton Gamma-Tech* **1995**. .

[270] Russ, J. C. Fundamentals of Energy Dispersive X-ray Analysis.*Butterworths*, London **1984**.

[271] Heywood, V. H. Scanning Electron Microscopy. *Academic Press* , London, New York The Netherlands .

[272] Verhulst, H. EDAX Genesis EDS Short Course Lecture Notes. *EDAX* The Netherlands **2008**.

[273] Gottfried, J. M. CO Oxidation over Gold. *FU Berlin*, Diss. **2003**.

[274] Käfer, D. Characterization and Optimization of Growth and Electronic Structure of Organic Thin Films for Applications in Organic Electronics. *Ruhr-University Bochum*, Diss. **2008**.

[275] Lüth, H.; Lüth, H. (Hrsg.)Solid Surfaces, Interfaces and Thin Films. *Springer*, Diss. **2001**.

[276] Kolasinski, Surface Science. *John Wiley and Son Ltd* **2007**.

[277] Masel, R. I. Principles of Adsorption and Reaction on Solid Surfaces. *Wiley*, New York, **1996**.

[278] Clark, A. The Theory of Adsorption and Catalysis. *Academic Press*, London, **1970**.

[279] Nilsson, A.; Pettersson, L. G. M.; Jens, K. N. Chemical Bonding at Surfaces and Interfaces. *Elsevier* **2008**.

[280] de Jong, A.; Niemantsverdriet, J. Thermal desorption analysis: Comparative test of ten commonly applied procedures. *Surf. Sci.* **1990**, *233*, 355-365. DOI 10.1016/0039-6028(90)90649-S

[281] King, D. A. THERMAL DESORPTION FROM METAL SURFACES: A REVIEW. *Surf. Sci.* **1975**, *47*, 384. DOI 10.1016/0039-6028(75)90302-7

[282] Gaines Jr, G. L. The Ion-exchange Properties of Muscovite Mica. *J. Phys. Chem.* **1957**, *61*, 1408–1413. DOI 10.1021/j150556a033

[283] Redhead, P. Thermal desorption of gases. *Vacuum* **1962**, *12*, 203-211. DOI 10.1016/0042-207X(62)90978-8

[284] Schmidt, C.; Götzen, J.; Witte, G. Temporal Evolution of Benzenethiolate SAMs on Cu(100). *Langmuir* **2011**, *27*, 1025. DOI 10.1021/la103533h

[285] Fichthorn, K. A.; Miron, R. A. Thermal Desorption of Large Molecules from Solid Surfaces. *Phys. Rev. Lett.* **2002**, *89*, 196103. DOI http://dx.doi.org/10.1103/PhysRevLett.89.196103

[286] Götzen, J.; Schwalb, C. H.; Schmidt, C.; Mette, G.; Marks, M.; Höfer, U.; Witte, G. Structural Evolution of Perfluoro-Pentacene Films on Ag(1 1 1): Transition from 2D to 3D Growth. *Langmuir* **2011**, *27*(3), 993-999. DOI 10.1021/la1022664

[287] Feulner, P.; Menzel, D. FSimple ways to improve *"flash desorption"* measurements from single crystal surfaces. *Journal of Vacuum Science and Technology 17* **1980**, *2*, 662-663. DOI http://dx.doi.org/10.1116/1.570537

[288] Meyer, J.; Hamwi, S.; Kröger, M.; Kowalsky, W.; Riedl, T.; Kahn, A. Transition Metal Oxides for Organic Electronics: Energetics, Device Physics and Applications. *Adv. Mater.* **2012**, *24*(40), 5408-5427. DOI 10.1002/adma.201201630

[289] Fortunato, E. M. C.; Barquinha, P. M. C.; Pimentel, A. C. M. B. G.; Goncalves, A. M. F.; Marques, A. J. S.; Martins, R. F. P.; Pereira, L. M. N. Wide-bandgap high-mobility ZnO thin-film transistors produced at room temperature. *Appl. Phys. Lett.* **2004**, *85*(13), 2541-2543. DOI http://dx.doi.org/10.1063/1.1790587

[290] Park, J. S.; Maeng, W. J.; Kim, H. S.; Park, J. S. Review of recent developments in amorphous oxide semiconductor thin-film transistor devices. *Thin Solid Films* **2012**, *520*(6), 1679-1693. DOI 10.1016/j.tsf.2011.07.018

[291] Pal, B. N.; Sun, J.; Jung, B. J.; Choi, E.; Andreou, A. G.; Katz, H. E. Pentacene-Zinc Oxide Vertical Diode with Compatible Grains and 15-MHz Rectification. *Adv. Mater.* **2008**, *20*, 1023–1028. DOI 10.1002/adma.200701550

[292] Love, J. C.; Estroff, L. A.; Kriebel, J. K.; Nuzzo, R. G.; Whitesides, G. M. Self-assembled monolayers of thiolates on metals as a form of nanotechnology. *Chem. Rev.* **2005**, *105*(4), 1103-1169. DOI 10.1021/cr0300789

[293] Perkins, C. L. Molecular Anchors for Self-Assembled Monolayers on ZnO: A Direct Comparison of the Thiol and Phosphonic Acid Moieties. *J. Phys. Chem. C* **2009**, *113*(42), 18276–18286. DOI 10.1021/jp906013r

[294] Chen, J.; Ruther, R. E.; Tan, Y.; Bishap, L. M. Hamers, R. J. Molecular Adsorption on ZnO($10\bar{1}0$) Single-Crysta Surfaces: Morphology and Charge Transfer. *Langmuir* **2012**, *28*, 10437-10445. DOI 10.1021/la301347t

[295] Pawsey, S.; Yach, K.; Reven, L. Self-Assembly of Carboxyalkylphosphonic Acids on Metal Oxide Powders. *Langmuir* **2002**, *18*, 5205-5212. DOI 10.1021/la015749h

[296] Zhang, B.; Kong, T.; Xu, W.; Su, R.; Gao, Y.; Cheng, G. Surface Functionalization of Zinc Oxide by Carboxyalkylphosphonic Acid Self-Assembled Monolayers. *Langmuir* **2010**, *26*(6), 4514–4522. DOI 10.1021/la9042827

[297] Timpel, M.; Nardi, M. V.; Krause, S.; Ligorio, G.; Christodoulou, C.; Pasquali, L.; Giglia, A.; Frisch, J.; Wegner, B.; Moras, P.; Koch, N. Surface Modification of ZnO(0001)–Zn with Phosphonate-Based Self-Assembled Monolayers: Binding Modes, Orientation, and Work Function. *Chem. Mater.* **2014**, *26*(17), 5042–5050. DOI 10.1021/cm502171m

[298] Lange, I.; Reiter, S.; Pätzel, M.; Zykov, A.; Nefedov, A.; Hildebrandt, J.; Hecht, S.; Kowarik, S.; Wöll, C.; Heimel, G.; Neher, D. Tuning the Work Function of Polar Zinc Oxide Surfaces using Modifed Phosphonic Acid Self-Assembled Monolayers. *Adv. Funt. Mater* **2014**, *24*, 7014-7024. DOI 10.1002/adfm.201401493

[299] Nam, S.-H.; Kim, M.-H.; Yoo, D. G.; Jeong, S. H.; Kim, D. Y.; Lee, N.-E.; Boo, J.-H. Metal-doped ZnO thin films: synthesis, etching characteristic, and application test for organic light emitting diode (OLED) devices. *Surf. Rev. Lett.* **2010**, *17*(1), 121-127. DOI 10.1142/S0218625X10014065

[300] Palacios-Lidn, E.; Pickup, D.E.; Johnson, P.S.; Ruther, R.E.; Tena-Zaera, R.; Hamers, R.J.; Colchero, J.; Himpsel, F.J.; Ortega, J.E.; Rogero, C. Face-Selective Etching of ZnO during Attachment of Dyes. *J. Phys. Chem. C.* **2013**, *117*, 18414-18422. DOI 10.1021/jp4045447

[301] Sakthivel, S.; Neppolian, B.; Shankar, M. V.; Arabindoo, B.; Palanichamy, M.; Murugesan, V. Solar photocatalytic degradation of azo dye: comparison of photocatalytic efficiency of ZnO and TiO_2. *Sol. Energy Mater. Sol. Cells* **2003**, *77*, 65-82. DOI 10.1016/S0927-0248(02)00255-6

[302] Gouva, C. A. K.; Wypych, F.; Moraes, S. G.; Durn, N.; Nagata, N.; Peralta-Zamora, P. Semiconductor-assisted photocatalytic degradation of reactive dyes in aqueous solution. *Chemosphere* **2000**, *40*, 433-440. DOI 10.1016/S0045-6535(99)00313-6

[303] Sharma, A.; Haldi, A.; Hotchkiss, P. J.; Marder, S. R. and Kippelen, B. Effect of phosphonic acid surface modifiers on the work function of indium tin oxide and on the charge injection barrier into organic single-layer diodes. *J. Appl. Phys.* **2009**, *105*, 074511. DOI http://dx.doi.org/10.1063/1.3095490

[304] Furbeth, W.; Stratmann, M. The delamination of polymeric coatings from electrogalvanised steel – a mechanistic approach: Part 1: delamination from a defect with intact zinc layer. *Corros. Sci.* **2001**, *43*, 207–227. DOI 10.1016/S0010-938X(00)00047-0

[305] Khranovskyy, V.; Ekblad, T.; Yakimova, R.; Hultman, L. Surface morphology effects on the light-controlled wettability of ZnO nanostructures. *Appl. Surf. Sci.* **2012**, *258*(20), 8146-8152. DOI 10.1016/j.apsusc.2012.05.011

[306] Duta, L.; Popescu, A. C.; Zgura, I.; Preda, N.; Mihailescu, I. N. Wettability of Nanostructured Surfaces. "Wetting and Wettability" Aliofkhazraei M. (ed) *InTech* **2015**. DOI 10.5772/60808

[307] Chickos J. S.; Acree Jr., W. E. Enthalpies of Sublimation of Organic and Organometallic Compounds. 1910–2001. *J. Phys. Chem. Ref. Data* **2002**, *31*, 537. http://dx.doi.org/10.1063/1.1475333

[308] Johns, I. B.; McElhill, E. A.; Smith, J. O. Thermal Stability of Some Organic Compounds. *J. Chem. Eng. Data* **1962**, *7*(2), 277-281. DOI 10.1021/je60013a036

[309] Johns, I. B.; McElhill, E. A.; Smith, J. O. Thermal Stability of Organic Compounds. *Ind. Eng. Chem. Prod. Res. Dev.* **1962**, *1*(1), 2-6. DOI 10.1021/i360001a001

[310] Martin, K. J.; Squattrito, P. J.; Clearfield, A. The Crystal and Molecular Structure of Zinc Phenylphosphonate. *Inorg. Chim. Acta* **1989**, *155*(11), 7-9. DOI 10.1016/S0020-1693(00)89271-3

[311] Gerbier, P.; Guerrerin, C.; Henner, B.; Unal, J.-R. An organometallic route to zinc phosphonates and theirintercalates. *J. Mater. Chem.* **1999**, *9*, 2559-2565. DOI 10.1039/A902854D

[312] Scott, K. J.; Zhang, Y.; Wang, R.-C.; Clearfeld, A. Synthesis, Characterisation, and Amine Intercalation Behavior of Zinc Phosphite Phenylphosphonate Mixed Derivatives. *Chem. Mater.* **1995**, *7*, 1095-1102. DOI 10.1021/cm00054a008

[313] Giannozzi, P.; Baroni, S.; Bonini, N.; Calandra, M.; Car, R.; Cavazzoni, C.; Ceresoli, D.; Chiarotti, G. L.; Cococcioni, M.; Dabo, I.; Dal Corso, A.; de Gironcoli, S.; Fabris, S.; Fratesi, G.; Gebauer, R.; Gerstmann, U.; Gougoussis, C.; Kokalj, A.; Lazzeri, M.; Martin-Samos, L.; Marzari, N.; Mauri, F.; Mazzarello, R.; Paolini, S.; Pasquarello, A.; Paulatto, L.; Sbraccia, C.; Scandolo, S.; Sclauzero, G.; Seitsonen, A. P.; Smogunov, A.; Umari, P.; Wentzcovitch, R. M. QUANTUM ESPRESSO: A Modular and Open-Source Software Project for Quantum Simulations of Materials. *J. Phys.: Condens. Matter* **2009**, *21*, 395502. DOI 10.1088/0953-8984/21/39/395502

[314] Perdew, J. P.; Burke, K.; Ernzerhof, M. Generalized Gradient Approximation Made Simple. *Phys. Rev. Lett.* **1996**, *77*, 3865-3868. DOI http://dx.doi.org/10.1103/PhysRevLett.77.3865

[315] Grimme, S.; Antony, J.; Ehrlich, S.; Krieg, H. A Consistent and Accurate Ab Initio Parametrization of Density Functional Dispersion Correction (DFT-D) for the 94 Elements H-Pu. *J. Chem. Phys.* **2010**, *132*, 154104. DOI 10.1063/1.3382344

[316] Vanderbilt, D. Soft Self-Consistent Pseudopotentials in a Generalized Eigenvalue Formalism. *Phys. Rev.* B **1990**, *41*, 7892-7895. DOI http://dx.doi.org/10.1103/PhysRevB.41.7892

[317] Meyer, B.; Marx, D.; Dulub, O.; Diebold, U.; Kunat, M.; Langenberg, D.; Wöll, C. Partial Dissociation of Water Leads to Stable Superstructures on the Surface of Zinc Oxide. *Angew. Chem. Int. Ed.* **2004**, *430*, 6641-6645. DOI 10.1002/anie.200461696

[318] Meyer, B.; Rabaa, H.; Marx, D. Water Adsorption on $ZnO(10\bar{1}0)$: From Single Molecules to Partially Dissociated Monolayers. *Phys. Chem. Chem. Phys.* **2006**, *8*, 1513-1520. DOI 10.1039/b515604a

[319] Killian, M.S.; Seiler, S.; Wagner, V.; Hahn, R.; Ebensperger, C.; Meyer, B.; Schmuki, P. Interface Chemistry and Molecular Bonding of Functional Ethoxysilane-Based Self-Assembled Monolayers on Magnesium Surfaces. ACS Appl. Mater. Interfaces 2015, 7, 9006-9014. DOI 10.1021/am5075634

[320] Stumm, W. COORDINATION CHEMISTRY OF WEATHERING: Kinetics of the Surface-Controlled Dissolutidn of Oxide Minerals. *Rev. Geophys* **1990**, *28*(1), 53-69. DOI 10.1021/jp0570317

[321] Taratula, O.; Galoppini, E.; Wang, D.; Chu, D.; Zhang, Z.; Chen, H.; Saraf, G.; Lu, Y. Binding Studies of Molecular Linkers to ZnO and MgZnO Nanotip Films. *J. Phys. Chem. B* **2006**, *110*, 6506-6515. DOI 10.1029/RG028i001p00053

[322] Arun, S. W.; Jeong, S. Y. Chemically Bonded Phosphate Ceramics: I, A Dissolution Model of Formation.*J. Am. Ceram. Soc.* **2003**, *86*(11), 1834-1844. DOI 10.1111/j.1151-2916.2003.tb03569.x

[323] Han, J.; Qiu, W.; Gao, W. Potential dissolution and photo-dissolution of ZnO thin Films. *J. Hazard. Mater.* **2010**, *178*, 115-122. DOI 10.1016/j.jhazmat.2010.01.050

[324] Horiuchi, H.; Katoh, R.; Hara, K.; Yanagida, M.; Murata, S.; Arakawa, H.; Tachiya, M. Electron Injection Efficiency from Excited N3 into Nanocrystalline ZnO Films: Effect of (N3-Zn2+) Aggregate Formation. *J. Phys. Chem. B.* **2003**, *107*, 2570-2574. DOI 10.1021/jp0220027

[325] Gerischer, H.; Sorg, N. Chemical dissolution of oxides: Experiments with sintered ZnO pellets and ZnO single crystals. *Werkst. Korros.* **1991**, *42*, 149-157. DOI 10.1039/B505422B

[326] Gerischer, H.; Sorg, N. Chemical dissolution of zinc oxide crystals in aqueous electrolyte – an analysis of the kinetics. *Electrochim. Acta* **1992**, *37*(5), 827-235. DOI 10.1016/0013-4686(92)85035-J

[327] Mariano, A. N.; Hanneman, R. E. Crystallographic Polarity of ZnO Crystals. *J. Appl. Phys.* **1963**, *34*, 384. DOI http://dx.doi.org/10.1063/1.170261

[328] Brown Jr., G. E.; Henrich, V.; Casey, W.; Clark, D.; Eggleston, C.; Felmy, A; Goodman, D. W.; Grätzel, M.; Maciel, G.; McCarthy, M. I.; Nealson, K. H.; Sverjensky, D.; Toney, M.; Zachara, J. M. Metal Oxide Surfaces and Their Interactions with

Aqueous Solutions and Microbial Organisms. *Chem. Rev.* **1999**, *99*, 77-174. DOI 10.1021/cr980011z

[329] Zhu, J.; Emanetoglu, N. W.; Chen, Y.; Yanshinskiy B. V.; Lu, Y. Wet-Chemical Etching of $(11\bar{2}0)$ ZnO Films. *J. Electron. Mater* **2004**, *33*(6), DOI 10.1007/s11664-004-0046-5

[330] Valtiner, M.; Torrelles, X.; Pareek, A.; Borodin, S.; Gies, H.; Grundmeier G. In Situ Study of the Polar ZnO(0001)-Zn Surface in Alkaline Electrolytes. *J. Phys. Chem. C* **2010**, *114*, 15440-15447. DOI 10.1021/jp1047024

[331] Persson, P.; Ojamäae, L. Periodic Hartree-Fock study of the adsorption of formic acid on ZnO $(10\bar{1}0)$. *Chem. Phys. Lett.* **2000**, *321*, 302-308. DOI 10.1016/S0009-2614(00)00347-X

[332] Castelli, I. E.; Thygesen, K. S.; Jacobsen, K. W. Calculated Pourbaix Diagrams of Cubic Perovskites for Water Splitting: Stability Against Corrosion. *Top. Catal.* **2014**, *57*, 265–272. DOI 10.1007/s11244-013-0181-4

[333] Reichle, R. A.; McCurdy, K. G.; Hepler, L. G. Zinc Hydroxide: Solubility Product and Hydroxy-complex Stability Constants from $12.5 - 75°$ C. *J. Chem.* **1975**, *53*, 3841. DOI 10.1139/v75-556

[334] Keis, K.; Bauer, C.; Boschloo, G.; Hagfeldt, A.; Westermark, K.; Rensmo, H.; Siegbahn, H. Nanostructures ZnO electrodes for dye-sensitizes colar cell application. *J. Photochem. Photobiol., A* **2002**, *148*, 57-64. DOI 10.1016/S1010-6030(02)00039-4

[335] Degen, A.; Kosec, M. Eect of pH and impurities on the surface charge of zinc oxide in aqueous solution. *J. Eur. Ceram. Soc.* **2000**, *20*, 667-673. DOI 10.1016/S0955-2219(99)00203-4

[336] Schwertmann, U. Solubility and dissolution of iron oxides. *Plant Soil* **1991**, *130*, 1-25. DOI 10.1007/BF00011851

[337] Gerischer, H. Neglected problems in the pH dependence of the flatband potential of semiconducting oxides and semiconductors covered with oxide layers. *Electrochim. Acta* **1989**, *34*(8), 1005-1009. DOI 10.1007/BF00011851

[338] Schreiber, F. Self-assembled monolayers: from 'simple' model systems to biofunctionalized interfaces. *J. Phys.: Condens. Matter* **2004**, *16*, 881-900. DOI 10.1088/0953-8984/16/28/R01

[339] Kind, M.; Wöll, C. Organic surfaces exposed by self-assembled organothiol monolayers: Preparation, characterization, and application. *Prog. Surf. Sci.* **2009**, *84*, 230-278. DOI 10.1016/j.progsurf.2009.06.001

[340] Alloway, D. M.; Hofmann, M.; Smith, D. L.; Gruhn, N. E.; Graham, A. L.; Colorado, R.; Wysocki, V. H.; Lee, T. R.; Lee, P. A.; Armstrong, N. R. Interface Dipoles Arising from Self-Assembled Monolayers on Gold: UV-Photoemission Studies of Alkanethiols and Partially Fluorinated Alkanethiols. *J. Phys. Chem. B* **2003**, *107*, 11690-11699. DOI 10.1021/jp034665+

[341] Zangmeister, C. D.; Picraux, L. B.; van Zee, R. D.; Yao, Y. X.; Tour, J. M. Energy-level alignment and work function shifts for thiol-bound monolayers of conjugated molecules self-assembled on Ag, Cu, Au, and Pt. *Chem. Phys. Lett.* **2007**, *442*, 390-393. DOI 10.1016/j.cplett.2007.06.012

[342] Heimel, G.; Rissner, F.; Zojer, E. Modeling the Electronic Properties of π-Conjugated Self-Assembled Monolayers. *Adv. Mater.* **2010**, *22*, 2494-2513. DOI 10.1002/adma.200903855

[343] Boudinet, D.; Benwadih, M.; Qi, Y. B.; Altazin, S.; Verilhac, J. M.; Kroger, M.; Serbutoviez, C.; Gwoziecki, R.; Coppard, R.; Le Blevennec, G.; Kahn, A.; Horowitz, G. Modification of gold source and drain electrodes by self-assembled monolayer in staggered n- and p-channel organic thin film transistors. *Org. Electron.* **2010**, *11*, 227-237. DOI 10.1016/j.orgel.2009.10.021

[344] Fortunato, E.; Ginlex, D.; Hosono, H.; Paine, D.C. Transparent Conducting Oxides for Photovoltaics. *MRS Bulletin* **2007**, *32*, 242-247. DOI http://dx.doi.org/10.1557/mrs2007.29

[345] Liu, H.Y.; Avrutin, V.; Izyumskaya, N.; Ozgur, U.; Morkoc, H. Transparent conducting oxides for electrode applications in light emitting and absorbing devices. *Superlatt. Microstruct.* **2010**, *48*, 458-484. DOI 10.1016/j.spmi.2010.08.011

[346] Cornil, D.; Regemorter, T.V.; Beljonne, D.; Cornil, J. Work function shifts of a zinc oxide surface upon deposition of self-assembled monolayers: a theoretical insight. *Phys.Chem.Chem.Phys.* **2014**, *16*, 20887-20899. DOI 10.1039/C4CP02811B

[347] Moreira, N. H.; Rosa, A. L.; Frauenheim, T. Covalent functionalization of ZnO surfaces: A density functional tight binding study. *Appl. Phys. Lett.* **2009**, *94*, 193109. DOI http://dx.doi.org/10.1063/1.3132055

[348] Tian, X.; Xu, J.; Xie, W. Controllable Modulation of the Electronic Structure of ZnO($10\bar{1}0$) Surface by Carboxylic Acids. *J. Phys. Chem. C* **2010**, *114*, 3973-3980. DOI 10.1021/jp908517j

[349] Liang, Y.; Thorne, J. E.; Kern, M. E.; Parkinson, B. A. Sensitization of ZnO Single Crystal Electrodes with CdSe Quantum Dots. *Langmuir* **2014**, *30*, 12551-12558. DOI 10.1021/la5023888

[350] Sadik, P. W.; Pearton, S. J.; Norton, D. P. Functionalizing Zn- and O-terminated ZnO with thiols. *J. Appl. Phys.* **2007**, *101*, 104514. DOI http://dx.doi.org/10.1063/1.2736893

[351] Kedem, N.; Blumstengel, S.; Henneberger, F.; Cohen, H.; Hodes, G.; Cahen, D. Morphology-, synthesis- and doping-independent tuning of ZnO work function using phenylphosphonates. *Phys.Chem.Chem.Phys.* **2014**, *16*, 8310-8319. DOI 10.1039/C3CP55083D

[352] Timpel, M.; Nardi, M. V.; Ligorio, G.; Wegner, B.; Pätzel, M.; Kobin, B.; Hecht, S.; Koch, N. Energy-Level Engineering at ZnO/Oligophenylene Interfaces with Phosphonate-Based Self-Assembled Monolayers. *Appl. Phys. Lett.* **2015**, *106*, 113302. DOI 0.1021/acsami.5b01669

[353] Lange, I.; Reiter, S.; Kniepert, J.; Piersimoni, F.; Pätzel, M.; Hildebrandt, J.; Brenner, T.; Hecht, S.; Neher, D. Zinc oxide modified with benzylphosphonic acids as transparent electrodes in regular and inverted organic solar cell structures. *Appl. Phys. Lett.* **2015**, *106*, 113302. DOI http://dx.doi.org/10.1063/1.4916182

[354] Braid, J.L.; Koldemir, U.; Sellinger, A.; Collins, R. T.; Furtak, T. E.; Olson, D. C. Conjugated Phosphonic Acid Modified Zinc Oxide Electron Transport Layers for Improved Performance in Organic Solar Cells. *ACS Appl. Mater. interfaces* **2014**, *6*, 19229-19234. DOI 10.1021/am505182c

[355] Bulusu, A.; Paniagua, S. A.; MacLeod, B. A.; Sigdel, A. K.; Berry, J. J.; Olson, D. C.; Marder, S. R.; Graham, S. Efficient Modification of Metal Oxide Surfaces with Phosphonic Acids by Spray Coating. *Langmuir* **2013**, *29*, 3935-3942. DOI 10.1021/la303354t

[356] Lim, M. S.; Smiley, K. J.; Gawalt, E. S. Thermally Driven Stability of Octadecylphosphonic Acid Thin Films Grown on Stainless Steel SS316L. *SCANNING* **2010**, *32*, 304–311. DOI 10.1002/sca.20192

[357] Gleskova, H.; Gupta, S.; Sutta, P. Structural changes in vapour-assembled n-octylphosphonic acid monolayer with post-deposition annealing: Correlation with bias-induced transistor instability. *Org. Electron.* **2013**, *14*, 3000-3006. DOI 10.1016/j.orgel.2013.08.025

[358] Meyer B.; Marx, D. Density-functional study of the structure and stability of ZnO surfaces. *Phys. Rev.* B **2003**, *67*, 035403. DOI http://dx.doi.org/10.1103/PhysRevB.67.035403

[359] Meyer, B.; Marx, D. Density-functional study of Cu atoms, monolayers, and coadsorbates on polar ZnO surfaces. *Phys. Rev. B* **2004**, *69*, 235420. DOI http://dx.doi.org/10.1103/PhysRevB.69.235420

[360] XPS database. http://www.xpsdata.com/HB2_demo.pdf

[361] Schmidt, C.; Götzen, J.; Witte, G. Temporal Evolution of Benzenethiolate SAMs on Cu(100). *Langmuir* **2011**, *27*, 1025–1032. DOI 10.1021/la103533h

[362] Söhnchen, A.; Lukas, S.; Witte, G. Epitaxial growth of pentacene films on Cu(110). *J. Chem. Phys.* **2004**, *121*, 525-534. DOI http://dx.doi.org/10.1063/1.1760076

[363] Tsud, N.; Yoshitake, M. Vacuum vapour deposition of phenylphosphonic acid on amorphous alumina. *Surf. Sci.* **2007**, *601*, 3060-3066. 10.1016/j.susc.2007.05.007

[364] Yagyu, S.; Yoshitake, M.; Tsud, N.; Chikyow, T. Adsorption structure of phenylphosphonic acid on an alumina surface. *Appl. Surf. Sci.* **2009**, *256*, 1140-1143. DOI 10.1016/j.apsusc.2009.05.110

[365] Wagstaffe, M.; Thomas, A. G.; Jackman, M. J.; Torres-Molina, M.; Syres, K. L.; Handrup, K. An Experimental Investigation of the Adsorption of a Phosphonic Acid on the Anatase $TiO_2(1\,0\,1)$ Surface. *J. Phys. Chem. C* **2016**, *120*, 1693–1700. DOI 10.1021/acs.jpcc.5b11258

[366] Wang, Y.; Muhler, M.; Wöll, C. Spectroscopic evidence for the partial dissociation of H_2O on $ZnO(10\bar{1}0)$. *Phys. Chem. Chem. Phys.* **2006**, *8*, 1521-1524. DOI 10.1039/b515489h

[367] Xie, R.; Sekiguchi, T.; Ishigaki, T.; Ohashi, N.; Li, D.; Yang, D.; Liu, B.; Bando, Y. Enhancement and patterning of ultraviolet emission in ZnO with an electron beam. *Appl. Phys. Lett.* **2006**, *88*, 134103. DOI http://dx.doi.org/10.1063/1.2189200

[368] Gliboff, M.; Li, H.; Knesting, K. M.; Giordano, A. J.; Nordlund, D.; Seidler, G. T.; Brédas, J. L.; Marder, A. R.; Ginger, D. S. Competing Effects of Fluorination on the Orientation of Aromatic and Aliphatic Phosphonic Acid Monolayers on Indium Tin Oxide. *J. Phys. Chem. C* **2013**, *117*, 15139–15147. DOI 10.1021/jp404033e

[369] Heister, K.; Rong, H. T.; Buvk, M.; Zharnikov, M., Grunze, M.; johansson, L. S. O. Odd-Even Effects at the S-Metal Interface and in the Aromatic Matrix of Biphenyl-Substituted Alkanethiol Self-Assembled Monolayers. *J. Phys. Chem. B* **2001**, *105*, 6888. DOI 10.1021/jp010180e

[370] Cyganik, P.; Buck, M.; Azzam, W.; Wöll, C. Self-Assembled Monolayers of ω-Biphenylalkanethiols on Au(1 1 1): Influence of Spacer Chein on Molecular Packing. *J. Phys. Chem. B* **2004**, *108*, 4989-4996. DOI 10.1021/jp037307f

[371] Ulman, A. Formation and Structure of Self-Assembled Monolayers. *Chem. Rev.* **1996**, *96*, 1533. DOI 10.1021/cr9502357

[372] Adams, D. M.; Brus, L.; Chidsey, C. E. D.; Creager, S.; Creutz, C.; Kagan, C. R.; Kamat, P. V.; Lieberman, M.; Lindsay, S.; Marcus, R. A. *et al.* Charge Transfer on the Nanoscale: Current Status. *J. Phys. Chem. B* **2003**, *107* (28), 6668. DOI 10.1021/jp0268462

[373] Flood, A. H.; Stoddart, J. F.; Steuerman, D. W.; Heath, J. R. Whence Molecular Electronics? *Science* **2004**, *306*, 2055. DOI 10.1126/science.1106195

[374] Nitzan, A. Electron Transmission through Molecules and Molecular Interfaces. *Annu. ReV. Phys. Chem.* **2001**, *52*, 681-750. DOI 10.1146/annurev.physchem.52.1.681

[375] Hill, I. G.; Rajagopal, A.; Kahn, A.; Hu, Y. Molecular Level Alignment at Organic Semiconductor-Metal Interfaces. *Appl. Phys. Lett.* **1998**, *73*, 662-664. DOI http://dx.doi.org/10.1063/1.121940

[376] Blumstengel, S.; Glowatzki, H.; Sadofev, S.; Koch, N.; Kowarik, S.; Rabe, J. P.; Henneberger, F. Band-Offset Engineering in Organic/inorganic Semiconductor Hybrid Structures. *Phys. Chem. Chem. Phys.* **2010**, *12*, 11642-11646. DOI 10.1039/c004944c

[377] Jee, S. H.; Kim, S. H.; Ko, J. H.; Kim, D.-J.; Yoon, Y. S. Wet Chemical Surface Modification of ITO by a Self Assembled Monolayer for an Organic Thin Film Transistor. *J. Ceram. Process. Res.* **2008**, *9*(1), 42-45. DOI 5493d6540cf25de74db4fa53

[378] Munoz, A.; Chetty, N.; Richard, M. Martin Modification of heterojunction band offsets by thin layers at interfaces: Role of the interface dipole. *Phys. Rev. B* **1990**, *41*, 5. DOI http://dx.doi.org/10.1103/PhysRevB.41.2976

[379] Greiner, M. T.; Helander, M. G.; Tang W.-M.; Wang, Z.-B.; Qiu, J.; Lu, Z.-H. Universal energy-level alignment of molecules on metal oxides. *Nature Materials* **2012**, *11*, 76–81. DOI 10.1038/nmat3159

[380] Salinas, M.; Jager, C. M.; Amin, A. Y.; Dral, P. O.; Meyer-Friedrichsen, T.; Hirsch, A.; Clark, T.; Halik, M. The Relationship between Threshold Voltage and Dipolar Character of Self-Assembled Monolayers in Organic Thin-Film Transistors. *J. Am. Chem. Soc* **2012**, *134*(30), 12648–12652. DOI 10.1021/ja303807u

[381] Knupfera, M.; Paasch, G. Origin of the interface dipole at interfaces between undoped organic semiconductors and metals. *J. Vac. Sci. Technol. A* **2005**, *23*, 1072. DOI 10.1116/1.1885021

[382] Crispin, X. Interface dipole at organic/metal interfaces and organic solar cells. *Sol. Energy Mater.* **2004**, *83*, 147–168. DOI 10.1016/j.solmat.2004.02.022

[383] Witte, G.; Lukas, S.; Bagus, P. S. , Wöll, C. Vacuum level alignment at organic/metal junctions: "Cushion" effect and the interface dipole. *Appl. Phys. Lett.* **2005**, *87*, 263502. DOI http://dx.doi.org/10.1063/1.2151253

[384] Cheng, X.; Noh, Y.-Y.; Wang, J.; Tello, M.; Frisch, J.; Blum, R.-P.; Vollmer, A.; Rabe, J. P.; Koch, N.; Sirringhaus, H. Controlling Electron and Hole Charge Injection in Ambipolar Organic Field-Effect Transistors by Self-Assembled Monolayers. *Adv. Funct. Mater.* **2009**, *19*, 2407. DOI 10.1002/adfm.200900315

[385] Paniagua, S. A.; Hotchkiss, P. J.; Jones, S. C.; Marder, S. R.; Mudalige, A.; Marrikar, F. S.; Pemberton, J. E.; Armstrong, N. R. J. Phosphonic Acid Modification of Indium-Tin Oxide Electrodes: Combined XPS/UPS/Contact Angle Studies. *Phys. Chem. C* **2008**, *112*, 7809. DOI 10.1021/jp710893k

[386] Blakely, J. M. Introduction to the Properties of Crystal Surfaces: International Series on Materials Science and Technology. *Elsevier* **2013**.

[387] Rusu, P. C.; Brocks, G. Surface Dipoles and Work Functions of Alkylthiolates and Fluorinated Alkylthiolates on Au($\bar{1}\bar{1}\bar{1}$). *J. Phys. Chem. B* **2006**, *110*, 22628-22634. DOI 10.1021/jp0642847

[388] Zehner, R. W.; Parsons, B. F.; Hsung, R. P.; Sita L. R. Tuning the Work Function of Gold with Self-Assembled Monolayers Derived from X-[C_6H_4-C≡C-]$_n C_6H_4$-SH (n = 0, 1, 2; X = H, F, CH_3, CF_3, and OCH_3). *Langmuir* **1999**, *15*, 1121-1127. DOI 10.1021/la981114f

[389] Rong, H. T.; Frey, S.; Yang, Y. J.; Zharnikov, M.; Buck, M.; Wühn, M.; Wöll, C.; Helmchen, G. On the Importance of the Headgroup Substrate Bond in Thiol Monolayers: A Study of Biphenyl-Based Thiols on Gold and Silver. *Langmuir* **2001**, *17*, 1582. DOI 10.1021/la0014050

[390] Azzam, W.; Cyganik, P.; Witte, G.; Buck, M.; Wöll, C. Pronounced Odd-Even Changes in the Molecular Arrangement and Packing Density of Biphenyl-Based Thiol SAMs: A Combined STM and LEED Study. *Langmuir* **2003**, *19*, 8262. DOI 10.1021/la030165w

[391] Long, Y. T.; Rong, H. T.; Buck, M.; Grunze, M. Odd–even effects in the cyclic voltammetry of self-assembled monolayers of biphenyl based thiols. *J. Electroanal. Chem.* **2002**, *524*, 62-67. DOI 10.1016/S0022-0728(02)00711-8

[392] Felgenhauer, T.; Rong, H. T.; Buck, M. Electrochemical and exchange studies of self-assembled monolayers of biphenyl based thiols on gold. *J. Electroanal. Chem.* **2003**, *550*, 309-319. DOI 10.1016/S0022-0728(03)00139-6

[393] Alloway, D. M.; Graham, A. L.; Yang, X.; Mudalige, A.; Colorado, R.; Wysocki, V. H.; Pemberton, J. E.; Lee, T. R.; Wysocki, R. J.; Armstrong, N. R. Tuning the Effective Work Function of Gold and Silver Using ω-Functionalized Alkanethiols: Varying Surface Composition through Dilution and Choice of Terminal Groups. *J. Phys. Chem. C* **2009**, *113*, 20328. DOI 10.1021/jp909494r

[394] Hu, W. S.; Tao, Y. T.; Hsu, Y. J.; Wei, D. H.; Wu, Y. S. Molecular Orientation of Evaporated Pentacene Films on Gold: Alignment Effect of Self-Assembled Monolayer. *Langmuir* **2005**, *21*, 2260-2266. DOI 10.1021/la047634u

[395] Wang, W. Y.; Lee, T.; Reed, M. A. J. Elastic and Inelastic Electron Tunneling in Alkane Self-Assembled Monolayers. *Phys. Chem. B* **2004**, *108*, 18398–18407. DOI 10.1021/jp048904k

[396] Käfer, D.; Witte, G.; Cyganik, P.; Terfort, A.; Wöll, Ch. A Comprehensive Study of Self-Assembled Monolayers of Anthracenethiol on Gold: Solvent Effects, Structure, and Stability. *J. Am. Chem. Soc.* **2006**, *128*, 1723. DOI 10.1021/ja0571592

[397] Sang, L.; Mudalige, A.; Sigdel, A. K.; Giordano, A. J.; Marder, S. R.; Berry, J. J.; Pemberton, J. E. PM-IRRAS Determination of Molecular Orientation of Phosphonic Acid Self-Assembled Monolayers on Indium Zinc Oxide. *Langmuir* **2015**, *31*(20), 5603-5613. DOI 10.1021/acs.langmuir.5b00129

[398] Prathima, N.; Harini, M.; Rai, N.; Chandrashekara, R. H.; Ayappa, K. G.; Sampath, S.; Biswas, S. K. Thermal Study of Accumulation of Conformational Disorders in the Self-Assembled Monolayers of C_8 and C_{18} Alkanethiols on the Au(1 1 1) Surface. *Langmuir* **2005**, *21*(6), 2364–2374. DOI 10.1021/la048654z

[399] Fenter, P.; Eisenberger, P.; Liang K. S. Chain-length dependence of the structures and phases of $CH_3(CH_2)_{n-1}SH$ self-assembled on Au(1 1 1). *Phys. Rev. Lett. 70*, 2447. DOI http://dx.doi.org/10.1103/PhysRevLett.70.2447

[400] Quinones, R.; Rodriguez, K.; Iuliucci, R. J. Investigation of phosphonic acid surface modifications on zinc oxide nanoparticles under ambient conditions. *Thin Solid Films* **2014**, *565*, 155-164. DOI 10.1016/j.tsf.2014.06.057

[401] Wang, M.; Li, X.; Lin, H.; Pechy, P.; Zakeeruddin, S. M.; Grätzel, M. Passivation of nanocrystalline TiO_2 junctions by surface adsorbed phosphinate amphiphiles enhances the photovoltaic performance of dye sensitized solar cells. *Dalton Trans.* **2009**, *45*, 10015-10020. DOI 10.1039/B908673K

[402] Marinado, T.; Hahlin, M.; Jiang, X.; Quintana, M.; Johansson, E. M. J.; Gabrielsson, E.; Plogmaker, S.; Hagberg, D. P.; Boschloo, G.; Zakeeruddin, Grätzel, M.; Siegbahn, H.; Sun, L.; Hagfeldt, A.; Rensmo, H. Surface Molecular Quantification and Photo-electrochemical Characterization of Mixed Organic Dye and Coadsorbent Layers on TiO$_2$ for Dye-Sensitized Solar Cells. *J. Phys. Chem. C* **2010**, *114*, 11903–11910. DOI 10.1021/jp102381x

[403] Shen, H.; Lin, H.; Liu, Y.; Li, X.; Zhang, J.; Wang, N.; Li, J. A novel diphenylphos-phinic acid coadsorbent for dye-sensitized solar cell. *Electrochim. Acta* **2011**, *56*, 2092-2097. DOI 10.1016/j.electacta.2010.11.087

[404] Allegrucci, A.; Lewcenko, N. A.; Mozer, A. J.; Dennany, L.; Wagner, P.; Officer, D. L.; Sunahara, K.; Moric, S.; Spiccia, L. Improved performance of porphyrin-based dye sensitised solar cells by phosphinic acid surface treatment. *Energy Environ. Sci.* **2009**, *2*, 1069-1073. DOI 10.1039/B909709K

[405] López-Durante, I.; Wang, M.; Humphry-Baker, R.; Ince, M.; Martínez-Díaz, M. V.; Nazeeruddin, M. K.; Torres, T.; Grätzel, M. Molecular Engineering of Zinc Phthalocyanines with Phosphinic Acid Anchoring Groups. *Angew. Chem. Int. Ed.* **2012**, *51*, 1895-1898. DOI Angew. Chem. Int. Ed.

[406] Guerrero, G.; Mutin, P. H.; Vioux, A. Anchoring of Phosphonate and Phosphinate Coupling Molecules on Titania Particles. *Chem. Mater.* **2001** , *13*(11), 4367-4373. DOI 10.1021/cm001253u

[407] Collinsova, M.; Jirócek, J. Phosphinic Acid Compounds in Biochemistry, Biology and Medicine. *Curr. Med. Chem.* **2000**, *7*, 629-647. DOI 10.2174/0929867003374831

[408] Mutin, P. H.; Guerrero, G.; Vioux, A. Hybrid materials from organophosphorus coupling molecules. *J. Mater. Chem.,* **2005**, *15*, 3761-3768. DOI 10.1039/b505422b

[409] Mehring, M.; Lafond, V.; Mutin, P. H.; Vioux, A. New Sol-Gel Routes to Organic-Inorganic Hybrid Materials: Modification of Metal Alkoxide by Phos-phonic or Phosphinic Acids. *J. Sol-Gel Sci. Technol.* **2003**, *26*, 99-102. DOI 10.1023/A:1020797520620

[410] Guerrero, G.; Mutin, P. H.; Vioux, A. Mixed Nonhydrolytic/Hydrolytic Sol-Gel Routes to Novel Metal Oxide/Phosphonate Hybrids. *Chem. Mater.* **2000**, *12*, 1268-1272. DOI 10.1021/cm991125+

[411] Nishihama, S.; Sakaguchi, N.; Hirai, T.; Komasawa, I. Extraction and separation of rare earth metals using microcapsules containing bis(2-ethylhexyl)phosphinic acid. *Hydrometallurgy* **2002**, *64*, 35-42(8). DOI http://dx.doi.org/10.1016/S0304-386X(02)00011-7

[412] Kubotaa, F.; Gotoa, M.; Nakashioa, F.; Hanob, T.Extraction Kinetics of Rare Earth Metals with 2-Ethylhexyl Phosphonic Acid Mono-2-ethylhexyl Ester Using a Hollow Fiber Membrane Extractor. *Sep. Sci. Technol.* **1995**, *30*, 777-792. DOI 10.1080/01496399508013891

[413] Nilsing, M.; Presson, P.; Ojamäe, L. Anchor group influence on molecule–metal oxide interfaces: Periodic hybrid DFT study of pyridine bound to TiO_2 via carboxylic and phosphonic acid. *Chem. Phys. Lett.* **2005**, *415*, 375-380. DOI 10.1016/j.cplett.2005.08.154

[414] NIST Mass Spec Data Center http://webbook.nist.gov/cgi/cbook.cgi?ID=C65850&Mask=200

[415] Lenz, T.; Schmaltz, T.; Novac, M.; Halik, M. Self-Assembled Monolayer Exchange Reactions as a Tool for Channel Interface Engineering in Low-Voltage Organic Thin-Film Transistors. *Langmuir* **2012**, *28*(39), 13900-13904. DOI 10.1021/la3027978

[416] Bauer, T.; Schmaltz, T.; Lenz, T.; Halik, M.; Meyer, B.; Clark, T. Phosphonate- and Carboxylate-Based Self-Assembled Monolayers for Organic Devices: A Theoretical Study of Surface Binding on Aluminum Oxide with Experimental Support. *ACS Appl. Mater. Interfaces* **2013**, *5*(3), 6073-6080. DOI 10.1021/am4008374

[417] Rajadurai, S. Pathways for Carboxylic Acid Decomposition on Transition Metal Oxides. *Catal. Rev.: Sci. Eng.* **1994**, *36*, 3. DOI 10.1080/01614949408009466

[418] Deng, S.-Z-; Fan, H.-M.; Wang , M.; Zheng, M. R.; Yi, J.-B.; Wu, R.-Q.; Tan, H.-R.; Sow, C.-H.; Ding, J.; Feng, Y.-P.; Loh, K.-P. Thiol-Capped ZnO Nanowire/Nanotube Arrays with Tunable Magnetic Properties at Room Temperature. *ASC Nano* **2010**, *4*(1), 495–505. DOI 10.1021/nn901353x

[419] Rhodes, C. L.; Lappi, S.; Fischer, D.; Sambasivan, S.; Genzer, J.; Franzen, S. Characterization of monolayer formation on aluminum-doped zinc oxide thin films. *Langmui* **2008**, *24*(2), 433–440. DOI 10.1021/la701741m

[420] Black, A. J.; Paul, K. E.; Aizenberg, J.; Whitesides, G. M. Patterning Disorder in Monolayer Resists for the Fabrication of Sub-100-nm Structures in Silver, Gold, Silicon, and Aluminum. *J. Am. Chem. Soc.* **1999**, *121*, 8356-8365. DOI 10.1021/ja990858s

[421] Aizenberg, J.; Black, A. J.; Whitesides, G. M. Controlling local disorder in self-assembled monolayers by patterning the topography of their metallic supports. *Nature* **1998**, *394*, 868-871. DOI 10.1038/29730

[422] Holleman, A. F.; Wiberg, E.; Wiberg, N. Lehrbuch der Anorganischen Chemie, 102nd Ed., *Walter de Gruyter & Co.*, Berlin, New York, **2007**.

[423] Geoffroy, M.; Lucken, E. A. C. The electron spin resonance spectrum of X-irradiated phenylphosphinic acid and its salts. *Molec. Phys.* **1972**, *24*, 335-340. DOI 10.1080/00268977200101481

[424] Shieh, M.; Martin, K. J.; Squattrito, P. J.; Clearfield, A. New Low-Dimensional Zinc Compounds Containing Zinc-Oxygen-Phosphorus Frameworks: Two-Layered Inorganic Phosphites and a Polymeric Organic Phosphinate. *Inorg. Chem.* **1990**, *29*, 958-963. DOI 10.1021/ic00330a012

[425] Plaschke, M.; Rothe, J.; Denecke, M.A.; Fanghanel, T. Soft X-ray spectromicroscopy of humic acid europium(III) complexation by comparison to model substances. *J. Electron Spectrosc.* **2004**, *135*, 53-62. DOI 10.1016/j.elspec.2003.12.007

[426] Plaschke, M.; Rothe, J.; Altmaier, M.; Denecke, M. A.; Fanghänel, T. Near edge X-ray absorption fine structure (NEXAFS) of model compounds for the humic acid/actinide ion interaction. *J. Electron Spectrosc. Relat. Phenom.* **2005**, *148*, 151–157. DOI 10.1016/j.elspec.2005.05.001

[427] Behyan, S.; Hu, Y.; Urquhart, S. G. Sulfur 1s near-edge x-ray absorption fine structure (NEXAFS) of thiol and thioether compounds. *J. Chem. Phys.* **2011**, *134*, 244304. DOI 10.1063/1.3602218

[428] Schmidt, C.; Witt, A.; Witte, G. Tailoring the Cu(100) Work Function by Substituted Benzenethiolate Self-Assembled Monolayers. *J. Phys. Chem. A* **2011**, *115*, 7234–7241. DOI dx.doi.org/10.1021/jp200328r

[429] Solomon, D.; Lehmann, J.; Kinyangi, J.; Liang, B.; Heymann, K.; Dathe, L.; Hanley, K. Carbon (1s) NEXAFS Spectroscopy of Biogeochemically Relevant Reference Organic Compounds. *Soil Sci. Soc. Am. J.* **2008**, *73*, 1817-1830. DOI 10.2136/sssaj2008.0228

[430] Lenz, T.; Schmaltz, T.; Novak, M.; Halik, M. Self-Assembled Monolayer Exchange Reactions as a Tool for Channel Interface Engineering in Low-Voltage Organic Thin-Film Transistors. *Langmuir* **2012**, *28* (39), 13900–13904. DOI 10.1021/la3027978

[431] Bauer, T.; Schmaltz, T.; Lenz, T.; Halik, M.; Meyer, B.; Clark, T. Phosphonate- and Carboxylate-Based Self-Assembled Monolayers for Organic Devices: A Theoretical Study of Surface Binding on Aluminum Oxide with Experimental Support. *ACS Appl. Mater. Interfaces* **2013**, *5*(13), 6073–6080. DOI 10.1021/am4008374

[432] Ko, K. H.; Lee, Y. C.; Jung, Y. J. Enhanced efficiency of dye-sensitized TiO_2 solar cells (DSSC) by doping of metal ions. *J. Colloid Interface Sci.* **2005**, *283*, 482-487. DOI 10.1016/j.jcis.2004.09.009

[433] O'Regan, B.; Grätzel, M. A low-cost, high-efficiency solar cell based on dye-sensitized colloidal TiO_2 films. *Nature* **1991**, *353*, 737-740. DOI 10.1038/353737a0

[434] Reddy, P. Y.; Giribabu, L.; Lyness, C.; Snaith, H. J.; Vijaykumar, C.; Chandrasekharam, M.; Lakshmikantam, M.; Yum, J.-H.; Kalyanasundaram, K.; Grätzel, M. et al. Efficient sensitization of nanocrystalline TiO_2 films by a near-IR-absorbing unsymmetrical zinc phthalocyanine. *Angew. Chem., Int. Ed* **2007**, *46*, 373-376. DOI 10.1002/anie.200603098

[435] Crossland, E. J. W.; Noel, N.; Sivaram, V.; Leijtens, T.; Alexander-Webber, J. A.; Snaith, H. J. Mesoporous TiO_2 single crystals delivering enhanced mobility and optoelectronic device performance. *Nature* **2013**, *495*, 215-219. DOI 10.1038/nature11936

[436] Thomas, A. G.; Syres, K. L. Adsorption of organic molecules on rutile TiO_2 and anatase TiO_2 single crystal surfaces. *Chem. Soc. Rev.* **2012**, *41*, 4207. DOI 10.1039/c2cs35057b

[437] Frank, A. J.; Kopidakis, N.; van de Lagemaat, J. Electrons in nanostructured TiO$_2$ solar cells: transport, recombination and photovoltaic properties. *Coord. Chem. Rev.* **2004**, *248*, 1165-1179. DOI 10.1016/j.ccr.2004.03.015

[438] Panda, M. K.; Ladomenou, K.; Coutsolelos, A. G. Porphyrins in bio-inspired transformations: Light-harvesting to solar cell. *Coord. Chem. Rev.* **2012**, *256*, 2601–2627. DOI 10.1016/j.ccr.2012.04.041

[439] Péhy, P.; Rotzinger, F. P.; Nazeeruddin, M. K.; Kohle, O.; Zakeeruddin, S. M.; Humphry-Baker, R.; Grätzel, M. Preparation of phosphonated polypyridyl ligands to anchor transition-metal complexes on oxide surfaces: application for the conversion of light to electricity with nanocrystalline TiO$_2$ films. *J. Chem. Soc., Chem. Commun.* **1995**, *1*, 65-66. DOI 10.1039/C39950000065

[440] Bose, S.; Soni, V.; Genwa, K. R. Recent Advances and Future Prospects for Dye Sensitized Solar Cells: A Review. *International Journal of Scientific and Research Publications (IJSRP)* **2015**, *5*. ISSN 2250-3153

[441] Morandeira, A.; López-Duarte, I.; Martínez-Díaz, V.; O'Regan, B.; Shuttle, C.; Haji-Zainulabidin, N. A.; Torres, T.; Palomares, E.; Durrant, J. R. Slow Electron Injection on Ru-Phthalocyanine Sensitized TiO$_2$. *J. Am. Chem. Soc.* **2007**, *129*, 9250-9251. DOI 10.1021/ja0722980

[442] He, J.; Hagfeldt, A.; Lindquist, S.-E.; Grennberg, H.; Korodi, F.; Sun, L.; Åkermark, B. Phthalocyanine-Sensitized Nanostructured TiO$_2$ Electrodes Prepared by a Novel Anchoring Method. *Langmuir* **2001**, *17*, 2743-2747. DOI 10.1021/la001651b

[443] Machado, A. E. H. ; França, M. D.; Velani, V. ; Magnino, G. A. ; Velani, H. M. M. ; Freitas, F. S. ; Müller Jr., P. S. ; Sattler, C. ; Schmucker, M. Characterization and Evaluation of the Efficiency of TiO$_2$/Zinc Phthalocyanine Nanocomposites as Photocatalysts for Wastewater Treatment Using Solar Irradiation. *Int. J. Photoenergy* **2008**, *2008*, Article ID 482373. DOI 10.1155/2008/482373

[444] Murakoshi, K.; Kano, G.; Wada, Y.; Yanagida, S.; Miyazaki, H.; Matsumoto, M.; Murasawa, S.; Electroanal. J. Importance of binding states between photosensitizing molecules and the TiO$_2$ surface for efficiency in a dye-sensitized solar cell. *J. Electroanal. Chem.* **1995**, *396*, 27–34. DOI 10.1016/0022-0728(95)04185-Q

[445] Robertson, N. Optimizing dyes for dye-sensitized solar cells. *Angew. Chem. Int. Ed.* **2006**, *45*, 2338–2345. DOI 10.1002/anie.200503083

[446] Mayor, L. C.; Ben Taylor, J.; Magnano, G.; Rienzo, A.; Satterley, C. J.; O'Shea, J. N.; Schnadt, J. Photoemission, resonant photoemission, and X-ray absorption of a Ru(II) complex adsorbed on rutile TiO$_2$(1 1 0) prepared by in situ electrospray deposition. *J. Chem. Phys.* **2008**, *129*, 114701. DOI http://dx.doi.org/10.1063/1.2975339

[447] Britton, A. J.; Weston, M.; O'Shea, J. N. Charge transfer from an aromatic adsorbate to a semiconductor TiO$_2$ surface probed on the femtosecond time scale with resonant inelastic X-ray scattering. *Phys. Rev. Lett.* **2012**, *109*, 017401. DOI 10.1103/PhysRevLett.109.017401

[448] Sauvage, F. A Review on Current Status of Stability and Knowledge on Liquid Electrolyte-Based Dye-Sensitized Solar Cells. *Adv. Chem.* **2014**, Article ID 939525. DOI 10.1155/2014/939525

[449] Katono, M.; Bessho, T.; Wielopolski, M.; Marszalek, M.; Moser, J.-E.; Humphry-Baker, R.; Zakeeruddin, S. M.; Gratzel, M. Influence of the Anchoring Modes on the Electronic and Photovoltsic Properties of D-π-A Dyes. *J. Phys. Chem. C* **2012**, *116*, 16876-16884. DOI dx.doi.org/10.1021/jp304490a

[450] Costaa, D.; Pradierb, C.-M.; Tielensc, F.; Savio, L. Adsorption and self-assembly of bio-organic molecules at model surfaces: A route towards increased complexity. *Surf. Sci. Rep.* **2015**, *70*, 449–553. DOI 10.1016/j.surfrep.2015.10.002

[451] Paz, Y. Self-assembled monolayers and titanium dioxide: From surface patterning to potential applications. *Beilstein J. Nanotechnol.* **2011**, *2*, 845–861. DOI 10.3762/bjnano.2.94

[452] Luschtinetz, R.; Gemming, S.; Seifert G. Anchoring functional molecules on TiO_2 surfaces: A comparison between the carboxylic and the phosphonic acid group. *EPJ Plus* **2011**, *126*, 98. DOI 10.1140/epjp/i2011-11098-4

[453] Woodward, J. T.; Ulman, A.; Schwartz, D. K. Self-Assembled Monolayer Growth of Octadecylphosphonic Acid on Mica. *Langmuir* **1996**, *12*, 3626-3629. DOI 10.1021/la9510689

[454] Yee, C.; Kataby, G.; Ulman, A.; Prozorov, T.; White, H.; King, A.; Rafailovich, M.; Sokolov, J.; Gedanken, A. Self-Assembled Monolayers of Alkanesulfonic and -phosphonic Acids on Amorphous Iron Oxide Nanoparticles. *Langmuir* **1999**, *15*, 7111-7115. 10.1021/la990663y

[455] Luschtinetz, R.; Frenzel, J.; Milek, T.; Seifert, G. Adsorption of phosphonic acid at the TiO_2 anatase (1 1 0) and rutile (1 1 0) surfaces. *J. Phys. Chem. C* **2009**, *113*, 5730-5740. DOI 10.1021/jp8110343

[456] Ambrosio, F.; Martsinovich, N.; Troisi, A. Effect of the anchoring group on electron injection: theoretical study of phosphonated dyes for dye-sensitized solar cells. *J. Phys. Chem. C* **2012**, *116*, 2622-2629.DOI 10.1021/jp209823t

[457] Nilsing, M.; Lunell, S.; Persson, P. Ojamäe, L. Phosphonic acid adsorption at the TiO_2 anatase (1 0 1) surface investigated by periodic hybrid HF-DFT computations. *Surf. Sci.* **2005**, *582*, 49. DOI 10.1016/j.susc.2005.02.044

[458] Nilsing, M.; Persson, P.; Lunell, S. Ojamäe, L. Dye-Sensitization of the TiO_2 Rutile (1 1 0) Surface by Perylene Dyes: Quantum-Chemical Periodic B3LYP Computations. *J. Phys. Chem. C* **2007**, *111*, 12116-12123. DOI 10.1021/jp072253l

[459] O'Rourke, C.; Bowler, D. R. DSSC anchoring groups: a surface dependent decision. *Phys, J. Condens. Matter* **2014**, *26*, 195302. DOI 10.1088/0953-8984/26/19/195302

[460] Wagstaffe, M.; Thomas, A. G.; Jackman, M. J.; Torres-Molina, M.; Syres, K. L.; Handrup, K. An Experimental Investigation of the Adsorption of a Phosphonic Acid on the Anatase TiO$_2$(110) Surface. *J. Phys. Chem. C* **2016**, *120*, 1693-1700. 10.1021/acs.jpcc.5b11258

[461] Brodard-Severac, F.; Guerrero, G.; Maquet, J.; Florian, P.; Gervais, C.; Hubert, P. M. High-Field17O MAS NMR Investigation of Phosphonic Acid Monolayers on Titania. *Chem. Mater.* **2008**, *20*(16), 5191–5196. DOI 10.1021/cm8012683

[462] Guerrero, G.; Mutin, P. H.; Vioux, A. Anchoring of Phosphonate and Phosphinate Coupling Molecules on Titania Particles. *Chem. Mater.* **2001**, *13*(11), 4367–4373. DOI 10.1021/cm001253u

[463] Kanta, A.; Sedev, R.; Ralston, J. The formation and stability of self-assembled monolayers of octadecylphosphonic acid on titania. *Colloids Surf., A* **2006**, *291*, 51-58. DOI 10.1016/j.colsurfa.2005.12.057

[464] Aslan, A.; Bozkurta, A. Nanocomposite polymer electrolyte membranes based on poly(vinylphosphonic acid)/ TiO$_2$ nanoparticles. *J. Mater. Res.* **2012**, *27*, 3090-3095. DOI 10.1557/jmr.2012.385

[465] Diebold, U.; Madey, T. E. TiO$_2$ by XPS. *Surf. Sci. Spectra* **1998**, *4*, 3. DOI 10.1116/1.1247794

[466] XPS database http://xpssimplified.com/elements/carbon.php

[467] Thompson, T. L.; Yates, J. T. Jr. Surface Science Studies of the Photoactivation of TiO$_2$-New Photochemical Processes. *Chem. ReV.* **2006**, *106*, 4428. DOI 10.1021/cr050172k

[468] Serpone, N. Is the Band Gap of Pristine TiO$_2$ Narrowed by Anion- and Cation-Doping of Titanium Dioxide in Second-Generation Photocatalysts? *J. Phys. Chem. B* **2006**, *110*, 24287. DOI 10.1021/jp065659r

[469] Templeton, A; Wang, X.; Penn, S. J.; Webb, S. J.; Cohen, L. F.; Alford, N. McN. Microwave Dielectric Loss of Titanium Oxide. *J. Am. Ceram. Soc.* **2000**, *83*(1), 95–100. DOI 10.1111/j.1151-2916.2000.tb01154.x

[470] Andrade, A.; Morcelli, A.; Lobo, R. Deformation and fracture of an alpha/beta titanium alloy. *Revista Matéria* **2010**, *15*, 364-370. http://www.scielo.br/pdf/rmat/v15n2/38.pdf

[471] Baufeld, B.; Brandl E.; van der Biest, O. Wire based additive layer manufacturing: Comparison of microstructure and mechanical properties of Ti–6Al–4V components fabricated by laser-beam deposition and shaped metal deposition. *J. Mater. Process. Technol.* **2011**, *211*, 1146-1158. DOI 10.1016/j.jmatprotec.2011.01.018

[472] Brandl, E.; Palm, F.; Michailov, V.; Viehweger, B.; Leyens, C. Mechanical properties of additive manufactured titanium (Ti–6Al–4V) blocks deposited by a solid-state laser and wire. *Materials and Design* **2011**, *32*, 4665–4675. DOI 10.1016/j.matdes.2011.06.062

[473] Li, M.; Hebenstreit, W.; Diebold, U.; Tyryshkin, A. M.; Bowman, M. K.; Dunham, G. G.; Henderson, M. A. The Influence of the Bulk Reduction State on the Surface Structure and Morphology of Rutile $TiO_2(1\,1\,0)$ Single Crystals. *J. Phys. Chem. B*. **2000**, *104*, 4944-4950. DOI 10.1021/jp9943272

[474] Bechstein, R.; Kitta, M.; Schütte, J.; Kühnle, A.; Onishi, H. Surface Reconstruction Induced by Transition Metal Doping of Rutile Titanium Dioxide$(1\,1\,0)$. *J. Phys. Chem. C*. **2009**, *113*, 13199–13203. DOI 10.1021/jp901626b

[475] Onishi, H.; Iwasawa, Y. Dynamic Visualization of a Metal-Oxide-Surface/Gas-Phase Reaction: Time-Resolved Observation by Scanning Tunneling Microscopy at 800 K. *Phys. Rev. Lett.* **1996**, *76*, 791. DOI http://dx.doi.org/10.1103/PhysRevLett.76.791

[476] Onishi, H.; Iwasawa, Y. Reconstruction of $TiO_2(1\,1\,0)$ surface: STM study with atomic-scale resolution. *Sur. Sci.* **1994**, *313*, 783-789. DOI 10.1016/0039-6028(94)91146-0

[477] Baumard , J. F.; Tani, E. Thermoelectric power in reduced pure and Nb-doped TiO_2 rutile at high temperature. *phys. stat. sol. (a)* **1977**, *39*, 373-382. DOI 10.1002/pssa.2210390202

[478] Castell, M. Scanning tunneling microscopy of reconstructions on the $SrTiO_3(0\,0\,1)$ surface. *Surf. Sci.* **2002**, *505*, 1-13. DOI 10.1016/S0039-6028(02)01393-6

[479] Sheppard, L. R.; Atanacio, A. J.; Bak, T.; Nowotny, J.; Prince, K. E. Bulk Diffusion of Niobium in Single-Crystal Titanium Dioxide. *J. Phys. Chem. B* **2007**, *111*, 8126-8130. DOI 10.1021/jp0678709

[480] Kitahara, M.; Shimasaki, Y.; Matsuno, T.; Kuroda, Y.; Shimojima, A.; Wada, H.; Kuroda, K. The Critical Effect of Niobium Doping on the Formation of Mesostructured TiO_2: Single-Crystalline Ordered Mesoporous Nb-TiO_2 and Plate-like Nb-TiO_2 with Ordered Mesoscale Dimples. *Chem. Eur.J.* **2015**, *21*,13073 –13079. DOI 10.1002/chem.201501509

[481] Jeonga, B.-S.; Heoa, Y. W.; Nortona, D. P.; Hebard A. F. Structure and composition of secondary phase particles in cobalt-doped TiO_2 films. *Physica B* **2005**, *370*, 46–51. DOI 10.1016/j.physb.2005.08.036

[482] Setvín, M.; Daniel, B.; Mansfeldova, V.; Kavan, L.; Scheiber, P.; Fidler, M.; ichael Schmid, M.; Diebold, U. Surface preparation of TiO_2 anatase $(1\,0\,1)$: Pitfalls and how to avoid them. *Surf. Sci.* **2014**, *626*, 61-67. DOI 10.1016/j.susc.2014.04.001

[483] Sasahara, A.; Tomitori, M. XPS and STM Study of Nb-Doped $TiO_2(1\,1\,0) - (1 \times 1)$ Surfaces. *J. Phys. Chem. C* **2013**, *117*(34), 17680–17686. DOI 10.1021/jp4057576

[484] Atanacio, A. J.; Bak, T.; Nowotny, J. Niobium Segregation in Niobium-Doped Titanium Dioxide (Rutile). *J. Phys. Chem. C* **2014**, *118*(21), 11174–11185. DOI 10.1021/jp4110536

[485] Sheppard, L. R. Niobium Surface Segregation in Polycrystalline Niobium-Doped Titanium Dioxide. *J. Phys. Chem. C* **2013**, *117*(7), 3407–3413. DOI 10.1021/jp311392d

[486] Bernasik, A.; Rekas, M.; Sloma, M.; Weppner, W. Electrical surface versus bulk properties of Fe-doped TiO_2 single crystals. *Solid State Ionics* **1994**, *72*, 12-18. DOI 10.1016/0167-2738(94)90118-X

[487] Ikeda, J. A. S.; Chiang, Y.-M.; Garratt-Reed, A. J.; Vander Sande, J. B. Space Charge Segregation at Grain Boundaries in Titanium Dioxide: II, Model Experiments. *J. Am. Ceram. Soc.* **1993**, *76*, 2447-2459. DOI 10.1111/j.1151-2916.1993.tb03965.x

[488] Meyer, R.; Waser, R.; Helmbold, J.; Borchardt, G. Cationic Surface Segregation in Donor-Doped $SrTiO_3$ Under Oxidizing Conditions. *J. Electroceram.* **2002**, *9*, 101-110. DOI 10.1023/A:1022898104375

[489] Gao, Y.; Liang, Y.; Chambers, S. A. Thermal stability and the role of oxygen vacancy defects in strong metal support interaction — Pt on Nb-doped $TiO_2(1\,1\,0)$. *Surf. Sci.* **1996**, *365*, 638-648. DOI 10.1016/0039-6028(96)00763-7

[490] Morgan, B. J.; Scanlon, D. O.; Watson, G. W. Small polarons in Nb- and Ta-doped rutile and anatase TiO_2. *J. Mater. Chem.* **2009**, *19*, 5175–5178. DOI 10.1039/b905028k

[491] dos Santosa, D. R.; Henriquesb, V. A. R.; Cairob, C. A. A.; dos Santos Pereira, M. Production of a Low Young Modulus Titanium Alloy by Powder Metallurgy. *Mat. Res.* **2005**, *8*, 439-442.DOI 10.1590/S1516-14392005000400014

List of Abbreviations

AFM atomic force microscopy

BA benzoic acid

CA carboxylic acid

DFT density functional theory

DPA n-dodecylphosphonic acid

DSSC dye-sensitized solar cell

EDX energy-dispersive X-ray spectroscopy

HOMO highest unoccupied molecular orbital

HPA phosphinic acid

IMFP inelastic mean free path

ITO indium tin oxide

IZO indium zinc oxide

LEED low energy electron diffraction

LUMO lowest unoccupied molecular orbital

NEXAFS near-edge X-Ray absorption fine structure

OLEDs organic light emitting diodes

OMBD organic molecular beam deposition

OPV organic photovoltaic cell

OTFT organic thin film transistor

PA phosphonic acid

PAH polycyclic aromatic hydrocarbon

PCE power conversion efficiency

PHPA phenylphosphinic acid

PPA phenylphosphonic acid

PZC point of zero charge

QMS quadrupole mass spectrometer

SAM self-assembled monolayer

SEM canning electron microscopy

TCO transparent conductive oxide

TDS thermal desorption specroscopy

TFPPA trifluorophenylphosphonic acid

TiO$_2$ titanium dioxide

TP thiophenol

UHV ultrahigh vacuum

XPS X-ray photoelectron spectroscopy

XRD X-Ray diffraction

ZnO zinc oxide

ZnPHP zinc-phenylphosphinate

ZnPP zinc-phenylphosphonate

ZnTFPP zinc-trifluorophenylphosphonate

List of Figures

List of Tables

APPENDIX A

Electronic structure of Nb-doped TiO_2

Figure A.1 shows a slice through a (110) plane of the calculated electronic densities of states for rutile TiO_2.[490] Ti and O atoms are illustrated in grey and red respectively. The Nb dopant is shown in green. The charge density is strongly located on single Ti site in a nearest-neighbor position relative to the Nb dopant.
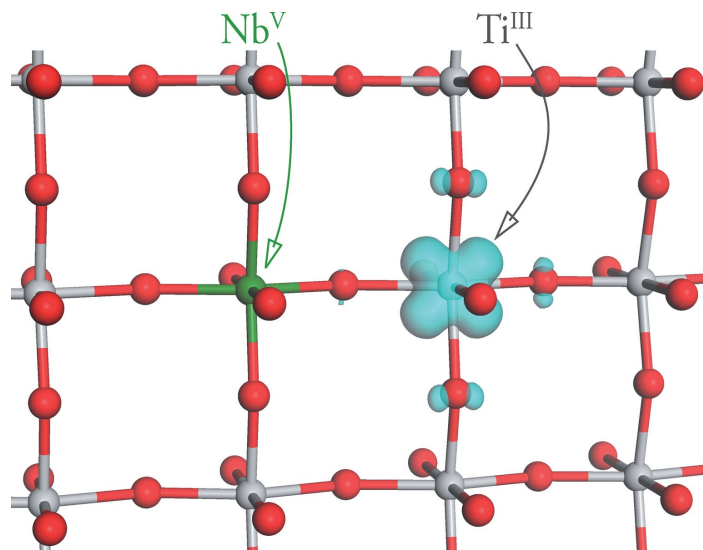
Figure A.1: The charge density distribution in Nb-doped TiO_2.

APPENDIX B

Structural changes in Ti-based materials induced by annealing

Different examples of surface structural changes of Ti-based materials are given below:

- Depending on a composition and a sintering temperature titanium alloys can undergo phase transitions and phase separations resulting in formation of distinct structures illustrated in Figure B.1
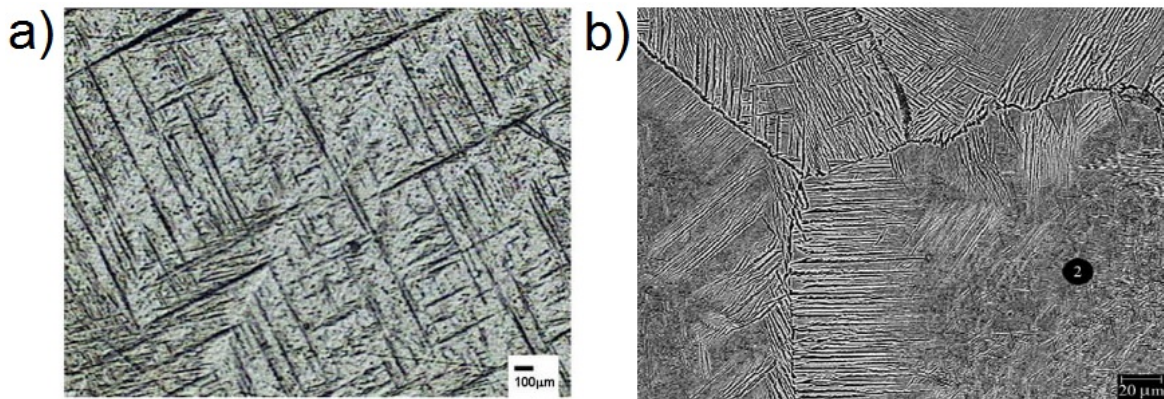
Figure B.1: (a) Optical micrograph of the sample of Ti-6Al-4V heat treated at 1000° C for two hours and cooled in water.[470] The sample exhibits formation of thin lamellar needles characteristic for α phase. (b) SEM micrograph of Ti-35Nb alloy sintered at 1600° C indicating formation of β phase areas.[491]

- Surface reconstruction was observed in Nb and Cr codoped TiO_2 samples leading to surface facetting by reconstruction-induced interlayer stress (cf. Fig. B.2.[474]
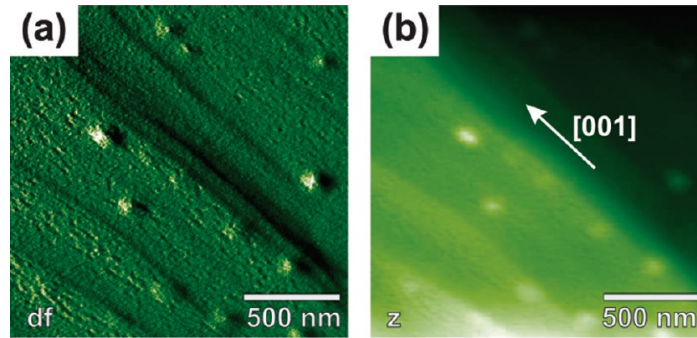
Figure B.2: (a,b) Non-contact AFM topography and frequency shift images of a $TiO_2(110)$ sample codoped with chromium and antimony. Overview images reveal formation of high steps aligned in $[001]$ direction.[474]

- Crystalline precipitations were found on (100) oriented donor-doped $SrTiO_3$ single crystals under the influence of high temperature oxygen annealing (cf. Fig. B.3).[488] Precipitations were identified as accumulations of SrO complexes which concentration increases with increasing Nb-doping level.
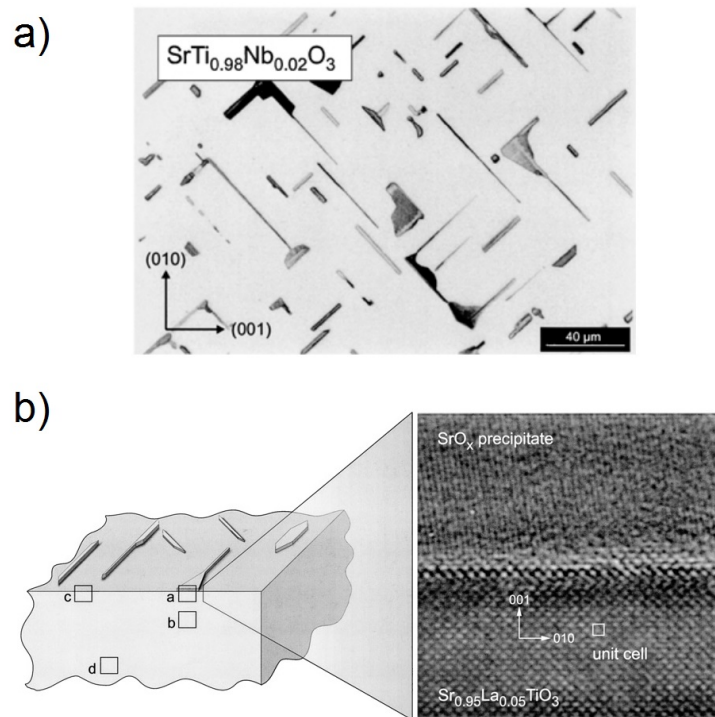
Figure B.3: (a) An optical image of polished 2.0 at.% Nb-doped $SrTiO_3$ single crystal surfaces after oxygen annealing at $1300°\,C$ for $24\,h$. (b) Perovskite/precipitate interface.[488]

APPENDIX C

First experimental results on Nb-doped TiO$_2$ samples with surface defects

---

First measurements to identify the composition of grown structures, in particular Nb excess were carried out. In order to investigate the distribution of Nb in TiO$_2$, EDX measurements were performed.
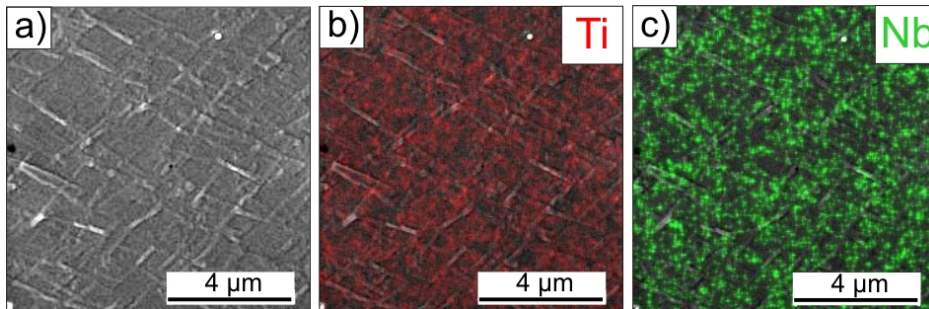
Figure C.1: (a) SEM micrograph of TiO$_2$:Nb (1 1 0) damaged surface. EDX analysis of sample composition reveal homogeneous distribution of (b) Ti and (c) Nb.

Figure C.1 shows a SEM micrograph in panel (a) and elemental mapping for Ti and Nb in panels (b) and (c) respectively. The homogeneous distribution of Nb atoms within the sample is clearly visible. If Nb segregates only in the utmost top layer of titania, the EDX is not sensitive to it, since detected signals are mostly bulk related.

Therefore, the surface composition was further analyzed by means of XPS technique. Figure C.2 demonstrates O*1s* and Ti*2p* spectra of three samples considered as representative: pure TiO$_2$ (red curve), new (black curve) and already several times utilized (blue curve) TiO$_2$:Nb. Binding energies for these spectra are in agreement with values mentioned found
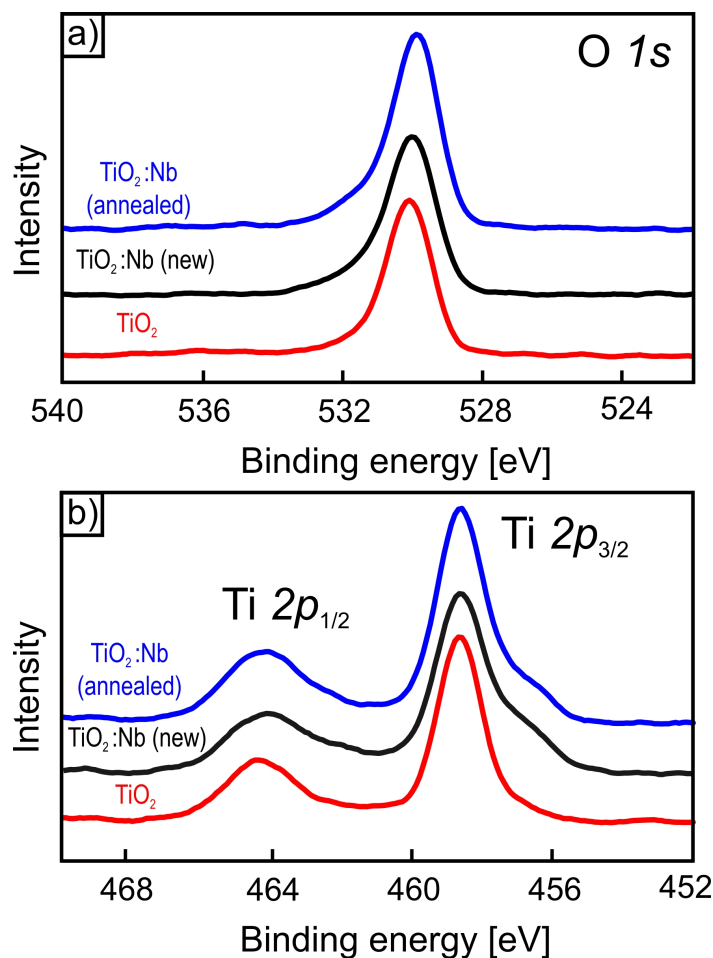
Figure C.2: XP-spectra for (a) O*1s* and (b) Ti*2p* regions of pure TiO$_2$ (red curve) and Nb-doped TiO$_2$: new (black curve) and several times utilized in experiments (blue curve).

in literature.[465] All spectral lines are energy calibrated to the position of Ti*2p* peak. Low energetic shoulders on the spectra for doped titania indicate the presence of Ti^{3+} ions. Figure C.3 (a) illustrates XP-spectra for Nb*3d* region of metal oxides. Signal intensity can be notably enhanced by sputtering samples for 5 minutes. Peak 1 at 220.7 eV corresponds to O*1s* signal excited by third order X-ray beam due to higher order light transmitted in the monochromator. Peaks 2 and 3 at 210.4 eV and 207.6 eV feature Nb $3d_{1/2}$ and $3d_{3/2}$ electrons respectively, which indicates the presence of Nb$_2$O$_5$. However, these spectral lines were found only for the new sample and not present in already used crystals. From that one can see that sample preparation by sputtering and annealing efficiently removes surface contamination. Multiple peaks 4, 5 and 6 at around 200 eV can be attributed to different Nb$_x$O$_y$ oxides, for example NbO. NbC contribution is also presented in this energy window.
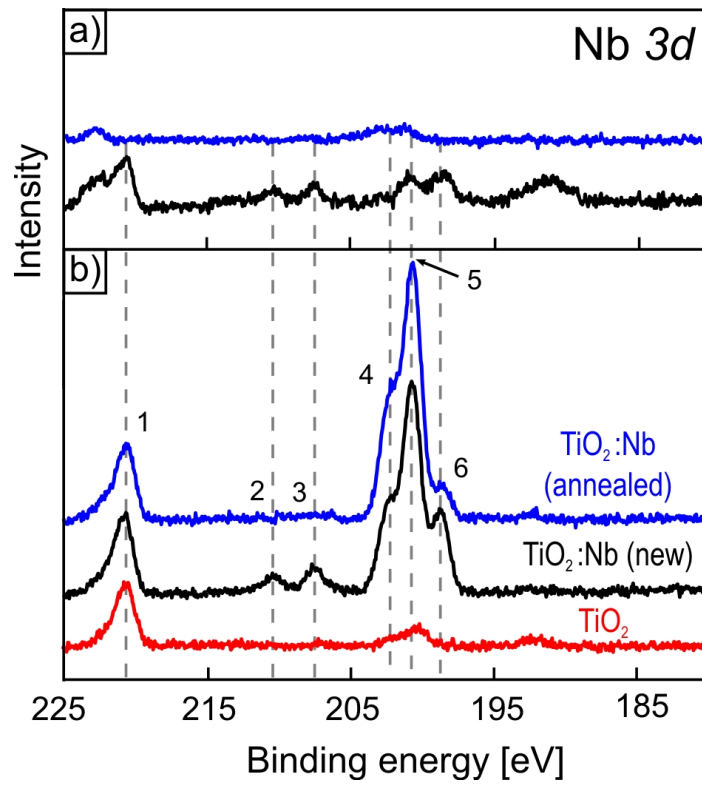
Figure C.3: XP-spectra for Nb*3d* region for TiO_2 samples (a) before and (b) after sputtering. Spectra were reordered for pure TiO_2 (red curve) and Nb-doped TiO_2: new (black curve) and several times utilized in experiments (blue curve).

Curriculum Vitae

Die Seiten 185-186 (Lebenslauf) enthalten persönliche Daten. Sie sind deshalb nicht Bestandteil der Online-Veröffentlichung.

Acknowledgements

and helping me putting pieces together in spite of many kilometers and some hours between us.